Universidade de Aveiro Departamento de Engenharia Mecânica
Ano 2014

NARENDAR NASANI

ÂNODOS PARA PILHAS DE COMBUSTÍVEL DE CERÂMICOS PROTÓNICOS

ANODES FOR PROTONIC CERAMIC FUEL CELLS (PCFCs)

Universidade de Aveiro Departamento de Engenharia Mecânica
Ano 2014

NARENDAR NASANI

ÂNODOS PARA PILHAS DE COMBUSTÍVEL DE CERÂMICOS PROTÓNICOS

ANODES FOR PROTONIC CERAMIC FUEL CELLS (PCFCs)

Tese apresentada à Universidade de Aveiro para cumprimento dos requisitos necessários à obtenção do grau de Doutor em Nanociências e Nanotecnologia, realizada sob a orientação científica do Doutor Duncan Paul Fagg, Investigador Auxiliar do Departamento de Engenharia Mecânica da Universidade de Aveiro.

Apoio financeiro da FCT_Fundação para a Ciência e a Tecnologia, Ministério da Educação e Ciência_ através da Bolsa SFRH/BD/80949/2011 e do Projeto PTDC/CTM/100412/2008.

“Dedicated to my parents, elder brother and sisters”

o júri

presidente

Prof. Doutor Jorge Ribeiro Frade
Professor Catedrático, Universidade de Aveiro

Prof. Doutor Albano Augusto Cavaleiro Rodrigues de Carvalho
Professor Catedrático, Faculdade de Ciências e Tecnologia, Universidade de Coimbra

Doutora Carmen Mireya Rangel Archila
Investigadora Coordenadora, Laboratório Nacional de Energia e Geologia, Lisboa

Doutor Andrei Kavaleuski
Investigador Principal, Centro de Investigação em Materiais Cerâmicos e Compósitos- CICECO, Universidade de Aveiro

Doutor Glenn Christopher Mather
Investigador Principal Contratado, *Instituto de Cerámica y Vidro*-CSIC, Madrid, Espanha

Doutor Duncan Paul Fagg
Investigador Auxiliar, Universidade de Aveiro

agradecimentos

I am sincerely indebted to my supervisor Dr. Duncan Paul Fagg for giving me the opportunity to pursue my PhD thesis work under his guidance. His constant endeavour for quality and incredible work ethic was a supreme source of motivation and excellence in research. With every conversation, the insight and perspectives I acquired were invaluable.

Special thanks to the late Professor Dr. José Grácio for his continuous inspiration and Professor Dr. Antonio Sousa for the incredible support, at TEMA, DEM.

I am also very grateful of Professor Jorge Ribeiro Frade for providing valuable and fruitful research discussions whenever needed throughout my PhD.

I wish to thank Dr. Aleksey A. Yaremchenko and Dr. Andrei Kavaleuski for providing the lab facilities and sharing the equipment on timely occasion during my PhD work.

Experimental work, design, and fabrication would have been infinitely harder without the expertise of Dr. Sergey Mikhalev in the laboratory fuel cell work setups.

I thank my co-workers Paulo A. N. Dias, Isabel Antunes, Dr. Jose Torre, Ana D. Brandao, Devaraj Ramasamy, Sofia Soares, Dr. Pukazh Selvan, Dr. Yang Tao and Dr. Aliaksandr L. Shaula for initial guidance and the establishment of our laboratory, special thanks to Dr. Jose Torre for his constant help regarding automatic LabVIEW program.

I am thankful to Dr. Marc G. Willinger, Department of Inorganic Chemistry, Fritz Haber Institute of the Max Planck Society, Berlin, Germany for performing redox cycling experiments in environmental scanning electron microscope (ESEM).

I would like to express my sincere gratitude to Dr. Budhendra Singh Post-doctoral fellow at NRD-TEMA, UA for sharing his wealth of knowledge during my PhD.

I wish to thank Ricardo Beja and Carla Lopes for their social conversations in the office. I would also like to thank all NRD, TEMA, DEM, UA members who has supported me during my PhD.

I feel a deep sense of gratitude to my family, especially my parents, Nirmala and Markendeya, whose many sacrifices and support allowed me to reach my educational goals. I must be grateful to my elder brother Ravi for his continuous support and persistent inspiration for my journey in life. Thanks to my sisters for keeping me well-grounded throughout my years at UA.

I am very grateful to all my friends in Aveiro whom I shared my happiness and sadness and their encouragement (when needed) during the Ph.D.

Finally, I would like to acknowledge the support of FCT, DEM, UA for providing the majority of the funding for this work.

Last but not the least I would like to express my gratitude to all those made the completion of this thesis possible.

palavras-chave

Ânodos, pilhas protónicas cerâmicas de combustível, pilhas de combustível de óxido sólido, protões condutores, resistência de polarização, espectroscopia de impedância, cermetos.

resumo

A pilha de combustível de cerâmicos protónicos (PCCP) é uma das mais promissoras possibilidades para a produção de energia elétrica “verde”. As PCCPs oferecem uma tecnologia limpa para a produção eletroquímica de energia elétrica com elevada eficiência. De forma a reduzir os custos de fabricação e melhorar a longevidade destes equipamentos é necessário reduzir a temperatura de operação das pilhas de combustível de óxido sólido (PCOSs) para o intervalo 500-700 °C. Este objetivo pode ser alcançado recorrendo às pilhas de combustível de cerâmicos protónicos (PCCPs) devido à superior condutividade do eletrólito face às tradicionais membranas condutoras iónicas. Esta tese baseia-se em cermetos anódicos de Ni-$BaZr_{0.85}Y_{0.15}O_{3-\delta}$, que correspondem ao material do estado-da-arte para PCCPs. O estudo das PCCPs encontra-se ainda no seu estágio inicial e até ao momento apenas alguns métodos foram desenvolvidos para preparar ânodos adequados através da moagem de alta-energia dos precursores de óxidos cerâmicos ou da síntese por combustão de nitratos. Esta tese pretende destacar as desvantagens destes métodos tradicionais de preparação de ânodos e, em vez disso, oferecer um novo, mais eficiente, de mais baixo custo e sem recorrência ao uso de nitratos, método de preparação de cermetos anódicos de Ni-$BaZr_{0.85}Y_{0.15}O_{3-\delta}$ para PCCPs.

No estudo dos cermetos anódicos foram utilizadas diversas técnicas experimentais, nomeadamente, difração de raios X (DRX), microscopia eletrónica de varrimento (MEV), microscopia eletrónica de varrimento ambiental (MEVA) e espetroscopia de impedância eletroquímica (EIE). Este trabalho inclui também uma análise fundamental dos aspetos relacionados com o efeito da porosidade, o comportamento *redox*, o papel da fase de óxido condutor protónico nos cermetos anódicos e ainda os últimos avanços do desempenho eletroquímico de um dos mais importantes materiais de ânodo para PCCPs.

O estudo do comportamento sob polarização destes materiais foi executado em função da temperatura (T), da pressão parcial de vapor de água (pH_2O), da pressão parcial de hidrogénio (pH_2) e também da pureza da fase, em elétrodos de microestrutura comparável. A 600 °C, o espetro de impedância apresenta em geral dois arcos: R2 nas altas frequências e R3 nas baixas frequências, que correspondem à resistência de polarização do elétrodo (Rp). Os resultados mostram que as respostas R2 e R3 correspondem, respetivamente, ao transporte de espécies condutoras protónicas e ao fenómeno de adsorção dissociativa do H_2 na superfície do elétrodo. Também, foi demonstrado que o valor de Rp é fortemente afetado pela porosidade, pelo que este atingiu o valor mais baixo no cermeto com menor nível de porosidade, em condições de operação.

Resumo (cont.)

Deste modo, este resultado descarta o uso de agentes porogéneos, muitas vezes utilizados na preparação dos materiais de ânodos quando estes são constituídos por condutores de iões óxido. Relativamente à avaliação da estabilidade em conduções oxidantes e redutoras, foi demonstrado que o comportamento sob polarização é extremamente comprometido pelo ciclo *redox* utilizado. Medidas *in-situ* através de microscopia eletrónica de varrimento ambiental (MEVA) revelaram que a degradação continua devido à expansão em volume da fase de Ni durante o estágio de reoxidação. As células eletroquímicas testadas em condições reais de operação (pilha de combustível), constituídas por um suporte anódico otimizado de Ni-$BaZr_{0.85}Y_{0.15}O_{3-\delta}$, sem uso de porogéneos, e um filme fino de eletrólito de BCZY44 apresentam resultados promissores a temperaturas intermédias, assegurando uma boa durabilidade e um desempenho global que excede os dados encontrados na literatura até ao momento.

.

keywords

Anodes, Protonic Ceramic Fuel Cells, Solid Oxide Fuel Cells, proton conductors, polarization resistance, electrochemical impedance spectroscopy, cermets.

abstract

One of the more promising possibilities for future “green” electrical energy generation is the protonic ceramic fuel cell (PCFC). PCFCs offer a low-pollution technology to generate electricity electrochemically with high efficiency. Reducing the operating temperature of solid oxide fuel cells (SOFCs) to the 500-700°C range is desirable to reduce fabrication costs and improve overall longevity. This aim can be achieved by using protonic ceramic fuel cells (PCFCs) due to their higher electrolyte conductivity at these temperatures than traditional ceramic oxide-ion conducting membranes. This thesis deals with the state of the art Ni-$BaZr_{0.85}Y_{0.15}O_{3-\delta}$ cermet anodes for PCFCs. The study of PCFCs is in its initial stage and currently only a few methods have been developed to prepare suitable anodes via solid state mechanical mixing of the relevant oxides or by combustion routes using nitrate precursors. This thesis aims to highlight the disadvantages of these traditional methods of anode preparation and to, instead, offer a novel, efficient and low cost nitrate free combustion route to prepare Ni-$BaZr_{0.85}Y_{0.15}O_{3-\delta}$ cermet anodes for PCFCs. A wide range of techniques mainly X-ray diffraction (XRD), scanning electron microscopy (SEM), environmental scanning electron microscopy, (ESEM) and electrochemical impedance spectroscopy (EIS) were employed in the cermet anode study. The work also offers a fundamental examination of the effect of porosity, redox cycling behaviour, involvement of proton conducting oxide phase in PCFC cermet anodes and finally progresses to study the electrochemical performance of a state of the art anode supported PCFC.

The polarisation behaviour of anodes has been assessed as a function of temperature (T), water vapour (pH_2O), hydrogen partial pressures (pH_2) and phase purity for electrodes of comparable microstructure. The impedance spectra generally show two arcs at high frequency R2 and low frequency R3 at 600 °C, which correspond to the electrode polarisation resistance. Work shows that the R2 and R3 terms correspond to proton transport and dissociative H_2 adsorption on electrode surface, respectively. The polarization resistance of the cermet anode (Rp) was shown to be significantly affected by porosity, with the PCFC cermet anode with the lowest porosity exhibiting the lowest Rp under standard operating conditions. This result highlights that porogens are not required for peak performance in PCFC anodes, a result contrary to that of their oxide-ion conducting anode counterparts. *In-situ* redox cycling studies demonstrate that polarisation behaviour was drastically impaired by redox cycling. In-situ measurements using an environmental scanning electron microscopy (ESEM) reveal that degradation proceeds due to volume expansion of the Ni-phase during the re-oxidation stage of redox cycling.

Abstract (cont.)

The anode supported thin BCZY44 based protonic ceramic fuel cell, formed using a peak performing Ni-$BaZr_{0.85}Y_{0.15}O_{3-\delta}$ cermet anode with no porogen, shows promising results in fuel cell testing conditions at intermediate temperatures with good durability and an overall performance that exceeds current literature data.

INDEX

List of Figures

List of Tables

List of Abbreviations and Symbols

ASR	Area specific resistance
BaY_2NiO_5	Barium yttrium nickelate
$Ba(NO_3)_2$	Barium nitrate
$BaCO_3$	Barium carbonate
BZO	Barium zirconate
BZY	Yttrium doped barium zirconate
CO_2	Carbon dioxide
EDS	Energy dispersive X-ray spectroscopy
EIS	Electrochemical impedance spectroscopy
H_2O_2	Hydrogen peroxide
Ni	Nickel
OCV	Open circuit voltage
pO_2	Oxygen partial pressure
pH_2	Hydrogen partial pressure
pH_2O	Water vapour partial pressure
PCFCs	Protonic Ceramic Fuel Cells
Pr_2NiO_4	Praseodymium nickelate
TPB	Three phase boundary length
R1	Ohmic resistance
R2	High frequency polarization resistance
R3	Low frequency polarization resistance
R4	Lowest frequency polarization resistance
Rp	Total polarization resistance
SOFCs	Solid Oxide Fuel Cells
SEM	Scanning electron microscopy
XRD	X-ray diffraction
YSZ	Yttria stabilized zirconia

Chapter 1

Introduction to Protonic Ceramic Fuel Cells

Abstract

Fuel cells are promising green energy devices to directly convert chemical energy of a fuel to electrical energy, with high efficiency, and silently. This chapter describes an introduction to fuel cells, with predominant focus on Protonic Ceramic Fuel Cells (PCFCs). The types of fuel cells, their principle operation and the choice of materials for PCFCs are briefly presented.

1.1 Introduction and Historical background

There are growing concerns over the acceleration of global warming and the serious consequences of climate change that arise due to massive increases in carbon dioxide emissions from intensified production and consumption of fossil fuels. A diversified energy system with wider access to renewable energies as well as highly efficient clean technologies for the use of petrochemical resources must be developed to incrementally reduce our heavy reliance on fossil fuels [1]. So far, significant efforts have been devoted to the developments of sustainable energy harvesting technologies, such as wind energy, solar panels etc. Nonetheless, efficient solutions to store the energy produced by these sustainable sources are yet to be finalized. At present, hydrogen is one potential energy carrier that can be synthesized efficiently; however, technical barriers related to its storage and distribution have contributed to the resistance that hydrogen has encountered in becoming practically viable despite a high gravimetric energy density and zero carbon emission [2, 3]. However, it is widely recognized that the development and the widespread use of fuel cell (FC) technology will become a keystone in the near future in this type of chemical to electrical energy conversion.

Sir Humphrey Davy described the first fuel cell concept in the early 18^{th} century by observing the decomposition of water into hydrogen and oxygen with passage of current, a process now known as electrolysis. In 1839, Sir William Grove built the first hydrogen-oxygen fuel cell using liquid electrolytes based on the reverse electrolysis of water concept described by Davy. Grove's "fuel cell" consisted of a zinc anode in sulphuric acid (liquid electrolyte) and a platinum cathode in nitric acid separated by a porous ceramic plate [4-6]. In 1899, Nernst investigated the electrical conduction of stabilized zirconia (ZrO_2) (in this case yttria (Y_2O_3) stabilized zirconia) showing it to be an insulator at room temperature but to possess ionic conduction at higher temperatures (>600 °C) [4, 5]. After this discovery, yttria stabilized zirconia (YSZ) became the most widely used solid oxide electrolyte in fuel cell applications [5]. Since then, fuel cell technology received regular attention during the 19^{th} century and this interest continues up to the present day. Recently the U.S department of energy (DOE) released a list documenting the main potential markets for fuel cell technology, these being stationary power (backup power or combined heat and power-

CHP), transportation power (Fuel cell electric vehicles and auxiliary power units) and portable power [4, 5, 7].

Several leading industrial companies (R&D investments) have successfully started commercializing the fuel cell technology. Some of the largest are, UTC Power (PureCell 400 system, based on phosphoric acid), Ballard power systems (FCgen, ClearGen), Hydrogenics corporation, Ceramic Fuel Cells, Australia., Siemens-Westinghouse, recently Bloom Energy, U.S., Panasonic, Japan and ENEOS CellTech, Japan [7].

A wide range of different fuel cells types have been developed that mainly differ from each other by the type of ionically conducting electrolyte and also their characteristic operation temperature range. On the other hand, common to all devices, are the major challenges of fabrication cost, efficiency and durability; factors that must be solved by choice of material and design engineering [8, 9].

1.2 Fuel Cells

Fuel cells are electrochemical devices that directly convert chemical energy into electrical energy with extremely high efficiencies. The basic structure of a fuel cell consists of an anode and a cathode separated by an electrolyte as shown in figure 1.1 [10]. The operating principle is similar to that of a battery, with the fundamental difference that in a fuel cell the chemical energy is provided by a fuel and an oxidant that are stored outside the cell, allowing fuel cell power generation as long as the reactants are supplied to the electrodes. Furthermore, compared with internal combustion engines, fuel cells produce lowered amounts of pollutants and allow large scalability, making the production of energy from mW to hundreds kW possible, while maintaining high efficiency; in other words, fuel cells can be used both for stationary and portable applications [3].

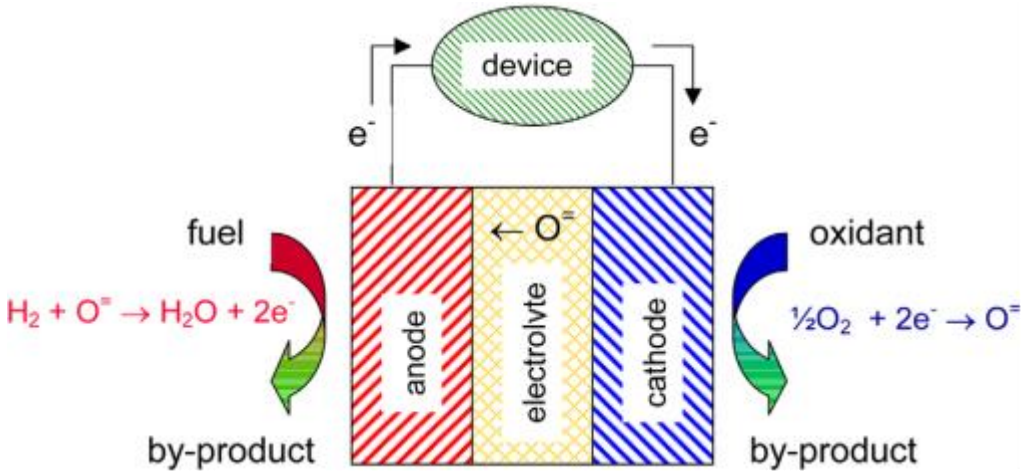

Figure 1.1 Schematic of a fuel cell comprised of an electrolyte, anode and a cathode [11]

1.2.1 Fuel cell types and its characteristics

The various types of fuel cells are generally classified on the basis of their electrolyte material, such as proton exchange membrane (PEMFC), molten carbonate (MCFC), solid oxide (SOFC) and phosphoric acid (PAFC) (table 1.1). Among them, SOFCs are very promising because they offer flexibility in terms of the type of fuel that can be used (e.g. hydrogen or hydrocarbons) and also do not contain corrosive liquids, as opposed to MCFCs for instance [11].

The majority of fuel cells being developed or used depends on the type of application. Generally, Proton Exchange Membrane Fuel Cells (PEMFC) are used for transportation power generation [12]; Direct Methanol Fuel Cells (DMFC) for portable power generation [13]; Alkaline fuel cells (AFC) for space program for producing electricity and drinking water for astronauts; Phosphoric Acid Fuel Cells (PAFC), Molten Carbonate Fuel Cells (MCFC) and Solid Oxide Fuel Cells (SOFC) [2, 14] for stationary power generation applications. Many other fuel cells are also being developed as some crossover of application for niche markets of the aforementioned fuel cells.

Table 1.1: Various types of fuel cells and its characteristics

Type	Temperature °C	Fuel	Electrolyte	Mobile Ion	Efficiency
polymer electrolyte membrane (PEM) & DMFC	70-110	H_2, CH_3OH	Sulfonated polymers	$(H_2O)_nH^+$	40%
Alkali Fuel cell (AFC)	100-250	H_2	Aqueous KOH	OH^-	40%
Phosphoric acid fuel cell (PAFC)	150-250	H_2	H_3PO_4	H^+	40%
Molten carboante fuel cell (MCFC)	500-700	Hydrocarbons, CO	$(Na,K)_2CO_3$	CO_3^{2-}	55-65%
Solid oxide fuel cell (SOFC)	700-1000	Hydrocarbons, CO	$(Zr,Y)O_{2-\delta}$	O^{2-}	55-65%
Protonic ceramic fuel cell (PCFCs)	400-700	Hydrocarbons, methanol, ammonia, H_2	$BaCeO_3$-$BaZrO_3$	H^+	55-65%

High power densities can be provided by alkali fuel cells but these are considered to be impractical for many applications because of the need to remove trace CO_2 from both the fuel and oxidant streams in order to prevent reaction of the electrolyte to form solid, non-conducting alkali carbonates [14]. The leading technologies in the early 1990s, phosphoric acid fuel cells, also have been largely abandoned due to their inability to reach high power densities, while molten carbonate fuel cells suffer from the difficulties of containing a corrosive liquid electrolyte [11]. In particular, dissolution of NiO at the cathode and its precipitation in the form of Ni at the anode can result in electrical shorts across the electrolyte in molten carbonate fuel cells and these can only be operated at higher temperatures and for stationary power generation. However, this short summary highlights that a wide range of fuel cells is being developed that each have their own merits and demerits [2, 3, 11].

1.2.2 Efficiency of fuel cells

Fuel cells are more efficient than combustion engines since these devices are not subject to the Carnot efficiency limit [4, 8, 9]. The efficiency of a fuel cell can be classified based on fuel cell type, temperature, fuel composition and its utilization. The overall cell efficiency can be defined as the ratio of electrical power produced divided by the Gibbs free energy change or the enthalpy change of electrochemical reaction [4]. In high temperature fuel cells (SOFCs), mainly ohmic, activation and concentration polarisation losses are important, detracting from overall efficiencies [4]. The theoretical Nernst voltage and cell voltage (V) to current density is shown in figure 1.2 [4].

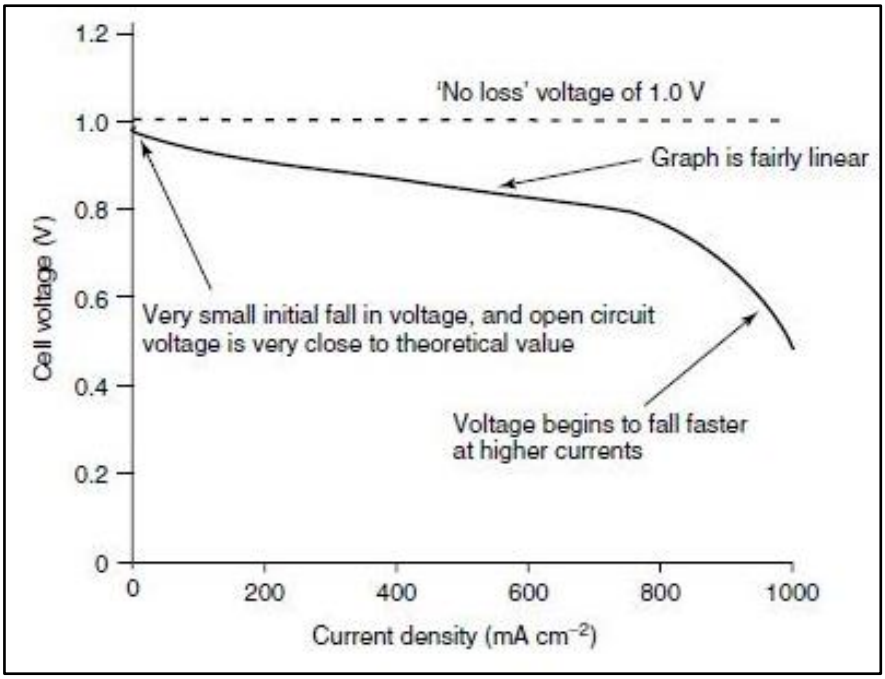

Figure 1.2 Cell voltage vs current density curve for a typical high temperature fuel cell [4]

The actual voltage obtained during the cell operation with electronic load is slightly lower than the theoretical voltage (Nernst voltage) due to losses such as, ohmic (IR), activation Aln(i/i_0), fuel crossover and internal current leakage Aln(in/i_0), and mass transport or concentration losses mexp(ni) [4]. The combination of all these losses can be written as

$$V = E - IR - A\,ln\left(\frac{i + i_n}{i_0}\right) + m\,exp(ni) \qquad (1.1)$$

Where E- reversible OCV; I- the current density, A/cm^2; R– area specific resistance (ASR), Ω/cm^2, A– coefficient in natural logarithm form of Tafel equation, V; i_n– fuel crossover current density, Ω/cm_2; i_0– exchange current density at an electrode/ electrolyte interface, Ω/cm^2; m, n– constants in the mass-transfer overvoltage.

1.3 Protonic Ceramic Fuel Cells (PCFCs)

Solid oxide fuel cells (SOFCs) potentially offer a low-pollution technology to generate electricity electrochemically, with high efficiency, from alternative hydrogen or bio-derived fuel stocks [15]. Reducing the SOFC operating temperature to the 400-700°C range is desirable to reduce fabrication costs and improve longevity [11, 16]. This aim can be facilitated by the use of proton conducting oxides as the electrolyte membrane. SOFCs that contain a proton conducting ceramic electrolyte are called protonic ceramic fuel cells (PCFCs). These devices provide a further advantage in that they form water at the cathode, hence, the fuel does not become diluted during cell operation. PCFC is of substantial interest since it has considerably high system efficiency compared to other fuel cell systems with potential cogeneration because of high operating temperatures, the potential ability to work on both hydrogen and hydrocarbon fuels and negligible deterioration in performance over several years [2, 3, 15].

The major difference between the SOFC, and PCFC types of fuel cells is, therefore, the type of mobile species, either oxide-ions or protons, respectively, which in turn alter the side in which the steam is produced, the cathode in the PCFCs and at the anode in the O^{2-}-SOFCs [2, 3, 15, 17], Fig. 1.3. In PCFCs hydrogen is oxidized at the anode, to form protons that pass through the electrolyte while meeting at the three phase boundary (TPB). At the cathode, these protons react with oxygen to produce steam [18]. The formation of the steam in the cathode side of PCFCs avoids the dilution of fuel, fig. 1.3(b). Moreover, the use of proton conducting ceramic oxides as electrolyte materials may reduce the operating temperature of SOFCs since the activation energy for proton conduction is smaller than the typical activation energy for oxygen migration [2, 18]. However, the

formation of water in the cathode side of PCFCs has been documented to result in larger cathode polarization resistances [17].

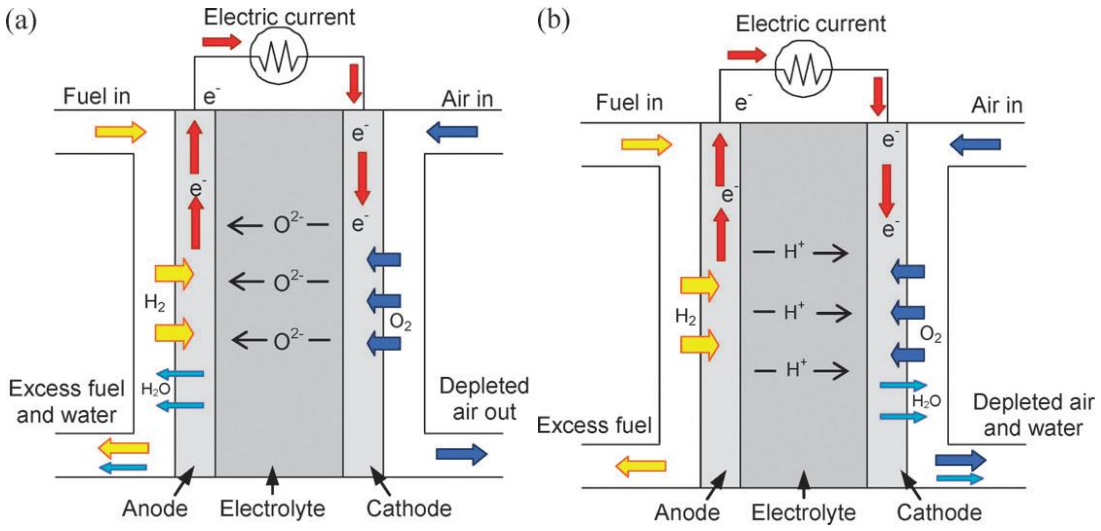

Figure 1.3 The illustration of operating principle of (a) O^{2-}-SOFCs and (b) PCFCs [19]

1.3.1 Working Principle

A PCFC is an all solid-state system comprised of proton conducting solid electrolyte sandwiched between two porous electrodes (the anode and the cathode). The working principle of PCFC is illustrated in Figure 1.3(b). In PCFCs, the fuel (hydrogen or alternative hydrocarbons) is oxidised at anode side by creating protons and releasing electrons while oxygen (from air) is reduced at cathode side. The protons formed at anode side migrate through the electrolyte towards cathode side where the formation of water takes place by reacting with oxygen. The difference in the chemical potential of gases at the electrodes is responsible for the movement of the ionic species. However, the electrochemical reactions occur mainly at electrode/electrolyte interface, within a range of few micrometers into the electrodes from the electrolyte [8, 9]. This interfacial zone is termed as the functional layer while the remaining part of the electrode is primarily a current collector microstructure that should be porous to allow gas access to the functional layer [8, 9]. The electrolyte must be dense enough and gas tight to avoid the direct mixing of fuel and oxidant gases. In PCFCs, both the electrolyte and electrodes are composed

based on stable ceramic materials. The current density is obtained under cell operating conditions as long as the fuel and oxidant gases are provided to the cell. An open circuit voltage (OCV) of ~1 volt is attained when the cell is at unloaded state [4, 8, 9], defined by the Nernst potential [4], which is expressed as

$$E = E^0 - \frac{RT}{2F} \ln \left[\frac{pH_2O}{pH_2 . \sqrt{pO_2}} \right] \qquad (1.2)$$

Where, E = Nernst potential

R = Universal gas constant

T = Temperature

F = Faraday constant

pH_2, hydrogen partial pressure

pH_2O, water vapour partial pressure

pO_2, oxygen partial pressure

As the maximum voltage of a single cell is close to 1V, in order several cells must be connected in series to form a so called fuel cell "stack" to obtain higher voltages for practical application purposes [5]. A stack can be defined as a set of cells; where each cell is separated by an interconnector, whereas, the fuel cell plant is designed based on the desired power in stacks, connected either in series or parallel [4, 8, 9].

1.3.2 Choice of materials for PCFCs

A PCFC is composed of two electrodes (the anode and the cathode) and a ceramic proton conducting solid electrolyte. Each and every component of the PCFC must be tailored to their specific function and, thus, must meet certain requirements [3, 5]. These are:

- tolerable chemical and structural stability during the cell operation at high temperatures
- suitable conductivity (ionic for the electrolyte and electronic or mixed electronic and ionic to function as an electrode).

- proper percolation pathway between metallic and ceramic phase in anodes
- no inter-diffusion of elements between the cell component materials
- should possess similar thermal expansion among the cell components, to avoid cracking during the fabrication and cell operation
- gas tight and dense electrolyte to prevent gas mixing
- porous electrodes to allow the gas transport near to the reaction sites
- good mechanical strength

In addition to the above criteria for PCFCs, the component materials must be of low cost, offer easy fabrication and should not affect the sequential fabrication processing upon addition of further cell components. The ceramic materials used for protonic ceramic fuel cells are described below.

1.3.2.1 Electrolytes

Proton conducting ceramic oxides are promising candidates as electrolytes for PCFCs at intermediate temperatures (400-700 °C) since in this temperature range they show larger ionic conductivities and smaller activation energies than conventional oxide-ion conducting electrolytes [18, 19]. The general formula of typical proton conducting perovskite oxides can be written as $AB_{1-x}R_xO_{3-\delta}$, where A and B represent the main crystallographic cation sites, R represents an acceptor dopant and where δ is the oxygen deficiency per unit cell. The substitution of the acceptor R dopant in the B site serves to create oxygen vacancies, which are required for subsequent hydration and proton conduction. Fig. 1.4 shows the ABO_3 perovskite structure. The cation B, which is usually a transition metal or a rare earth, typically has a valency of +4 and forms a six-coordinated octahedron with its neighboring oxygen ions, being itself located in the centre. The cation, A which generally has a larger ionic radius than the cation B, presents a typical valency of +2, and possesses a coordination number of 12 [2].

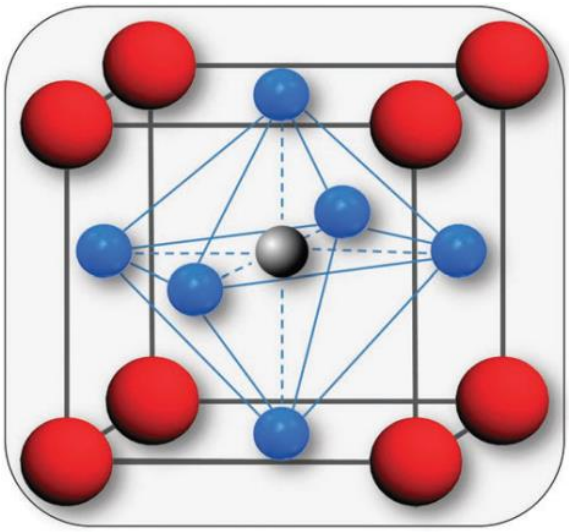

Figure 1.4 Perovskite type crystal structure (ABO_3), where the red and grey spheres are the cations A and B respectively, and the blue spheres are the oxygen ions [2]

To date, acceptor doped barium cerate ($BaCeO_3$) and barium zirconate ($BaZrO_3$) perovskite materials have dominated the research field of high temperature proton conductors. Although doped $BaCeO_3$ materials exhibit the larger total conductivities, they have been shown to be chemically unstable in H_2O and CO_2-containing atmospheres, resulting in electrolyte degradation and difficult fuel cell deployment [3, 20, 21]. In contrast, acceptor doped $BaZrO_3$ materials are regarded as potential candidates for electrolytes in PCFCs as they show an excellent chemical stability against H_2O and CO_2, as well as high bulk proton conductivity [2, 22, 23]. The bulk proton conductivity of BZY material is compared with other proton conducting and oxide-ion conducting materials, as shown in Fig. 1.5[18], highlighting its advantageous conductivity at intermediate temperatures. Owing to its high proton mobility and entropically stabilized protonic defects, even at high dopant concentrations (20% Y) and high solubility limit, this material is considered as a promising proton conductor for various applications including protonic ceramic fuel cells running on hydrogen, methane, ammonia and hydrazine [24, 25], and for hydrogen permeable separation membranes [15, 18].

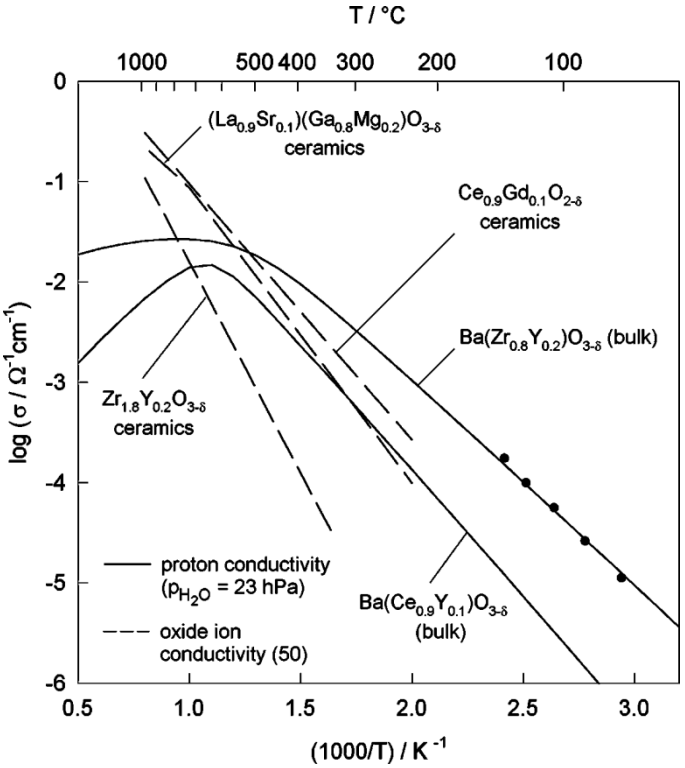

Figure 1.5 Bulk conductivity of $BaZr_{0.8}Y_{0.2}O_{3-\delta}$ compared with the proton conductivity of $BaCe_{0.9}Y_{0.1}O_{3-\delta}$ and the oxide ion conductivity of the best oxide ion conductors [18]

Nonetheless, the sinterability of BZY is notoriously poor, necessitating extremely high temperatures (~1600–1800 °C) to densify the $BaZrO_3$-based electrolyte membranes. Such high temperatures can lead to barium evaporation, which has been reported to reduce conductivity [23], while the difficult sintering also hinders grain growth causing a large grain boundary volume content to be present for BZY that limits total conductivity, due to the highly resistive nature of BZY grain boundaries to proton transport. Thus, improving the total conductivity of dense BZY membranes still remains a great challenge [2, 20]. Such elevated temperatures can also seriously complicate cell fabrication, by typical co-sintering techniques, due to elemental inter-diffusion between components [2, 17, 21-23, 26]. The most used strategy to overcome the BZY sintering problems is the use of transition metal oxides to promote densification [2, 20]. However, often it has been demonstrated that these sintering aids have a negative impact on the bulk BZY proton conductivity. Therefore, solving the BZY densification problem, without using sintering aids is still an ongoing goal for PCFC development and, thus, studies on high temperature

proton conducting electrolytes remain at the fundamental stage for use in PCFC applications.

The chemical stability of barium cerates can be increased by the introduction of zirconium (e.g. $Ba(Ce,Zr)_{1-y}Y_yO_{3-\delta}$) [26, 27]. However, this advantage comes at the cost of the level of total conductivity. Despite this limitation, it has been shown that upon adjustment of the Ce:Zr ratio, one can achieve a compromise between the achievement of chemical and mechanical stability, while still retaining adequate conductivity for practical application [26-28]. The introduction of 40% Ce into Zr site or vice versa improves the chemical stability of $BaCeO_3$ and sinterability, while maintaining acceptable global proton conductivity [28, 29]. In proton conducting oxides, conduction occurs by the formation of protonic defects. These defects form from the dissociation of water vapour into a hydroxide ion and proton [18], then this hydroxide ion occupies an available oxide ion vacancy in the crystal structure with the formation of a covalent bond between the proton and a lattice oxygen. In Kroger-Vink notation [18] this process can be expressed as

$$H_2O + V_O^{\bullet\bullet} + O_O^x \leftrightarrow 2OH_O^{\bullet} \qquad (1.3)$$

The proton conducting perovskite oxides $BaZr_{0.85}Y_{0.15}O_{3-\delta}$ (BZY15), $BaCe_{0.7}Zr_{0.1}Y_{0.2}O_{3-\delta}$ (BCZY71) and $BaCe_{0.4}Zr_{0.4}Y_{0.2}O_{3-\delta}$ (BCZY44) are used as electrolytes in the present thesis.

1.3.2.2 Cermet anodes

The state-of-the-art cermet anode for a PCFC currently mirrors that of anodes for oxide-ion conducting SOFC, being a composite material composed of nickel and a ceramic ionically conducting phase, patented by Spacil [30]. This type of cermet structure can successfully limit polarisation losses by maximising the three phase boundary length (TPB), by maximising the interface between the ionically-conducting, the electronically-conducting and the gaseous phases. For oxide-ion conducting SOFC anodes a large body of theoretical research exists to indicate that the electrode performance of such structures should increase as the microstructure becomes finer, as long as enough porosity is maintained to prevent gas phase limitations [31]. Thus, nanoscale control of SOFC cermet

anode microstructure has become a hot topic. Nonetheless, nanostructuration is often shown to be incompatible with the additional anode requirements of high mechanical strength, sufficient gas phase diffusion, high ionic conductivity, carbon and sulphur tolerance and longevity [32]. These problems still plague oxide-ion conducting SOFC design and continue to hinder their implementation in the marketplace

In the case of PCFCs, the cermet material is formed between Ni and a ceramic proton conducting phase, such as the highly stable material yttrium doped barium zirconate (BZY). This thesis mainly deals with Ni-BZY cermets containing 60vol% proton conducting ceramic oxide (BZY) and 40vol% nickel, as a minimum requirement to obtain percolation in the anode. The existence of pores in the anode allows gas diffusion, while the reduced nickel provides electronic percolation paths and catalytic properties. The reason behind the selection of a cermet anode is the possibility to increase the number of electrochemically active reaction sites per nominal electrode area, an important characteristic of SOFC anodes in terms of microstructure [33]. However, it remains a very important and open topic to attain basic knowledge on PCFC anodes due to their current infancy. Such work is especially interesting since both nickel and BZY are protonic carriers in PCFC anode cermets, which can extend the three phase boundary length (TPB) over that which would possible in oxide-ion conducting SOFC anodes where ionic mobility is limited to solely the ceramic phase. Due to this feature, it is interesting to study if the level of proton conductivity offered by the ceramic oxide matrix can influence the electrochemical performance of these PCFC anodes, and, thus, to know if performance is limited when protonic transport in the matrix is insufficient. The possible kinetic steps involved in fuel (hydrogen) oxidation on nickel particles and a nickel cermet anode with a proton conducting phase is illustrated in Fig. 1.6 [21]. Here, it can be noted that the proton conducting phase can enhance the three phase boundary length (TPB) active sites through the transfer of protons (H^+) to electrolyte [21]. Here the overall hydrogen oxidation reaction taking place at the anode can be expressed as

$$H_2 + 2O_O^x \rightarrow 2OH_O^\bullet + 2e^- \qquad (1.4)$$

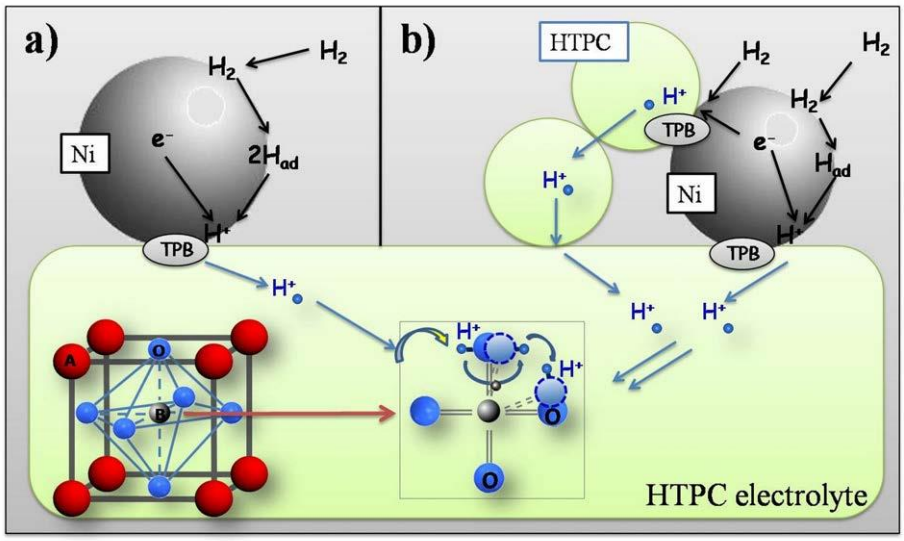

Figure 1.6 The mechanism of hydrogen oxidation at anode site (a) nickel and (b) nickel cermet-containing proton conducting oxide [21]

Preliminary experiments have studied Ni-$CaZr_{0.95}Y_{0.05}O_{2.975}$ (Ni-CZY) and Ni-$SrZr_{0.95}Y0.05O_{2.975}$ (Ni-SZY) cermet anodes for PCFCs prepared by similar methods, and have suggested that the overall polarization resistance is sensitive to the level of proton conductivity in the ceramic-oxide phase [34]. The Ni-CZY anode was shown to produce a higher polarisation resistance than Ni-SZY cermet anode and this was suggested to be related to the higher proton conductivity of $SrZr_{0.95}Y_{0.05}O_{2.975}$ with respect to $CaZr_{0.95}Y_{0.05}O_{2.975}$ [34]. Based on this knowledge, the best choice for the matrix material may be that of the Ba-based perovskite materials, due to their superior proton conductivities. Nevertheless, cermet anodes that contain $BaCeO_3$-based matrices may be unsuitable for practical operation in alternative carbonaceous fuels, due to the instability of $BaCeO_3$ in H_2O and CO_2 containing atmospheres [21, 26]. On the contrary, acceptor doped $BaZrO_3$-based materials demonstrate higher chemical stability in H_2O and CO_2 containing atmospheres and, thus, may be more promising for use as anode cermet matrixes in these devices [2, 21].

The following PCFC cermet anodes have been formed with perovskite, matrix compositions, up to the present time, Ni-$Ca(Zr,Y)O_{3-\delta}$ and Ni-$Sr(Zr,Y)O_{3-\delta}$ [34], Ni-$Ba(Zr,Y)O_{3-\delta}$ [35, 36], Ni-$Ba(Ce,Y)O_{3-\delta}$ [37, 38], Ni-$SrCe_{0.9}Yb_{0.1}O_{3-\delta}$ [39], Ni-$Ba(Ce,Zr,Y,Yb)O_{3-\delta}$ [40] and Ni-$Ba(Ce,Zr,Y)O_{3-\delta}$ [41]. Bi et al. studied composite NiO-

$BaZr_{0.8}Y_{0.2}O_{3-\delta}$ anodes with varying weight ratios of nickel to BZY and they found that (50:50wt%) NiO-BZY composite anode shows the lower polarization resistance [35]. They also proved that the composite anode $BaCe_{0.7}Zr_{0.1}Y_{0.2}O_{3-\delta}$–NiO (50:50 weight ratio, BCZY71-NiO) was unstable in CO_2 and H_2O containing atmospheres, due to the decomposition of BCZY71 into carbonates and hydroxides, thus, being an anode matrix composition that is unsuitable for PCFCs. Another PCFC composite anode Ni-$BaCe_{0.9}Y_{0.1}O_{2.95}$ of 40, 50 and 60 wt% Ni (36, 45 and 55 vol% Ni, respectively) was studied by Zunic et al., a clear percolation pathways between Ni and BCY was observed [38], providing a typical metallic behaviour upon reduction. These authors proposed that 40wt% nickel anode is suitable for PCFCs due to offering the lowest polarisation resistance. Coors et al. thoroughly examined the microstructure of a dense Ni-$BaCe_{0.2}Zr_{0.6}Y_{0.2}O_{3-\delta}$ cermet anode containing 68wt% (~40 vol%) Ni. Their studies stated that the porosity ~26% formed by the reduction of NiO to Ni in reducing atmospheres may be enough for PCFC functionality, with no extra pore former being required [41]. Essoumhi et al. studied the conductivity and electrochemical behaviour of a Ni-BCY cermet anode containing 35 and 45 vol% Ni using symmetrical cells and their findings stated that cermet containing 45 vol% Ni showed a low ASR value of 0.4 Ωcm^2 at 600 °C [42]. The same researchers later studied the microstructure and conductivity of a 40 vol% Ni-$BaCe_{0.9}Y_{0.1}O_{2.95}$ cermet anode using a gelled starch as a pore former and observed that conductivity slightly decreased with increasing the porosity level [43]. Recently, Rainwater et al. reported a decrease in PCFC cell performance on increasing the anode porosity level in Ni-$BaZr_{0.1}Ce_{0.7}Y_{0.1}Yb_{0.1}O_{3-\delta}$ (Ni-BZCYYb) anode supported based BZCYYb electrolyte cells with a $La_{0.6}Sr_{0.4}Co_{0.2}Fe_{0.8}O_{3-\delta}$ (LSCF) cathode[40]. The available literature, therefore, shows that both porosity and anode cermet matrix composition, for any fixed metal/ceramic ratio, are important factors to be further understood with respect to their impact on anode performance.

The nickel cermet anode material is unstable under redox conditions due to volume expansion of Ni upon re-oxidation [44]. To minimize or avoid the problems with nickel, and improve the performance of the anode, a number of alternative materials have therefore, also been tested as electrodes in oxide-ion conducting SOFCs [21, 45-47]. The main groups are nickel alloys of Cu and Co. However, these materials have been shown to

be less effective electrocatalysts than nickel and are also unstable [45, 46]. Another major problem with nickel cermet anodes is carbon mitigation and sulphur poisoning when the cell is operating on hydrocarbon fuels, such as methane or biogas [46, 48]. In oxide-ion conducting SOFC this effect has been shown to be able to be supressed by modifying the anode surface with basic or alkali oxides [49] and a few studies have also stated that nickel anodes that contain barium based mixed or proton conducting perovskite can also withstand in sulphur and carbon containing atmospheres [50, 51]. Nonetheless, even for SOFC this area of study is in a preliminary stage and a detailed study is needed before plant operation for long term in alternative hydrocarbon fuels. For PCFCs, research on suitable anodes is in its infancy, even for operation in basic hydrogen fuel. This thesis, therefore, aims to provide a deep fundamental knowledge of PCFC Ni-cermet anodes for the first time.

1.3.2.3 Cathodes

The cathodes employed in oxide-ion conducting SOFCs such as $La_{1-x}Sr_xMnO_3$ (LSM), $Sm_{0.5}Sr_{0.5}CoO_3$ (SSC) etc may not be compatible with PCFCs due to limited availability of active sites, La, Zr and Sr interaction and inter diffusion between electrolyte and cathode materials [52, 53]. The chemical interaction between the materials leads to secondary phases, such as $Sm_2Zr_2O_7$, $BaCoO_3$ and $La_2Zr_2O_7$ [52, 54]. Moreover, water is formed at the cathode side and, thus, it has been suggested that it may be beneficial for the cathode to also possess some protonic conductivity along with electronic and oxide-ion conductivity [21]. Nonetheless, according to the bulk of literature studies, the most commonly suggested requirements for a PCFC cathode material should be the availability of mixed electronic and protonic conductivity to prolong the three phase boundary (TPB) length at the electrode/electrolyte interface to the whole cathode area [17, 21]. This aim can be achieved either by making a composite cathode *via* introduction of proton conducting phase into phase offering high electronic conductivity or to intrinsically modify a proton conductor to become mixed protonically and electronically conducting by introducing a multivalent element into its basic structure [17, 21, 52].

The most widely studied cathode materials so far for PCFC applications are rare earth doped nickelates (R_2NiO_4, R = Pr, Nd, rare earth elements) [55], $Ba(Pr_{1-x}Gd_x)O_{3-\delta}$, $PrBaCuFeO_{5+x}$ and the composite cathodes $La_{0.6}Sr_{0.4}Co_{0.2}Fe_{0.8}O_3/Ba(Zr_{0.1}Ce_{0.7}Y_{0.2})O_3$, $Sm_{0.5}Sr_{0.5}CoO_3/BaCe_{0.8}Sm_{0.2}O_{2.9}$, and $Ba_{0.5}Sr_{0.5}Co_{0.8}Fe_{0.2}O_3/BaCe_{0.8}Sm_{0.2}O_{2.9}$ [2, 17]. Among all the homogeneous materials, the nickelate, Pr_2NiO_4, cathode has shown the lowest overpotential losses [55-57]. For the composite cathodes, more compositional flexibility is available and phases offering high electronic conductivity are generally mixed together with well-known proton conducting oxides from the zirconate and cerate perovskite families to increase the performance of the cell. The applicability of a cathode material for PCFC is dependent on its conductivity, thermal expansion coefficient and chemical compatibility with electrolyte material. Platinum has also been used as cathode but is shown to degrade upon long time operation, to exhibit large overpotential losses and is also too expensive. It has been stated that the cathode may play a key role in the overall performance of PCFCs, due to the formation of water in the cathode side that can result in larger cathode polarization resistances [17]. The cathode reaction of a PCFC involves the simultaneous reduction of oxygen and formation of water given as [2, 17]

$$4OH_O^{\bullet} + O_2 + 4e^- \rightarrow 2H_2O + 4O_O^x \qquad (1.5)$$

However, to date, the peak criteria for suitable mixed electronic and ionic (oxide-ion or protonic) conducting cathode materials has not yet been concluded for PCFC applications [17].

1.4 Scope of the thesis

Protonic Ceramic fuel cells (PCFCs) offer the benefit of efficient and low-polluting electricity generation with high fuel conversion. Over the past decade, rapid progress has been made in the materials and the technology of PCFCs. However, the current scientific community is facing the problems *viz.* the synthesis of phase pure materials, sinterability, stability in CO_2 and water containing atmospheres, fabrication methods of proton conducting materials and the selection of suitable electrodes. Hence the PCFC-technology is still in a pre-commercial state. The main aim of this thesis is to gain a fundamental knowledge on electrochemical behaviour of PCFC cermet anodes and to better understand

the effect of composition, hydrogen and water vapour partial pressures (pH_2 and pH_2O) and microstructure on anode performance. A large focus has also been made on the attainment of anode phase purity and the impact of purity on resultant polarisation resistance.

Chapter 1 describes the introduction to fuel cells especially PCFCs, types of fuel cells, operating principle and the materials design. In chapter 2, the synthesis of materials and experimental design for microstructure and electrochemical measurements are described. A novel combustion route for anode fabrication, with resultant phase purity, percolation behaviour and electrochemical behaviour is described in chapter 3. Here, the emphasis on anode phase purity is highlighted by comparison of results with those of impure anodes prepared by traditional nitrate-based combustion routes. In chapter 4, the relation between porosity, pH_2, pH_2O and polarisation resistance is elaborated. Here the effect of porosity on PCFC anode performance is shown to be contradictory to that required in oxide-ion conducting anode solid oxide fuel cells (O^{2-}-SOFCs). A detailed study on redox cycling behaviour of anodes under hydrogen and air atmospheres is described in chapter 5 using impedance spectroscopy supported by information provided from environmental scanning electron microscopy (ESEM) under operating conditions. The results demonstrate that back-bone of the proton conducting phase is sensitive towards degree of nickel re-oxidation and re-reduction steps with time due to Ni volume expansion on re-oxidation. In chapter 6, the importance of the inclusion of a proton conducting phase in PCFC cermet anodes on electrochemical behaviour is addressed. Comparison is made by employing a non-proton conducting phase and comparing results to a proton conducting phase from the same chemical family in cermet anodes and observation of the resultant reaction dynamics. The most difficult task in protonic ceramic fuel cells is the fabrication step, because of its high sintering temperature requirement. Thus, chapter 7 pronounces the successful fabrication of anode supported PCFC cell, scalability and their performance at intermediate temperatures. A detailed description of the problems while fabricating the cell is presented. The future aspects and prospective of PCFCs are briefly elaborated in chapter 8. Appendix (A) outlines a new synthesis route and subsequent electrical characterisation of the electrolyte material $Ba(Ce_{1-x}Zr_x)_{0.8}Y_{0.2}O_{3-\delta}$.

1.5 References

[1] Marbán G, Valdés-Solís T. Towards the hydrogen economy? Int J Hydrogen Energy. 2007;32:1625-37.

[2] Fabbri E, Pergolesi D, Traversa E. Materials challenges toward proton-conducting oxide fuel cells: a critical review. Chem Soc Rev. 2010;39:4355-69.

[3] Stambouli AB, Traversa E. Solid oxide fuel cells (SOFCs): a review of an environmentally clean and efficient source of energy. Renewable Sustainable Energy Rev. 2002;6:433-55.

[4] Larminie J, Dicks A. Fuel Cell Systems Explained. Second Edition ed: John Wiley & Sons, Ltd; 2003.

[5] Singhal SC, Kendall K. High Temperature Solid Oxide Fuel Cells: Fundamentals, Design and Applications: Elsevier; 2003.

[6] Boudghene Stambouli A, Traversa E. Fuel cells, an alternative to standard sources of energy. Renewable Sustainable Energy Rev. 2002;6:295-304.

[7] http://www1.eere.energy.gov/hydrogenandfuelcells/pdfs/2012_market_report.pdf. U.S. Department of Energy.; 2013.

[8] Primdahl S. Nickel/yttria-stabilised zirconia cermet anodes for solid oxide fuel cells. Netherlands: University of Twente, The Netherlands; 1999.

[9] Cuenca MMG. Novel Anode Materials For Solid Oxide Fuel Cells. Netherlands: University of Twente; 2002.

[10] "The fuel cell Review". Institute of Physics and IOP publishing. 2005;1:15.

[11] Haile S. Fuel cell materials and components. Acta Mater. 2003;51:5981-6000.

[12] Song S, Zhang H, Ma X, Shao Z, Baker RT, Yi B. Electrochemical investigation of electrocatalysts for the oxygen evolution reaction in PEM water electrolyzers. Nano. 2008;33:4955-61.

[13] Ahmad H, Kamarudin SK, Hasran UA, Daud WRW. Overview of hybrid membranes for direct-methanol fuel-cell applications. Int J Hydrogen Energy. 2010;35:2160-75.

[14] Wachsman ED, Lee KT. Lowering the temperature of solid oxide fuel cells. Science. 2011;334:935-9.

[15] Coors WG. Protonic ceramic fuel cells for high-efficiency operation with methane. J Power Sources. 2003;118:150-6.

[16] Antolini E, Gonzalez ER. Alkaline direct alcohol fuel cells. J Power Sources. 2010;195:3431-50.

[17] Peng R, Wu T, Liu W, Liu X, Meng G. Cathode processes and materials for solid oxide fuel cells with proton conductors as electrolytes. J Mater Chem. 2010;20:6218-25.

[18] Kreuer KD. Proton-Conducting oxides. Ann Rev Mater Res. 2003;33:333-59.

[19] Malavasi L, Fisher CaJ, Islam MS. Oxide-ion and proton conducting electrolyte materials for clean energy applications: structural and mechanistic features. Chem Soc Rev. 2010;39:4370-87.

[20] Fabbri E, Bi L, Pergolesi D, Traversa E. Towards the next generation of solid oxide fuel cells operating below 600 °C with chemically stable proton-conducting electrolytes. Adv Mater. 2012;24:195-208.

[21] Fabbri E, Pergolesi D, Traversa E. Electrode materials: a challenge for the exploitation of protonic solid oxide fuel cells. Sci Technol Adv Mater. 2010;11:044301.

[22] Magrez A, Schober T. Preparation, sintering, and water incorporation of proton conducting $Ba_{0.99}Zr_{0.8}Y_{0.2}O_{3-\delta}$: comparison between three different synthesis techniques. Solid State Ionics. 2004;175:585-8.

[23] Yamazaki Y, Hernandez-Sanchez R, Haile SM. Cation non-stoichiometry in yttrium-doped barium zirconate: phase behavior, microstructure, and proton conductivity. J Mater Chem. 2010;20:8158-66.

[24] Lin Y, Ran R, Guo Y, Zhou W, Cai R, Wang J, et al. Proton-conducting fuel cells operating on hydrogen, ammonia and hydrazine at intermediate temperatures. Int J Hydrogen Energy. 2010;35:2637-42.

[25] Shimada H, Li X, Hagiwara a, Ihara M. Proton-Conducting Solid Oxide Fuel Cells with Yttrium-Doped Barium Zirconate for Direct Methane Operation. J Electrochem Soc. 2013;160:F597-F607.

[26] Fabbri E, Depifanio A, Dibartolomeo E, Licoccia S, Traversa E. Tailoring the chemical stability of $Ba(Ce_{0.8-x}Zr_x)Y_{0.2}O_{3-\delta}$ protonic conductors for Intermediate Temperature Solid Oxide Fuel Cells (IT-SOFCs). Solid State Ionics. 2008;179:558-64.

[27] Guo Y, Lin Y, Ran R, Shao Z. Zirconium doping effect on the performance of proton-conducting $BaZr_yCe_{0.8-y}Y_{0.2}O_{3-\delta}$ ($0.0 \leq y \leq 0.8$) for fuel cell applications. J Power Sources. 2009;193:400-7.

[28] Koji K, Yoshirou K, Tetsuo S, Hiroyasu I. Protonic conduction in Zr-substituted $BaCeO_3$. Solid State Ionics. 2000;138:91-8.

[29] Nasani N, Dias PAN, Saraiva JA, Fagg DP. Synthesis and conductivity of $Ba(Ce,Zr,Y)O_{3-\delta}$ electrolytes for PCFCs by new nitrate-free combustion method. Int J Hydrogen Energy. 2013;38:8461-70.

[30] H.S.Spacil. Electrical device including nickel-containing stabilized zirconia electrode. US patent 3, 503, 8091970.

[31] Tanner CW, Fung KZ, Virkar AV. The Effect of Porous Composite Electrode Structure on Solid Oxide Fuel Cell Performance: I. Theoretical Analysis. J Electrochem Soc. 1997;144:21-30.

[32] Gorte RJ, Vohs JM. Nanostructured anodes for solid oxide fuel cells. Curr Opin Colloid Interface Sci. 2009;14:236-44.

[33] Suzuki T, Hasan Z, Funahashi Y, Yamaguchi T, Fujishiro Y, Awano M. Impact of anode microstructure on solid oxide fuel cells. Science. 2009;325:852-5.

[34] Mather GC, Figueiredo FM, Jurado JR, Frade JR. Synthesis and characterisation of cermet anodes for SOFCs with a proton-conducting ceramic phase. Solid State Ionics. 2003;162–163:115-20.

[35] Bi L, Fabbri E, Sun Z, Traversa E. $BaZr_{0.8}Y_{0.2}O_{3-\delta}$-NiO Composite Anodic Powders for Proton-Conducting SOFCs Prepared by a Combustion Method. J Electrochem Soc. 2011;158:B797.

[36] Narendar N, Mather GC, Dias PAN, Fagg DP. The importance of phase purity in Ni–$BaZr_{0.85}Y_{0.15}O_{3-\delta}$ cermet anodes – novel nitrate-free combustion route and electrochemical study. RSC Adv. 2013;3:859.

[37] Chevallier L, Zunic M, Esposito V, Di Bartolomeo E, Traversa E. A wet-chemical route for the preparation of Ni–$BaCe_{0.9}Y_{0.1}O_{3-\delta}$ cermet anodes for IT-SOFCs. Solid State Ionics. 2009;180:715-20.

[38] Zunic M, Chevallier L, Radojkovic A, Brankovic G, Brankovic Z, Di Bartolomeo E. Influence of the ratio between Ni and $BaCe_{0.9}Y_{0.1}O_{3-\delta}$ on microstructural and electrical

properties of proton conducting Ni–$BaCe_{0.9}Y_{0.1}O_{3-\delta}$ anodes. J Alloys Compd. 2011;509:1157-62.

[39] Mather GC, Figueiredo FM, Fagg DP, Norby T, Jurado JR, Frade JR. Synthesis and characterisation of Ni–$SrCe_{0.9}Yb_{0.1}O_{3-\delta}$ cermet anodes for protonic ceramic fuel cells. Solid State Ionics. 2003;158:333-42.

[40] Rainwater BH, Liu M, Liu M. A more efficient anode microstructure for SOFCs based on proton conductors. Int J Hydrogen Energy. 2012;37:18342-8.

[41] Coors WG, Manerbino A. Characterization of composite cermet with 68wt% NiO and $BaCe_{0.2}Zr_{0.6}Y_{0.2}O_{3-\delta}$. Journal of Membrane Science. 2011;376:50-5.

[42] Essoumhi A, Taillades G, Taillades-jacquin M, Jones D, Roziere J. Synthesis and characterization of Ni-cermet/proton conducting thin film electrolyte symmetrical assemblies. Solid State Ionics. 2008;179:2155-9.

[43] Taillades G, Batocchi P, Essoumhi A, Taillades M, Jones DJ, Rozière J. Engineering of porosity, microstructure and electrical properties of Ni–$BaCe_{0.9}Y_{0.1}O_{2.95}$ cermet fuel cell electrodes by gelled starch porogen processing. Microporous Mesoporous Mater. 2011;145:26-31.

[44] Ettler M, Timmermann H, Malzbender J, Weber A, Menzler NH. Durability of Ni anodes during reoxidation cycles. J Power Sources. 2010;195:5452-67.

[45] Atkinson A, Barnett S, Gorte RJ, Irvine JTS, McEvoy AJ, Mogensen M, et al. Advanced anodes for high-temperature fuel cells. Nat Mater. 2004;3:17-27.

[46] Ge X-M, Chan S-H, Liu Q-L, Sun Q. Solid Oxide Fuel Cell Anode Materials for Direct Hydrocarbon Utilization. Adv Energy Mater. 2012;2:1156-81.

[47] Mohammed Hussain A, Høgh JVT, Jacobsen T, Bonanos N. Nickel-ceria infiltrated Nb-doped $SrTiO_3$ for low temperature SOFC anodes and analysis on gas diffusion impedance. Int J Hydrogen Energy. 2012;37:4309-18.

[48] Selman JR. Materials science. Poison-tolerant fuel cells. Science. 2009;326:52-3.

[49] Yang L, Choi Y, Qin W, Chen H, Blinn K, Liu M, et al. Promotion of water-mediated carbon removal by nanostructured barium oxide/nickel interfaces in solid oxide fuel cells. Nat Commun. 2011;2:357-.

[50] Shishkin M, Ziegler T. Coke-Tolerant Ni/$BaCe_{1-x}Y_xO_{3-\delta}$Anodes for Solid Oxide Fuel Cells: DFT+U Study. J Phys Chem C. 2013;117:7086-96.

[51] Yang L, Wang S, Blinn K, Liu M, Liu Z, Cheng Z, et al. Enhanced Sulfur and Coking Tolerance of a Mixed Ion Conductor for SOFCs: $BaZr_{0.1}Ce_{0.7}Y_{0.2-x}Yb_xO_{3-\delta}$. Science. 2009;326:126-9.

[52] Yang L, Zuo C, Wang S, Cheng Z, Liu M. A Novel Composite Cathode for Low-Temperature SOFCs Based on Oxide Proton Conductors. Adv Mater. 2008;20:3280-3.

[53] Holtappels P, Vogt U, Graule T. Ceramic Materials for Advanced Solid Oxide Fuel Cells. Adv Eng Mater. 2005;7:292-302.

[54] Song HS, Lee S, Hyun SH, Kim J, Moon J. Compositional influence of LSM-YSZ composite cathodes on improved performance and durability of solid oxide fuel cells. J Power Sources. 2009;187:25-31.

[55] Dailly J, Fourcade S, Largeteau A, Mauvy F, Grenier JC, Marrony M. Perovskite and A_2MO_4-type oxides as new cathode materials for protonic solid oxide fuel cells. Electrochim Acta. 2010;55:5847-53.

[56] Dailly J, Marrony M, Taillades G, Taillades-Jacquin M, Grimaud A, Mauvy F, et al. Evaluation of proton conducting BCY10-based anode supported cells by co-pressing method: Up-scaling, performances and durability. J Power Sources. 2014;255:302-7.

[57] Quarez E, Oumellal Y, Joubert O. Optimization of the Lanthanum Tungstate/Pr_2NiO_4 Half Cell for Application in Proton Conducting Solid Oxide Fuel Cells. Fuel Cells. 2013;13:34-41.

Chapter 2

Experimental Methods

The material components (ceramic oxide powers) for fuel cells are generally prepared by the solid-state method or wet chemical routes, such as combustion and sol-gel process [1-4]. The solid-state method is the easiest and common method for the preparation of multicomponent oxides but it has some drawbacks such as, the potential for inhomogeneity, requiring multiple grinding and firing steps to attain pure phases and also high reaction temperatures [4, 5]. In contrast, wet chemical synthesis methods show the advantage that they allow mixing of elements at a molecular level to provides homogenous mixing and can facilitate the production of the desired stoichiometric ceramic phase at lower temperatures [5-8]. In this work greater part of the materials for PCFCs were prepared by a wet chemical, novel nitrate free, acetate-hydrogen peroxide (H_2O_2) combustion method designed by the author. In contrast, the ceramic-oxide powders of barium zirconate ($BaZrO_3$) and yttrium doped barium zirconate ($BaZr_{0.85}Y_{0.15}O_{3-\delta}$) were synthesized by mechanosynthesis under ambient conditions to provide the pure perovskite phase.

2.1 Materials synthesis

2.1.1 Synthesis of proton conducting electrolyte powders

2.1.1.1 Mechanosynthesis

The ceramic-oxide powders of barium zirconate ($BaZrO_3$) and yttrium doped barium zirconate ($BaZr_{0.85}Y_{0.15}O_{3-\delta}$) were synthesized by the mechanosynthesis method [9]. Stoichiometric quantities of the oxide precursors barium peroxide (≥95%purity, Sigma Aldrich), and ZrO_2 (Riedel-de-Haen, 99% purity) or $(ZrO_2)_{0.92}(Y_2O_3)_{0.08}$ (YSZ8, TOSOH Co.), respectively were used in the mechanosynthesis. The commercial BaO_2 powder was shown to have composition 96mol% BaO_2 with 4mol% $BaCO_3$ confirmed by complete carbonation in carbon dioxide using thermogravimetric analysis (TGA), Netsch-Jupiter. Before the mechanosynthesis reaction, the particle sizes of the zirconium powders were approximately 200nm for the pure ZrO_2 and in the range 60–80nm for the YSZ8, as

confirmed by surface area measurements. A planetary ball mill (Retsch PM200) was used for mechanosynthesis at a constant rotation speed of 650 rpm for 420 min using zirconia vials (Retsch) and balls (Tosoh Co.) under ambient conditions. For this, the ball to powder weight ratio was ~10:1. Excess heating of vials was avoided by milling the powders for 5 min and followed by a pause for the same period. The progression of the mechanochemcial reaction was monitored by collecting the powders at regular intervals and performing XRD analysis.

2.1.1.2 Novel nitrate free acetate-H_2O_2 combustion method

$BaCe_{0.7}Zr_{0.1}Y_{0.2}O_{3-\delta}$ (BCZY71) $BaCe_{0.4}Zr_{0.4}Y_{0.2}O_{3-\delta}$ (BCZY44) electrolyte powders were synthesized by a new acetate-H_2O_2 combustion method developed by the author, Appendix-A [8]. $Ba(CH_3COO)_2$ (>99.9% pure, Sigma Aldrich), Zr(IV) $(CH_3COO)_x$ $(OH)_y$ (99.9% pure, Sigma Aldrich), $Ce(CH_3COO)_3$ $.1.5H_2O$ (99.9% pure, Alfa Aesar), $Y(CH_3COO)_3$ $.4H_2O$ (99.9% pure, Alfa Aesar) and 30% H_2O_2 (Sigma Aldrich, 30% by weight) were used as starting materials for the combustion method. First, stoichiometric amounts of the metal acetates were dissolved in distilled water with constant stirring at 25 °C to obtain a clear, transparent solution. To the solution 30 % H_2O_2 was added slowly to achieve a fuel to oxidant ratio of unity as per the propellant chemistry [10]. An orange-brown colour solution with bubbles was observed and subsequently the solution was heated on a hot plate at 80 °C with constant stirring to form a viscous gel. Upon heating the orange-brown colour transforms to a pale yellow. The viscous gel was then subjected to microwave heating, under rotation, in a domestic 2.45 GHz, 800 W microwave oven set at the maximum power. After a few minutes, the dried gel burnt with a flame in a self-propagating combustion manner, releasing plentiful fumes, to form a black powder. The combustion powder was calcined at 1100 °C for 6h in order to obtain the pure perovskite phase.

2.1.2 Synthesis of nickel anode powders

2.1.2.1 Nitrate-free route (Ni-acetate/H_2O_2)

A range of NiO-BZY cermet anodes (20,30,40,50 vol% Ni) were prepared by dispersing nickel in pre-made BZY by the method of microwave-assisted combustion, using a novel, nitrate-free combustion route, again developed by the author [11]. The

$BaZr_{0.85}Y_{0.15}O_{3-\delta}$ powder was pre-prepared by mechanosynthesis (crystallite size ~30 nm, av. particle size ~1 μm) [9].

$Ni(OCOCH_3)_2.4H_2O$ (Aldrich, 99% pure) and 30% H_2O_2 (Riedel-de Haen, 30% by weight) were used for the combustion reaction. A stoichiometric amount of nickel acetate was dissolved in distilled water, and the pre-prepared BZY was dispersed using an ultrasonic bath. An appropriate amount of 30% H_2O_2 was then slowly added, fixing the fuel to oxidant ratio of Ni-acetate/H_2O_2 to 1:1, according to the propellant chemistry [10]. The solution was heated on a hot plate at 80 °C until a viscous gel formed. The viscous gel was then heated and simultaneously rotated in a domestic 2.45 GHz, 800 W microwave oven set at the maximum power. After a few minutes, the dried gel burnt with a flame in a self-propagating combustion manner, releasing plentiful fumes until the gels were completely burnt to form a black powder. The powder was calcined in ambient air in the temperature range of 1000-1200 °C for 5h for phase analysis. Note, the microwave-assisted combustion technique is a standard method that has been previously shown to provide a homogenous reaction throughout the whole volume of the gel, in contrast with simple hot-plate reactions that typically initiate combustion at the base of the gel in contact with the hotplate [12].

2.1.2.2 Classical nitrate-based route

NiO-$BaZr_{0.85}Y_{0.15}O_{3-\delta}$ anodes of identical composition were also prepared by the common microwave-assisted nitrate-glycine combustion method to compare with the novel acetate-H_2O_2 method. $Ni(NO_3)_2.6H_2O$ (Riedel-de Haen, 96% pure), and glycine as fuel (Aldrich, 99.9% pure) were dissolved in distilled water, again at a fuel to oxidant ratio of 1:1, and pre-prepared BZY was dispersed. Note that in the nitrate-glycine method, the Ni-precursor is the oxidant, whereas in the novel acetate-H_2O_2 method, the Ni-precursor constitutes the fuel. In an identical process, the nitrate-glycine solution was heated on a hot plate at 80 °C until a viscous gel formed. The gel was then heated in the same microwave oven, again set at the maximum power and under rotation. After a few minutes the dried gel ignited to a flame. The resulting black powder was calcined in the temperature range of 1000-1200 °C for 5h, as for the nitrate-free route.

2.1.2.3 Preparation of porous anode powders

The porogen starch from potatoes (Sigma Aldrich) was used to create varying levels of porosity. The calculated amount of starch (0 wt%, 5 wt%, 10 wt% and 20 wt%) and combusted NiO-BZY anode powder (Table 2.1) were mixed in acetone by using mortar-pestle and dried at 80 °C for 30 min. The obtained NiO-BZY anode powder was used to fabricate samples for the electrochemical measurements.

Table 2.1: Compositional porogen content corresponding to 40 vol% Ni-BZY cermet anode

Starch (wt%) in 40 vol% Ni-BZY	Starch (wt%) in NiO-BZY precursor
0	-
5	5.26
10	11.11
20	25.0

2.1.3 Synthesis of cathode powder

Cathode $Pr_2NiO_{4+\delta}$ powder was prepared by a citrate-nitrate combustion route using praseodymium hexahydrate (99.9% pure, Sigma-Aldrich) and nickel nitrate hexahydrate (≥ 96% pure, Sigma-Aldrich) chemicals. Stoichiometric amounts of the precursors were dissolved in distilled water and a small amount of nitric acid was added. After addition of citric acid (≥ 99.5% pure, Sigma-Aldrich) the solution was stirred vigorously for 30 min to obtain a clear solution. Then, the solution was slowly heated to 120 °C and the dried gel burned with a self-combustion process. The final combusted powder was calcined at 1100 °C for 12 h with a heating and cooling rate of 5 °C/min to obtain pure phase. The calcined powder was ball-milled at 250 rpm about 5h to break weak agglomerates.

2.2 Fabrication of bar shaped samples for electrical conductivity measurements

For the electrical conductivity measurements, bar shaped samples 15 mm x 3 mm x 5 mm were prepared by pressing anode powder isostatically at 200 MPa. These bar shaped samples were made to evaluate the bulk conductivity of the anode materials. All the samples were sintered at 1000 °C for 2 h to burn out the starch, followed by 1400 °C for 6

h with a heating and cooling rate of 2 °C/min. Then the porous platinum electrodes were applied on the bar shaped samples in a 4-point configuration and fired at 900 °C for 30min.

2.3 Fabrication of symmetrical anode/electrolyte/anode cell assemblies

For polarisation resistance measurements, disc-shaped, symmetrical anode/electrolyte/anode assemblies were fabricated by the co-pressing technique. A schematic representation of the cell is shown in Fig. 2.1. First, $BaCe_{0.7}Zr_{0.1}Y_{0.2}O_{3-\delta}$ (BCZY71) electrolyte powder was uniaxially pressed with 18 mm diameter under a light pressure of 50 MPa. Then NiO-BZY nanopowder (prepared by the novel acetate-H_2O_2 combustion method or the typical nitrate-glycine method) was deposited manually on one side of BCZY substrate, pressed at 100 MPa, and then repeated on the other side with slightly higher pressure of 150 MPa. Isostatic pressing was used to achieve good adherence between anode and electrolyte layer. All the symmetrical trilayer cells were sintered at 1400 °C for 6h with a heating and cooling rate of 2 °C/min. The sintered trilayer symmetrical cell diameter was ~16mm and thicknesses of the Ni-BZY anodes were ~110 µm. For these studies, BCZY71 electrolyte was chosen due to its lower sintering temperature than BZY.

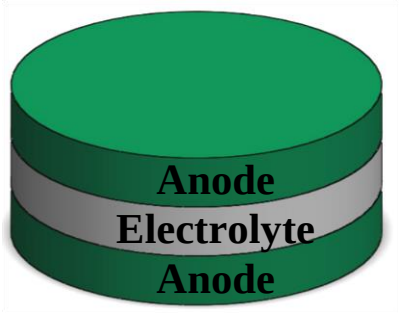

Figure 2.1. A schematic representation of symmetrical anode/electrolyte/anode cells

2.3.1 Fabrication of porous samples for electrochemical characterisation

Four symmetrical anode/electrolyte/anode cells were fabricated by the co-pressing technique [11], and designated as Ni-BZY0, Ni-BZY5, Ni-BZY10 and Ni-BZY20 where the number indicates the varying starch content. $BaCe_{0.7}Zr_{0.1}Y_{0.2}O_{3-\delta}$ (BCZY71) electrolyte powder was pressed uniaxially in a 20 mm diameter die at a pressure of 50 MPa. Then a

fixed amount of NiO-BZY combusted powder was deposited manually on one side of BCZY substrate, pressed at 100 MPa, and then repeated on the other side with pressure of 150 MPa. The amount of NiO was chosen to give a final anode composition of 40vol% Ni-BZY. The green symmetrical trilayer assemblies were isostatically pressed at 200 MPa for 5 min. All the four symmetrical trilayer cells were sintered at 1000 °C for 2h to burn out the starch, followed by 1400 °C for 6h with a heating and cooling rate of 2 °C/min. The thicknesses of the sintered Ni-BZY anodes were ~110 μm.

2.4 Materials Characterisation

X-ray diffraction (XRD) analysis was used to identify the phase purity and the cell parameters of resultant crushed pellets in the 2θ range between 20° and 85° using a Rigaku Geigerflex diffractometer (CuKα radiation, scan rate 1°/min). The lattice parameters of BZY were refined by the Rietveld method with the Fullprof program [13, 14], employing Ni metal as internal standard.

A Scanning Electron Microscope (SEM), model Hitachi SU-70, was used to investigate the anode microstructure of the combusted powder, the morphology of the pellets before and after reduction and before and after the complete redox cycling experiment. Energy dispersive X-ray spectroscopy (EDS), model Bruker Quantax-Germany, was used to perform elemental mapping analysis and line scan for the identification of inter-diffusion of elements.

In-situ Environmental scanning electron microscopy (ESEM) analysis was performed using a FEI Quanta 200 SEM. For the ESEM investigation, an identical Ni-BZY/BCZY/Ni-BZY symmetrical cell was fractured in order to access the electrode/electrolyte interface. Redox cycling was performed at 600 °C under flow of 3 sccm of pure H_2 or O_2 at a total pressure of 2.0×10^{-2} Pa to provide complementary dynamic information on redox cycling.

Reduction of the NiO-BZY composite to the Ni-BZY cermet anode was performed by annealing in a flowing 10% H_2/N_2 gas mixture at 700 °C for 6-10h. The porosity of reduced cermet anodes were measured in different solvents by the Archimedes technique, using pellets of Ni-BZY cermet anodes that had been isostatically pressed and fired at the same conditions as utilized for the preparation of the symmetrical cells.

2.4.1 Electrical and Electrochemical impedance measurements

Electrochemical impedance spectroscopy was performed using an Electrochemie-Autolab PGSTAT302N frequency response analyser in the frequency range 1 MHz-0.01 Hz, amplitude 50 mV. The total conductivity of bulk Ni-BZY anodes was measured by A.C. impedance, on bar shaped specimens in an isolated chamber under both wet and dry 10% H_2/N_2, with a flow rate of 50 ml/min as a function of temperature using a 4 electrode geometry. Measurements were made at 50 ºC intervals in the direction of decreasing temperature in the temperature range 900–100 °C. Stability was confirmed by performing repeated impedance measurements at each temperature. Humidification was obtained by bubbling gases through water followed by a saturated KCl solution in contact with solid KCl, producing approximately 86% relative humidity at room temperature. Humidity levels were controlled by mixing wet and dry gases and measured using a humidity meter (Jumo), while oxygen partial pressure was recorded with an inbuilt oxygen sensor. The obtained Impedance spectra were fitted using the ZView software (Scribner Associates). The interrelationship between measured pH_2O values and calculated values of pH_2 during the experiments were obtained using equation 1 [15].

$$pH_2O = 10^{-(2.9858-\frac{13022}{T})}.pH_2.pO_2^{1/2} \qquad (2.1)$$

2.4.2 Electrochemical impedance measurements for porous cermet anodes

Electrochemical impedance measurements (EIS) were performed to evaluate the polarisation behaviour of the disc shaped symmetrical anode/electrolyte/anode cells, Ni-BZY0, Ni-BZY5, Ni-BZY10 and Ni-BZY20 with varying starch content, using an Electrochemie-Autolab PGSTAT302N frequency response analyser in the frequency range 1 MHz-0.01 Hz with signal amplitude 50 mV. All the signals were recorded using LabVIEW program attached to autolab. The symmetrical cell assembly was fixed on alumina tube using platinum wires in a single atmosphere as shown in Fig. 2.2.

Figure 2.2. The illustration of a symmetrical cell-testing holder for impedance measurements

Measurements were performed at 50 ºC intervals in the direction of decreasing temperature in the temperature range of 800–100 °C. The dwell time at each temperature before each measurement was 1h and stability was confirmed by performing repeated impedance measurements after an additional 1h. Tests as a function of hydrogen partial pressure (pH_2) and water vapour partial pressure (pH_2O) were performed at 600 °C. Impedance spectra were recorded with 3h stabilization time between each measurement. Stability was confirmed by performing repeated impedance measurements at each condition after an additional 30 min. Humidification was obtained by bubbling gases through water followed by a saturated KCl solution in contact with solid KCl, producing approximately 86% relative humidity at room temperature. Humidity was controlled by mixing fractions of wet and dried gases, using Bronkhorst Thermal Mass flow Controllers (EL_Flow) with a maximum total flow rate of 50 ml/min. Humidity levels were measured using a humidity meter (Jumo), while oxygen partial pressure was monitored by an inbuilt oxygen sensor.

2.5 Fabrication of anode supported single cell

The anode powder NiO-BZY (obtained from combustion) was pressed uniaxially in a stainless steel die of 1.5 cm diameter and sintered at 1000 °C for 3h to attain sufficient mechanical support. Then, the stable electrolyte suspension was prepared using BCZY44 electrolyte powder (made by combustion, calcined at 1100 °C) (26wt% concentration), dispersed in ethanol (pure), 1wt% polyvinylpyrrolidone (PVP) and then ball milled (Retsch PM200) at 400 rpm for 2h followed by 1h ultrasonication, [16]. Then the suspension was deposited on pre-sintered anode by spin coating technique (Laurell automated spin coater, model WS-650-23). The thickness of electrolyte film was controlled by the number of spin

coated layers. Then, the half cells (anode/electrolyte) were co sintered at 1450 °C for 5h in ambient air to obtain the dense electrolyte films.

A complete single cell was fabricated by applying cathode on the center of the electrolyte side using cathode slurry with the help of a mask. The cathode slurry was prepared by mixing the cathode powder with 10wt% starch as a poreformer using terpineol as a binder and brush painted on the center of thin electrolyte surface and co-fired at 1100 °C for 3h. The effective cathode area of the cell was 0.237 cm^2. The final sintered cells had a diameter of ~1.3 cm and anode thickness of ~590 µm. The thickness of electrolyte and cathode layers was around ~5 µm and 25 µm. For the fuel cell test, Pt mesh and Pt paste (brush painted and fired at 960 °C for 30 min) was used as a current collector on anode and cathode surface respectively.

2.6 Electrochemical Fuel cell testing

The electrochemical performance of anode supported single cell was evaluated using a home built fuel cell testing station, Fig. 2.3. The button shaped single cell was sealed to alumina tube end with a glass sealant at 900 °C [17], where it separates both anode and cathode gas chambers in a tubular furnace. Then, the furnace was cooled down slowly to working temperature in the absence of gases. Humidified H_2 (3% water) as the fuel and dry air as the oxidant was fed to anode and cathode chambers respectively at a flow rate of 50 ml/min using mass flow controllers (Agilent). Platinum paste was employed on cathode side as a current collector and Pt wires were used as leads to carry the electrochemical measurements. The electrochemical performance of the single cell was evaluated using Electrochemie-Autolab PGSTAT302N Potentiostat/Galvanostat through Nova program. The electrochemical impedance spectra (EIS) were recorded under open circuit potential conditions (OCV) in the temperature range of 550-700 °C using the same autolab, frequency response analyzer in the frequency range of 1 MHz-0.01 Hz with an amplitude of 10 mV. The current-voltage (I-V) characteristic of the single cell was appraised once the open circuit potential was stabilized. The impedance spectra were fitted using *ZView* software (Scriber Associates). A humidity meter (Jumo) was used to record the relative humidity levels during the measurements.

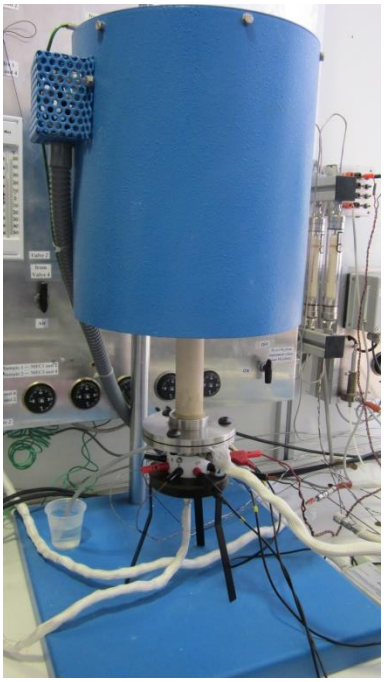

Figure 2.3. The fuel cell testing station and reactor in furnace

2.7 References

[1] Haile S. Fuel cell materials and components. Acta Mater. 2003;51:5981-6000.

[2] Ishihara T. Perovskite Oxide for Solid Oxide Fuel Cells: Springer US; 2009.

[3] Singhal SC, Kendall K. High Temperature Solid Oxide Fuel Cells: Fundamentals, Design and Applications: Elsevier; 2003.

[4] Tong J, Clark D, Hoban M, O'Hayre R. Cost-effective solid-state reactive sintering method for high conductivity proton conducting yttrium-doped barium zirconium ceramics. Solid State Ionics. 2010;181:496-503.

[5] Aruna ST, Mukasyan AS. Combustion synthesis and nanomaterials. Curr Opin Solid State Mater Sci. 2008;12:44-.

[6] Chevallier L, Zunic M, Esposito V, Di Bartolomeo E, Traversa E. A wet-chemical route for the preparation of Ni–$BaCe_{0.9}Y_{0.1}O_{3-\delta}$ cermet anodes for IT-SOFCs. Solid State Ionics. 2009;180:715-20.

[7] Magrez A, Schober T. Preparation, sintering, and water incorporation of proton conducting $Ba_{0.99}Zr_{0.8}Y_{0.2}O_{3-\delta}$: comparison between three different synthesis techniques. Solid State Ionics. 2004;175:585-8.

[8] Nasani N, Dias PAN, Saraiva JA, Fagg DP. Synthesis and conductivity of $Ba(Ce,Zr,Y)O_{3-\delta}$ electrolytes for PCFCs by new nitrate-free combustion method. Int J Hydrogen Energy. 2013;38:8461-70.

[9] Antunes I, Brandão A, Figueiredo FM, Frade JR, Gracio J, Fagg DP. Mechanosynthesis of nanopowders of the proton-conducting electrolyte material $Ba(Zr, Y)O_{3-\delta}$. J Solid State Chem. 2009;182:2149-56.

[10] Jain SR, Adiga KC, Pai Verneker VR. A new approach to thermochemical calculations of condensed fuel-oxidizer mixtures. Combust Flame. 1981;40:71-9.

[11] Narendar N, Mather GC, Dias PAN, Fagg DP. The importance of phase purity in Ni–$BaZr_{0.85}Y_{0.15}O_{3-\delta}$ cermet anodes – novel nitrate-free combustion route and electrochemical study. RSC Adv. 2013;3:859.

[12] Mohebbi H, Ebadzadeh T, Hesari Fa. Synthesis of nano-crystalline NiO-YSZ by microwave-assisted combustion synthesis. Powder Technol. 2009;188:183-6.

[13] McCusker LB, Von Dreele RB, Cox DE, Louër D, Scardi P. Rietveld refinement guidelines. J Appl Crystallogr. 1999;32:36-50.

[14] Rodríguez-Carvajal J. Recent advances in magnetic structure determination by neutron powder diffraction. Physica B. 1993;192:55-69.

[15] Hartung R, Mobius H-H. Potentiometrische Bestimmung des Wasserdampf-Dissoziationsgleichgewichtes zwischen 1000 und 1300°K rnit einer Festelektrolytzelle. Chem Ingenieur Technik. 1968;40:592-600.

[16] Dias PAN, Nasani N, Horozov TS, Fagg DP. Non-aqueous stabilized suspensions of $BaZr_{0.85}Y_{0.15}O_{3-\delta}$ proton conducting electrolyte powders for thin film preparation. J Eur Ceram Soc. 2013;33:1833-40.

[17] Pascual MJ, Guillet A, Durán A. Optimization of glass–ceramic sealant compositions in the system MgO–BaO–SiO_2 for solid oxide fuel cells (SOFC). J Power Sources. 2007;169:40-6.

Chapter 3

The importance of phase purity in Ni-$BaZr_{0.85}Y_{0.15}O_{3-\delta}$ cermet anodes – Novel nitrate-free combustion route and electrochemical study [‡]

Abstract

This chapter deals with the synthesis and electrochemical behaviour of state-of-the-art Ni-$BaZr_{0.85}Y_{0.15}O_{3-\delta}$ (Ni-BZY) cermet anodes for PCFCs. A novel, nitrate-free, combustion method has been developed to prepare Ni-$BaZr_{0.85}Y_{0.15}O_{3-\delta}$ (Ni-BZY) cermet anodes for protonic ceramic fuel cells (PCFCs). The advantages of this nitrate-free, combustion method have been demonstrated by comparison to a more common nitrate/glycine combustion route. The results demonstrate that use of the nitrate-free precursors is essential to avoid partial decomposition of the pre-prepared BZY phase. Employment of the more common nitrate-based precursors, due to their acidic nature, results in removal of Ba from the perovskite phase and formation of $Ba(NO_3)_2$, subsequently leading to the presence of BaY_2NiO_5 in the final product. Partial decomposition of the perovskite phase limits performance by increasing the higher frequency polarisation resistance and this phenomenon is suggested to be associated with impaired proton transport in the oxide cermet phase. The novel actetate-H_2O_2 combustion method here described is proposed for the formation of other ceramic oxide materials, offering economical advantages over more classical nitrate-based combustion routes, as well as significant environmental benefits due to the avoidance of releasing NO_x gases.

[‡] This Chapter has been published as Narendar N, Mather GC, Dias PAN, Fagg DP. The importance of phase purity in Ni–$BaZr_{0.85}Y_{0.15}O_{3-\delta}$ cermet anodes – novel nitrate-free combustion route and electrochemical study. RSC Adv. 2013;3:859.

3.1 Introduction

The study of PCFCs is in its infancy, with the bulk of previous work on potential anodes for these cells concentrated on proton-conducting analogues of Ni-cermet anodes found in typical high temperature SOFCs. Examples include composite anodes such as Ni-$BaCe_{1-x}Y_xO_{3-\delta}$ [1, 2] or Ni-$SrCe_{1-x}Y_xO_{3-\delta}$ cermets [3]. Cermet anodes based on the alkaline earth cerates typically suffer from poor chemical stability in CO_2- and H_2O-containing atmospheres [4-7], whereas, barium zirconate-based cermets, e.g. Ni-$BaZr_{1-x}Y_xO_{3-\delta}$ (Ni-BZY) or doped analogues, Ni-$Ba(Zr_{1-y}Ce_y)_{1-x}Y_xO_{3-\delta}$ have been shown to offer improved chemical stabilities that open the possibility for operation on alternative fuels [8-11]. Nonetheless, due to the lesser development of PCFCs only the more straightforward cermet-preparation methods like mechanical mixing with nickel oxide powders [12-16] or combustion synthesis using nitrate precursors [2, 3, 17] have been suggested to prepare these materials, to date, and only limited electrochemical studies have been realised to assess their performance.

Although one-step, nitrate-based, combustion processes have received the most attention for the preparation of Ni-BZY cermet anodes [18, 19], it may be preferential to follow an alternative preparation route in which the BZY phase is made prior to formation of the cermet anode. This is due to the large volume of recent literature that has underscored the importance of the processing route and resultant homogeneity of BZY on the level of protonic conductivity [20-24]. Deviations from the nominal stoichiometry have been shown to significantly deplete levels of proton conductivity obtained in both the grain and grain boundary. This factor can be understood with reference to the available phase diagrams of this system that show the pure, cubic-perovskite phase field to be very narrow in the BaO direction [25, 26]. Thus, small deviations from stoichiometry can easily lead to the presence of secondary-phase impurities or inhomogenities, a factor that is compounded by the refractive nature of this material and low cation mobilities. The presence of such inhomogenities can most easily be identified by lattice-parameter assessment [20, 22-24]. Employing this method, Schöber *et al.* have highlighted that typical nitrate-based combustion methods for the production of BZY phase are unsuitable for obtaining the required homogeneity, even after high-temperature annealing [22].

In the current work, we demonstrate that typical nitrate/fuel combustion routes cannot be used for Ni-phase dispersion in pre-prepared BZY powders, due to partial decomposition of the perovskite phase. Instead, a novel, efficient, inexpensive nitrate-free combustion synthesis route is developed to prepare Ni-$BaZr_{0.85}Y_{0.15}O_{3-\delta}$ that avoids decomposition of the pre-prepared BZY. In addition, a detailed electrochemical study is provided that highlights the importance of BZY phase-purity in Ni-BZY cermets, to ensure achievement of low polarisation resistances. The new acetate-H_2O_2 combustion route is also suggested to be a suitable replacement for many traditional nitrate-based combustion routes currently used in the production of ceramic oxide materials, due to offering a more environmentally friendly method that avoids the release of NO_X gases. To the best of our knowledge, to date, there has been no combustion synthesis method using these precursors documented in the literature. The experimental details of the syntheses can be found in Chapter 2, sections 2.1.1 and 2.1.2.

3.2 Results and Discussion

3.2.1 Phase formation

To compare the novel acetate combustion method with a more conventional nitrate method, XRD analysis has been performed before and after the combustion reactions, Fig. 3.1(a), 3.1(b), for 40 vol% Ni-$BaZr_{0.85}Y_{0.15}O_{3-\delta}$ cermet anodes.

In the case of novel combustion method, the pre-prepared BZY phase is shown to be stable in the precursor gel, Fig. 3.1(a). In contrast, the pre-prepared BZY phase partially decomposes in the common nitrate/glycine precursor gel, as revealed by a decrease of the perovskite relative peak intensity and formation of $Ba(NO_3)_2$, Fig. 3.1(b). The dissolution of Ba in acidic solutions has been previously documented by authors studying analogous $BaTiO_3$ materials and it is shown that there is an approximately linear relationship between the concentration of leached Ba^{2+} and pH [27]. Accordingly, the novel acetate combustion method employed in the current work successfully avoids BZY phase decomposition by providing a non-acidic medium for powder dispersion. In a similar strategy, one also attempted to raise the pH of the common nitrate/glycine process by the addition of ammonia. Unfortunately, the pH could not be raised sufficiently in this way to avoid the formation of $Ba(NO_3)_2$, while still remaining within the constraints of a suitable propellant

chemistry to maintain self-propagating combustion. It is, therefore, essential to adopt novel synthesis routes for the formation of Ni-BZY cermets, such as the acetate route here described.

After combustion, both the nitrate-free and nitrate/glycine processes show the presence of the perovskite phase, NiO and small amounts of Ni-metal due to the high heats of reaction, Fig. 3.1(a), 3.1(b). Notably, in the nitrate/glycine route, a significant amount of $BaCO_3$ can also be observed in the XRD pattern, Fig. 3.1(b). As the BZY phase is expected to offer good stability against carbonation [9], the presence of $BaCO_3$ in the nitrate/glycine process is believed to arise directly due to carbonation of the $Ba(NO_3)_2$ phase that was present after the dissolution of Ba in the acidic precursor gel. In contrast, the non-acidic precursor solution of the acetate process avoided any dissolution of Ba from the perovskite phase and, hence, the formation of $BaCO_3$ as an impurity in the combustion product, Fig. 3.1(a), was prevented.

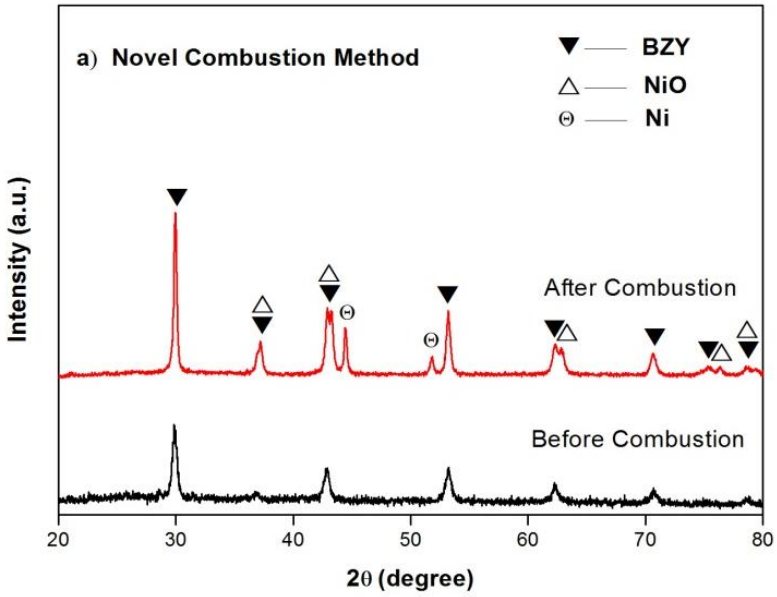

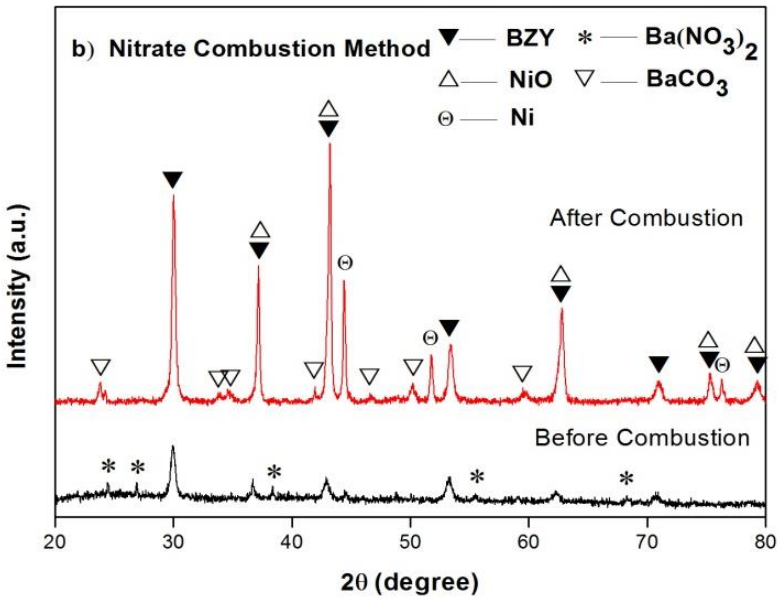

Figure 3.1. (a) XRD patterns of 40vol% Ni-BZY cermet anodes before and after combustion by the novel acetate combustion method (b) XRD patterns of Ni-BZY cermet anodes before and after combustion by a typical nitrate/glycine combustion method

Fig. 3.2 provides the XRD patterns of powders prepared by the novel acetate combustion method after calcination at 1000-1200 °C for 5h in air. The patterns exhibit only two phases, that of the perovskite (BZY) and NiO. In contrast, in the XRD patterns of powders prepared by the conventional nitrate method calcined at the same temperatures (Fig. 3.3), an impurity phase of BaY_2NiO_5 (PDF 00-041-0463) can be observed at all temperatures, in addition to the perovskite and NiO phases.

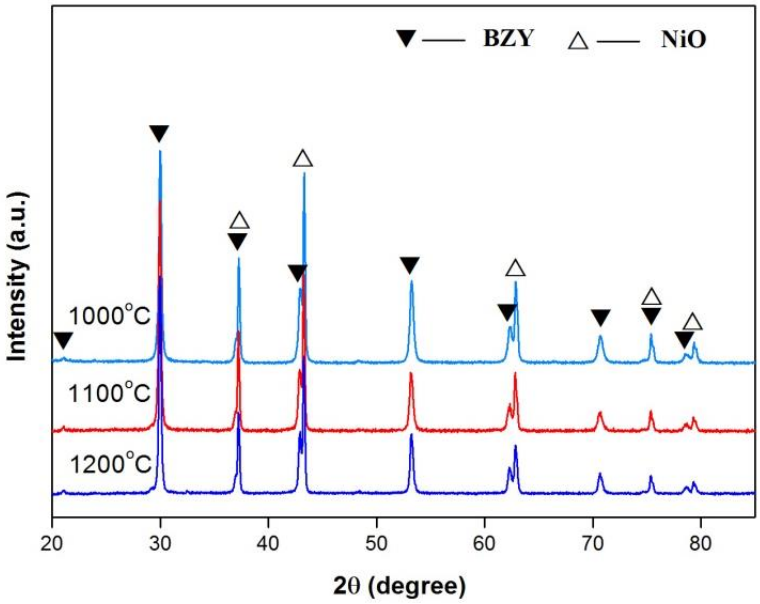

Figure 3.2. XRD patterns for NiO-BZY composite powders (40 vol% Ni-BZY) calcined at 1000-1200 °C for 5h (Novel acetate combustion method)

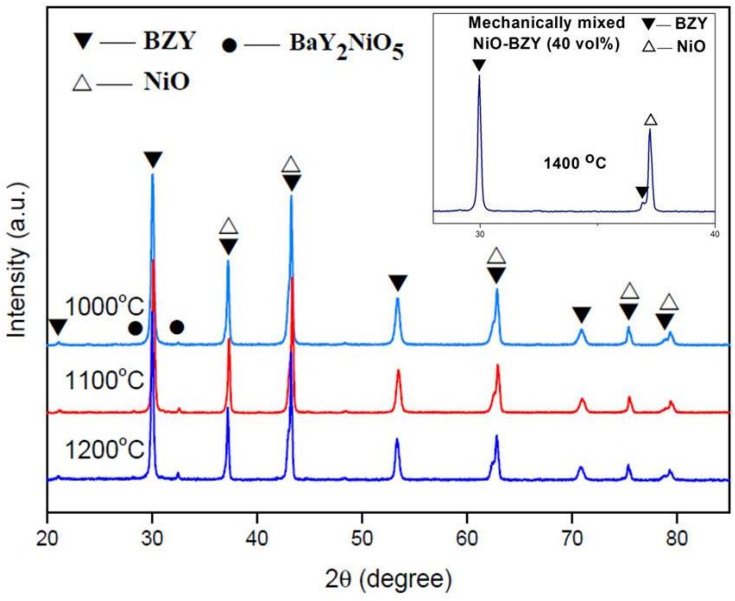

Figure 3.3. XRD patterns for NiO-BZY composite powders (40 vol% Ni-BZY) calcined at 1000-1200 °C for 5h (Conventional nitrate combustion method). Inset: mechanically mixed BZY+NiO of the same composition fired at 1400 ºC, highlighting the absence of BaY_2NiO_5 impurity.

The BaY_2NiO_5 phase is a common impurity that has been found in many one-step preparations of BZY materials containing Ni. The phase has been observed during standard solid-state syntheses from $BaCO_3$ and the oxides [27, 28], and also nitrate-based combustion routes [18, 19]. Tong et al. provided an in-depth study of the formation of this impurity phase and documented that it forms at temperatures higher than 900 ºC and cannot be totally removed even upon firing up to 1500 ºC [28]. They also noted that the presence of this impurity significantly enhanced densification and grain growth in BZY materials [28], although subsequent work has suggested that proton conductivity is hindered, leading to an increased activation energy for conduction [29, 30]. In the present study, the formation of this impurity during the nitrate/glycine combustion route, Fig. 3.3, is in accord with previous studies. This is because the pre-prepared BZY phase is shown to be partially decomposed in the acidic nitrate precursor gel, forming $Ba(NO_3)_2$ and subsequently $BaCO_3$ in the combusted product. As significant Ba-deficiency in the perovskite material is typically shown to be accompanied by loss of Y_2O_3 [24], all the elements required to form the BaY_2NiO_5 phase (Y_2O_3, $BaCO_3$ and NiO) are likely to be available in the nitrate/glycine combusted powder. In contrast, the BZY phase was preserved in the acetate combustion route and, consequently, no BaY_2NiO_5 impurity phase was observed, Fig. 3.2.

Thus, the current work highlights that the presence of the BaY_2NiO_5 impurity phase is not a prerequisite in BZY/NiO composites. On the contrary, BZY appears to be stable in the presence of NiO, under the conditions studied, allowing anodes to be formed that are free of this impurity phase. To underscore this important observation, BZY has been mixed with NiO manually in a pestle and mortar, at the same composition, and fired at 1400 ºC for 5h. In accordance with the findings of combustion from acetate precursors, no reaction of BZY and NiO can be observed, even at this high temperature, inset Fig. 3.3. Upon reduction in 10% H_2/N_2 at 700 °C for 6h, high purity is again attained for the Ni-cermet produced by the novel acetate route, exhibiting only the desired BZY and Ni-metal phases, Fig. 3.4. In contrast, the BaY_2NiO_5 impurity phase persists in the cermet produced by the nitrate/glycine combustion route, in addition to the perovskite and Ni-phases.

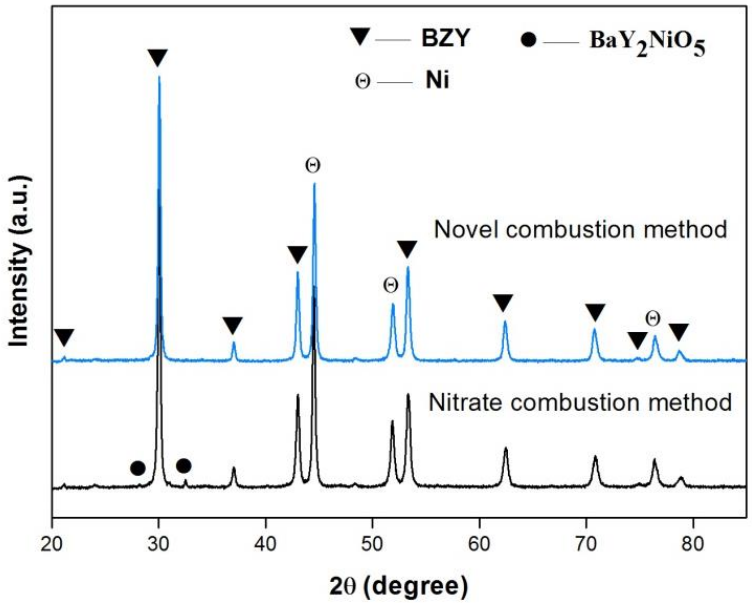

Figure 3.4. XRD patterns for 40 vol% Ni-BZY composite powders (reduced at 700 °C for 6h under 10% H_2/N_2)

One should reemphasise at this juncture that it is highly desirable to preserve the pre-prepared BZY phase and avoid impurities and associated loss of Ba and Y, as extensive previous literature has shown that this is the best way to preserve high levels of proton conductivity in the perovskite phase [22-24]. In order to examine the stoichiometry further, the lattice parameters of the perovskite phase have been calculated for the two preparation methods for powders calcined at 1200 ºC and compared to that expected for stoichiometric BZY. The perovskite lattice parameter of the nitrate/glycine prepared material, 4.2067(1)Å, is significantly lower than that formed by the novel nitrate-free process, 4.2107(2)Å, as a result of the expected elemental losses of Ba and Y on formation of BaY_2NiO_5 [24]. Rietveld refinement suggests the formation of approx. 3mol% this impurity phase with respect to BZY. In contrast, the nitrate-free route leads to a perovskite lattice parameter comparable to that of the base BZY material, 4.2129(3) Å, indicating retention of the desired stoichiometry.

The stability of pre-made BZY in the presence of NiO should be of great interest for those studying Ni as a potential sintering additive, as it may offer a possible method to avoid depletions in protonic conductivity noted for other one-step preparation routes [29, 30].

3.2.2 Microstructure

Fig. 3.5(a) shows the SEM micrograph of as synthesized 40 vol% NiO-BZY anode powder produced by the nitrate-free combustion method. A homogeneous distribution of nanoscale NiO and BZY particles can be observed, and this is further confirmed by SEM-EDS elemental analysis in Fig. 3.5(b).

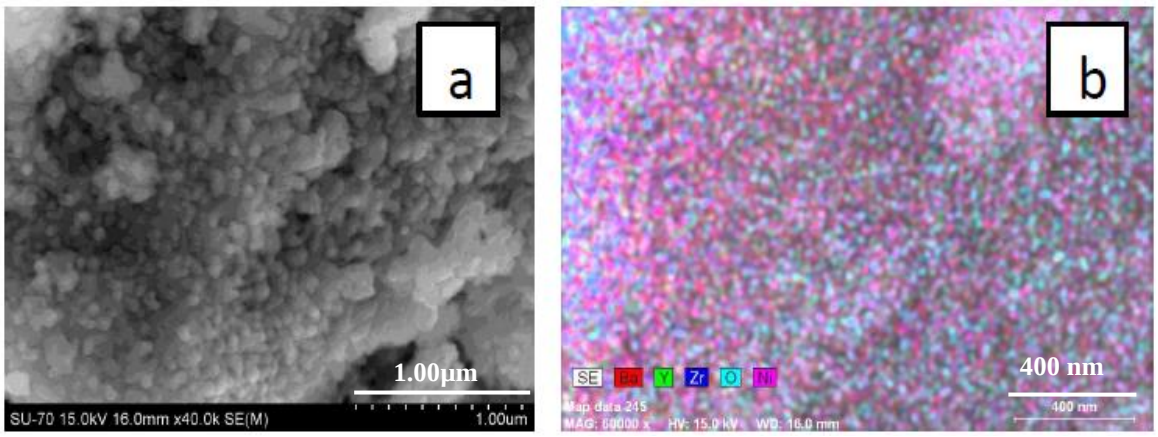

Figure 3.5. (a) SEM micrograph and (b) SEM-EDS elemental analysis of as-synthesized 40vol% Ni-BZY anode powder prepared by the novel acetate combustion route.

The microstructure of the acetate-prepared NiO-BZY anode material before reduction is shown in Fig. 3.6(a). Large and small grains correspond to NiO and BZY, respectively, and percolation pathways appear to exist throughout the NiO and BZY phases. Fig. 3.6(b) shows the microstructure of the anode after reduction at 700 °C for 6h in 10% H_2/N_2 atmosphere, while Fig. 3.6(c) highlights the fact that there are no significant differences in microstructure between Ni-BZY prepared by the novel acetate combustion and the traditional nitrate methods. In agreement, the resultant porosity of the two samples, measured by the Archimedes method using ethanol, also appears to be independent of preparation route: Acetate - 34.9% cf. Nitrate - 34.7%.

As highlighted by Coors et al. [12], reduction of the NiO phase to Ni metal in cermet anodes is associated with a volume reduction of about 40%. In the present sample the Ni content is 40 vol% in the form of Ni metal. Hence, these values correlate to a maximum attainable porosity, introduced solely due to the reduction of NiO, of around 24%. The result of this volume contraction can be clearly observed in the microstructure presented in Fig. 3.6(b) and (c). The Ni particles separate from the surrounding BZY

matrix, leaving narrow channel gaps, while the nickel particles themselves take on a pocketed appearance due to the presence of pores. This microstructure is typical of reported Ni-BZY cermets [2, 12, 13, 15]. The intrinsic porosity created by NiO reduction is suggested to be sufficient for a functional PCFC anode due to the following factors. Firstly, the performance of a PCFC has lower dependence on the three-phase-boundary length than a SOFC, due to the high mobility of protons in both the metallic Ni-phase and the ceramic matrix. Secondly, hydrogen is the only diffusing gas species in a PCFC anode, in contrast to that of a SOFC anode in which water vapour must also counter-diffuse [12, 15]. Clear percolation pathways for Ni and BZY grains are maintained after reduction, Fig. 3.6(b),(c) and this is further highlighted by Fig. 3.7, which provides SEM-EDS elemental mapping of the formed Ni-BZY anode.

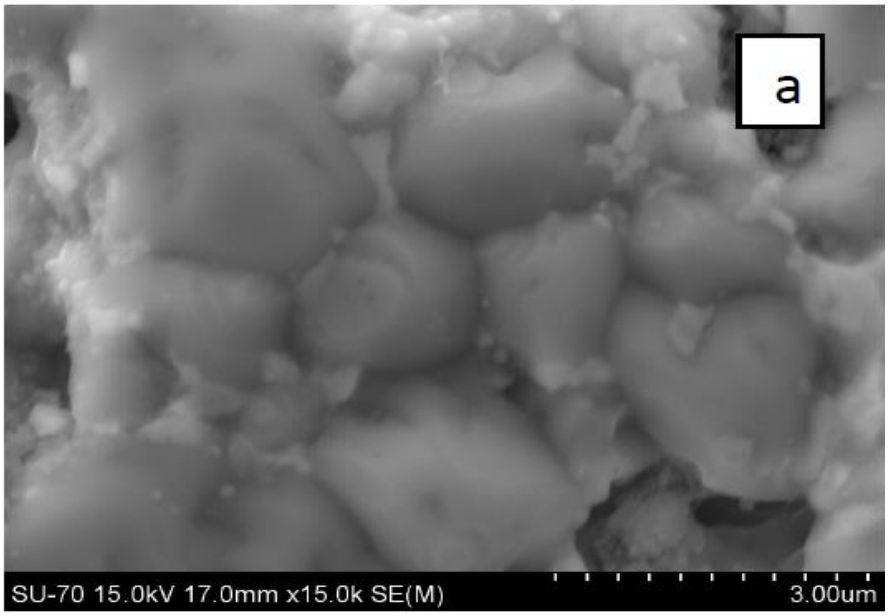

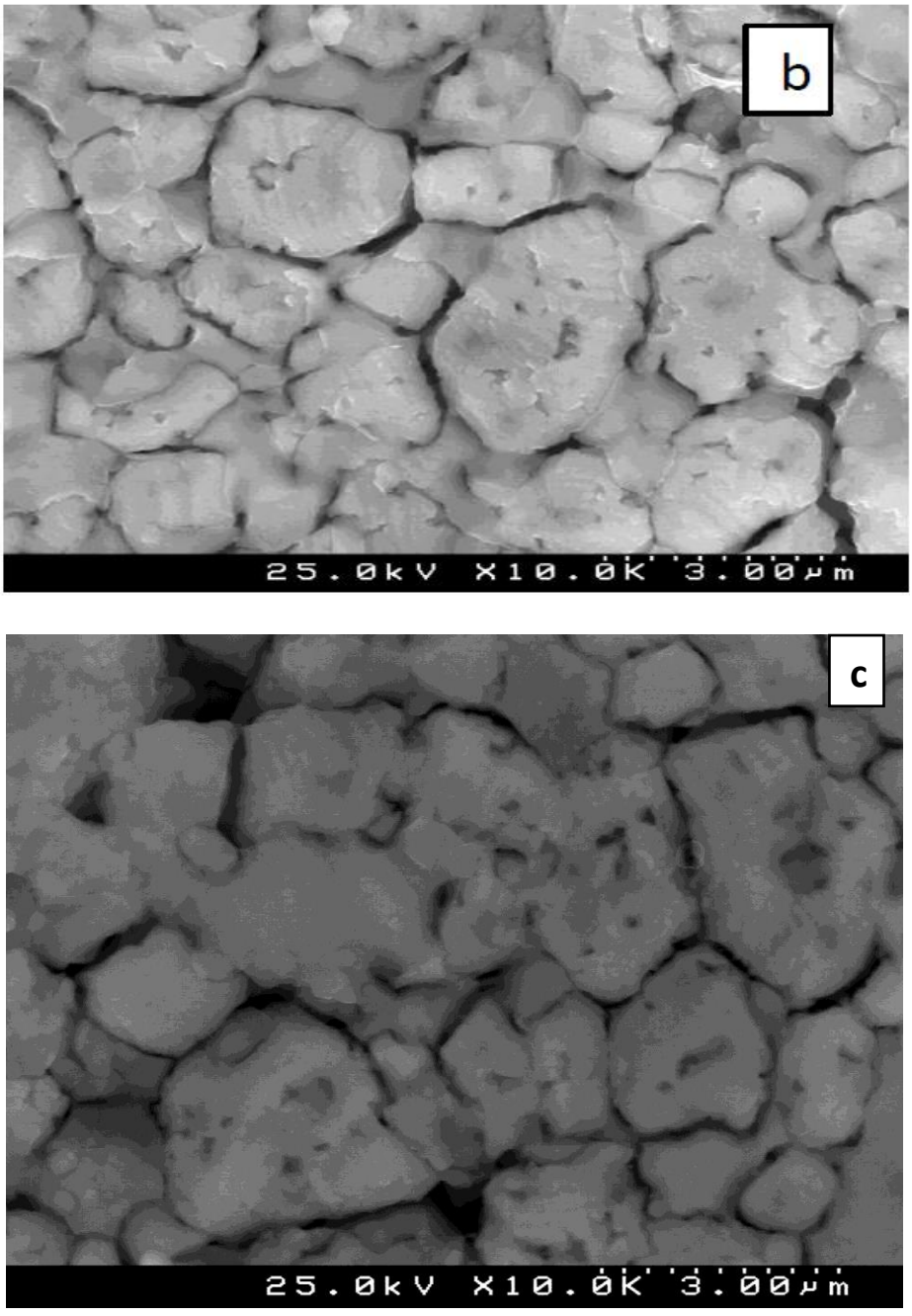

Figure 3.6. SEM micrographs of 40 vol% Ni-BZY anode pellets formed by the novel acetate combustion route (a) before and (b) after reduction compared to that of (c) the analogue prepared by the traditional nitrate method after reduction.

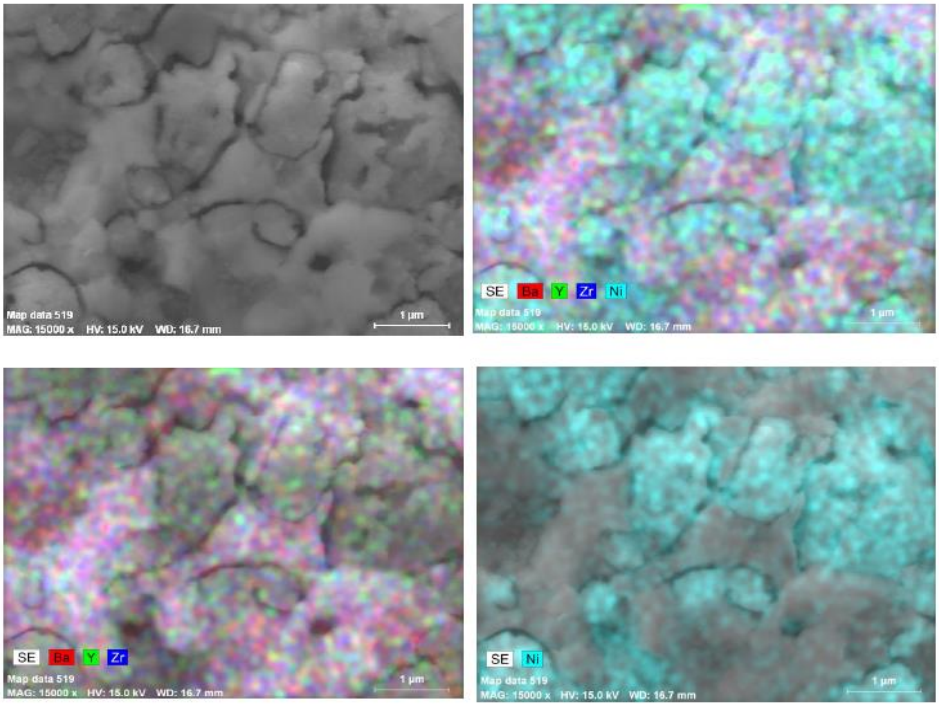

Figure 3.7. SEM-EDS elemental analysis of 40 vol% Ni-BZY anode pellets formed by the novel acetate combustion route.

3.2.3 Electrical Behaviour

Fig. 3.8 shows the total conductivity of Ni-BZY cermets, prepared by the novel acetate combustion method, as a function of Ni content, measured in wet and dry 10% H_2/N_2. At 20 vol.% Ni, conductivity increases in wet conditions, suggesting a protonic contribution to total transport. An activation energy of around 0.58 eV is recorded in wet conditions in the low temperature range, similar to that typically recorded for proton conduction in BZY ceramics (0.45-0.55 eV) [9]. On increasing the Ni-content to 30 vol.% Ni, conductivity shows a negative dependence on temperature, typical of metallic behaviour. The conductivity in this composition is lower in wet than in dry conditions, a phenomenon possibly explained by the slight increase in oxygen partial pressure (pO_2) in wet conditions and its potential influence on partial oxidation of Ni. On further increases in Ni content, the conductivity attains percolation with a similar metallic-like conductivity measured for all compositions regardless of humidity. The observed percolation in the 40 vol% Ni composition confirms the appearance of connectivity indicated by the microstructural investigation, Fig. 3.6 and 3.7.

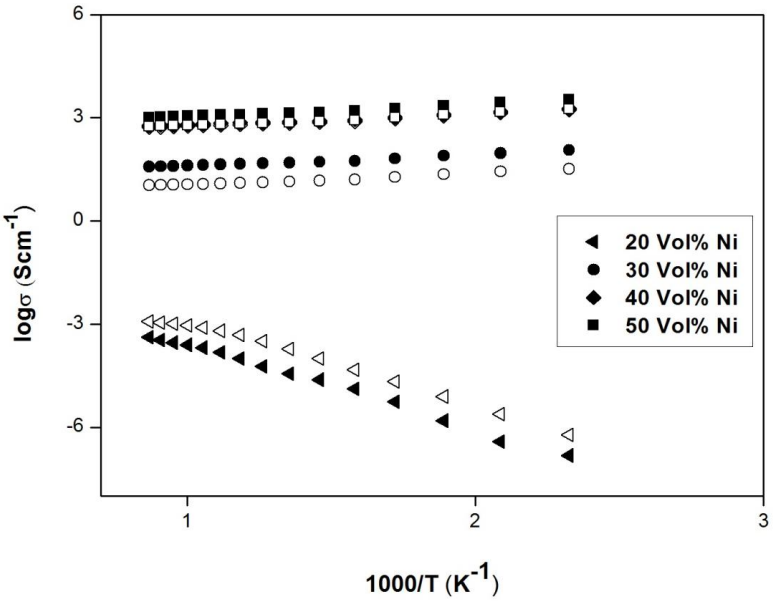

Figure 3.8. Arrhenius plots of Ni-BZY anodes formed by the acetate combustion method under wet (empty symbols) and dry (filled symbols) 10% H_2/N_2

3.2.4 Polarisation Behaviour

A SEM micrograph of a typical 40 vol.% Ni-BZY reduced symmetrical cell is shown in Fig. 3.9. The thicknesses of the sintered electrodes assemblies were approximately 110 µm for both the acetate- and nitrate-prepared samples, formed on a dense electrolyte with no observable delamination or cracks between electrolyte/electrode layers.

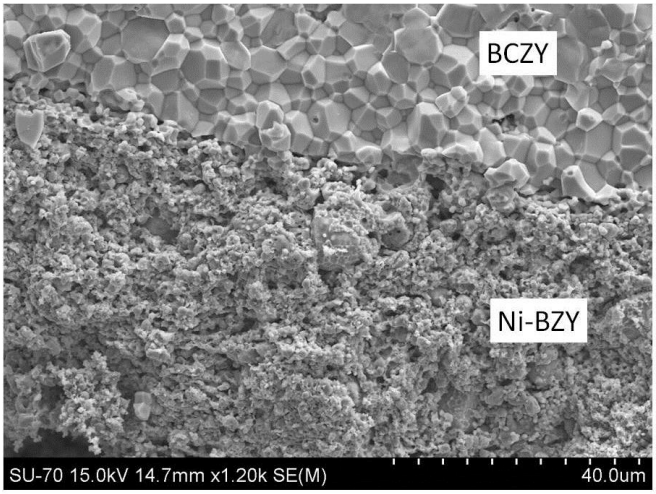

Figure 3.9. SEM micrograph of anode/electrolyte interface formed by the novel acetate combustion route

Fig. 3.10 shows the progression of the electrochemical impedance spectra of a symmetrical cell of BCZY electrolyte with 40 vol% Ni-BZY electrodes, measured in wet 10% H_2/N_2, as a function of temperature. The presented impedance spectra correspond to cermet electrodes prepared by the novel acetate combustion process. The impedance spectra of electrodes produced by the traditional nitrate route are similar. The two samples are subsequently labeled "Acetate" and "Nitrate", respectively.

At the lowest temperature, 100 ºC, two responses are observed at high and intermediate frequencies, which can be attributed to bulk and grain-boundary contributions by consideration of their characteristic capacitances [31], together with a trace of a further response at lower frequency. On increasing the temperature to 300 ºC, the relaxation dispersion of the bulk response shifts beyond the available frequency window of measurement, leaving only the grain-boundary response and two distinct low-frequency responses observable. With further increases in temperature, the impedance spectra gradually lose information associated with the grain boundary and become dominated by the two electrode responses. Correspondingly, the impedance spectrum at 600 ºC reveals only the electrode responses, accompanied by an inductive effect at higher frequency.

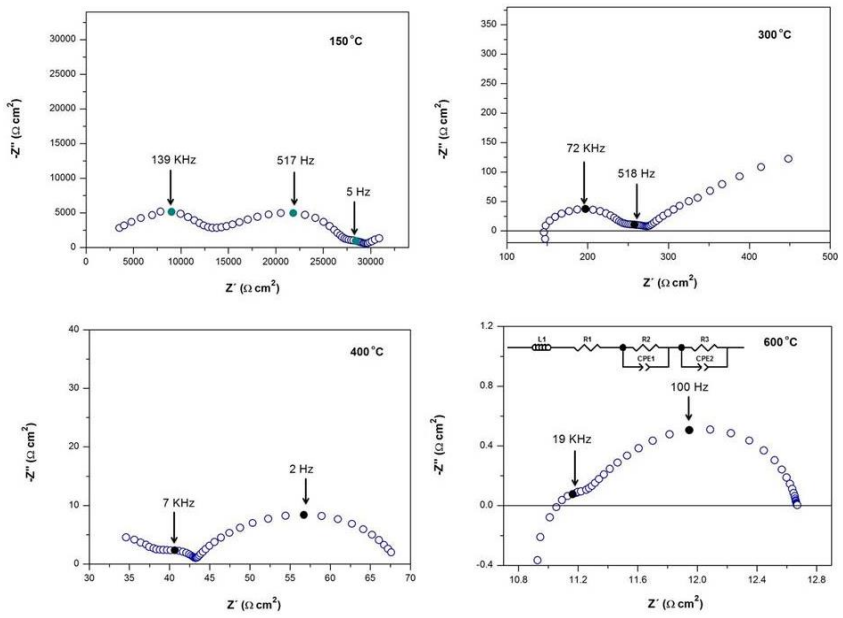

Figure 3.10. The electrochemical impedance spectra of a symmetrical cell with 40 vol% Ni-BZY electrodes, measured in wet 10% H_2/N_2, as a function of temperature.

Due to the novelty of PCFCs, the origin of electrode responses in proton-conducting cermet electrodes has not received detailed study to date. Nevertheless, the majority of reported proton cermet anodes have been described to show a similar electrode behavior, consisting of two distinct phenomena [1, 13, 18]. The impedance spectra at 600 ºC were fitted using the equivalent circuit outlined in Fig. 3.10, which consists of an inductance in series with a resistor, R1, and two distributed elements, RQ. The fitting parameters extracted for each distributed arc are the resistance, R, the pseudo-capacitance, Q, and an additional parameter n that can be related to the true capacitance by the equation

$$C = R^{(1-n)/n} Q^{1/n} \qquad (3.1)$$

In this way, the true capacitance values of the distributed responses have been calculated to be in the order of 10^{-6} Fcm^{-2} for the higher frequency response, associated with resistance R2, and 10^{-3} Fcm^{-2} for the lower frequency response, associated with resistance R3. The obtained capacitance values correspond well to those previously noted for Ni-BZY electrodes [18]. The current work extends present knowledge by assessing the influence of phase purity on the performance of the Ni-BZY cermet electrodes and also provides new information with which to clarify the origin of the electrode responses in proton-conducting cermets, by analysis of their water vapour (pH_2O) and hydrogen (pH_2) partial pressures dependencies.

Figure 3.11 shows the pH_2 dependencies of the polarization resistances R2 and R3 for symmetrical cells of 40 vol% Ni-BZY electrodes formed by the novel acetate and traditional nitrate combustion processes, measured at 600 ºC under humid, reducing conditions. The polarisation data were multiplied by the electrode area and the factor 0.5 to account for both electrodes. The R2 values demonstrate only a weak dependence on pH_2, whereas the R3 values exhibit much stronger pH_2 dependence. The higher frequency polarisation resistance, R2, of the Nitrate sample is shown to be substantially greater than that measured for the novel Acetate sample. On the contrary, the lower frequency polarisation resistance, R3, is shown to be less in the Nitrate case. The combination of these factors leads the Nitrate sample to exhibit a progressively higher overall polarisation resistance, Rp, than the Acetate sample, in reducing conditions, Fig. 3.12.

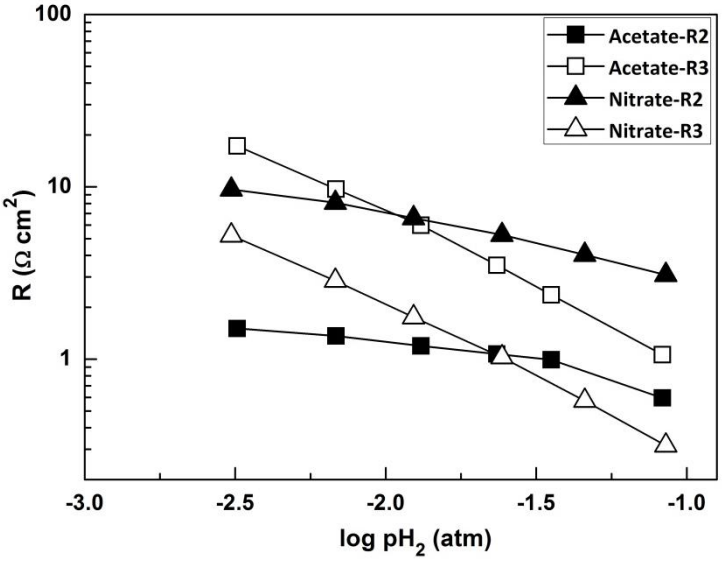

Figure 3.11. Comparison of polarization resistance (R2 and R3) with pH_2 in wet reducing atmosphere at 600 °C for both acetate- and nitrate-prepared cermets.

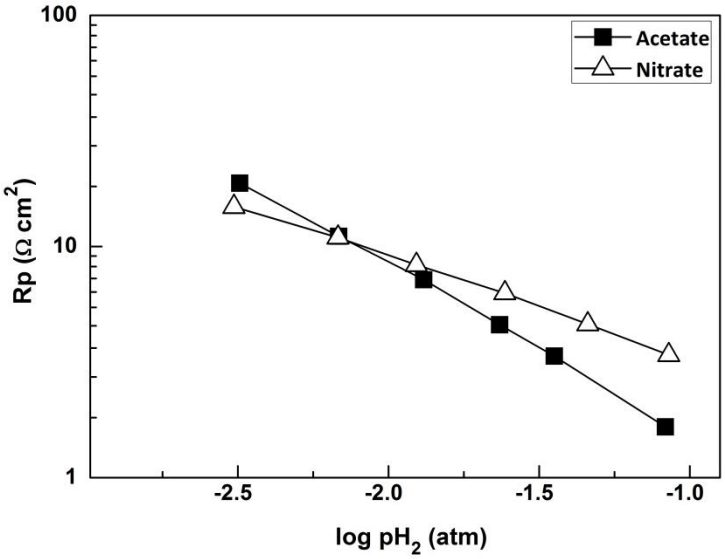

Figure 3.12. Comparison of total polarization resistance (Rp) with pH_2 in wet reducing atmosphere at 600 °C for both acetate and nitrate

Figure 3.13 shows the pH_2O dependencies of the polarization resistances R2 and R3 for the Acetate and Nitrate samples, measured at 600 ºC. The high-frequency polarisation resistance, R2, of the Nitrate sample shows a significant dependence on pH_2O,

whereas the R2 values of the Acetate sample only show this dependence at low values of pH_2O, being independent of pH_2O at high humidites. The R3 values show only a weak dependence on pH_2O, in contrast to their significant pH_2 dependence noted in the previous experiment described in Fig. 3.11. The combination of these tendencies and the considerably larger values of R2 than R3 lead the total polarisation resistance, Rp, obtained for both samples under these conditions to be dominated by the high-frequency response, R2, Fig. 3.14. The significance pH_2O and pH_2 dependencies of polarisation resistance of cermet anodes are discussed in more detail in the forthcoming chapter 4.

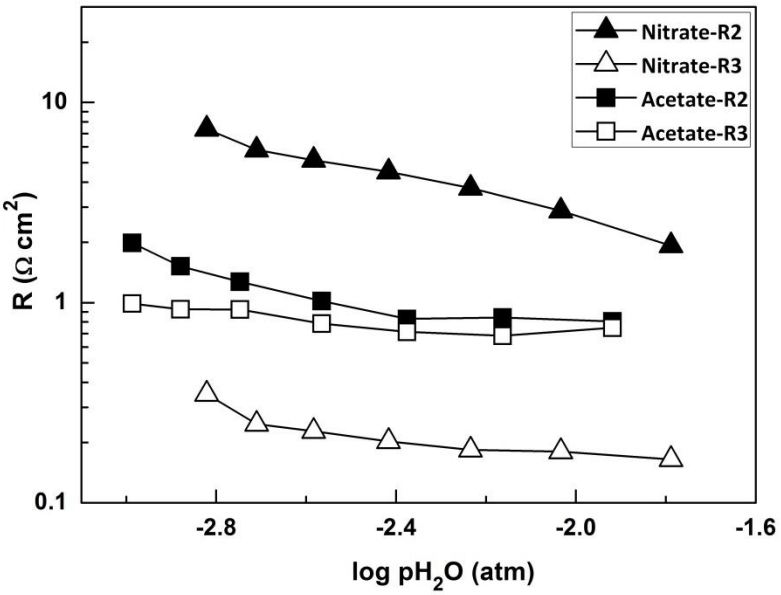

Figure 3.13. Comparison of polarization resistance (R2 and R3) with pH_2O in wet 10% H_2/N_2 at 600 °C for acetate- and nitrate-prepared cermets

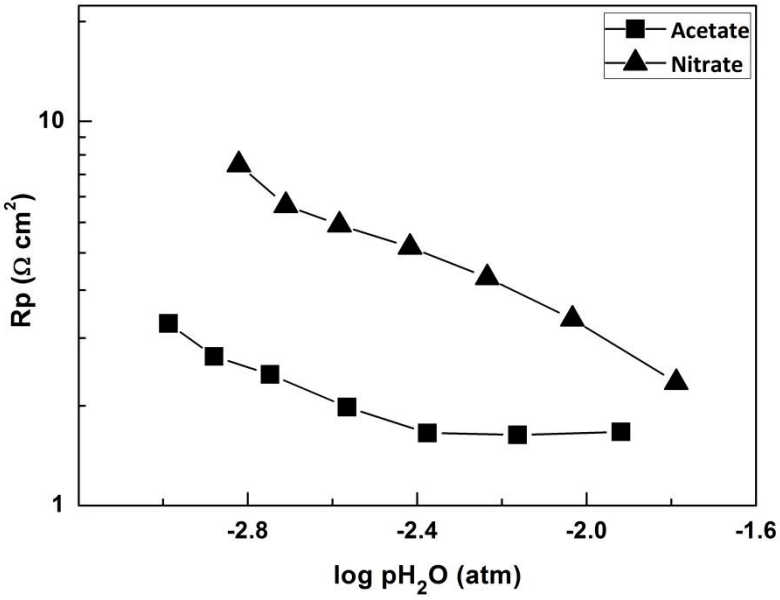

Figure 3.14. Comparison of total polarization resistance (Rp) with pH_2O in wet 10% H_2/N_2 at 600 °C for acetate- and nitrate-prepared cermets.

The R2 response has been suggested to have a possible relationship to proton conduction in the oxide phase of the cermet anode, based on the observation that it manifests an activation energy that is similar to that reported for BZY [18]. The activation energy of R2 measured in wet 10%H_2/N_2 in the current Ni-BZY anodes is calculated to be around 0.6 eV for both Nitrate and Acetate samples in the temperature range 400-600 ºC, in agreement to that previously reported [18]. It is important to restate that the Ni-BZY anode formed by the nitrate combustion technique was shown to have an impurity phase of BaY_2NiO_5 in contrast to the pure Ni-BZY anode formed by the novel acetate process, Fig. 3.4. As the bulk BZY material has been reported to exhibit lower conductivity with Ba-loss [23, 24], the formation of impurity phases and the associated formation of a barium-deficient perovskite can analogously be suggested to hinder proton conductivity in the nitrate produced anode. For the Ni-BZY anodes of comparable microstructure presented here, this effect appears to limit performance by increasing the R2 polarisation resistance associated with impaired proton transport in the oxide cermet phase.

3.3 Conclusions

A novel acetate, combustion method has been developed to synthesize Ni-BZY cermet anodes for proton-conducting SOFCs. The acetate combustion route avoids the decomposition of pre-prepared BZY powders, in contrast to the classical nitrate method where $Ba(NO_3)_2$ forms as an impurity phase in the precursor gel. Such segregation of Ba from the perovskite phase during the classical nitrate route leads to formation of $BaCO_3$ in the combusted powders and, subsequently, to a BaY_2NiO_5 impurity phase in the final anode cermet. Both combustion routes produce a homogeneous distribution of NiO particles in a BZY matrix with similar microstructure and porosity. Percolation behaviour is achieved for Ni contents equal to or greater than 40 vol.%. The polarisation behaviour appears to consist of two phenomena, R2 and R3, at high and low frequency respectively. The formation of impurity phases during the traditional nitrate/glycine route and the associated partial decomposition of the perovskite cermet phase are shown to limit overall performance by increasing the R2 polarisation resistance in anodes of comparable microstructure. This phenomenon is suggested to be due to impaired proton transport in the oxide anode cermet phase. The nitrate-free combustion route, here described, is a simple, low cost and rapid process to synthesize high-purity Ni-BZY cermet anodes and the importance of phase purity of resultant polarisation behaviour is proven. This combustion method can also be employed for the formation of many other ceramic-oxide materials from their component acetates, providing a more environmentally friendly synthesis route than the classical nitrate combustion method, due to the avoidance of NO_x emissions.

3.4 References

[1] Chevallier L, Zunic M, Esposito V, Di Bartolomeo E, Traversa E. A wet-chemical route for the preparation of Ni–$BaCe_{0.9}Y_{0.1}O_{3-\delta}$ cermet anodes for IT-SOFCs. Solid State Ionics. 2009;180:715-20.

[2] Zunic M, Chevallier L, Radojkovic A, Brankovic G, Brankovic Z, Di Bartolomeo E. Influence of the ratio between Ni and $BaCe_{0.9}Y_{0.1}O_{3-\delta}$ on microstructural and electrical properties of proton conducting Ni–$BaCe_{0.9}Y_{0.1}O_{3-\delta}$ anodes. J Alloys Compd. 2011;509:1157-62.

[3] Mather GC, Figueiredo FM, Fagg DP, Norby T, Jurado JR, Frade JR. Synthesis and characterisation of Ni–$SrCe_{0.9}Yb_{0.1}O_{3-\delta}$ cermet anodes for protonic ceramic fuel cells. Solid State Ionics. 2003;158:333-42.

[4] Frontera P, Modafferi V, Frusteri F, Bonura G, Bottari M, Siracusano S, et al. Catalytic features of Ni/Ba–$Ce_{0.9}$–$Y_{0.1}$ catalyst to produce hydrogen for PCFCs by methane reforming. Int J Hydrogen Energy. 2010;35:11661-8.

[5] Scholten MJ, Schoonman J, van Miltenburg JC, Oonk HAJ. Synthesis of strontium and barium cerate and their reaction with carbon dioxide. Solid State Ionics. 1993;61:83-91.

[6] Sneha BR, Thangadurai V. Synthesis of nano-sized crystalline oxide ion conducting fluorite-type Y_2O_3-doped CeO_2 using perovskite-like $BaCe_{0.9}Y_{0.1}O_{2.95}$ (BCY) and study of CO_2 capture properties of BCY. J Solid State Chem. 2007;180:2661-9.

[7] Zakowsky N, Williamson S, Irvine JTS. Elaboration of CO_2 tolerance limits of $BaCe_{0.9}Y_{0.1}O_{3-\delta}$ electrolytes for fuel cells and other applications. Solid State Ionics. 2005;176:3019-26.

[8] Fabbri E, Depifanio A, Dibartolomeo E, Licoccia S, Traversa E. Tailoring the chemical stability of $Ba(Ce_{0.8-x}Zr_x)Y_{0.2}O_{3-\delta}$ protonic conductors for Intermediate Temperature Solid Oxide Fuel Cells (IT-SOFCs). Solid State Ionics. 2008;179:558-64.

[9] Kreuer KD. On the development of proton conducting materials for technological applications. Solid State Ionics. 1997;97:1-15.

[10] Tu C-S, Chien RR, Schmidt VH, Lee S-C, Huang C-C, Tsai C-L. Thermal stability of $Ba(Zr_{0.8-x}Ce_xY_{0.2})O_{2.9}$ ceramics in carbon dioxide. J Appl Phys. 2009;105:103504.

[11] Zhong Z. Stability and conductivity study of the $BaCe_{0.9-x}Zr_xY_{0.1}O_{2.95}$ systems. Solid State Ionics. 2007;178:213-20.

[12] Coors WG, Manerbino A. Characterization of composite cermet with 68wt.% NiO and $BaCe_{0.2}Zr_{0.6}Y_{0.2}O_{3-\delta}$. Journal of Membrane Science. 2011;376:50-5.

[13] Essoumhi A, Taillades G, Taillades-jacquin M, Jones D, Roziere J. Synthesis and characterization of Ni-cermet/proton conducting thin film electrolyte symmetrical assemblies. Solid State Ionics. 2008;179:2155-9.

[14] Lee T, Dorris S, Balachandran U. Thin film preparation and hydrogen pumping characteristics of $BaCe_{0.8}Y_{0.2}O_{3-\delta}$. Solid State Ionics. 2005;176:1479-84.

[15] Rainwater BH, Liu M, Liu M. A more efficient anode microstructure for SOFCs based on proton conductors. Int J Hydrogen Energy. 2012;37:18342-8.

[16] Song SJ, Moon JH, Lee TH, Dorris SE, Balachandran U. Thickness dependence of hydrogen permeability for Ni–$BaCe_{0.8}Y_{0.2}O_{3-\delta}$. Solid State Ionics. 2008;179:1854-7.

[17] Mather GC, Figueiredo FM, Jurado JR, Frade JR. Synthesis and characterisation of cermet anodes for SOFCs with a proton-conducting ceramic phase. Solid State Ionics. 2003;162–163:115-20.

[18] Bi L, Fabbri E, Sun Z, Traversa E. $BaZr_{0.8}Y_{0.2}O_{3-\delta}$-NiO Composite Anodic Powders for Proton-Conducting SOFCs Prepared by a Combustion Method. J Electrochem Soc. 2011;158:B797.

[19] Bi L, Fabbri E, Sun Z, Traversa E. Sinteractive anodic powders improve densification and electrochemical properties of $BaZr_{0.8}Y_{0.2}O_{3-\delta}$ electrolyte films for anode-supported solid oxide fuel cells. Energy Environ Sci. 2011;4:1352.

[20] Azad AK, Savaniu C, Tao S, Duval S, Holtappels P, Ibberson RM, et al. Structural origins of the differing grain conductivity values in $BaZr_{0.9}Y_{0.1}O_{2.95}$ and indication of novel approach to counter defect association. J Mater Chem. 2008;18:3414-8.

[21] Duval SBC, Holtappels P, Vogt UF, Stimming U, Graule T. Characterisation of $BaZr_{0.9}Y_{0.1}O_{3-\delta}$ Prepared by Three Different Synthesis Methods: Study of the Sinterability and the Conductivity. Fuel Cells. 2009;9:613-21.

[22] Magrez A, Schober T. Preparation, sintering, and water incorporation of proton conducting $Ba_{0.99}Zr_{0.8}Y_{0.2}O_{3-\delta}$: comparison between three different synthesis techniques. Solid State Ionics. 2004;175:585-8.

[23] Magrez A, Schober T. Thermal degradation of proton conductors $Ba_yM_{1-x}Y_x$ $O_{3-\delta}$ (M=Zr, Ce). Ionics. 2005;11:171-6.

[24] Yamazaki Y, Hernandez-Sanchez R, Haile SM. Cation non-stoichiometry in yttrium-doped barium zirconate: phase behavior, microstructure, and proton conductivity. J Mater Chem. 2010;20:8158-66.

[25] Imashuku S, Uda T, Nose Y, Awakura Y. To Journal of Phase Equilibria and Diffusion Phase Relationship of the BaO-ZrO_2-$YO_{1.5}$ System at 1500 and 1600 °C. Journal of Phase Equilibria and Diffusion. 2010;31:348-56.

[26] Oyama Y, Kojima A, Li X, Cervera RB, Tanaka K, Yamaguchi S. Phase relation in the BaO–ZrO_2–$YO_{1.5}$ system: Presence of separate $BaZrO_3$ phases and complexity in phase formation. Solid State Ionics. 2011;197:1-12.

[27] Lencka MM, Riman RE. Thermodynamic modeling of hydrothermal synthesis of ceramic powders. Chem Mater. 1993;5:61-70.

[28] Tong J, Clark D, Bernau L, Sanders M, O'Hayre R. Solid-state reactive sintering mechanism for large-grained yttrium-doped barium zirconate proton conducting ceramics. J Mater Chem. 2010;20:6333.

[29] Ricote S, Bonanos N. Enhanced sintering and conductivity study of cobalt or nickel doped solid solution of barium cerate and zirconate. Solid State Ionics. 2010;181:694-700.

[30] Tong J, Clark D, Hoban M, O'Hayre R. Cost-effective solid-state reactive sintering method for high conductivity proton conducting yttrium-doped barium zirconium ceramics. Solid State Ionics. 2010;181:496-503.

[31] Bauerle JE. Study of solid electrolyte polarization by a complex admittance method. J Phys Chem Solids. 1969;30:2657-70.

Chapter 4

The impact of porosity, pH_2 and pH_2O on the polarisation resistance of Ni-$BaZr_{0.85}Y_{0.15}O_{3-\delta}$ cermet anodes [‡]

Abstract

The effect of porosity and atmosphere on the polarisation resistance of Ni-BZY cermet anodes for protonic ceramic fuel cells (PCFCs) was investigated using electrochemical impedance spectroscopy (EIS) and scanning electron microscopy (SEM). The level of porosity was adjusted by the use of differing amounts of starch porogen. The total polarisation resistance of the cermet anode (Rp) generally showed an increase with increasing porosity. The high frequency polarisation resistance (R2) was shown to have low atmosphere dependence but presented a strong correlation to microstructural variations. In contrast, the low frequency polarisation resistance (R3) was shown to have a low dependence on humidity but demonstrated a strong negative dependence on pH_2 with a value of unity. Subsequent discussion relates the lower frequency response to the dissociative adsorption of H_2 on the anode surface. The present study highlights that porogens are not required for peak performance in PCFC anodes under standard operating conditions, a result contrary to that of their oxide-ion conducting cermet counterparts.

[‡] This Chapter has been published as Narendar N, Ramasamy D, Brandão AD, Yaremchenko AA, Fagg DP. The impact of porosity, pH_2 and pH_2O on the polarisation resistance of Ni-$BaZr_{0.85}Y_{0.15}O_{3-\delta}$ cermet anodes for Protonic Ceramic Fuel Cells (PCFCs). Int J Hydrogen Energy. 2014;39:21231–41.

4.1 Introduction

The anode materials suggested for PCFC devices have typically mirrored traditional concepts proposed for their oxide-ion conducting counterparts, involving a cermet structure consisting of a metallic phase, such as Ni, and an ionically conducting ceramic matrix. It has been demonstrated, that the performance of these PCFC anodes can be strongly influenced by the level of proton conductivity offered by the ceramic oxide matrix, with performance being limited when protonic transport in the matrix is insufficient [1–3]. Preliminary studies of such Ni-Ba(Zr,Y)$O_{3-\delta}$ cermets have shown polarisation resistances that are well within the appropriate range for efficient fuel cell operation [1,4].

In oxide-ion conducting SOFCs (O-SOFC), the performance of a cermet anode is shown to depend heavily on its microstructure. The porosity, phase distribution, tortuosity and particle size of Ni-yttria stabilized zirconia (Ni-YSZ) cermets have been reported to impact both gas phase diffusion and the three phase boundary length (TPB), between the electronic, ionic and the gas phases, radically altering the electrochemical performance [5,6]. The optimal microstructure of cermet anodes for O-SOFC has received several decades of study and is well placed in the literature; in order to achieve a high electrochemical performance, the O-SOFC cermet anode should possess a long three phase boundary (TPB), to maximize electrochemical reactions, while maintaining open porosity to facilitate gas phase diffusion [7]. Nonetheless, a careful balance must be made between these two criteria, as a too high porosity can adversely affect the TPB length. For this reason the optimal porosity of cermet anodes for O-SOFC has been documented to approach ~50% [5,8,9]. This porosity is higher than that obtainable from solely Ni-reduction and, therefore, external porogens such as rice starch [8], carbon microspheres [9] and polymer fibers [10] are commonly employed to increase levels of final porosity.

In contrast, the optimal microstructure for cermet anode in PCFCs has not yet been finalized. In the aforementioned PCFC cermet anodes, both the matrix phase and the nickel metallic phase may act as proton carriers [11]. It has been proposed that this unique feature may lead to extension of the three phase boundary length (protons, electrons and gas phase) where the electrochemical reaction may occur [12,13]. Moreover, Coors etc al. have suggested that high porosity may not be essential in PCFC anodes, as hydrogen (a small molecule) was outlined to be the only diffusing gas species in this case, in contrast to

that of an oxide-ion conducting anode in which water vapour must also counter-diffuse [14]. Coors et al. studied the microstructure of a Ni-$BaCe_{0.2}Zr_{0.6}Y_{0.2}O_{3-\delta}$ anode, at a Ni content of 68 wt% (~40 vol% Ni), upon reduction without the addition of a porogen. From microstructural analysis and the observation of metallic–like conductivity the authors suggested that the resultant porosity ~26% created solely from the reduction of NiO to Ni may be adequate for operation without the necessity of further porogen [14]. However, no measurements of electrode kinetics were performed.

Taillades et al. studied the electrochemical behaviour of two Ni-$BaCe_{0.9}Y_{0.1}O_{2.95}$ cermets with 35 and 45 vol% Ni using symmetrical anode/electrolyte/anode assemblies and showed slightly lower polarisation resistance in the anode of highest Ni-content [15]. The same team later analysed the effect of a gelled starch porogen on the resultant porosity and microstructure of a bulk pellet of 40 vol% Ni-$BaCe_{0.9}Y_{0.1}O_{2.95}$ cermet and noted that its DC conductivity slightly decreased when porosity levels approached 44% [16]. Zunic et al. studied the influence of Ni content on electrochemical behaviour in Ni-$BaCe_{0.9}Y_{0.1}O_{2.95}$ cermets, for 40, 50 and 60 wt% Ni (36, 45 and 55 vol% Ni, respectively), noting that percolation was obtained for all compositions, while only minor variations of electrochemical performance could be obtained by compositional variation [17]. By observation of the electrochemical behaviour of fuel cells with a BZCYYb electrolyte and $La_{0.6}Sr_{0.4}Co_{0.2}Fe_{0.8}O_{3-\delta}$ (LSCF) cathode, Rainwater et al. reported that Ni-$BaZr_{0.1}Ce_{0.7}Y_{0.1}Yb_{0.1}O_{3-\delta}$ (Ni-BZCYYb) anodes prepared with different quantities of porogen exhibited a monotonous decrease in performance with increasing levels of porosity [18]. The authors noted that the I-V curves obtained for these fuel cells were essentially linear, differing only in their gradient. The results of Rainwater et al. suggest that a higher area specific resistance (ASR) results from an increasing porosity. Nonetheless, one is unable to distinguish the underlying cause of the increase in ASR by complete fuel cells tests (without a reference electrode). For example, if the depletion in performance should be attributed to a higher anode polarisation resistance, variations in the cathode performance or to a varying contact resistance with increasing anode porosity.

The potential high sensitivity of Ni-cermet anode performance on the microstructure [6,7], emphasizes the critical importance of the processing route. The chapter 3 outlined a new acetate-H_2O_2 combustion route for the preparation of Ni-$BaZr_{0.85}Y_{0.15}O_{3-\delta}$ (Ni-BZY) anodes [1]. This novel method was shown to be essential to

avoid the formation of BaY_2NiO_5 impurity phase; a common impurity noted in more traditional nitrate-based combustion routes for Ni-Ba(Ce,Zr,Y)$O_{3-\delta}$ anode preparation [1,19–23]. This work is to provide a detailed study of the effect of porosity on the polarisation behaviour of phase pure Ni-BZY anodes. The impact of porosity on the anode polarisation resistance is revealed by a combination of electrochemical impedance spectroscopy and scanning electron microscopy for anodes prepared using different starch contents (5%, 10% and 20%). Mechanistic information on polarisation behaviour is provided by varying the temperature, water vapor and hydrogen partial pressure during the electrochemical assessment of the resultant anodes. The work uses Ni-BZY/BCZY/Ni-BZY symmetrical cells, thereby, eliminating potential secondary effects relating to variations in contact resistance, electrolyte resistance or cathode polarisation that are inherent in complete fuel cell testing and, thus, can present a clear picture of anode behaviour. The experimental details of the syntheses can be found in Chapter 2 under section 2.1.

4.2 Results

4.2.1 Phase and microstructure analysis

Fig. 4.1 depicts the XRD patterns of as-sintered and reduced 40 vol% Ni-BZY cermet anode prepared by the acetate-H_2O_2 combustion route. Phases of BZY and NiO can be observed for the as-sintered samples, whereas BZY and Ni phases are observed for the reduced cermet. The absence of NiO phase indicates that complete reduction can be achieved in these materials under the conditions of 10% H_2/N_2 mixture at 700 °C for 8h.

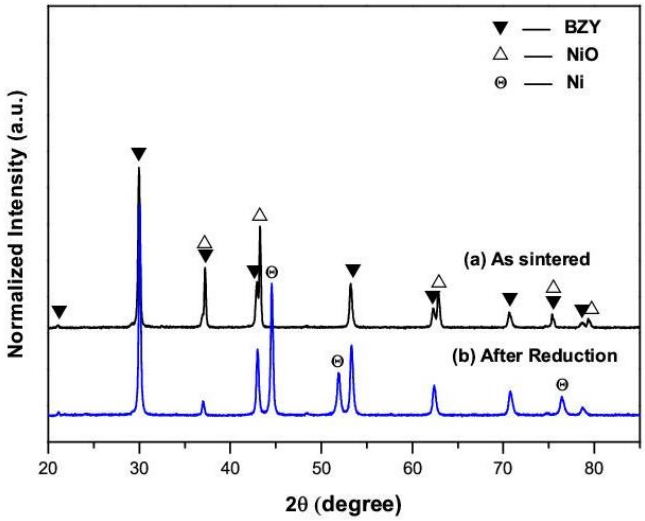

Figure 4.1. XRD patterns of 40 vol% Ni-BZY cermet anode (a) as sintered and (b) after reduction at 700 ºC for 8h in 10%H_2/N_2.

The porosity of the reduced Ni-BZY anodes was determined using the Archimedes method in two different solvents, water and dibutyl phthalate. The total porosity of reduced Ni-BZY0, Ni-BZY5, Ni-BZY10 and Ni-BZY20 cermet anodes with respect to starch content, is as shown in table 4.1. The porosity values measured by the two solvents are shown to be similar. The anode without additional porogen, Ni-BZY0, shows the lowest porosity with value ~34%, while the porosity is shown to increase with increasing starch content to finally exhibit ~56% porosity in the anode Ni-BZY20 prepared from 20 wt% starch.

Table 4.1: Total porosity of 40 vol% Ni-BZY cermet anodes with respect to porogen content and solvent medium

Ni-BZY(X) X= Porogen (Starch in wt%)	**Total porosity (%)**	
	Water	**Dibutyl phthalate**
0	34.05	33.70
5	42.25	45.27
10	46.38	50.02
20	55.74	56.08

Fig. 4.2 shows a SEM micrograph of a reduced 40 vol% Ni-BZY cermet anode formed without additional porogen. By mercury intrusion porosimetry, Coors et al. noted that pore size distribution in reduced PCFC cermet anodes that do not contain additional porogens is strongly bimodal [14]. Pore sizes at the nanometric scale were attributed to the presence of reduced Ni-metal particles with a pocketed microstructure containing very fine porosity and high surface area. Larger pores of ~0.3-0.7 μm were attributed to the channels formed between the Ni-grains and the ceramic matrix due to the volume contraction associated with reduction of NiO particles to Ni-metal. Both these features can be clearly observed in Fig. 4.2.

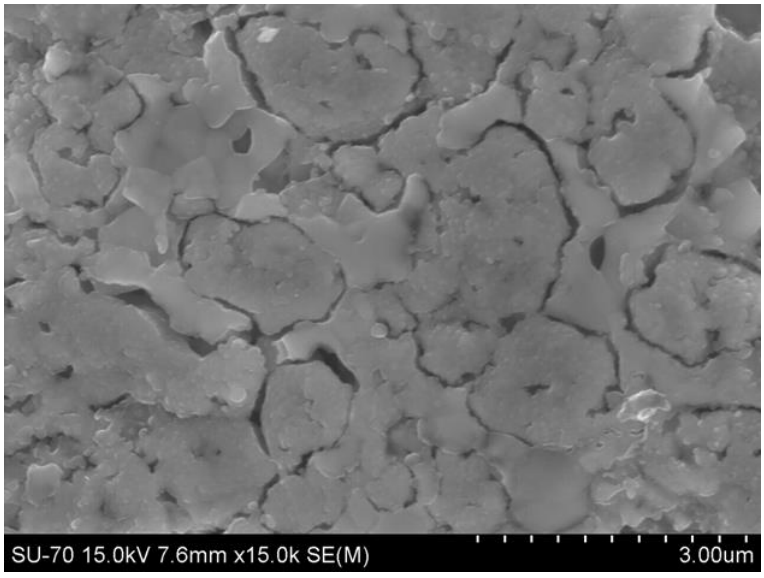

Figure 4.2. SEM micrograph of 40 vol% Ni-BZY reduced cermet anode formed without porogen

Fig. 4.3 shows SEM micrographs of reduced 40 vol% Ni-BZY cermet anodes as a function of starch porogen content. The micrographs clearly exhibit an increase in porosity with increasing starch content, in agreement with Table 4.1. The macro pores apparent in Ni-BZY5, Ni-BZY10 and Ni-BZY20 anodes, Fig. 4.3(b), (c) & (d), are, therefore, as a direct result of burning out the starch porogen, as noted by Taillades et al. [28].

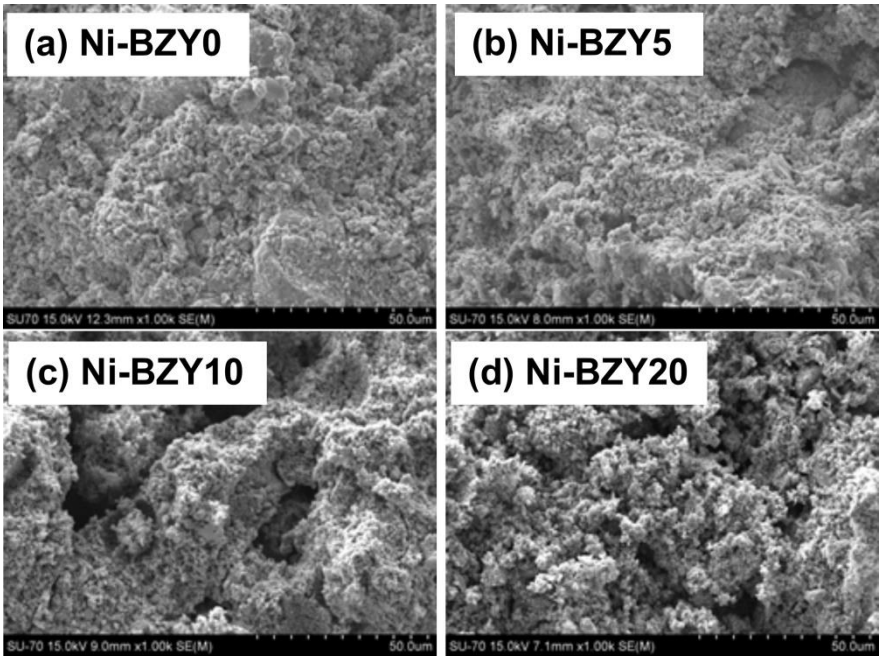

Figure 4.3. SEM micrographs of 40 vol% Ni-BZY reduced cermet anode formed with (a) 0 wt% starch, (b) 5 wt% starch, (c) 10 wt% starch and (d) 20 wt% starch

Fig. 4.4(a) shows the SEM micrographs of fractured Ni-BZY0/BCZY71 interface after reduction at 700 °C in 10% H_2/N_2 gas mixture. No delamination or cracks can be observed at the anode/electrolyte interface and a good adherence between anode and electrolyte has been achieved. A line scan at anode/electrolyte interface was performed to assess possible elemental diffusion by SEM-EDS and concludes that no apparent interdiffusion of cerium occurs from the electrolyte to the anode layer, Fig. 4.4(b).

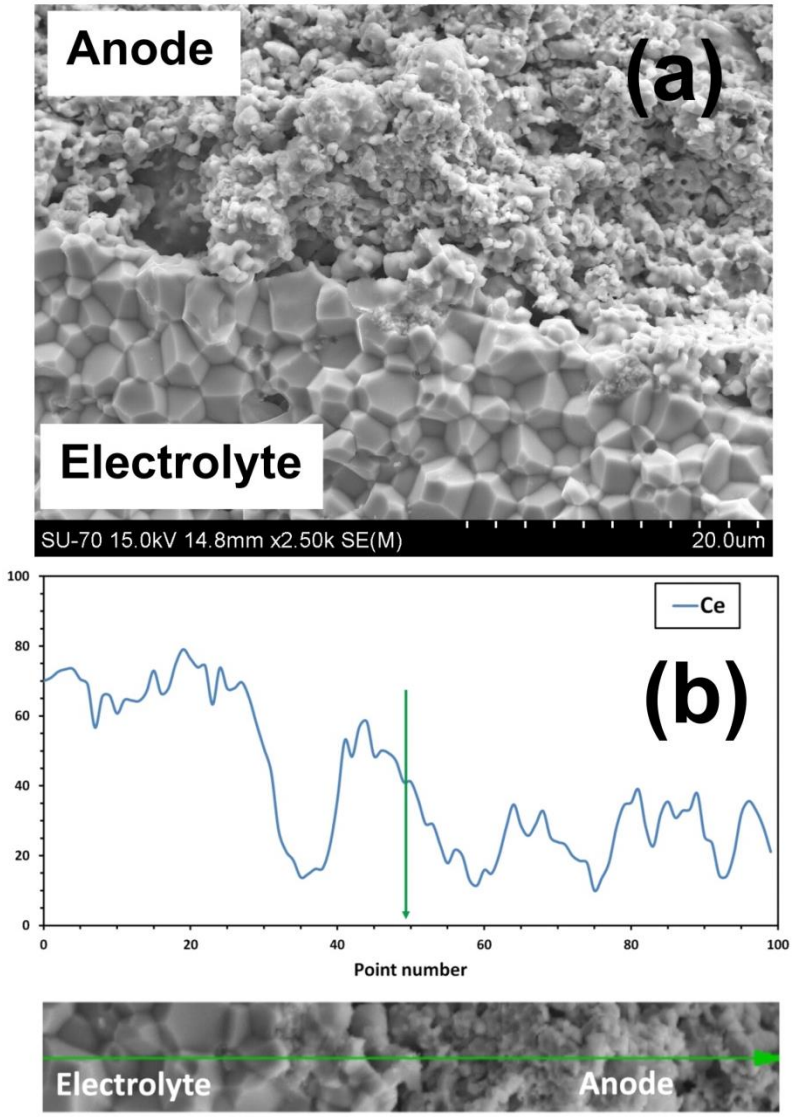

Figure 4.4. SEM micrographs of (a) electrolyte/anode interface and (b) SEM-EDS line scan at electrolyte/anode interface

4.2.2 Effect of porosity on the bulk conductivity of Ni-BZY anodes

The total conductivities of bar shaped samples of the anode materials, Ni-BZY0, Ni-BZY5, Ni-BZY10 and Ni-BZY20, prepared with increasing amounts of starch, are presented in Fig. 4.5. One can see that the total conductivity of the anode materials is significantly impaired with increasing starch content, a factor that suggests a decreased interconnectivity upon an increasing level of porosity. On the other hand, the conductivity of these electrodes can be observed to remain several orders of magnitude higher than the electrolyte resistance measured under the same conditions, Fig. 4.5, suggesting that the serial resistance of the symmetrical anode/electrolyte/anode assemblies in the following sections will continue to be extensively dominated by the electrolyte resistance.

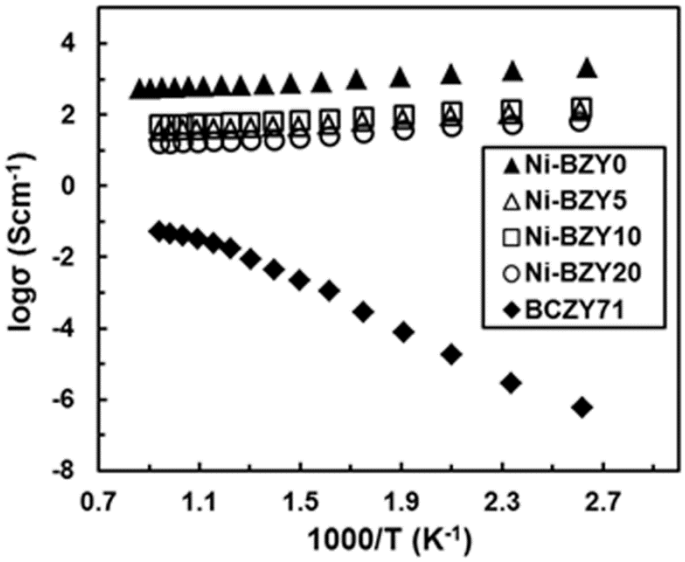

Figure 4.5. The total conductivity of 40 vol% Ni–BZY (differing starch content) cermet and electrolyte, measured in wet 10% H_2/N_2 gas atmosphere

4.2.3 Electrochemical behaviour of Ni-BZY anodes

4.2.3.1. Impedance Spectra

Four symmetrical anode/electrolyte/anode cells (Ni-BZY0, Ni-BZY5, Ni-BZY10 and Ni-BZY20) were prepared for the electrochemical measurements using a BCZY71 electrolyte. Preliminary electrochemical measurements were performed by impedance spectroscopy in wet 10% H_2/N_2 gas mixture for all symmetrical cells as a function of temperature. At 600 °C, the shape of the impedance spectra for all samples is shown to be consistent with previous results of Ni-BZY cermet anodes, chapter 3, consisting of two

clearly resolvable semicircles and an inductive component at the highest frequencies, Fig. 4.6 [11,12]. The impedance data were, thus, analysed via a typical equivalent circuit consisting of an inductance in series with a resistor, R1 (representing the cell ohmic resistance) and two distributed RQ elements (inset in Fig. 4.6). The fitting parameters extracted for each distributed semicircle are the resistance, R, the pseudo-capacitance, Q, and the parameter n that relates to the true capacitance by the equation

$$C = R^{(1-n)/n} Q^{1/n} \qquad (4.1)$$

Using this equation, the true capacitance values of the distributed responses were calculated to be in the order of 10^{-5}-10^{-6} Fcm^{-2} for the higher frequency response arc (associated with resistance R2) and 10^{-3}-10^{-4} Fcm^{-2} for the lower frequency response arc (associated with resistance R3), in agreement to those previously noted for Ni-BZY electrodes formed without an additional porogen [1,4]. Due to their widely separated time constants, the two semicircles represent two distinct electrode responses occurring at the anode [1]. At temperatures below 400 ºC, an additional response at high frequency could be observed in the impedance spectra of capacitance values in the order of 10^{-9} Fcm^{-2}, corresponding to the grain boundary phenomenon of the electrolyte. In this way, the correct attribution of the impedance spectra at higher temperatures to that of electrode responses can be confirmed [12]. The values of polarisation resistance were multiplied with electrode area and a factor 0.5 to account for the presence of both symmetrical electrodes.

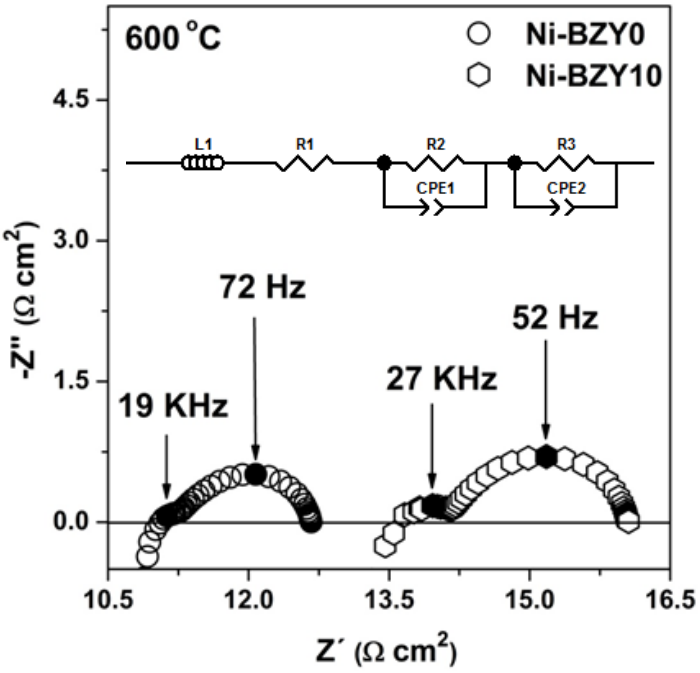

Figure 4.6. The EIS spectrum of a symmetrical cell with 40 vol% Ni–BZY (0wt% and 10wt% starch) cermet anode, measured in wet 10% H_2/N_2 at 600 °C

4.2.3.2. Effect of Porosity

Table 4.2 shows that the high frequency offset resistance, R1, representing the cell ohmic resistance, increases with increasing porosity, in agreement with the depleted total conductivity of the anode materials, and likely impaired contact resistance with increasing porosity.

Table 4.2: The dependence of ohmic offset resistance, R1, on porosity.

Cermet anode	R1 (Ω cm^2)
Ni-BZY0	10.78
Ni-BZY5	11.28
Ni-BZY10	13.48
Ni-BZY20	20.78

Fig. 4.7 shows total polarisation resistance Rp, where Rp = R2 + R3, of the cermet anodes Ni-BZY0, NiBZY5, Ni-BZY10 and Ni-BZY20 as a function of temperature. The anode containing the lowest porosity, Ni-BZY0, demonstrates the lowest values of

polarisation resistance. On increasing the level of porosity the value of Rp suffers substantial increase. Nonetheless, a monotonous increase with increasing porosity is not observed, with Ni-BZY5 and Ni-BZY10 cermet anodes demonstrating similar polarisation behaviour, despite dissimilar levels of porosity, Table 4.1. With the highest level of porosity studied (~56%) the sample Ni-BZY20 shows the highest Rp value of all anodes analysed.

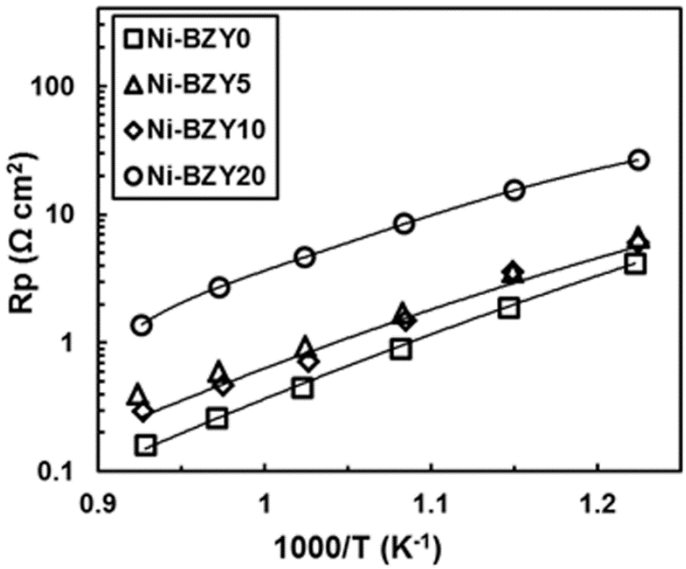

Figure 4.7. Temperature dependence of the total polarisation resistance, Rp, of Ni-BZY cermet anodes (differing starch content) in wet 10% H_2/N_2

4.2.3.3 Effect of pH_2

Fig. 4.8(a), (b) & (c) show the dependence of polarisation resistance on pH_2 in wet reducing atmospheres at 600 °C for Ni-BZY anodes of varying starch content. The high frequency polarisation resistance R2 is shown to have a weak inverse dependence on pH_2 for all Ni-BZY cermet anodes, Fig. 4.8(a). In contrast, the low frequency polarisation resistance R3 of Ni-BZY cermet anode is shown to be strongly influenced by pH_2, exhibiting a negative dependence of approximately unity ($R3 \alpha pH_2^{-1}$), Fig. 4.8(b). The much greater values of R3 than R2 at low pH_2 lead the R3 response to dominate the total polarisation resistance, resulting in a similar pH_2^{-1} dependence of Rp, Fig. 4.8(c). The values of R2, R3 and Rp are shown to increase with increasing porosity, Fig. 4.8(a-c).

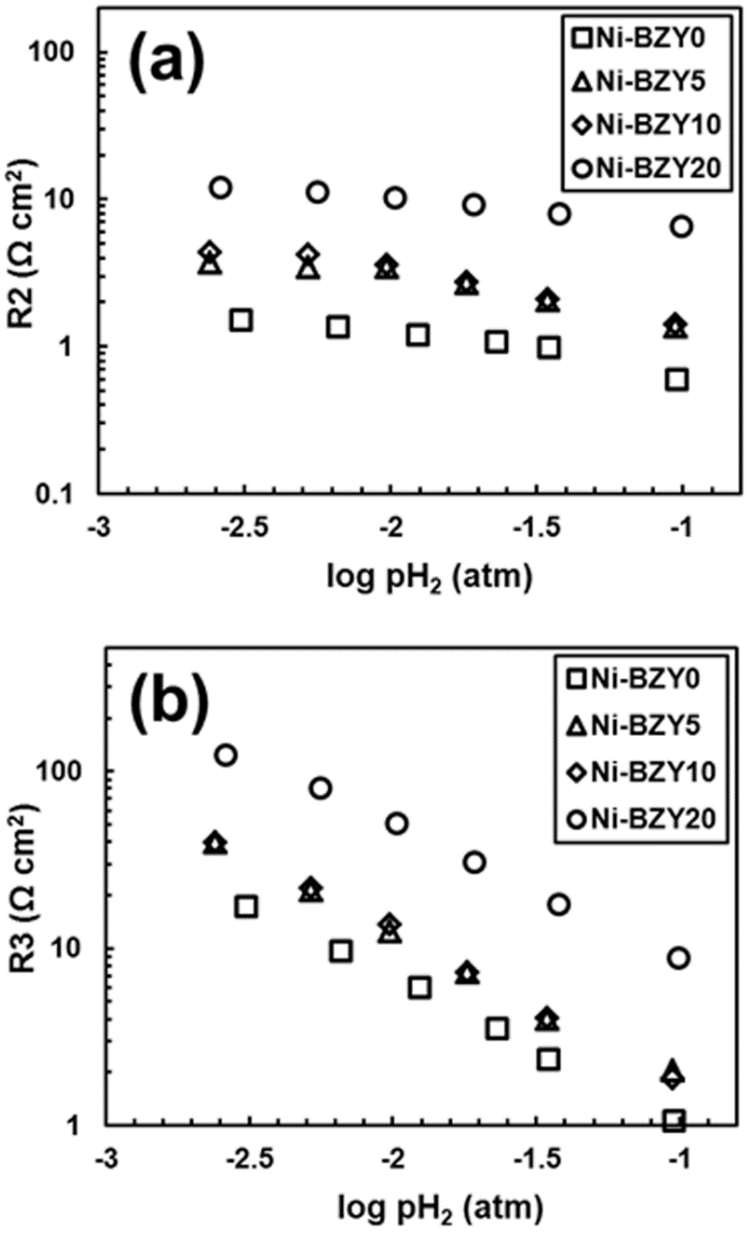
(a)
Ni-BZY0
Ni-BZY5
Ni-BZY10
Ni-BZY20
R2 (Ω cm²)
100
10
1
0.1
-3
-2.5
-2
-1.5
-1
log pH₂ (atm)
(b)
Ni-BZY0
Ni-BZY5
Ni-BZY10
Ni-BZY20
R3 (Ω cm²)
100
10
1
-3
-2.5
-2
-1.5
-1
log pH₂ (atm)

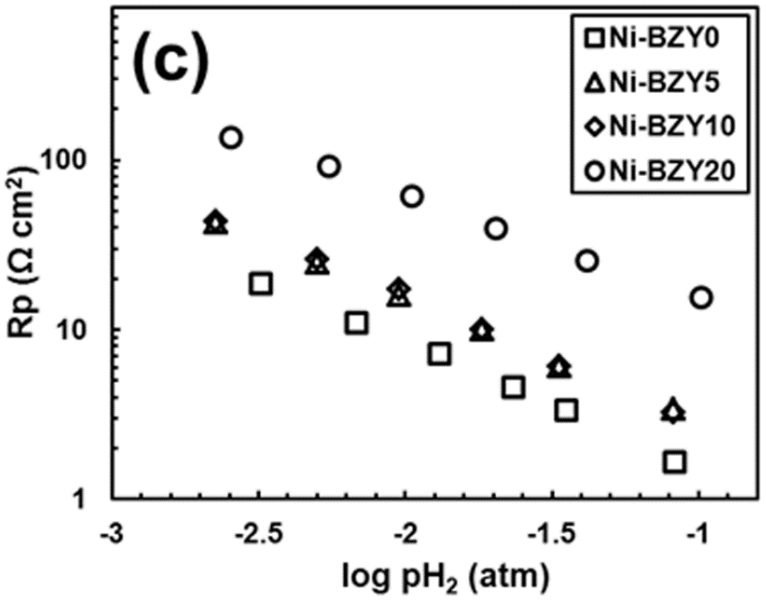

Figure 4.8. Variation of polarisation resistance (a) R2, (b) R3 and (c) total Rp with pH_2 for Ni-BZY cermet anode (with different starch content) in wet conditions at 600 °C

4.2.3.4 Effect of pH_2O

The effect of water vapour partial pressure (pH_2O) on the electrochemical performance of PCFC cermet anode (Ni-BZY) is studied for samples of different porosity in reducing atmospheres at 600 °C. Fig. 4.9(a), (b) & (c) depict the pH_2O dependencies of polarisation resistances for Ni-BZY anodes with varying levels of porogen, presenting the values for R2, R3, and Rp, respectively. The high frequency polarisation resistance R2 shows effective pH_2O independence, with the exception of the densest anode (Ni-BZY0). The densest anode demonstrates apparent pH_2O independence at high humidities followed by slight pH_2O-dependence upon moving towards the driest conditions, Fig. 4.9(a). Fig. 4.9(a) reveals that the polarisation resistance, R2, increases significantly by increasing the quantity of starch.

The low frequency polarisation resistance R3 shows effective pH_2O independence for the densest samples, Fig. 4.9(b), while the samples formed with more elevated amounts of starch demonstrate slight positive dependencies of R3 on pH_2O. The values of R3 for the densest samples are shown to be similar, while that of the most porous sample is shown to be substantially higher. Combination of the R2 and R3 terms, leads to an effective independence of total polarisation resistance, Rp, on pH_2O, Fig. 4.9(c), with the exception of the least porous sample Ni-BZY0 in the driest conditions, where an increase in

polarisation resistance is observed with decreasing humidity, reflecting the aforementioned trend in the R2 term for this composition.

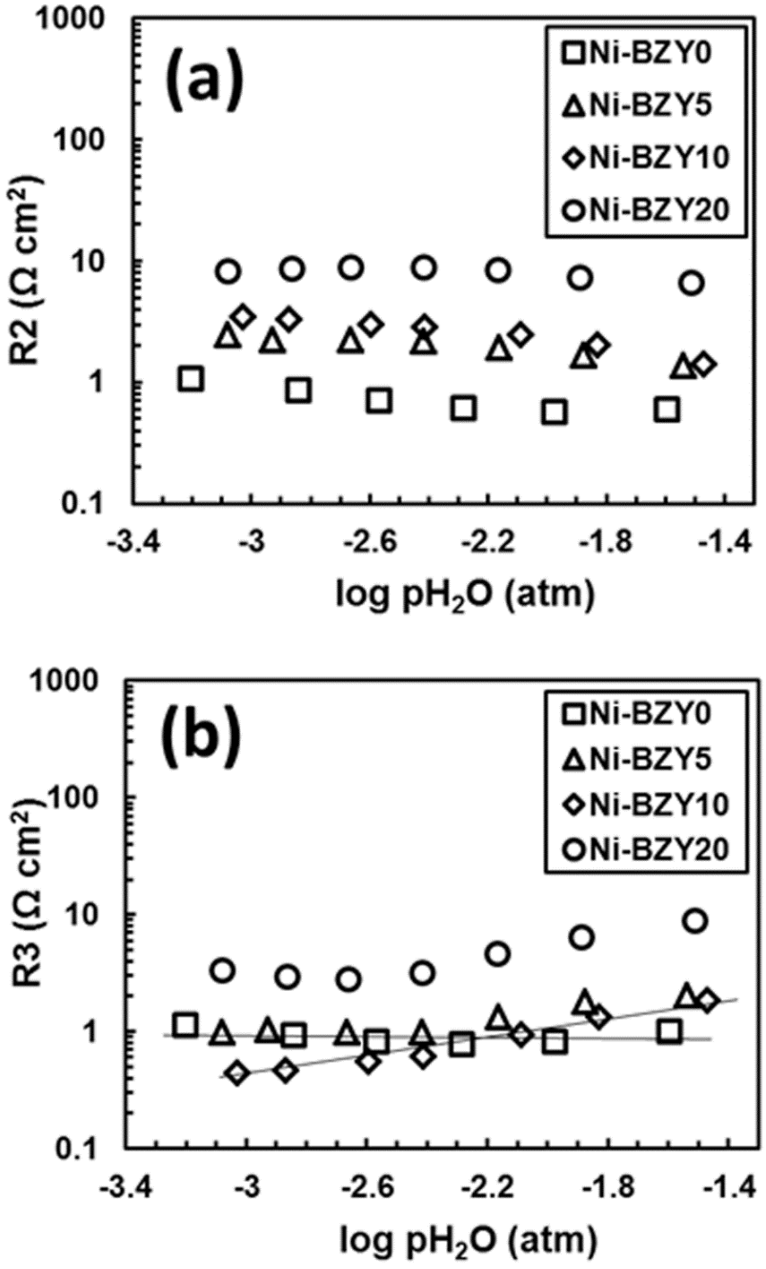

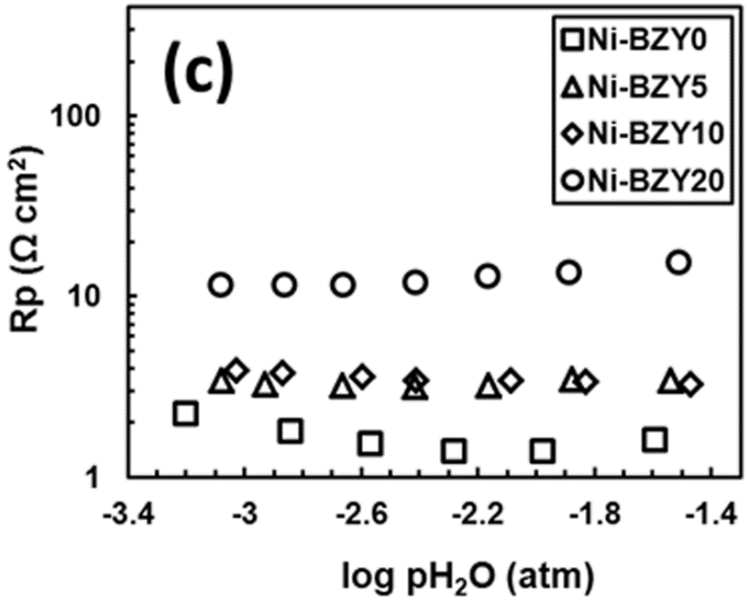

Figure 4.9. Variation of polarisation resistance (a) R2, (b) R3 and (c) total Rp with pH_2O in 10% H_2/N_2 at 600 °C for Ni-BZY cermet anode (with different starch content)

4.3 Discussion

4.3.1 Discussion of the porosity dependence on the electrochemical behaviour of Ni-BZY anodes

Significant increases in polarisation resistances, R2, R3 and Rp, have been noted in the previous sections with increasing porosity. By analysis of anodes of fixed geometries, Bieberle et al. revealed a linear dependence between the three phase boundary length and the inverse of polarisation resistance (1/R) in the oxide-ion conducting cermet analogue, Ni-YSZ [24]. Furthermore, direct relationships between the level of porosity and the overall TPB length have been suggested by simulation studies of composite electrode materials based on percolation theory [25,26]. The works proposed that porosity negatively impacts the TPB length by depleting both the number of contacts between phases and their connection probabilities as well as the number of particles per unit volume. To assess possible links between the electrode conductivity and porosity for the current PCFC cermet anodes, Fig. 4.10 plots the inverse of the polarsation resistances R2, R3 and Rp as a function of porosity measured in moist 10%H_2/N_2 measured at 600 ºC. It can be seen that, in general, the responses, 1/R2, 1/R3 and 1/Rp, decrease with increasing porosity and that the greatest decrease is observed for the higher frequency polarisation response, R2. Based

on the aforementioned literature, the observed decrease in these terms with porosity, shown in Fig. 4.10 can be stated to most likely result from a decrease in the available three phase boundary length for electrochemical reaction, which may arise due to a loss in interconnectivity of the anode cermet.

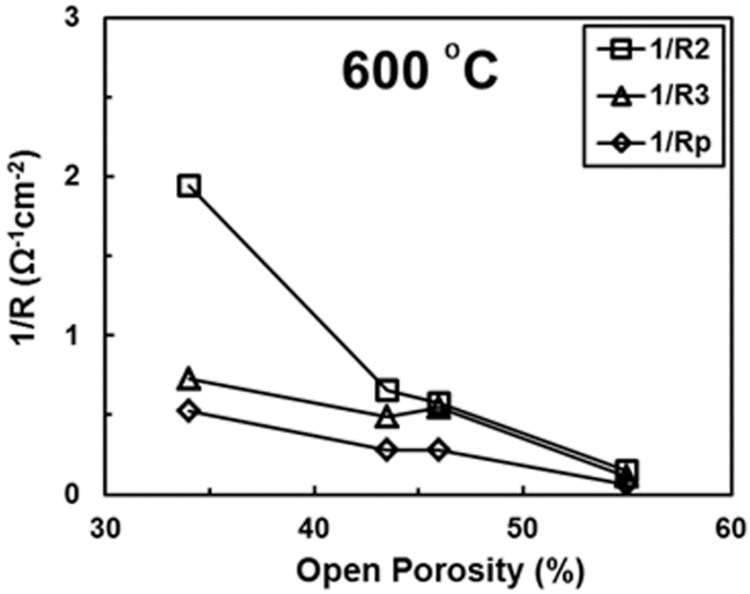

Figure 4.10. Inverse of polarisation resistance (1/R2, 1/R3 and 1/Rp) as a function of porosity at 600 °C for Ni-BZY cermet anode

Contrary to oxide-ion conducting SOFCs, where the cermet porosity required for optimal polarisation behaviour has been documented to be ~50% to achieve sufficient gas transport (thus requiring the use of porogens) [5,8,9], in PCFCs the anode of the lowest porosity is shown to exhibit the peak electrochemical performance under typical working conditions. This result agrees with that suggested by Rainwater in Ni-BZCYYb anodes [18]. These studies, therefore, indicate that for PCFC applications there is no need to modify the cermet anode microstructure by additional porogens under typical working conditions. In this case, the unique microstructure formed upon Ni-reduction, consisting of pocketed Ni particles and fine channels between Ni-grains and the ceramic matrix, already can facilitate sufficient gas transport to offer the peak electrochemical behaviour for the hydrogen oxidation reaction.

4.3.2 Discussion of the pH_2 and pH_2O dependence of the electrochemical behaviour

4.3.2.1 High frequency electrode response, R2

In the previous sections, the higher frequency electrode response, R2, was demonstrated to generally have a weak dependence on both humidity and hydrogen partial pressure, Fig. 4.8(a) & 4.9(a). The absence of significant atmosphere dependence for R2, for the samples formed using porogens, is reminiscent of that noted for the high frequency polarisation of oxide-ion conducing SOFC cermet anodes [27,28]. In these classical works on oxide-ion conducting cermets, the high frequency semicircle is commonly suggested to arise partly from the transfer of ions across the TPB line and to the resistance of ionic motion inside the ceramic electrode matrix. Typically, this response presents low atmosphere dependence but a strong dependence on microstructure. Note the latter trend again coincides well with the current results, in which the value of 1/R2 is shown to suffer considerably by variations in porosity, Fig. 4.10. Thus, the main trends of the R2 polarisation resistance, of low atmosphere dependence but a strong microstructural dependence, suggest similar arguments as in the classical literature for Ni-YSZ, but where the mobile species are modified to be specific for the PCFC case; migration of protonic species across the TPB line and to the resistance of protonic transport.

The minor variations of R2 observed with variations in pH_2, Fig. 4.8(a), likely results from the strong dependence of R3 on pH_2, Fig. 4.8(b); a dependence which causes increased difficulty of fitting of R2 on moving to lower values of pH_2, due to domination of the impedance spectra by the R3 term.

4.3.2.2 Low frequency electrode response, R3

The lower frequency electrode response, R3, was demonstrated in the previous sections to generally have only a low dependence on humidity, Fig. 4.9(b), whilst, manifesting a very strong dependence on pH_2, Fig. 4.8(b). Due to the large capacitance value associated with the R3 response (~10^{-3} Fcm^{-2}), Fabbri [4] and Kek [29] related this term to surface reactions, described by the following reaction steps

Step 1 : $H_2(g) \leftrightarrow 2H_{ad}$ (4.3)

Step 2: $H_{ad} \leftrightarrow H_{ad}^{+} + e^{-}$ (4.4)

As in our previous work [23], using the approach adopted by He et al. [30], the rate equations associated with these steps can be described by

$$r_1 = k_1 P_{H_2} - k_1^{/} a_{H_{ad}}^2 \tag{4.5}$$

$$r_2 = k_2 a_{H_{ad}} \exp\left(-\frac{FE}{2RT}\right) - k_2^{/} a_{H_{ad}^+} \exp\left(\frac{FE}{2RT}\right) \tag{4.6}$$

Here the rate equations are expressed as $r_i = r_{i\ forward} - r_{i\ reverse}$, where r_i is the reaction rate of any step i and the symmetry coefficient is assumed to be ½ [44]. The rate constants for the forwards and backwards reactions are described by k_i and $k_i^{/}$, respectively, while a_M is the activity of species, E is the Nernst electrode potential in the forward direction (equation 4.7) and R, F, and T have their usual meanings.

$$E_{eq} = E_o + \left(\frac{RT}{2F}\right) \ln P_{H_2} \tag{4.7}$$

The activity of dissociated hydrogen in Step 1 is given by

$$a_{H_{ad}} = \left(\frac{k_1}{k_1^{/}}\right)^{1/2} P_{H_2}^{1/2} \tag{4.8}$$

Thus, by substitution of equation (4.8) into equation (4.5) one can observe that a reaction order of unity with respect to hydrogen partial pressure will be predicted in both the forward and reverse directions for Step 1.

$$r_{forward} = k_1 P_{H_2} \tag{4.9}$$

$$r_{reverse} = k_1^{/} \left(\frac{k_1}{k_1^{/}}\right) P_{H_2} \tag{4.10}$$

On the contrary, for Step 2 the combination of equations (4.6) and (4.8) allows the activity of protons to be expressed as

$$a_{H^+_{ad}} = \left(\frac{k_2}{k_2^/}\right)\left(\frac{k_1}{k_1^/}\right)^{1/2} P_{H_2}^{1/2} \exp\left(-\frac{FE}{RT}\right) \quad (4.11)$$

While combination of equations (4.6), (4.8) and (4.11) allow the forward and reverse reaction rates for Step 2 to be expressed as

$$r_{forward} = k_2\left(\frac{k_1}{k_1^/}\right)^{1/2} P_{H_2}^{1/2} \exp\left(-\frac{FE}{2RT}\right) \quad (4.12)$$

$$r_{reverse} = k_2^/\left(\frac{k_2}{k_2^/}\right)\left(\frac{k_1}{k_1^/}\right)^{1/2} P_{H_2}^{1/2} \exp\left(-\frac{FE}{RT}\right)\exp\left(\frac{FE}{2RT}\right) \quad (4.13)$$

and by substituting the Nernst equation (4.5) into these relations gives

$$r_{forward} = k_2\left(\frac{k_1}{k_1^/}\right)^{1/2} P_{H_2}^{1/4} \exp\left(-\frac{FE_0}{2RT}\right) \quad (4.14)$$

and

$$r_{reverse} = k_2^/\left(\frac{k_2}{k_2^/}\right)\left(\frac{k_1}{k_1^/}\right)^{1/2} P_{H_2}^{1/4} \exp\left(-\frac{FE_0}{RT}\right)\exp\left(\frac{FE_0}{2RT}\right) \quad (4.15)$$

Thus, equations 4.14 and 4.15 describe the rate of Step 2 to have a reaction order with respect to hydrogen partial pressure of ¼.

The experimental dependence of the polarisation resistance R3 on pH_2 in the current work was shown to be negative with a strong dependence of approximately unity (R3 α pH_2^{-1}). From the above discussion, the low frequency response, R3, can be best related to the dissociative adsorption of H_2 on the anode surface, Step 1. Note limitation of the low frequency polarisation resistance on adsorption or diffusion of hydrogen species on the metallic cermet surface is a result again reminiscent of that observed for oxide-ion

conducting SOFC anodes [29]. The slight positive pH_2O dependences of R3 demonstrated by the most porous samples may result from competitive adsorption of water vapour on the metallic Ni surface in these anodes of higher porosity [31].

4.4 Conclusions

The effect of anode porosity and atmosphere on the polarisation behaviour of Ni-BZY cermet anodes for protonic ceramic fuel cells (PCFCs) has been elaborated. The Ni-BZY cermet anode with 34% porosity (formed without porogen) shows lower Rp values than anodes of higher porosity fabricated using porogens under normal PCFC operating conditions. This result is, therefore, contrary to the well-known oxide-ion conducting SOFC anodes in which much higher levels of porosity are required for optimal performance. The electrochemical results reveal that Ni-BZY anodes show only a weak dependence of polarisation resistance on pH_2O, but, in contrast, are highly pH_2 sensitive. The strong pH_2 dependence arises from the lower frequency R3 term that manifests a strong negative dependence on pH_2. The strong negative pH_2 dependence of unity of the R3 term has been related to the dissociative adsorption of H_2 on the anode surface. In contrast, the higher frequency polarisation response, R2, generally, shows low atmosphere dependence but significant dependence on microstructure. These results draw parallels to that observed in oxide-ion conducting SOFC anodes, related to migration of ionic species across the TPB line and to the resistance of ionic transport.

4.5 References

[1] Narendar N, Mather GC, Dias P a. N, Fagg DP. The importance of phase purity in Ni–$BaZr_{0.85}Y_{0.15}O_{3-\delta}$ cermet anodes – novel nitrate-free combustion route and electrochemical study. RSC Adv 2013;3:859.

[2] Mather G. Synthesis and characterisation of cermet anodes for SOFCs with a proton-conducting ceramic phase. Solid State Ionics 2003;162-163:115–20.

[3] Nasani N, Wang Z-J, Willinger MG, Yaremchenko AA, Fagg DP. In-situ redox cycling behaviour of Ni–$BaZr_{0.85}Y_{0.15}O_{3-\delta}$ cermet anodes for Protonic Ceramic Fuel Cells. Int J Hydrogen Energy 2014;39:19780–8.

[4] Bi L, Fabbri E, Sun Z, Traversa E. $BaZr_{0.8}Y_{0.2}O_{3-\delta}$-NiO Composite Anodic Powders for Proton-Conducting SOFCs Prepared by a Combustion Method. J Electrochem Soc 2011;158:B797.

[5] Zhao F, Virkar a. Dependence of polarization in anode-supported solid oxide fuel cells on various cell parameters. J Power Sources 2005;141:79–95.

[6] Suzuki T, Hasan Z, Funahashi Y, Yamaguchi T, Fujishiro Y, Awano M. Impact of anode microstructure on solid oxide fuel cells. Science 2009;325:852–5.

[7] Tsipis E V., Kharton V V. Electrode materials and reaction mechanisms in solid oxide fuel cells: a brief review. J Solid State Electrochem 2007;12:1039–60.

[8] Haslam JJ, Pham A-Q, Chung BW, DiCarlo JF, Glass RS. Effects of the Use of Pore Formers on Performance of an Anode Supported Solid Oxide Fuel Cell. J Am Ceram Soc 2005;88:513–8.

[9] Horri BA, Selomulya C, Wang H. Characteristics of Ni/YSZ ceramic anode prepared using carbon microspheres as a pore former. Int J Hydrogen Energy 2012;37:15311–9.

[10] Pan W, Lü Z, Chen K, Huang X, Wei B, Li W, et al. Novel polymer fibers prepared by electrospinning for use as the pore-former for the anode of solid oxide fuel cell. Electrochim Acta 2010;55:5538–44.

[11] Malagoli M, Liu ML, Park HC, Bongiorno A. Protons crossing triple phase boundaries based on a metal catalyst, Pd or Ni, and barium zirconate. Phys Chem Chem Phys 2013;15:12525–9.

[12] Ge X-M, Chan S-H, Liu Q-L, Sun Q. Solid Oxide Fuel Cell Anode Materials for Direct Hydrocarbon Utilization. Adv Energy Mater 2012;2:1156–81.

[13] Fabbri E, Pergolesi D, Traversa E. Electrode materials: a challenge for the exploitation of protonic solid oxide fuel cells. Sci Technol Adv Mater 2010;11:044301.

[14] Coors WG, Manerbino A. Characterization of composite cermet with 68 wt.% NiO and $BaCe_{0.2}Zr_{0.6}Y_{0.2}O_{3-\delta}$. J Memb Sci 2011;376:50–5.

[15] Essoumhi A, Taillades G, Tailladesjacquin M, Jones D, Roziere J. Synthesis and characterization of Ni-cermet/proton conducting thin film electrolyte symmetrical assemblies. Solid State Ionics 2008;179:2155–9.

[16] Taillades G, Batocchi P, Essoumhi A, Taillades M, Jones DJ, Rozière J. Engineering of porosity, microstructure and electrical properties of Ni–$BaCe_{0.9}Y_{0.1}O_{2.95}$ cermet fuel cell electrodes by gelled starch porogen processing. Microporous Mesoporous Mater 2011;145:26–31.

[17] Zunic M, Chevallier L, Radojkovic A, Brankovic G, Brankovic Z, Di Bartolomeo E. Influence of the ratio between Ni and $BaCe_{0.9}Y_{0.1}O_{3-\delta}$ on microstructural and electrical properties of proton conducting Ni–$BaCe_{0.9}Y_{0.1}O_{3-\delta}$ anodes. J Alloys Compd 2011;509:1157–62.

[18] Rainwater BH, Liu M, Liu M. A more efficient anode microstructure for SOFCs based on proton conductors. Int J Hydrogen Energy 2012;37:18342–8.

[19] Bi L, Fabbri E, Sun Z, Traversa E. Sinteractive anodic powders improve densification and electrochemical properties of $BaZr_{0.8}Y_{0.2}O_{3-\delta}$ electrolyte films for anode-supported solid oxide fuel cells. Energy Environ Sci 2011;4:1352.

[20] Tong J, Clark D, Bernau L, Sanders M, O'Hayre R. Solid-state reactive sintering mechanism for large-grained yttrium-doped barium zirconate proton conducting ceramics. J Mater Chem 2010;20:6333.

[21] Tong J, Clark D, Bernau L, Subramaniyan A, O'Hayre R. Proton-conducting yttrium-doped barium cerate ceramics synthesized by a cost-effective solid-state reactive sintering method. Solid State Ionics 2010;181:1486.

[22] Tong J, Clark D, Hoban M, O'Hayre R. Cost-effective solid-state reactive sintering method for high conductivity proton conducting yttrium-doped barium zirconium ceramics. Solid State Ionics 2010;181:496.

[23] Magrasó A, Li Z, Ricote S, Bonanos N, Manerbino A, Coors WG. Conductivity study of dense $BaCexZr_{(0.9-x)}Y_{0.1}O_{(3-\delta)}$ prepared by solid state reactive sintering at 1500 °C. Int J Hydrogen Energy 2012;37:7954–61.

[24] Bieberle A, Meier LP, Gauckler LJ. The Electrochemistry of Ni Pattern Anodes Used as Solid Oxide Fuel Cell Model Electrodes. J Electrochem Soc 2001;148:A646.

[25] Bertei A, Nicolella C. Percolation theory in SOFC composite electrodes: Effects of porosity and particle size distribution on effective properties. J Power Sources 2011;196:9429–36.

[26] Chen D, Lin Z, Zhu H, Kee RJ. Percolation theory to predict effective properties of solid oxide fuel-cell composite electrodes. J Power Sources 2009;191:240–52.

[27] M. Mogensen and T. Lindegaard. The kinetics of hydrogen oxidation on a Ni/YSZ SOFC electrode at 1000^{o}C,. Proc 3rd Int Symp Solid Oxide Fuel Cells, Honolulu, Hawaii, 1993:pp. 484–493.

[28] Primdahl S, Mogensen M. Oxidation of Hydrogen on Ni/Yttria-Stabilized Zirconia Cermet Anodes. J Electrochem Soc 1997;144:3409.

[29] Kek D, Bonanos N, Mogensen M, Pejovnik S. Effect of electrode material on the oxidation of H_2 at the metal–$Sr_{0.995}Ce_{0.95}Y_{0.05}O_{2.970}$ interface. Solid State Ionics 2000;131:249–59.

[30] He F, Wu T, Peng R, Xia C. Cathode reaction models and performance analysis of $Sm_{0.5}Sr_{0.5}CoO_{3-\delta}$–$BaCe_{0.8}Sm_{0.2}O_{3-\delta}$ composite cathode for solid oxide fuel cells with proton conducting electrolyte. J Power Sources 2009;194:263–8.

[31] Ihara M, Kusano T, Yokoyama C. Competitive Adsorption Reaction Mechanism of Ni/Yttria-Stabilized Zirconia Cermet Anodes in H_2-H_2O Solid Oxide Fuel Cells. J Electrochem Soc 2001;148:A209.

Chapter 5

In-situ redox cycling behavior of Ni-$BaZr_{0.85}Y_{0.15}O_{3-\delta}$ cermet anodes [ǂ]

Abstract

A detailed redox cycling behaviour of peak performing Ni-$BaZr_{0.85}Y_{0.15}O_{3-\delta}$ (Ni-BZY) cermet anodes for protonic ceramic fuel cells (PCFCs) is studied by electrochemical impedance measurements, scanning electron microscopy (SEM) and X-ray diffraction (XRD). Peak performing PCFC cermet anodes are documented to require much lower porosity levels than those needed in oxide-ion conducting counterparts. The polarisation behaviour of these optimised PCFC anodes is shown to be drastically impaired by redox cycling, with depletions in performance of around 80% noted after the first redox cycle. The ohmic resistance (Rohmic) is also shown to be increased due to delamination at the electrode/electrolyte interface, as confirmed by postmortem microstructural analysis. In-situ measurements by environmental scanning electron microscopy (ESEM) reveal that degradation proceeds due to volume expansion of the nickel phase during the re-oxidation stage of redox cycling. The present study reveals degradation to be very fast for peak performing Ni-BZY cermets of low porosity. Hence, methods to improve redox stability can be considered to be essential before such anodes can be implemented in practical devices.

[ǂ] This Chapter has been published as Nasani N, Wang Z-J, Willinger MG, Yaremchenko AA, Fagg DP. *In-situ* redox cycling behaviour of Ni–$BaZr_{0.85}Y_{0.15}O_{3-\delta}$ cermet anodes for Protonic Ceramic Fuel Cells. Int J Hydrogen Energy. 2014;39:19780-8.

5.1 Introduction

A novel synthesis route to form Ni-BZY cermets and their resultant electrochemical behavior has been elaborated in chapter 3. The previous studies and further works in the literature, have shown the area specific resistance (ASR) of Ni-BZY to be within the suitable range <1.5 Ω cm^2 for efficient fuel cell operation [1, 2]. The performance of PCFC cermet anodes has been shown to be tailorable by changes in the Ni content, the proton conductivity of the ceramic matrix phase [1] and the porosity [3]. Nonetheless, to date, none of the optimized PCFC anode materials have been tested in long-term fuel cell operation, where the robustness of PCFC systems will be strongly impacted by real operating conditions that may include system shutdown, interruption of fuel supply, fluctuating power demand and minor seal leakage; factors that have commonly been shown to lead to degradation of performance in oxide-ion conducting SOFCs [4]. In addition, many ceramic proton conductors have been reported to offer mixed transport for both protons and oxide-ions [5]. In such a case, steam may permeate through the membrane upon the existence of a water vapor partial pressure gradient. This effect has been described for a PCFC, where the water vapor partial pressure of the exhaust is commonly an order of magnitude higher than the fuel atmosphere [5]. This gradient provides a large driving force for steam permeation to the anode compartment that may have negative impact on the anode stability by potential nickel oxidation.

In order to achieve a high electrochemical performance, cermet anodes should possess a long three phase boundary length (TPB) (between the metallic phase, ceramic phase and gas phase) to maximize electrochemical reactions. However, it is well-known that redox cycling can adversely affect the TPB length [6]. The redox behavior of state-of-the-art Ni-YSZ anodes for oxygen-ion conducting fuel cells has been well documented in the literature [6-9] with several authors noting that the original microstructure and phase distribution cannot be restored when re-oxidation and re-reduction take place [6, 8, 10, 11]. Moreover, previous studies have shown that the durability of anodes is critically dependent on their microstructure and the cermet phase distribution [4, 12]. The available data highlight that Ni-YSZ is strongly affected by redox cycling and that the degradation rate of the cell can be very fast, especially at low porosity. Re-oxidation of Ni to NiO leads to a

bulk volume expansion of the cermet, which commonly causes micro-cracks and also delamination at the electrode/electrolyte interface; factors that reduce the fuel cell performance [4, 13].

To date there has been no literature data available on the redox behavior of PCFC cermet anodes. Moreover, due to some unique features of PCFC anodes, their redox tolerance may differ radically in comparison to their oxide-ion conducting counterparts. Firstly, in a PCFC cermet anode both the Ni phase and the ceramic oxide matrix phase can offer proton conductivity. This unique factor has led us to state that a PCFC cermet anode may have a lower dependence on the three phase boundary length than an oxide-ion conducting counterpart, due to the high mobility of protons through both the metallic nickel phase and the ceramic matrix [14]. As such, this factor may lead to lower performance degradation upon alteration of the microstructure (thus, three phase boundary length) during redox cycling. On the other hand, it has also been noted that lower porosity is desirable to obtain peak performance in PCFC anodes (as hydrogen is the only diffusing gas species), in contrast to that of an oxide-ion conducting anode in which water vapour must also counter-diffuse, outlined in chapter 4 [2, 3, 15]. This second factor may produce a very serious negative effect on redox cycling stability, as it has been noted that a higher porosity is preferable to minimize bulk volume expansion upon Ni re-oxidation in oxide-ion conducting cermets [16]. Hence, these unique features may radically alter the redox tolerance of PCFC anodes, in contrast to their oxide-ion conducting counterparts.

Thus, this chapter elaborate the degradation of peak performing 40vol% Ni-BZY anodes, of low porosity, by redox cycling using electrochemical impedance measurements, SEM and in-situ ESEM techniques. The content of 40vol%Ni was selected as it represented the lowest Ni content required to ensure percolation [15]. The redox cycles were performed on a Ni-BZY/BCZY/Ni-BZY symmetrical cell, cycling between a 10% H_2/N_2 gas mixture and an air stream. The experimental details of the syntheses can be found in Chapter 2 under section 2.1.

5.2 Redox cycling experimental procedure

The redox cycling experiments were performed at 800 °C. The cermet was first reduced in flowing 10% H_2/N_2 gas mixture and then re-oxidized in air. Before every redox cycle the symmetrical cell was maintained in the 10% H_2/N_2 gas mixture and thermally cycled between 800 ºC and 600 ºC, during which impedance measurements were performed. The redox cycling was repeated during the tests according to the steps shown in Fig. 5.1. Before each redox cycle step, electrochemical impedance measurements were performed to evaluate the performance degradation of the cermet anode.

a) The symmetrical cell was reduced at 800 °C in moist 10% H_2/N_2 gas mixture (pH_2O = ~0.031 atm and pO_2 = ~2.8×10^{-20} atm) for 6 h.
b) The 10% H_2/N_2 gas flow was stopped and the cell purged with N_2 gas for 5 min.
c) For the re-oxidation experiment, the N_2 gas flow was stopped and synthetic air ($80\%N_2/20\%O_2$) was passed for 4 h.
d) The air flow was stopped and the cell purged with N_2 gas for 5 min.

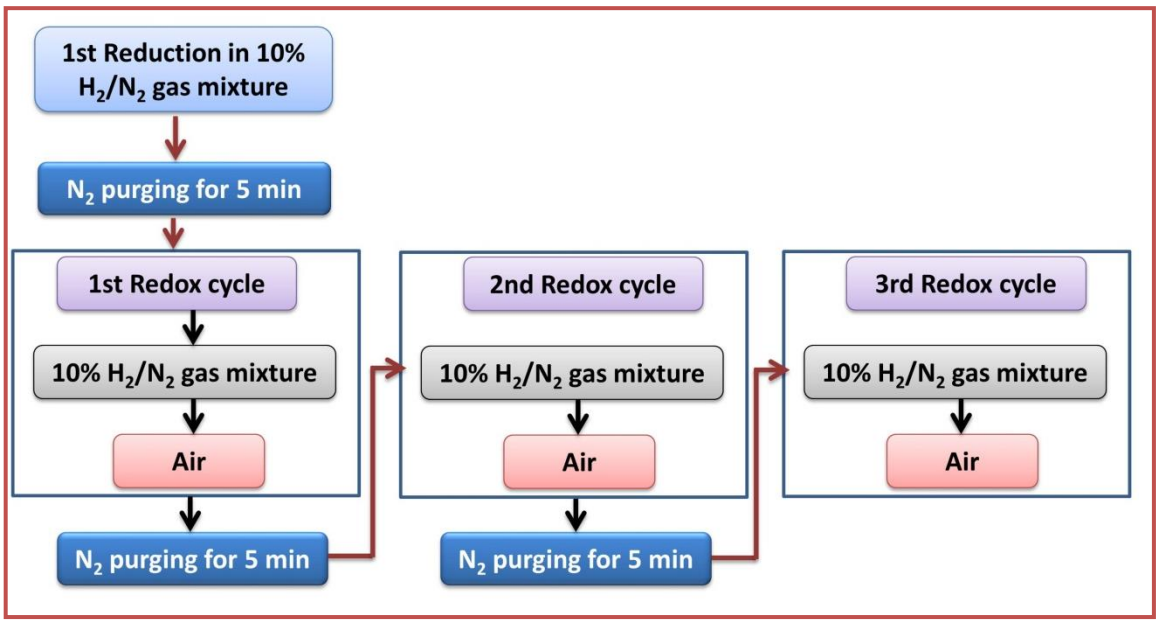

Figure 5.1. Redox cycling flow chart where one redox cycling consists of (a) the re-oxidation step in air (b) N_2 purging for 5 min and (c) the re-reduction step in 10% H_2/N_2 gas mixture.

5.3 Results and Discussion

5.3.1 Phase analysis

Complete reduction of the precursor NiO-BZY anode to the Ni-BZY cermet was performed in 10% H_2/N_2 mixture at 800 °C for 6h. Subsequent re-oxidation of anode was accomplished in ambient air at 800 °C for 4h. The XRD patterns of the as-sintered NiO-BZY anode and those measured after first reduction and re-oxidation steps are shown in Fig. 5.2. All the patterns exhibit the pure perovskite BZY phase, accompanied by NiO for the as-sintered and re-oxidized samples and the Ni phase for the reduced cermet. After re-oxidation the absence of the Ni phase indicates that complete re-oxidation had occurred. Hence, complete Ni redox cycling is accomplished during each redox step, in agreement with the measured oxygen partial pressures during the reduction step, which were shown from oxygen sensor readings to be $10^{-19.5}$-10^{-24} atm in the temperature range 800 ºC-600 ºC. These values are significantly more reducing than the values required for NiO reduction from a thermodynamic perspective, $pO_2 = 10^{-14}$-10^{-19} atm respectively, in the same temperature range [17]. The perovskite BZY phase was shown to be unaffected during redox cycling.

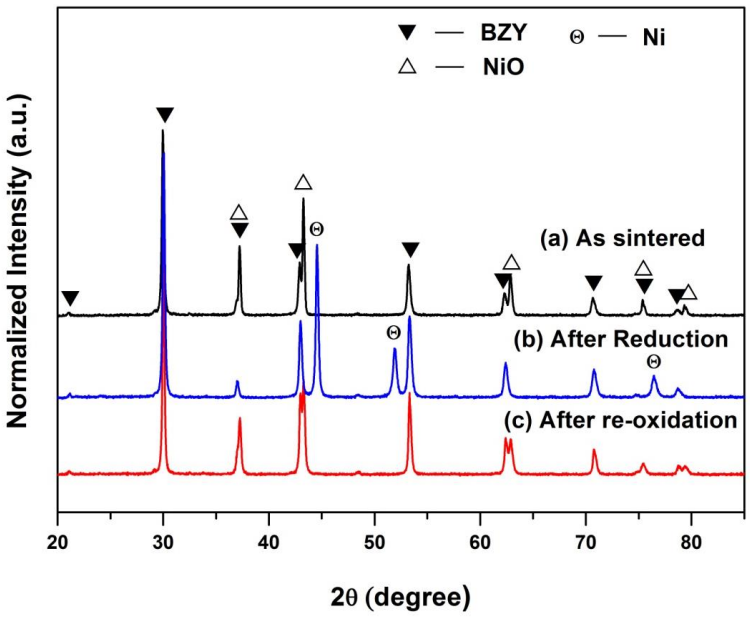

Figure 5.2. XRD patterns for 40 vol% Ni-BZY cermet anode (a) as sintered (b) after reduction for 6 h and (c) after re-oxidation for 4h.

5.3.2 Microstructural analysis

Fig. 5.3(a) shows the SEM micrographs of the Ni-BZY/BCZY71 interface after initial reduction at 800 °C in 10% H_2/N_2 gas mixture before the redox cycling experiment. No delamination or cracks can be observed at the anode/electrolyte interface. However, after 3 redox cycles, serious delamination is shown to have occurred at the anode/electrolyte interface, Fig. 5.3(b). The contact between electrolyte and anode has partially been lost, damaging the area of electrical contact with the electrolyte. In addition, micro cracks in the BZY network and across the anode can be observed after the third redox cycle as shown in surface images of the anode in Fig. 5.3(c) and 5.3(d). These factors can be expected to significantly deteriorate the electrochemical cell performance. During real life PCFC operation, the cermet anode may have to support several re-oxidation and reduction cycles [11]. However, the current investigation shows that, even with only 3 redox cycles, rapid microstructural degradation has occurred. To investigate the origin of this phenomenon, complementary information is provided by *in-situ* measurements made with the environmental scanning electron microscope (ESEM).

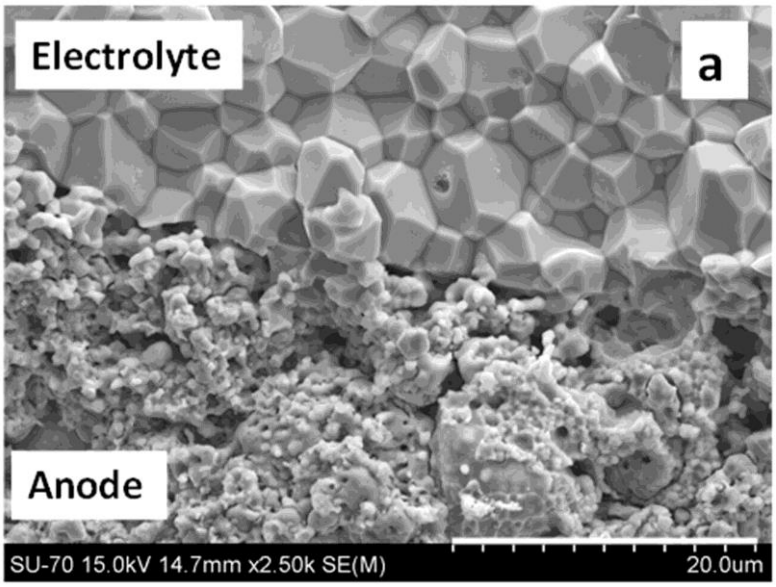

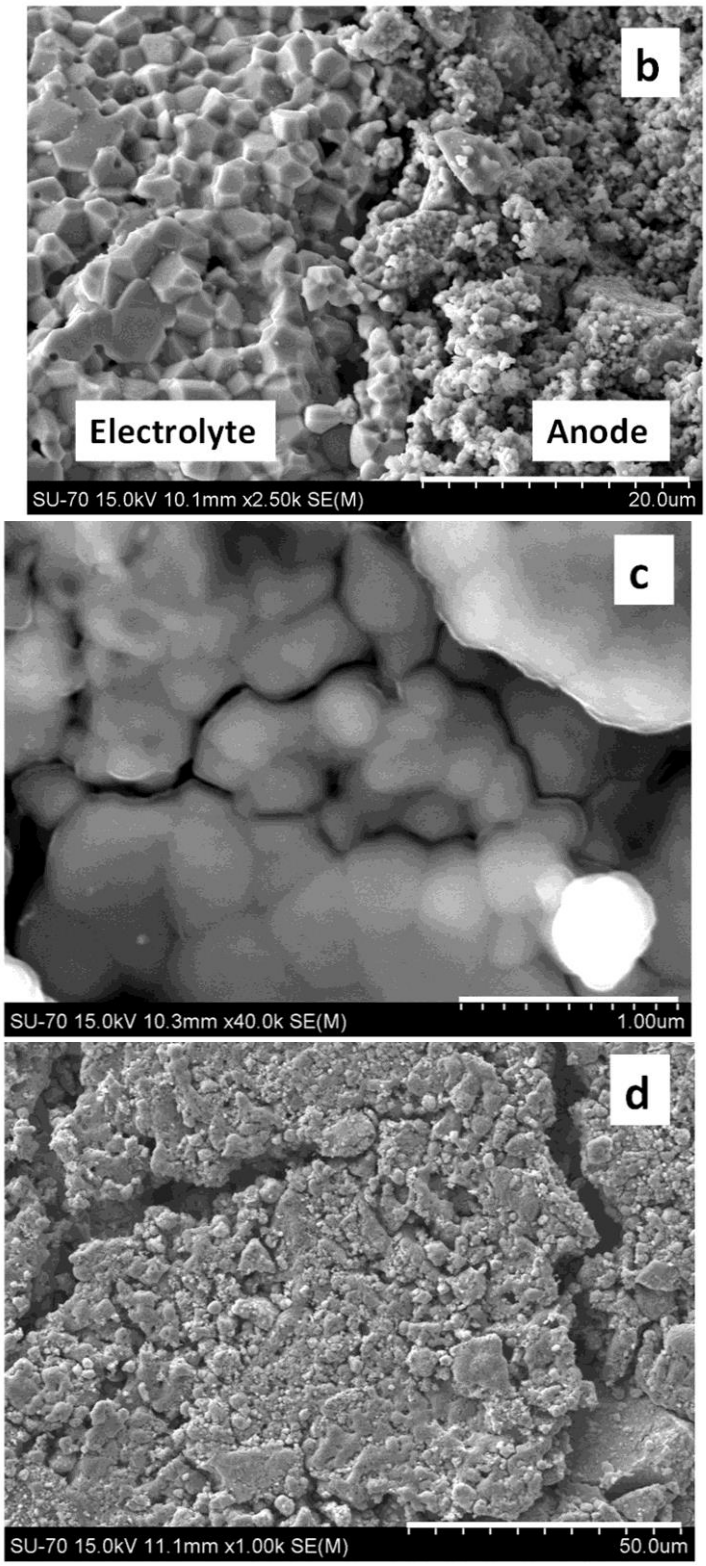

Figure 5.3. SEM micrographs of cross-sectional anode/electrolyte interface (a) before redox cycle, (b) after three redox cycles, (c) and (d) surface of the anode after 3rd redox cycling

5.3.3 ESEM analysis

For the ESEM investigation, the sintered symmetrical cell was fractured in order to access the electrode/electrolyte interface. Typical redox cycling was performed at 600 °C under flowing pure H_2 (3 sccm) or O_2 at a total pressure of 2.0 x 10^{-2} Pa to provide complementary dynamic information on redox cycling. Fig. 5.4(a) shows the anode material in its initial reduced state. An intimate and homogenous distribution between the ceramic BZY and Ni metal phases can also be observed. The darker particles are those of Ni metal, which present a pocketed microstructure containing very fine porosity. Such fine pores in PCFC anodes were previously measured by mercury intrusion porosimetry to be in the nanometer scale with high surface area [18]. The presence of larger pores of ~0.3-0.7 μm has also been noted in reduced PCFC anodes and attributed to channels formed between the Ni grains and the ceramic matrix. These larger pores result from an overall volume contraction of the nickel particle, associated with NiO reduction to Ni metal. Similar channels can be readily seen in Fig. 5.4(a), where the dark Ni particles appear to have pulled away from the lighter coloured BZY matrix. Upon re-oxidation after 10 min., Fig. 5.4(b), the Ni particles are observed to increase in size, losing some of their fine pocketed structure and closing channels that were previously present between the Ni phase and the BZY ceramic backbone. Upon re-oxidation to NiO, Fig. 5.4(c), the NiO particles now, not only completely fill the available voids in the BZY backbone, but also appear to mushroom outwards as their volume extends beyond the available space in the original BZY matrix, Fig. 5.4(c). The maximum volume of the NiO particle is achieved after approximately 2h in these conditions. Such extended growth of Ni particles agrees with that previously noted in oxide-ion conducting Ni-YSZ cermets, where an initial volume change due to NiO reduction (~40%) is significantly exceeded on subsequent re-oxidation (~66%) due to the so called pseudo Kirkendall effect [19]. This phenomenon occurs due to the faster outward diffusion of nickel cations than the inward diffusion of oxide-ions, leading to the creation of internal porosity that produces NiO particles of a larger overall volume. Upon re-reduction, the Ni particles reduce in size once more, pulling away from the BZY backbone and reforming their pocketed appearance, Fig. 5.4(d,e).

The greater volume change noted for the Ni-particles upon re-oxidation than reduction is a phenomenon that has been reported to be undesirable in Ni-YSZ cermets due to expansion of the cermet anode and delamination of the electrolyte/electrode layer and/or potential cracking of the YSZ backbone [19]. Moreover, these effects have been reported to be more prolific in Ni-YSZ anodes of low porosity [16, 19]. In this respect, PCFC anodes have been reported to offer the highest electrochemical performance at the lowest porosities [3, 15]; a factor that is in direct conflict with the aforementioned criterion for redox stability. The PCFC anodes in the current work were formed without the use of additional porogens and correspond to peak electrochemically performing cermets with final porosity levels of ~34% [3, 20]. This value is much lower than that of state of the art oxide-ion conducing SOFC anodes, which typically contain porosity levels ~50% [21]. Nonetheless, the current ESEM analysis of PCFC anodes reveals a similar expansion of the NiO particles upon re-oxidation as documented for oxide-ion conducting Ni-YSZ anodes. Consequently, the low porosity PCFC anodes present undesirable microstructural damage upon redox cycling, with extensive degradation phenomena of electrolyte/electrode delamination and fracture of the BZY matrix, as noted in the postmortem SEM images of redox cycled BZY-Ni anodes in the previous section. This degradation is also shown to be very rapid, occurring after only a few redox cycles. Thus, the salient question is if such microstructural damage will lead to serious impairment of the electrochemical properties of PCFC anodes, or if the aforementioned property of ionic transport in both the ceramic and metallic phases of a PCFC cermet anode (and associated extension of the three phase boundary length), as well as a higher initial interconnectivity can offset this microstructural degradation.

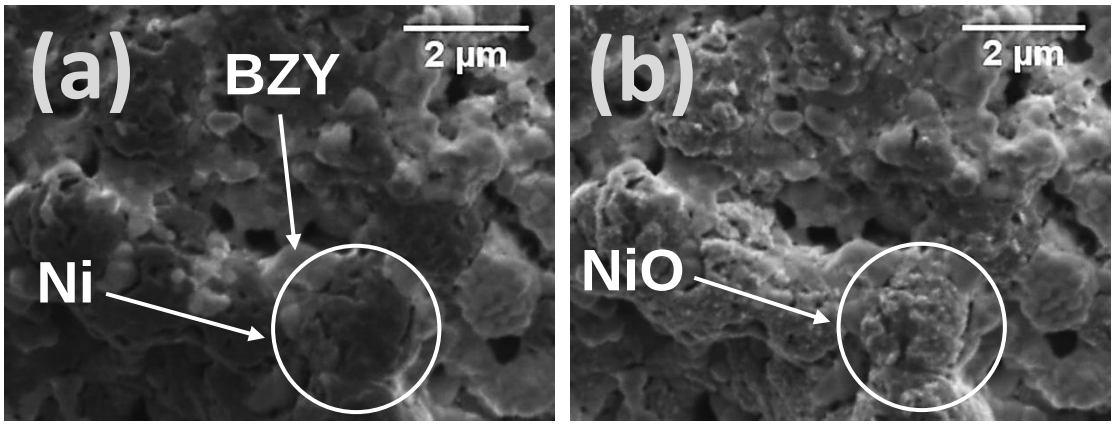

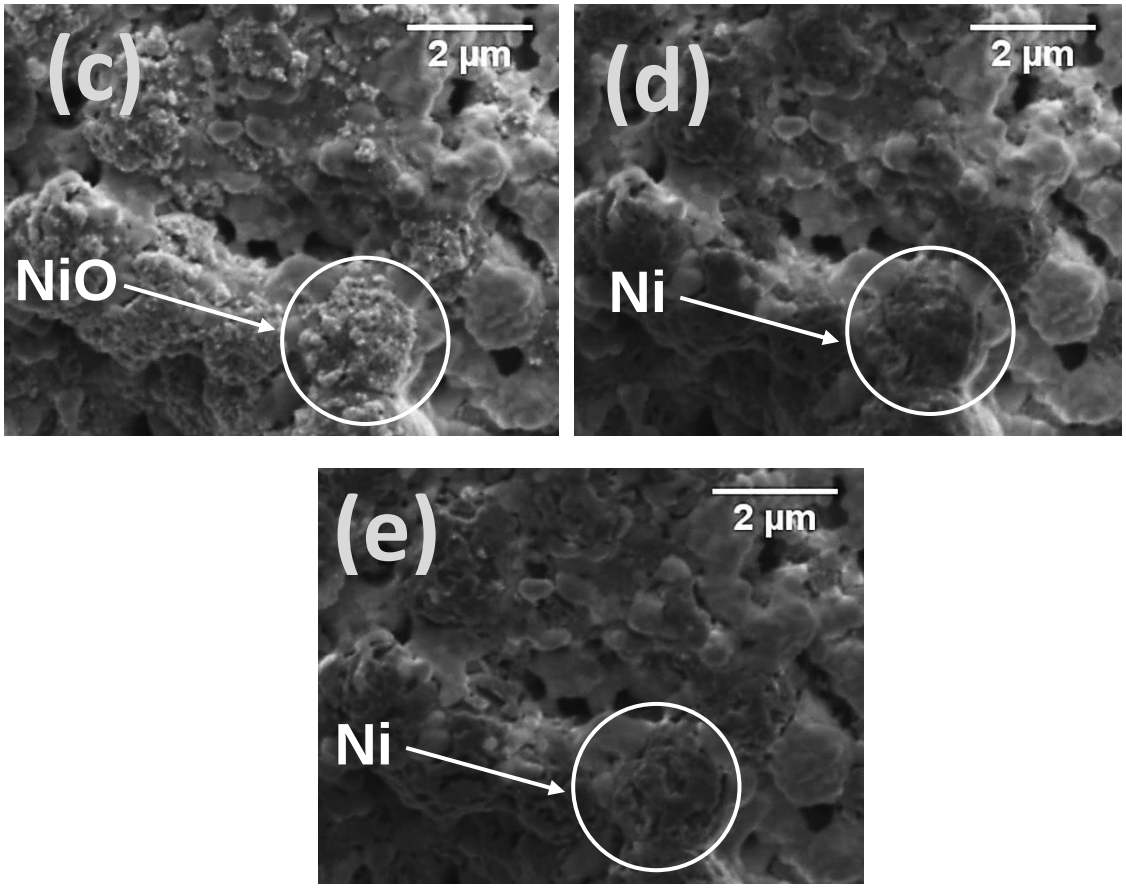

Figure 5.4. ESEM micrographs of Ni-BZY anode (a) first reduced state, (b) re-oxidation after 10 min, (c) re-oxidised anode after 120 mins (Ni volume expansion is clearly visible upon re-oxidation), (d) re-reduced after 10 min and (e) re-reduced anode after 180 mins.

5.3.4 Effect of Redox cycling on polarization resistance of Ni-BZY anode

Analysis of the effect of redox cycling on polarization resistance was carried out by impedance spectroscopy using an anode/electrolyte/anode symmetrical cell. The impedance spectra were recorded before each redox cycle in reducing conditions. All measured impedance spectra from 800 °C-650 °C consist of an offset along the real axis, an inductance effect at high frequency and two depressed semi circles at lower frequencies. An example spectrum is presented at 600 °C, in Fig. 5.5; all measured spectra were similar in form. The two semi circles observable at lower frequencies are clearly separated from each other and represent two distinct electrochemical reactions occurring at the anode. The impedance diagrams were, therefore, analyzed by using an equivalent circuit comprising of an inductance in series with a resistor, R, and two distributed RQ elements, as shown in the

inset of Fig. 5.5. The fitting parameters extracted for each distributed semicircle are the resistance, R, the pseudo-capacitance, Q, and an additional parameter n which can be related to the true capacitance by the equation

$$C = R^{(1-n)/n} Q^{1/n} \qquad (5.1)$$

In this way, the true capacitance values of the distributed responses have been calculated to be in the order of 10^{-5}-10^{-6} Fcm^{-2} for the higher frequency response, associated with resistance R2, and 10^{-3}-10^{-4} Fcm^{-2} for the lower frequency response, associated with resistance R3. The obtained capacitance values correspond well to those previously noted for Ni-BZY electrodes [1, 2].

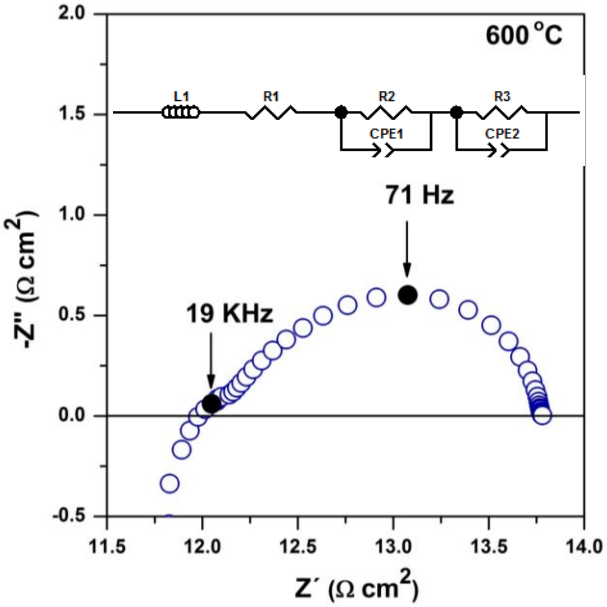

Figure 5.5. The electrochemical impedance spectrum of a symmetrical cell with 40 vol% Ni-BZY electrode, measured in wet 10% H_2/N_2 at 600 °C.

The higher frequency semicircle (R2) and the lower frequency semicircle (R3) were attributed to the polarization resistance of the PCFC anode, Rp = R2 +R3, as outlined in chapter 3 and 4 [2], while the high frequency intercept (R1) was associated with the ohmic resistance of the symmetrical cell.

Upon redox cycling the overall shapes of the impedance spectra remain similar, while each term in the impedance spectra, R1, R2 and R3, are shown to increase in resistance, Fig. 5.6.

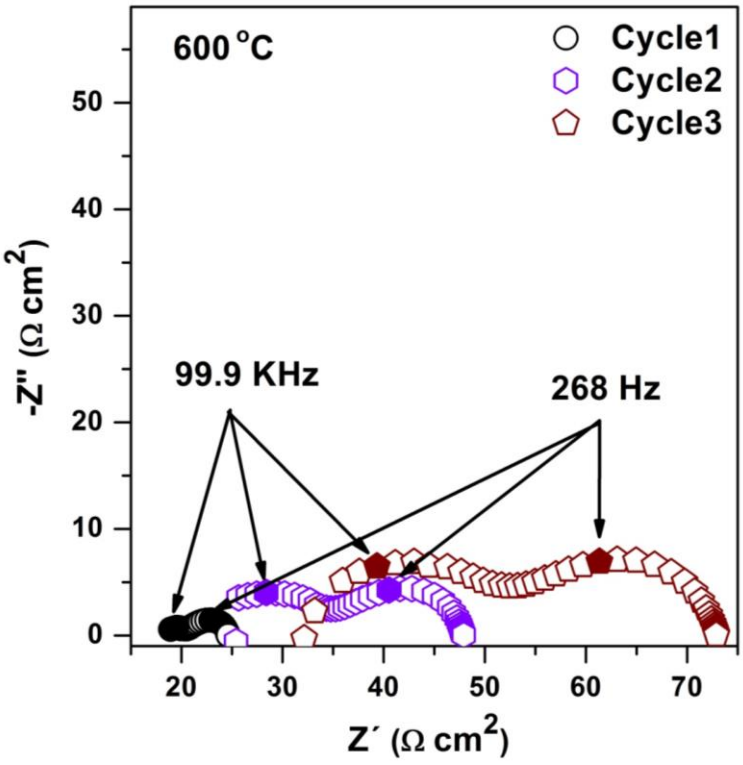

Figure 5.6. The effect of redox cycling on impedance spectra for 40 vol% Ni-BZY cermet anode measured in wet 10% H_2/N_2 at 600 ºC.

Fig. 5.7 shows the total polarization resistance Rp of Ni-BZY cermet as a function of temperature for each redox cycle. The results show that Rp increases dramatically from the first redox cycle to third redox cycle, in agreement with Fig. 5.6. To investigate the detailed electrochemical degradation of Ni-BZY upon redox cycling, total polarization resistance was separated into each contribution, R2 and R3. The high frequency polarization resistance R2 and low frequency polarization resistance R3 were plotted as a function of temperature as shown in Fig. 5.8(a) and 5.8(b). Both polarization resistances R2 and R3 are substantially affected by redox cycling. After the 1st redox cycle R2 and R3 increase and continue to increase with each redox cycle, as one can observe in Fig. 5.8(a) and 5.8(b). The high frequency response, R2, was the most highly affected term, as

compared to R3. This is consistent with previous results reported for Ni-BZY, which showed the R2 term to be predominately a microstructural dependent term related to the three phase boundary length [15] where the presence of microcracks would be expected to have a negative impact. Similarly, a decrease in the three phase boundary length would be expected on loss of connectivity between the BZY matrix and the Ni phase, or due to depleted interconnectivity within the Ni and BZY networks [4, 8]. Fig. 5.8(c) depicts the ohmic resistance (Rohmic) as a function of temperature. After each redox cycle the Rohmic of the symmetrical cell was also significantly increased. From the microscopy study, delamination occurs with redox cycling at the anode/electrolyte interface, (Fig. 5.3(b) and Fig. 5.3(c)). Hence, the increase in ohmic resistance appears to result from the observed delamination at the anode/electrolyte interfaces and the associated increase in contact resistance.

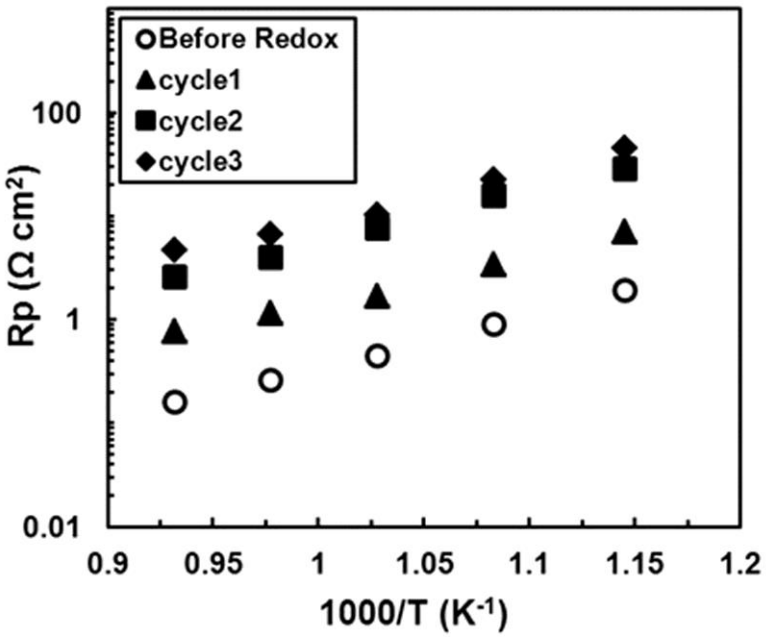

Figure 5.7. The effect of redox cycling on total polarization resistance (Rp) as a function of temperature for 40 vol% Ni-BZY cermet anode measured in wet 10% H_2/N_2.

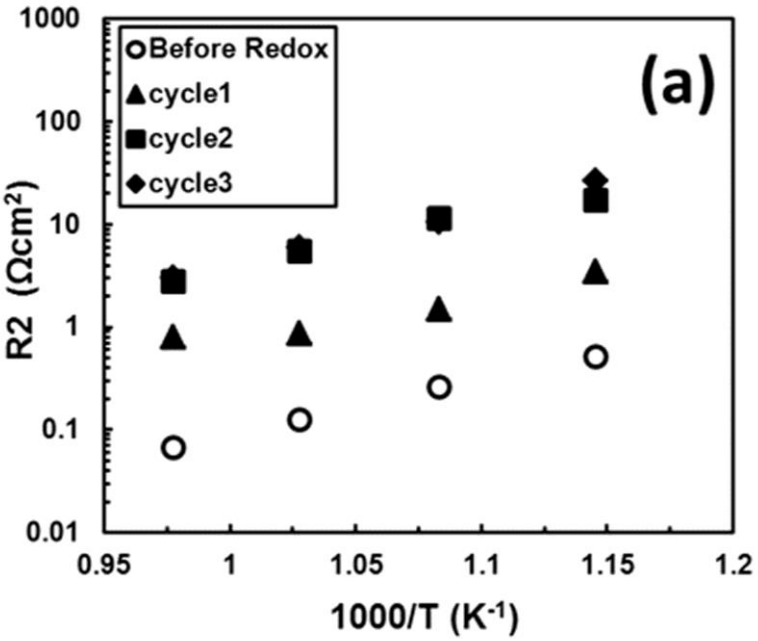
Before Redox
cycle1
cycle2
cycle3
(a)
R2 (Ωcm²)
1000/T (K⁻¹)
1000
100
10
1
0.1
0.01
0.95
1
1.05
1.1
1.15
1.2

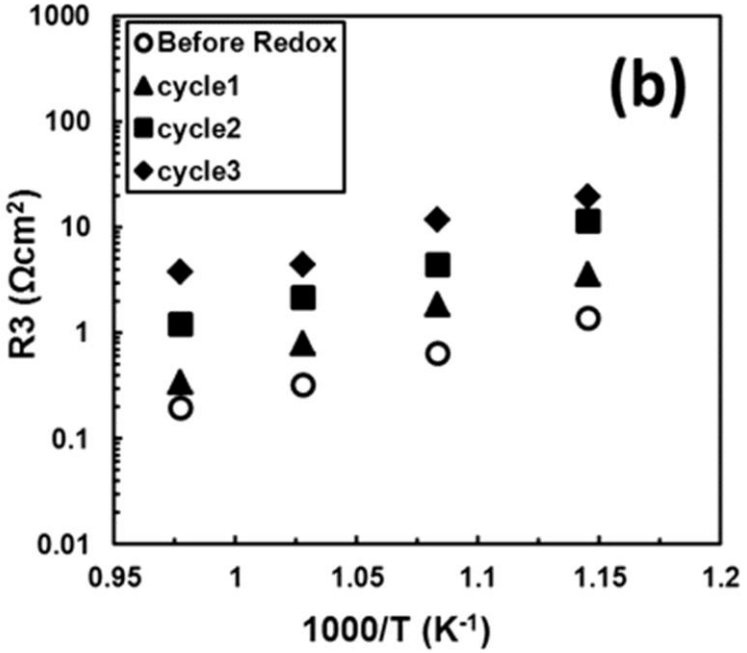
Before Redox
cycle1
cycle2
cycle3
(b)
R3 (Ωcm²)
1000/T (K⁻¹)
1000
100
10
1
0.1
0.01
0.95
1
1.05
1.1
1.15
1.2

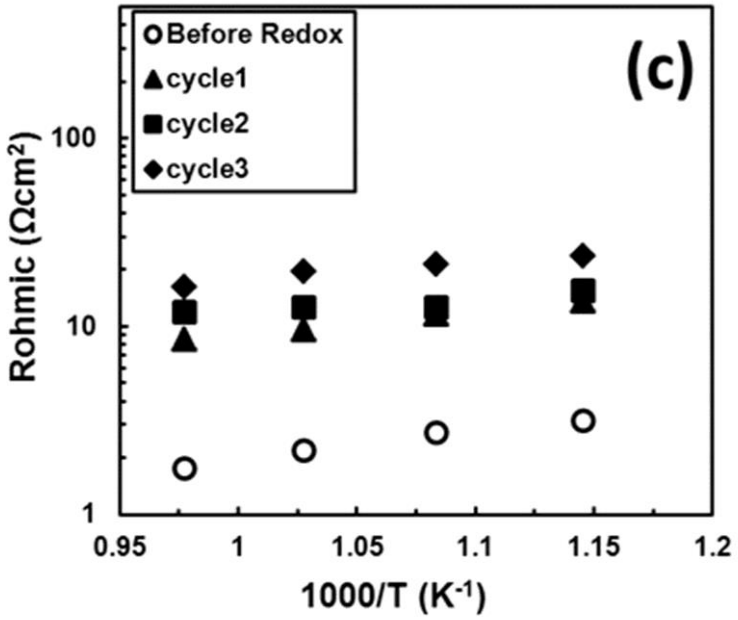

Figure 5.8. The effect of redox cycling on (a) High frequency polarization resistance R2, (b) low frequency polarization resistance R3 and (c) ohmic resistance Rohmic as a function of temperature for 40 vol% Ni-BZY cermet anode measured in wet 10% H_2/N_2 and air.

To put these results into context, Fig. 5.9 plot the percentage change in the values of the polarization resistances R2 and R3 and the ohmic resistance Rohmic as a function of number of redox cycles, given by the equation

$$\Delta R\% = 100.\frac{R_i^{//} - R_i^{/}}{R_i^{/}} \qquad (5.2)$$

where $R_i^{/}$ and $R_i^{//}$ are the resistances before and after redox cycling, respectively, of any resistance component i. The most severe degradation issues are manifested by the polarization resistances R2 and R3. Both these terms demonstrate performance impairments that have a magnitude of up to 100% that of the initial resistance after a few redox cycles. Large degradation issues are also shown by the ohmic resistance, where diminished interfacial contacts produce a performance depletion that is approximately 80%

of its original resistance upon redox cycling. The most perturbing feature of Fig. 5.9 is the extremely rapid depletion of each of these electrochemical terms. A single redox event is shown to be able to impair the polarization and interfacial resistances of peak performing PCFC cermet anodes, producing increases that correspond to at least 80% of their original values. The severity of this degradation highlights the conundrum facing state of the art PCFC anodes; the low porosity desirable for high electrochemical performance is likely to be contrary to that required for high redox stability. It is, therefore, imperative that innovative methods to circumvent this impasse are proposed by the protonics community.

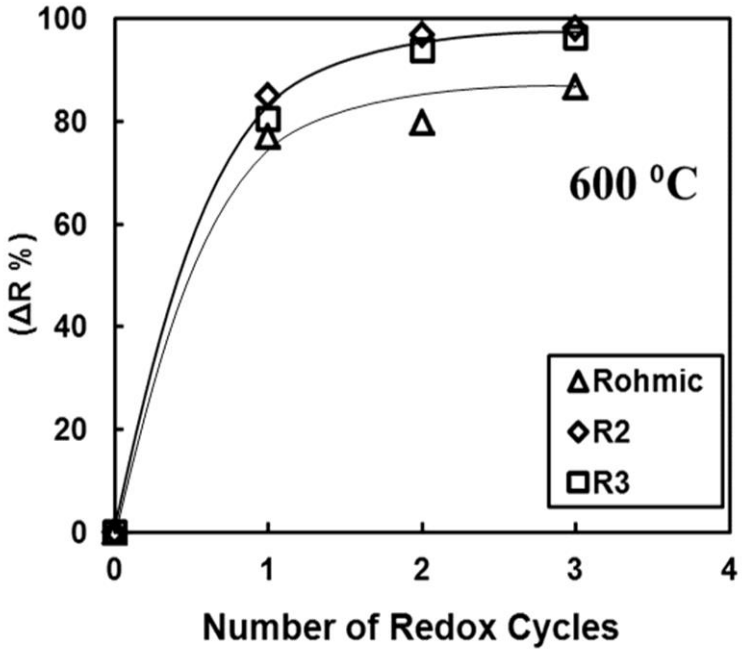

Figure 5.9. The percentage change in the high frequency polarization resistance, R2, the low frequency polarization resistance, R3, and the ohmic resistance, Rohmic, as a function of redox cycling for 40 vol% Ni-BZY cermet anode measured at 600 ºC.

5.4 Conclusions

The redox cycling behavior of Ni-BZY anodes for PCFCs were investigated by using electrochemical impedance measurements under 10% H_2/N_2 gas mixture and air. The impedance spectra show that both the high frequency semi-circle, R2, and the low

frequency semi-circle, R3, were increased by re-oxidation and reduction cycles. The ohmic resistance (Rohmic) was also increased due to delamination at anode/electrolyte interface, as confirmed by SEM analysis after redox cycling. The formation of microcracks in the cermet BZY oxide network and across the symmetrical cell was also observed upon redox cycling. ESEM analysis highlights that these microcracks and delamination form due to the volume expansion of the Ni cermet phase upon re-oxidation. As such, a rapid depletion in performance is observed in peak performing PCFC anodes of low porosity upon redox cycling, despite their high initial connectivity and the potential for proton migration in both cermet phases. This result can be considered to be highly detrimental to practical exploitation of PCFCs. Thus, the study of methods to minimise this factor can be considered to be imperative before PCFCs may become commercially feasible.

.

5.5 References

[1] Bi L, Fabbri E, Sun Z, Traversa E. $BaZr_{0.8}Y_{0.2}O_{3-\delta}$-NiO Composite Anodic Powders for Proton-Conducting SOFCs Prepared by a Combustion Method. J Electrochem Soc. 2011;158:B797.

[2] Narendar N, Mather GC, Dias PAN, Fagg DP. The importance of phase purity in Ni–$BaZr_{0.85}Y_{0.15}O_{3-\delta}$ cermet anodes – novel nitrate-free combustion route and electrochemical study. RSC Adv. 2013;3:859-69.

[3] Rainwater BH, Liu M, Liu M. A more efficient anode microstructure for SOFCs based on proton conductors. Int J Hydrogen Energy. 2012;37:18342-8.

[4] Ettler M, Timmermann H, Malzbender J, Weber A, Menzler NH. Durability of Ni anodes during reoxidation cycles. J Power Sources. 2010;195:5452-67.

[5] Coors WG. Protonic ceramic steam-permeable membranes. Solid State Ionics. 2007;178:481-5.

[6] Laurencin J, Delette G, Sicardy O, Rosini S, Lefebvre-Joud F. Impact of 'redox' cycles on performances of solid oxide fuel cells: Case of the electrolyte supported cells. J Power Sources. 2010;195:2747-53.

[7] Zhang Y, Liu B, Tu B, Dong Y, Cheng M. Understanding of redox behavior of Ni–YSZ cermets. Solid State Ionics. 2009;180:1580-6.

[8] Sarantaridis D, Atkinson A. Redox Cycling of Ni-Based Solid Oxide Fuel Cell Anodes: A Review. Fuel Cells. 2007;7:246-58.

[9] Klemensø T, Chung C, Larsen PH, Mogensen M. The Mechanism Behind Redox Instability of Anodes in High-Temperature SOFCs. J Electrochem Soc. 2005;152:A2186.

[10] Klemensø T, Mogensen M. Ni–YSZ Solid Oxide Fuel Cell Anode Behavior Upon Redox Cycling Based on Electrical Characterization. J Am Ceram Soc. 2007;90:3582-8.

[11] Heo Y-H, Lee J-W, Lee S-B, Lim T-H, Park S-J, Song R-H, et al. Redox-induced performance degradation of anode-supported tubular solid oxide fuel cells. Int J Hydrogen Energy. 2011;36:797-804.

[12] Laurencin J, Delette G, Morel B, Lefebvre-Joud F, Dupeux M. Solid Oxide Fuel Cells damage mechanisms due to Ni-YSZ re-oxidation: Case of the Anode Supported Cell. J Power Sources. 2009;192:344-52.

[13] Baek S-W, Bae J. Anodic behavior of $8Y_2O_3$–ZrO_2/NiO cermet using an anode-supported electrode. Int J Hydrogen Energy. 2011;36:689-705.

[14] Coors WG. Protonic ceramic fuel cells for high-efficiency operation with methane. J Power Sources. 2003;118:150-6.

[15] Narendar N, Devaraj R, Brandão AD, Yaremchenko A, Fagg DP. The impact of porosity, pH_2 and pH_2O on the polarisation resistance of Ni-$BaZr_{0.85}Y_{0.15}O_{3-\delta}$ cermet anodes for Protonic Ceramic Fuel Cells (PCFCs). Int J Hydrogen Energy. 2014;39:21231–41.

[16] Pihlatie M, Ramos T, Kaiser A. Testing and improving the redox stability of Ni-based solid oxide fuel cells. J Power Sources. 2009;193:322-30.

[17] Atkins P, de Paula J. Physical Chemistry: Thermodynamics And Kinetics. 8th ed. New York: W.H. Freeman; 2006.

[18] Coors WG, Manerbino A. Characterization of composite cermet with 68wt.% NiO and $BaCe_{0.2}Zr_{0.6}Y_{0.2}O_{3-\delta}$. J Membr Sci. 2011;376:50-5.

[19] Faes A, Hessler-Wyser A, Zryd A, Van herle J. A Review of RedOx Cycling of Solid Oxide Fuel Cells Anode. Membranes. 2012;2:585-664.

[20] Essoumhi A, Taillades G, Taillades-jacquin M, Jones D, Roziere J. Synthesis and characterization of Ni-cermet/proton conducting thin film electrolyte symmetrical assemblies. Solid State Ionics. 2008;179:2155-9.

[21] Zhao F, Virkar AV. Dependence of polarization in anode-supported solid oxide fuel cells on various cell parameters. J Power Sources. 2005;141:79-95.

Chapter 6

Electrochemical behaviour of Ni-BZO and Ni-BZY cermet anodes - A comparative study [‡]

Abstract

The matrix phase of protonic ceramic fuel cell (PCFC) cermet anodes potentially plays a vital role in hydrogen oxidation kinetics. The present work aims to investigate such involvement by selecting ceramic-oxide matrices with widely dissimilar levels of proton conduction. The materials chosen were that of the proton-conducting phase $BaZr_{0.85}Y_{0.15}O_{3-\delta}$ and the nominal composition $BaZrO_3$ of negligible proton conduction. Cermet anodes Ni-$BaZrO_3$ and Ni-$BaZr_{0.85}Y_{0.15}O_{3-\delta}$ were synthesized by the acetate-H_2O_2 combustion method for Ni contents of 40vol%. The microstructure and electrochemical performance of the cermet anodes were investigated by scanning electron microscopy (SEM) and electrochemical impedance measurements (EIS) respectively. The polarisation behaviour of the two nickel cermet anodes was studied as a function of temperature, hydrogen partial pressure (pH_2) and water vapor partial pressure (pH_2O). The results confirm that polarisation resistance is highly sensitive to the composition of the ceramic phase of the cermet anode and that the higher frequency electrode response exhibits strong links to levels of proton transport in the ceramic-oxide matrix.

[‡] This Chapter has been published as Narendar N, Devaraj R, Antunes I, Perez J, Fagg DP. Electrochemical behaviour of Ni-BZO and Ni-BZY cermet anodes for Protonic ceramic fuel cells (PCFCs) - A comparative study. Electrochim Acta. DOI: 10.1016/j.electacta.2014.12.094.

6.1 Introduction

To date, research in PCFCs has mainly focused on categorisation of the physical and electrical properties of proton conducting oxides as potential electrolytes, while the study of suitable anodes for these devices has received lesser attention [1]. The available literature primarily suggests the use of Ni-cermets as potential anode materials, in an analogous approach to that utilized in SOFCs [2, 3]. Thus, the adequacy of such proton conducting cermet anodes may be dependent on the transport properties of the corresponding ceramic-oxide, matrix phase and its stability. Several potential matrixes can be suggested from proton conducting, perovskite materials such as doped alkaline earth cerates ($ACe_{1-x}R_xO_{3-\delta}$), alkaline earth zirconates ($AZr_{1-x}R_xO_{3-\delta}$) (A= Ca, Sr, Ba, R = Y, Yb, In, Pr ,Gd, Dy) and their solid solutions ($A(Zr_{(1-y)}Ce_y)_{1-x}R_xO_{3-\delta}$) [2-7]. The literature shows that yttrium doped barium cerates ($BaCe_{1-x}Y_xO_{3-\delta}$-BCY) and zirconates ($BaZr_{1-x}Y_xO_{3-\delta}$-BZY) may be the most attractive, due to offering high levels of proton conductivity in the intermediate temperature range 500-700 °C [2, 8]. On the other hand, the cerate materials have been shown to be unstable in H_2O and CO_2 containing atmospheres, rapidly decomposing to the respective alkaline earth hydroxides and carbonates and preventing their application in devices that operate in hydrocarbon atmospheres [7]. In contrast, the zirconate analogues offer superior levels of stability in these atmospheres and, thus, are considered to provide the greater relevance for such applications [2, 9].

Due to their physical similarity, it may be tempting to extrapolate potential guidelines for PCFC cermet anodes from that of more established SOFC anode research. Such attempts would suggest that a PCFC cermet anode should ideally consist of a homogeneous distribution of metallic and ionic conducting ceramic-oxide phases, a high ionic conductivity in the ceramic matrix, suitable percolation of each phase, and sufficient porosity to ensure the absence of gas phase limitations [1, 2, 10, 11]. However, to date, insufficient literature studies exist on PCFC anode materials to be able to corroborate such comparison. The following PCFC cermet anodes have been formed with perovskite, matrix compositions, up to the present time, Ni-$Ca(Zr,Y)O_{3-\delta}$ and Ni-$Sr(Zr,Y)O_{3-\delta}$ [12], Ni-$Ba(Zr,Y)O_{3-\delta}$ [13, 14], Ni-$Ba(Ce,Y)O_{3-\delta}$ [15, 16], Ni-$SrCe_{0.9}Yb_{0.1}O_{3-\delta}$ [17], Ni-$Ba(Ce,Zr,Y,Yb)O_{3-\delta}$ [18] and Ni-$Ba(Ce,Zr,Y)O_{3-\delta}$ [19]. However, direct comparison between these works is often complicated due to the use of different volume fractions of the Ni-phase, different preparation methods (leading to different anode morphologies),

different substrate materials, as well as differing measurement conditions and techniques. By studying Ni-$CaZr_{0.95}Y_{0.05}O_{2.975}$ (Ni-CZY) and Ni-$SrZr_{0.95}Y_{0.05}O_{2.975}$ (Ni-SZY) cermet anodes for PCFCs prepared by similar methods, Mather et al. suggested that the overall polarization resistance was sensitive to the level of proton conductivity in the ceramic-oxide phase [12]. The Ni-CZY anode was shown to produce a higher polarisation resistance than Ni-SZY cermet anode and this was suggested to be related to the higher proton conductivity of $SrZr_{0.95}Y_{0.05}O_{2.975}$ with respect to $CaZr_{0.95}Y_{0.05}O_{2.975}$ [12]. Detailed studies of the importance of the phase purity of the proton conducting matrix, the level of cermet porosity, redox behaviour and the dependence of electrode kinetics on water vapour (pH_2O) and hydrogen partial pressures (pH_2) have been described in the previous chapters, measured on 40vol% Ni-BZY anodes deposited on $BaCe_{0.7}Zr_{0.1}Y_{0.2}O_{3-\delta}$ electrolytes, prepared and tested under identical conditions [14, 20, 21].

To extend understanding of the dependence of PCFC anode performance on the transport properties of the matrix phase, this chapter describes a comparative study of two Ni-cermet anodes, comprising the ceramic-oxide phases $BaZrO_3$ (BZO) and $BaZr_{0.85}Y_{0.15}O_{3-\delta}$ (BZY), prepared and tested under identical conditions. These ceramic-oxides phases are chosen to offer widely dissimilar levels of proton conductivity. High proton conductivity would be expected in the BZY anode matrix [8, 22], while the nominal composition $BaZrO_3$ should offer negligible proton conduction due to the absence of oxygen vacancies that can be hydrated. The electrochemical behaviour of the cermet anodes have been studied as a function of temperature, water vapour (pH_2O) and hydrogen partial pressures (pH_2) in reducing atmospheres and compared. The results demonstrate that the total polarisation resistance Rp of Ni-BZO is significantly higher than that of Ni-BZY in wet 10% H_2/N_2 and strong links are observed between the magnitude of the high frequency response and the level of proton transport in the matrix phase of the cermet anode. The experimental details of the syntheses can be found in Chapter 2 under section 2.1 and 2.3.

6.2 Results and Discussion

6.2.1 Phase purity and microstructure

Fig. 6.1 represents the XRD patterns of sintered NiO-BZY and NiO-BZO anode powders. All the XRD peaks can be attributed to the pure perovskite barium zirconate (PDF 01-074-1299) or NiO (PDF 01-075-0197) phases, with no phase impurities observed.

Note, the common impurity phase BaY_2NiO_5 is shown to be absent in both barium zirconate-based cermet anodes prepared in this study, an observation that is consistent with previous chapter studies that highlighted high phase purity in Ni-BZY anodes prepared by the nickel acetate-H_2O_2 combustion method [14, 20].

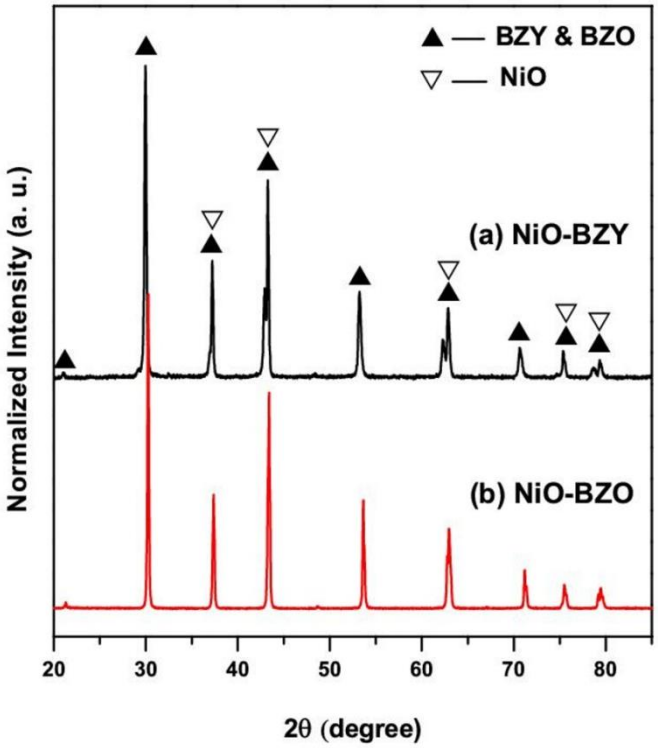

Figure 6.1. XRD patterns of (40 vol% Ni) (a) NiO-BZY and (b) NiO-BZO anodes.

Fig. 6.2(a) & (b) illustrates the microstructure of the formed cermet anodes (40 vol% Ni) Ni-BZO and Ni-BZY after reduction at 700 °C in 10% H_2/N_2 gas mixture for 10h supported by SEM-EDS elemental analysis. Both anode compositions demonstrate interconnecting pathways between the Ni and ceramic-oxide phases, suggesting potential percolation pathways. The ceramic BZY and BZO cermet phases are shown to form these networks by interfusion of particles with typical sizes in the range of 0.51-0.83 μm. These particle sizes are greater than those predicted on sintering pure BZO and BZY phases at this temperature, where particle sizes of ~100 nm have been reported for both compositions from identical mechanosynthesised powders [23]. The larger particle sizes of the BZY and BZO phases in the current cermet materials can be related to the presence of Ni, an element that has, previously, been suggested as a sintering aid for barium zirconate-

based materials [24]. The metallic nickel phase of the cermet demonstrates a pocketed appearance in both anodes, due to the volume decrease on reduction of NiO to Ni metal [14, 19]. This volume reduction also induces narrow channel gaps to appear between the metallic and ceramic phase, a factor that has been suggested to be beneficial to aid gas phase diffusion [19]. The resultant open porosity of the reduced Ni-BZO and Ni-BZY anodes is shown to be similar ~38% and 34%, respectively, measured by Archimedes method using ethanol as solvent. The microstructures of the formed cermets mirror those previously reported for comparable PCFC cermet anodes by Coors [19], Rainwater [18] and Narendar [14]. Recent reports have illustrated that this level of porosity is adequate to achieve good electrochemical performance of PCFC cermet anodes, under typical operating conditions, with no requirement to use an external porogen [18-20]. Note this is contrary to that required for oxide-ion conducting SOFCs, where porosity levels approaching 50% are needed that necessitate the use of external pore formers [25]. The size of the nickel metal particles is in the range 1.31 μm to 1.42 μm for both anode compositions, as expected due to the same combustion preparation process adopted for Ni-distribution in both cases.

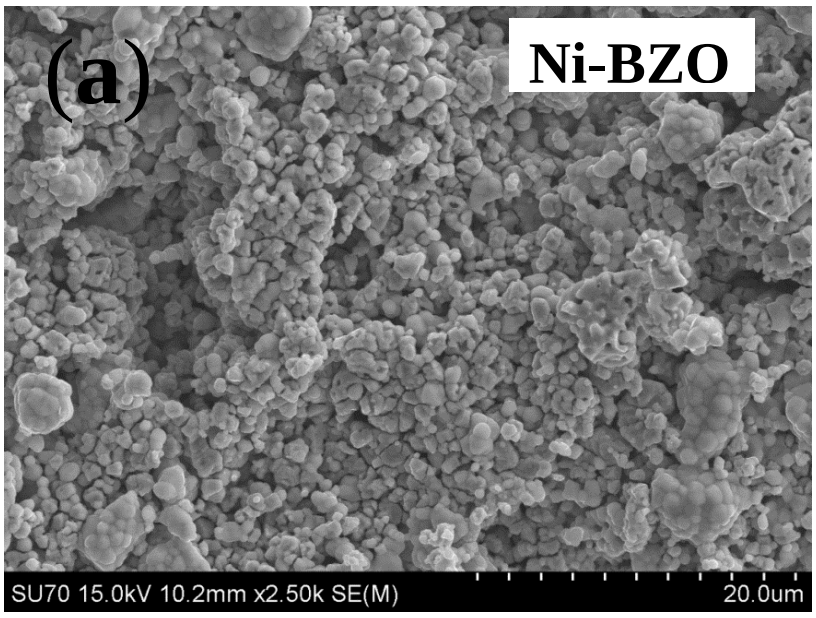

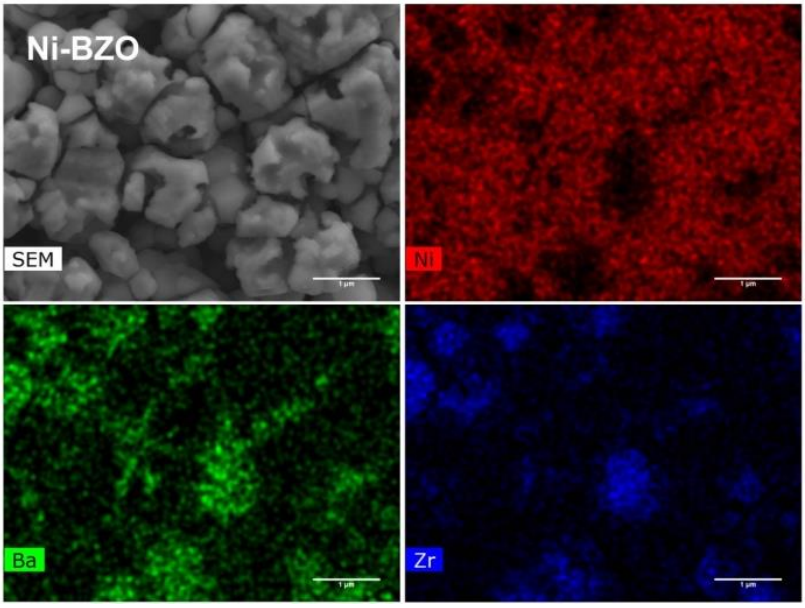
Ni-BZO
SEM
Ni
Ba
Zr


(b)
Ni-BZY
SU70 15.0kV 12.3mm x2.50k SE(M)
20.0um

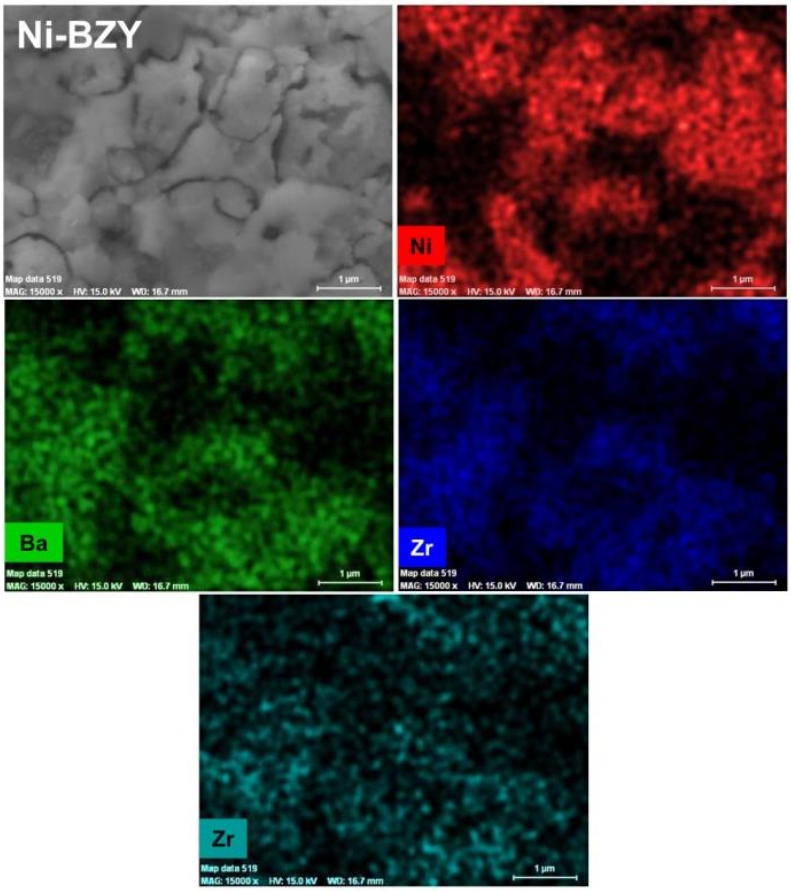

Figure 6.2. SEM micrographs and EDS chemical analyses of 40 vol% Ni-cermet anodes (a) Ni-BZO, (b) Ni-BZY after complete reduction at 700 ºC in dry 10%H_2/N_2 gas mixtures for 10h.

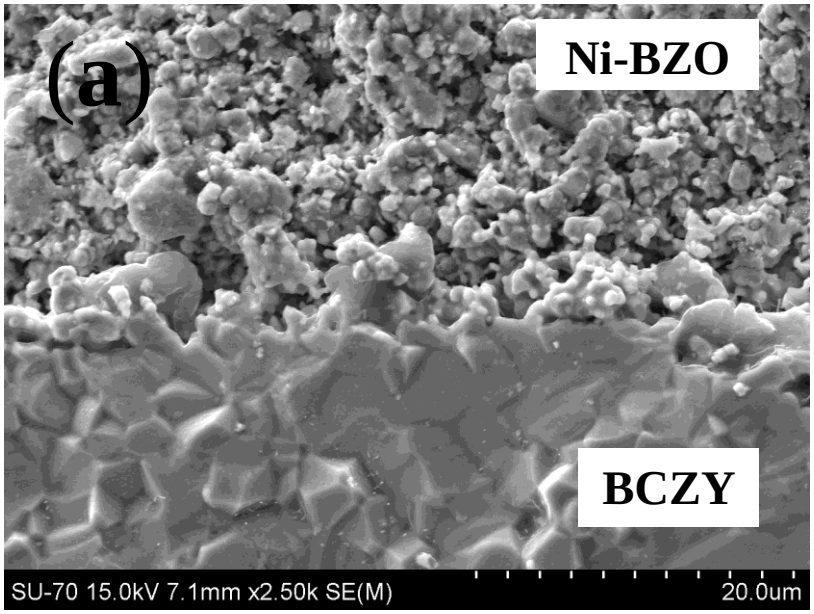

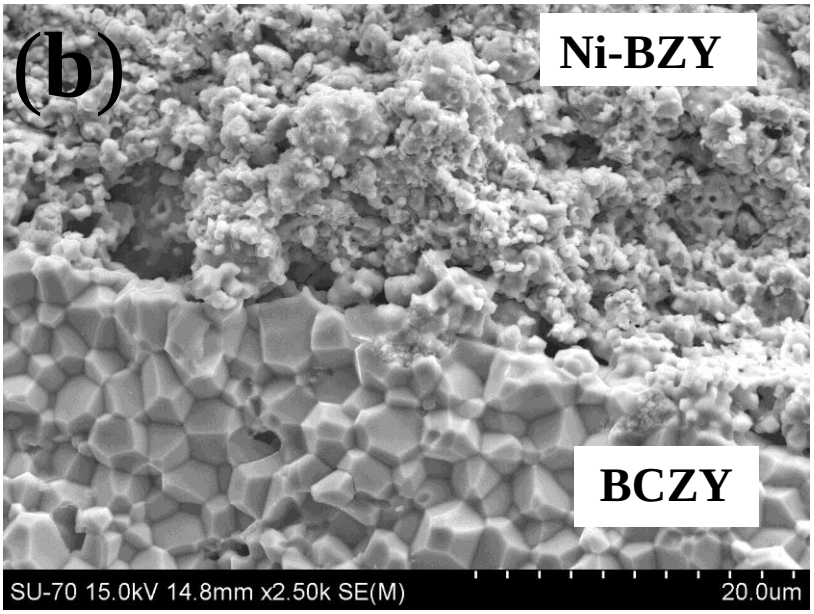

Figure 6.3. SEM micrographs of the electrode/electrolyte interface of reduced a) Ni-BZO/BCZY and (b) Ni-BZY/BCZY assemblies.

Fig. 6.3(a) & (b) show SEM micrographs of the cross sectional view at the interface of anode/electrolyte assemblies for both symmetrical cells Ni-BZO/BCZY and Ni-BZY/BCZY respectively. In both cases good adherence is achieved between the anodes and the electrolyte with no observable delamination at the anode and electrolyte interface. The formed cermet anode thicknesses are ~110 μm for both symmetrical cells.

6.2.2. Electrochemical study of symmetrical cell assemblies

In order to compare the electrochemical behavior of Ni-BZO and Ni-BZY anodes, A.C. impedance spectroscopy was performed on anode/electrolyte/anode symmetrical cell assemblies. The symmetrical cell assemblies were reduced before the start of measurement at 700 °C in dry 10% H_2/N_2 gas mixture for 10h. The electrochemical impedance spectra were recorded as a function of temperature in wet 10% H_2/N_2 gas mixture and also at the fixed temperature of 600 ºC as a function of varying pH_2O and pH_2. Fig. 6.4 demonstrates the progression of the electrochemical impedance spectra of Ni-BZO/BCZY/Ni-BZO assemblies measured in wet 10% H_2/N_2, as a function of temperature. At 150 ºC three responses were observed which appear at high, intermediate and low frequency ranges. These responses can be attributed to the electrolyte bulk, electrolyte grain-boundary and an electrode response, respectively, by consideration of their characteristic capacitances [26]. On increasing the temperature to 300 ºC, the time constant of the electrolyte bulk response

shifts beyond the available frequency window of measurement, leaving only the grain-boundary response and an electrode response observable. At 400 ºC an additional electrode response is revealed at low frequency. With further increases in temperature, the impedance spectra gradually lose information associated with the electrolyte grain boundary and become dominated by the electrode responses. Correspondingly, the impedance spectrum at 600 ºC reveals an offset along the real Z´ axis corresponding to the electrolyte resistance of the symmetrical cells and two main electrode responses that are accompanied by an inductive effect at higher frequency. The presence of two main electrode responses is consistent with previous reports on Ni-BZY cermet anodes [13, 14]. A similar temperature progression of the impedance spectra for the Ni-BZY sample is also observed [13, 14]. For the Ni-BZO cermet anodes at the lowest frequencies, a very small third electrode response can also be observed (notable in the 600 ºC measurement shown in Fig. 6.4). This response becomes increasingly significant with decreasing pH_2 and, thus, will be discussed in the later section where the pH_2 dependence of polarisation resistance is characterised.

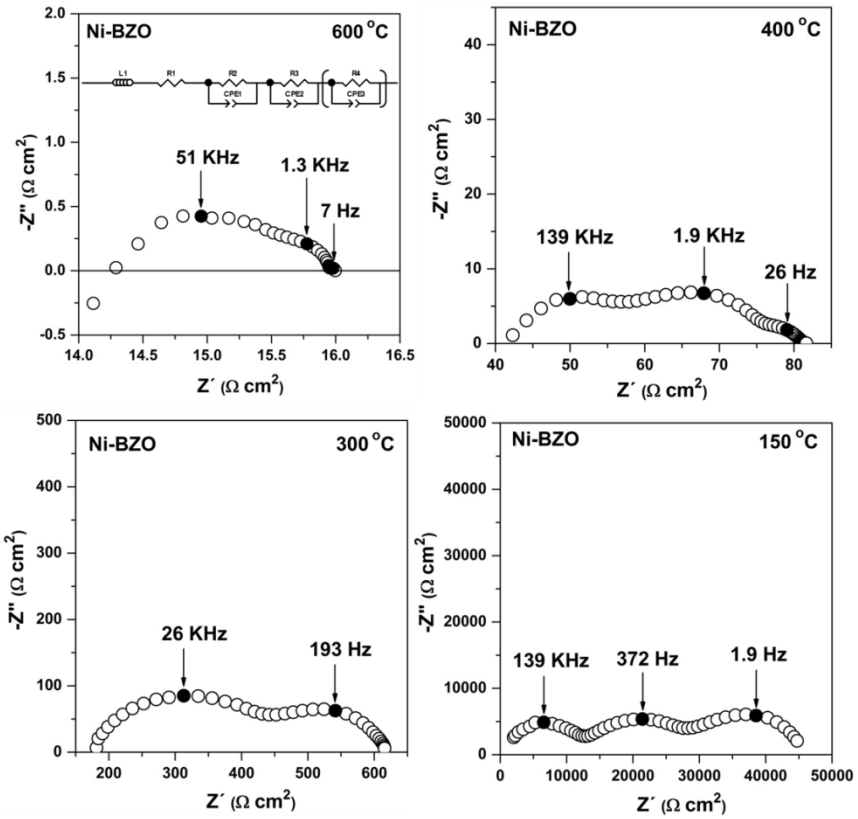

Figure 6.4. The impedance spectra of (40 vol% Ni) Ni-BZO cermet anode, recorded at 600 °C in wet 10% H_2/N_2 gas mixture.

Thus, the equivalent circuit fitted to the data consisted of an inductance (L) in series with a resistor (R), and two or three distributed RQ elements to accommodate the observable semicircular responses in impedance spectra, inset Figure 6.4. The true capacitance values were calculated using the fitting parameters, resistance (R), the pseudo-capacitance (Q), and a parameter n, which can be related to the true capacitance by the following equation.

$$C = R^{(1-n)/n} Q^{1/n} \qquad (6.1)$$

The true capacitance values corresponding to the distributed responses of Ni-BZO cermet anode were calculated to be in the order of 10^{-6}-10^{-7} Fcm^{-2} for the higher frequency response (R2), 10^{-4} Fcm^{-2} for the middle frequency response (R3) and 10^{-1}-10^{-2} Fcm^{-2} for the lowest frequency response (R4). Slightly larger capacitances were noted for the R2 term for the Ni-BZY sample, in the range 10^{-5}-10^{-6} Fcm^{-2}, while the capacitance values for the R3 term were similar [14].

The total polarisation resistance (Rp = R2 + R3) for Ni-BZO and Ni-BZY was measured as a function of temperature in wet 10% H_2/N_2 gas mixture and is shown in Fig. 6.5. The total polarisation resistance of Ni-BZO is observed to be higher than the Ni-BZY cermet anode in the higher temperature range, but becomes comparable at the lowest temperatures. The temperature dependence of total polarisation resistance shows curvature for both samples with a lower activation energy shown in the lower temperature range, Table 6.1.

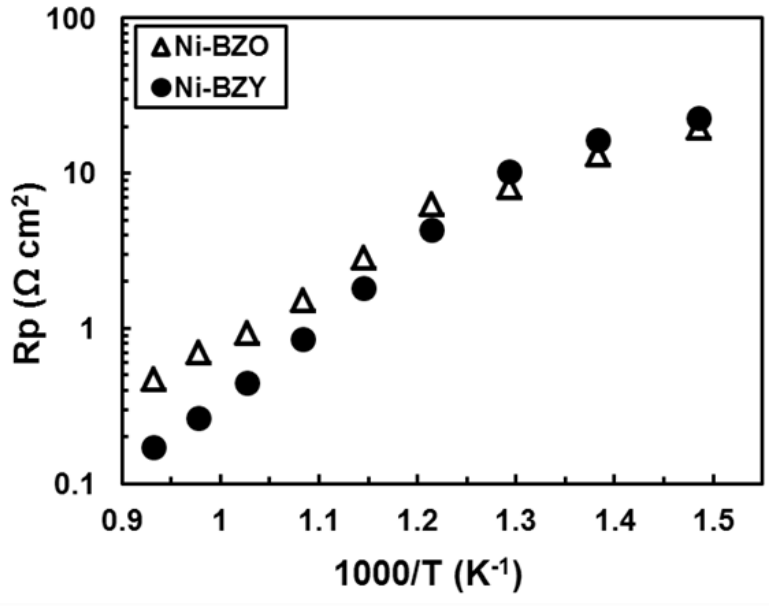

Figure 6.5. Total polarisation resistance (Rp) for (40 vol% Ni) Ni-BZO and Ni-BZY cermet anodes as a function of temperature in wet 10% H_2/N_2 gas mixture.

Table 6.1. Activation energy of two cermet anodes in reducing atmospheres

Anode	**Activation Energy, E_a (eV)**	
	(800-500 °C)	**(500-400 °C)**
Ni-BZO	0.72	0.40
Ni-BZY	0.99	0.35

6.2.3 Effect of water-vapour partial pressure (pH_2O)

Fig. 6.6 illustrates the effect of water vapour partial pressure (pH_2O) on the impedance spectra of Ni-BZO and Ni-BZY anode symmetrical cell assemblies measured at 600 ºC. A notable feature is the changing offset resistance along the real Z´axis that is shown to increase with decreasing pH_2O. As outlined in the previous section, the offset resistance (corresponding to term R1) is related to the electrolyte resistance of the

symmetrical cells. Hence, a changing electrolyte resistance with altering pH_2O is a characteristic feature that corresponds to the proton conducting electrolyte BCZY used in the current work [5, 27].

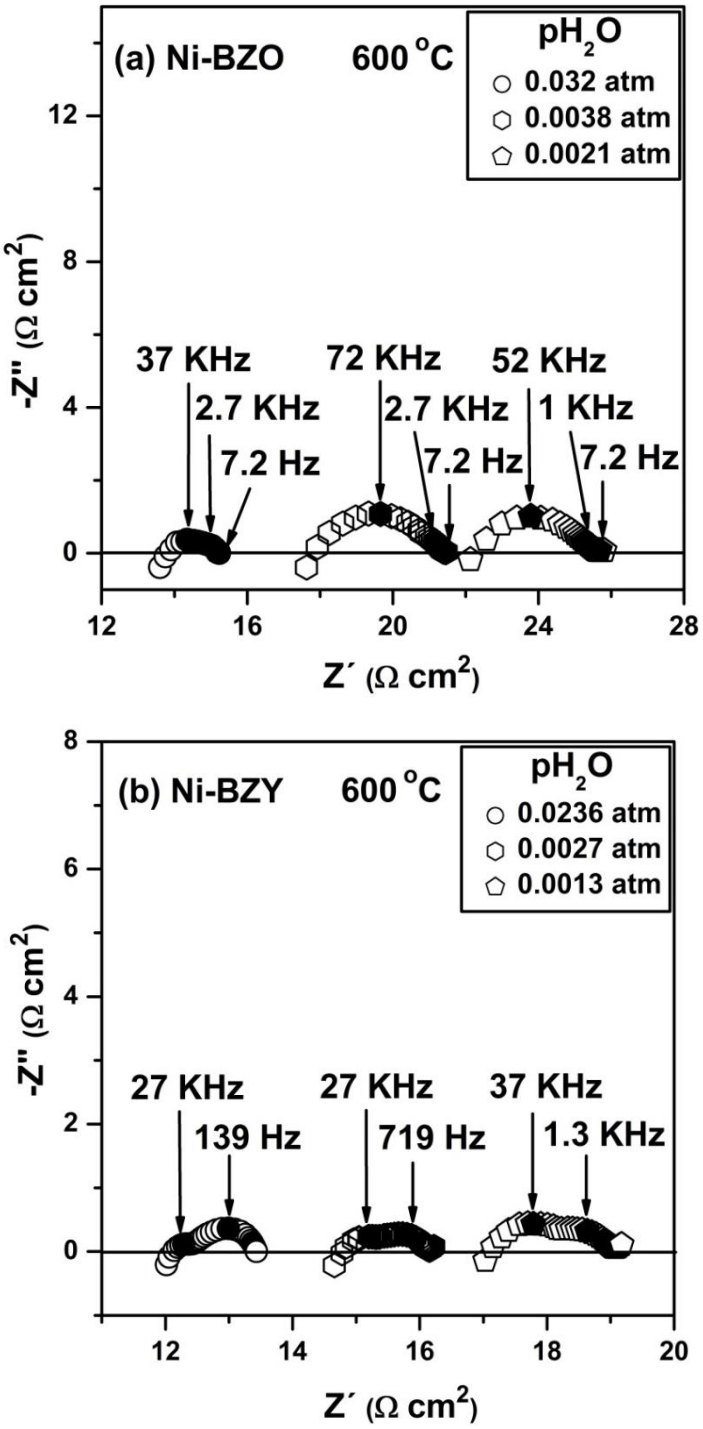

Figure 6.6. The impedance spectra of (40 vol% Ni) (a) Ni-BZO and (b) Ni-BZY cermet anodes, recorded at 600 °C as a function of water vapour partial pressure (pH_2O) measured in reducing conditions.

The impedance responses were fitted to the equivalent circuit shown in the inset of Fig. 6.4 and the resulting dependences of the anode polarisation resistances R2 and R3 are summarised in Fig. 6.7(a) as a function of pH_2O. The higher frequency semicircle ascribed to resistance R2, represents a polarisation resistance that is approximately an order of magnitude greater in the case of Ni-BZO anode than that obtained for Ni-BZY. For the Ni-BZO anode, the R2 polarisation resistance exhibits a negative pH_2O dependency, which corresponds to improved anode performance under wetter conditions. Under the driest conditions a similar pH_2O dependence of R2 for the Ni-BZY anode is also observed, but this tendency shifts to pH_2O independence under higher humidities.

The lower frequency impedance response corresponding to R3 is shown to be insensitive to pH_2O in the case of the Ni-BZY anode but shows slight positive dependence in the Ni-BZO case. The pH_2O dependence of R3 has previously been shown to be porosity sensitive, with slight positive pH_2O dependences demonstrated by anodes of the highest porosity [20]. Nonetheless, the levels of porosity of the Ni-BZO and Ni-BZY anodes are measured to be similar (38 cf. 34%, respectively). Thus, this small variation is considered insufficient to justify the markedly different pH_2O dependences recorded for the R3 term. The R3 polarisation resistance is also shown to be considerably greater for the Ni-BZY anode than Ni-BZO throughout the measured pH_2O range. These features will be discussed further in the following section 6.2.4. The impedance spectra of Fig. 6.6 show no significant pH_2O dependence of the lowest frequency response, related to R4, and this term is shown to take a negligible value thought the measured range. The combination of the polarisation resistance terms R2+R3+R4 leads to a total polarization resistance (Rp) that is dominated by the R2 term. Correspondingly, the total polarisation resistance of Ni-BZO is noted to be significantly higher than that of the Ni-BZY anode, Fig. 6.7(b).

The current work highlights that the choice of the matrix phase is highly significant to obtain low polarisation resistances. Improved anode behavior can be obtained in cermet anodes that contain ceramic matrix materials of high proton conduction, in agreement with previous literature that demonstrated lower polarisation resistances upon comparison of Ni-$SrZr_{0.95}Y_{0.05}O_{2.975}$ (Ni-SZY) with Ni-$CaZr_{0.95}Y_{0.05}O_{2.975}$ (Ni-CZY) anodes [16].

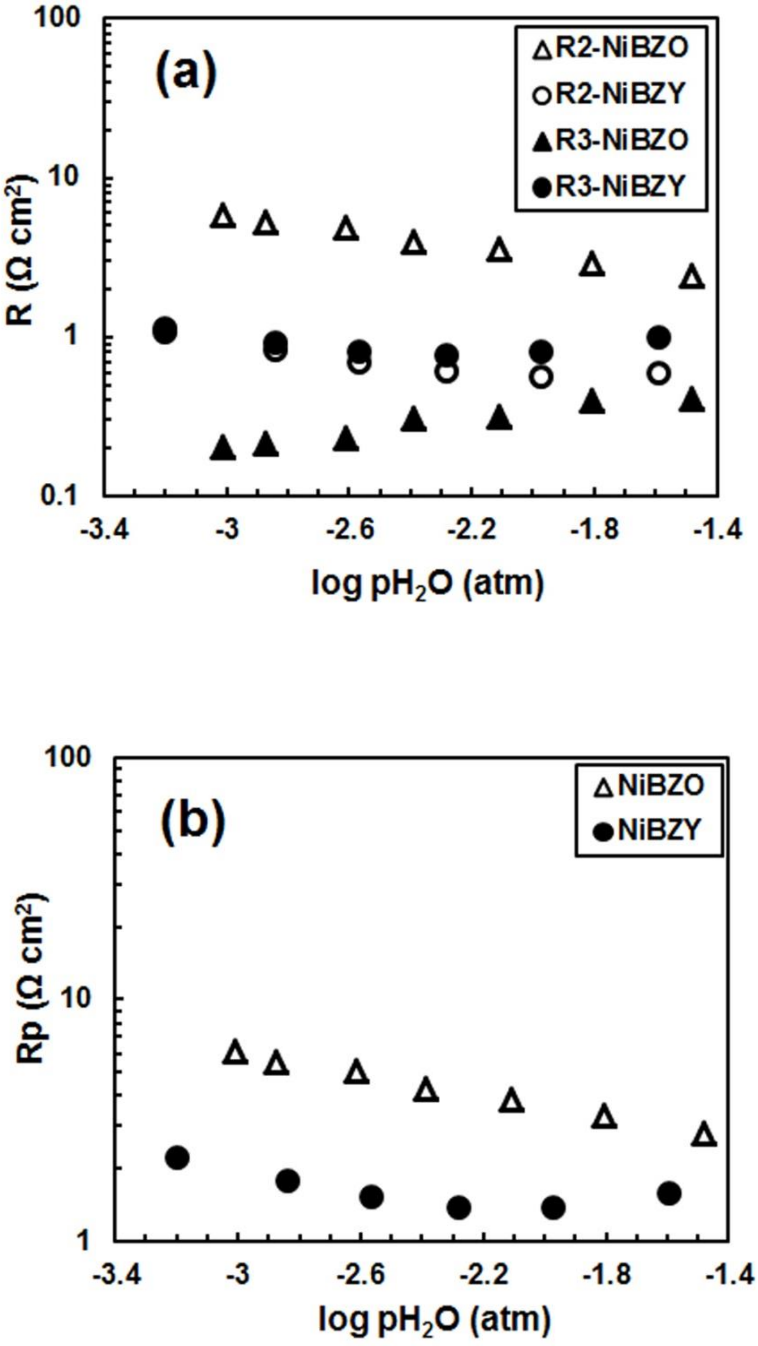

Figure 6.7. Polarisation resistance (a) R2, R3 and (b) Rp of Ni-BZO & Ni-BZY as a function of water vapour partial pressure (pH_2O) in a reducing atmosphere at 600 °C.

Due to the importance of the R2 term on the total polarization resistance, the R2 term is now discussed in more detail. It has been previously suggested that the R2 polarisation term for proton conducting cermet anodes may be related to migration of

protonic species across the TPB line and to the resistance of protonic transport [20]. This concept corresponds well to the current results that showed an order of magnitude higher polarisation resistance, R2 in the Ni-BZO anode than that obtained for an anode containing a matrix material of higher proton conduction, Ni-BZY, Fig. 6.7. Hence, to assess whether direct correlations can be made between protonic conduction in the matrix material and anode performance, Fig. 6.8 re-plots the pH_2O dependence of R2 for the anode cermets under study together with resistivities measured for bulk samples of the BZO and BZY matrix materials. In this respect, it is interesting that both bulk matrix materials appear to demonstrate negative dependences of resistivity on pH_2O; an observation that signifies that both BZO and BZY offer some proton conduction [28]. Although nominal $BaZrO_3$ would have been expected to offer zero proton conductivity, due to the absence of required oxygen vacancies that may be hydrated [29], it is clear that the actual $BaZrO_3$ material contains some intrinsic defects that permit a small amount of hydration and slight proton conduction. Even so, the resistivity of the BZO sample is observed to be substantially higher than that of BZY, by approximately 1.5 orders of magnitude, thus, permitting the global aim of the current study.

Gorelov et al. outlined that a theoretical $pH_2O^{-1/2}$ dependence of resistivity would be predicted under conditions of low proton concentration for typical acceptor doped perovskites [28]. These authors also reported measured dependences that were lower than the theoretical value and attributed this observation to competitive filling of the available oxygen vacancies by oxide-ions at elevated temperatures [28]. The measured pH_2O dependences for the bulk BZO and BZY materials of Fig. 6.8 are calculated to be 0.301 (±0.012) and 0.444 (±0.015) respectively; values that correspond well with those measured by Gorelov et al. for similar materials [28]. Moreover, Fig. 6.8 highlights that similar negative pH_2O dependences can be observed for the high frequency polarisation resistance, R2, for the Ni-BZO and Ni-BZY anode cermets, reinforcing links between R2 and protonic conduction in the cermet ceramic matrix, as suggested in previous literature [12, 20]. However, in the case of the Ni-BZY anode, such correspondence between the pH_2O dependences appears to be approached only under the driest conditions.

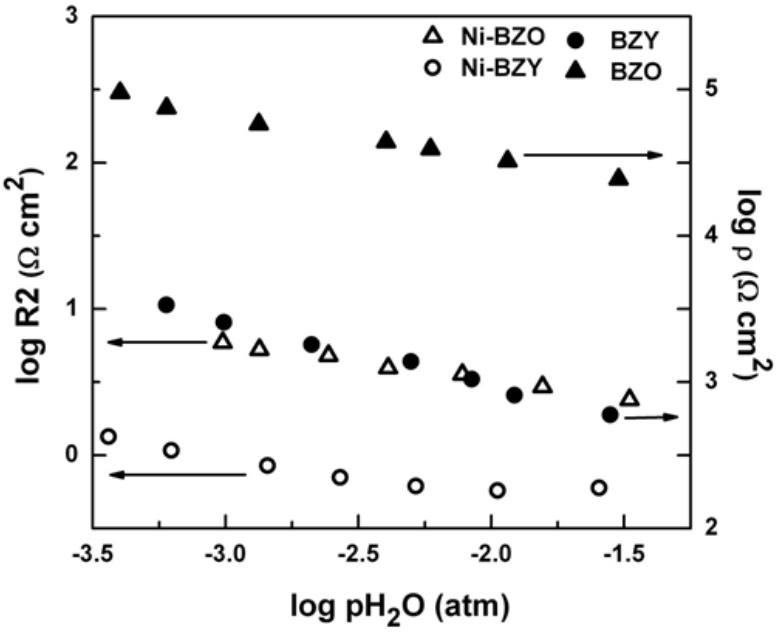

Figure 6.8. Comparison of polarisation resistance (R2) of Ni-BZO and Ni-BZY anodes and resistivity of BZO and BZY bulk samples with pH_2O at 600 °C in reducing atmospheres

6.2.4. Effect of hydrogen partial pressure (pH_2)

Fig. 6.9(a) and (b) demonstrate the progression of the impedance spectra of Ni-BZY and Ni-BZO, respectively, as a function of pH_2, measured in wet reducing atmospheres at 600 °C. While the offset along the real Z´axis, corresponding to the electrolyte resistance, is shown to be invariant on pH_2, the impedance responses are observed to become significantly more resistive as pH_2 decreases.

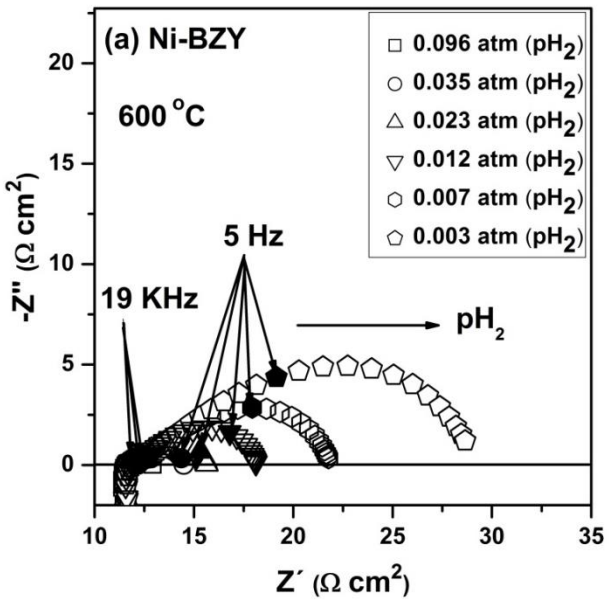

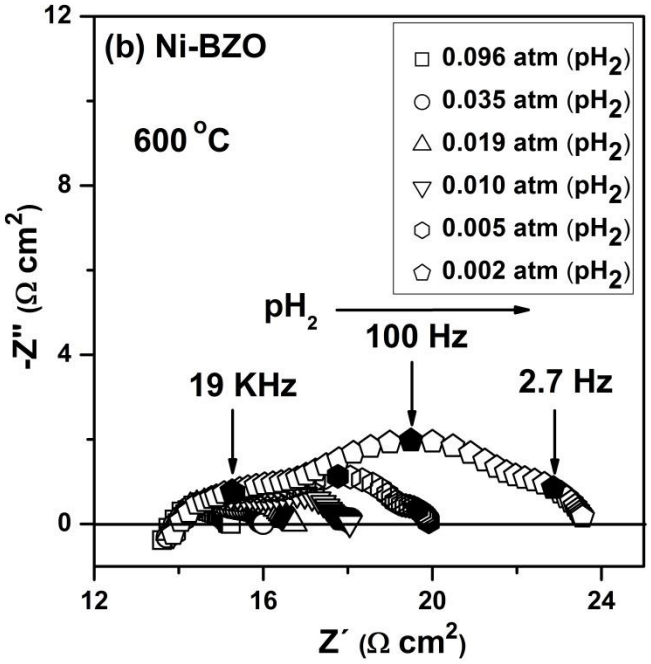

Figure 6.9. The impedance spectra of (a) Ni-BZY and (b) Ni-BZO anodes, as a function of pH_2, measured in humid atmospheres at 600 °C respectively.

Fig. 6.10 summarizes the associated changes of the polarisation resistance (R2, R3 and R4) calculated by fitting the impedance data to the equivalent circuit shown in the inset of Fig. 6.4. The higher frequency response, corresponding to resistance R2, is relatively insensitive to levels of pH_2 for both Ni-BZO and Ni-BZY anodes and is of significantly larger magnitude in the case of Ni-BZO, in agreement with the results of the previous section 6.2.3. In contrast, the low frequency response, associated to resistance R3, demonstrates strong negative pH_2 dependences for both cermet anodes, with values close to unity across most of the pH_2 range. These results are in accordance to those previously observed for Ni-BZY anodes in the literature [14, 20], where the negative unity dependence R3 on pH_2 has been associated with dissociative adsorption of H_2 on the anode surface [20]. The polarisation resistance R3 is shown to be lower in the Ni-BZO anode than the Ni-BZY anode, concurring with the results of the previous section 6.2.3. In this respect, the competitive adsorption of water vapour on the metallic Ni surface is a feature that has previously been noted in oxide-ion conducting SOFC anodes and one that may hinder the number of available sites for the dissociative adsorption of H_2 [20, 30]. Such an effect could explain the higher R3 values noted in the Ni-BZY anode and would result

from a higher level of hydration in the matrix of Ni-BZY, due to its a larger oxygen vacancy concentration [29]. Fig. 6.10(b) shows that the combination of these polarisation resistances leads to a total polarisation resistance that is shown to be lower in Ni-BZO than that of the Ni-BZY anode upon moving to low pH_2.

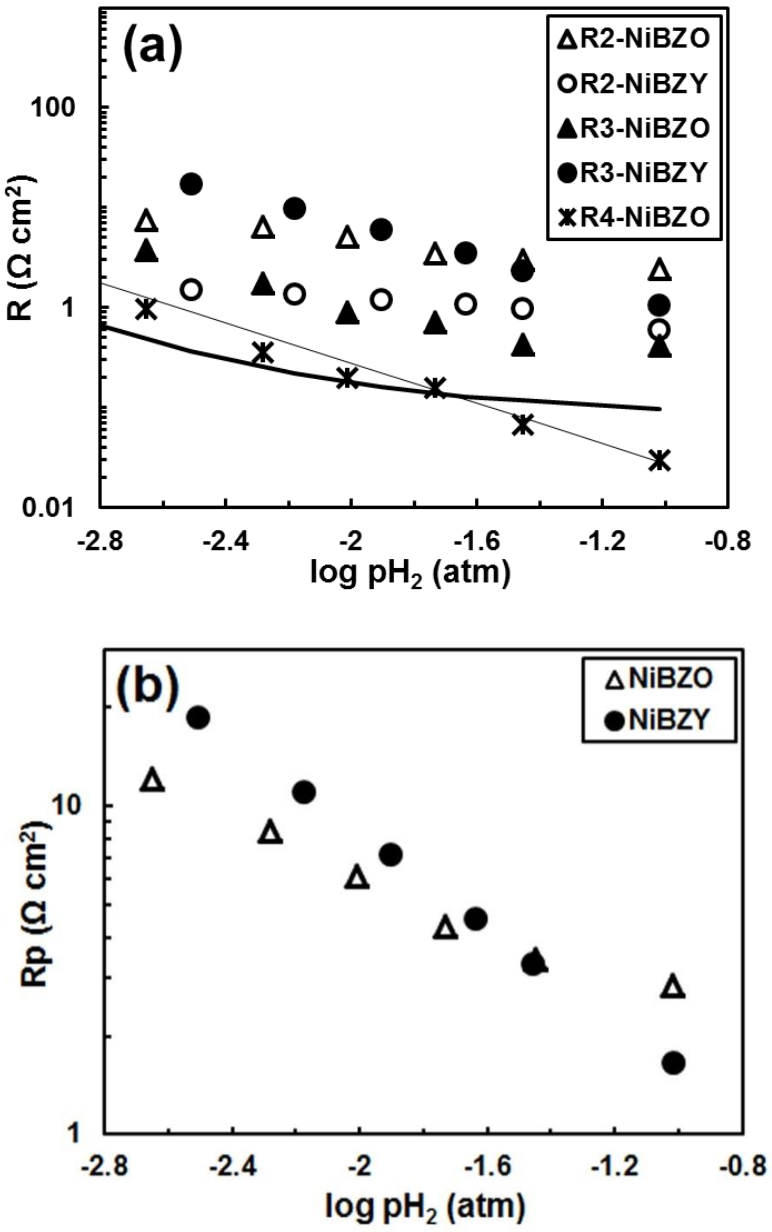

Figure 6.10. Polarisation resistance (a) R2, R3, R4 and (b) Rp of Ni-BZO and Ni-BZY as a function of hydrogen partial pressure (pH_2) in a humid atmosphere at 600 °C. In Figure 6.10(a), the thick line corresponds to fitting using equation 6.3 with stagnant layer thickness of 0.3mm, while the thin line corresponds to fitting using equation 6.5 with stagnant layer thickness of 1mm. Note stagnant layer thicknesses scale results vertically but do not have impact on gradient, eqs. 6.3 and 6.5.

6.2.5 Gas phase polarization resistance, R4

A striking feature of the impedance spectra shown in Fig. 6.9 is the major difference in behaviour noted for the lowest frequency response in the Ni-BZY and Ni-BZO samples with changing pH_2. This response, corresponding to resistance R4, is shown to be highly sensitive to pH_2 in the Ni-BZO anode, increasing rapidly with decreasing pH_2. In stark contrast, this term is observed to be negligible across the whole pH_2 range for the Ni-BZY anode. The capacitance corresponding to this response is calculated to be large, with values in the region of 10^{-1} Fcm^{-2}. Capacitance values of this order are typically associated with diffusional limitations in the gas phase of cermet materials for classical oxide-ion conducing SOFC anodes [31]. In the SOFC case, previous researchers have proposed a one-dimensional stagnant model to explain this phenomenon based on the interrelationship between the additional gas diffusion overpotential, η_D, and the deviation of the gas composition at the anode surface $Cj,_A$ from that of the bulk $Cj,_B$, expressed by the following equation for any gaseous species j, [31].

$$\eta_D = \frac{RT}{2F} \ln\left(\frac{C_{H_2O,A}.C_{H_2,B}}{C_{H_2O,B}.C_{H_2,A}}\right) \tag{6.2}$$

Under the condition that the changes in gas phase composition at the anode surface are much less than that in the bulk composition ($\Delta Cj << C_{j,B}$), Mogensen et al. showed that this relationship leads to a gas phase polarization resistance, R_D, given by [31, 32]

$$R_D = \frac{\eta_D}{i} = \left(\frac{RT}{2F}\right).\frac{d}{P}\left(\frac{1}{X_{H_2}.D_{H_2-mix}} + \frac{1}{X_{H_2O}.D_{H_2O-mix}}\right) \tag{6.3}$$

where, X_{H_2} and X_{H_2O} are the molar fractions of H_2 and H_2O in the bulk gas composition, d is the stagnant layer thickness and D_{H_2-mix} and D_{H_2O-mix} are the ternary bulk diffusion coefficients of H_2 and H_2O, respectively, when diluted by an inert gas (N_2 or He) [32]. It should be noted that the ternary diffusion coefficient of a $H_2/H_2O/N_2$ mixture will be significantly greater that of a H_2/H_2O/He mixture of identical ratio, due to the significantly lower diffusion volume of He than N_2 [32]. From equation 6.3, this factor can be predicted

to lead to a reduction in the diffusion polarisation resistance when He is the diluting gas. This feature provides a common and simple method to confirm the presence of diffusion limitations [32, 33]. Fig. 6.11 shows the impedance spectra of the Ni-BZO anode measured at 600 ºC in humidified reducing atmospheres of $H_2O/H_2/N_2$ or H_2O/H_2/He mixtures, under identical ratios (0.032/0.095/0.904). In both cases, the measured oxygen sensor reading was shown to be identical. In agreement with the above discussion, it is clear that the polarization resistance R4 is significantly reduced in the He diluted mixture, thus, reinforcing the conclusion that the observed R4 term is that of diffusion polarisation.

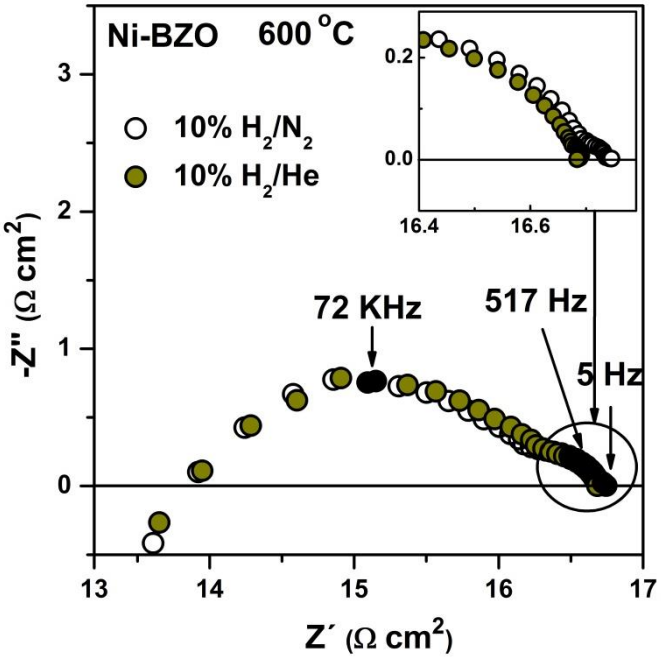

Figure 6.11. Impedance spectra recorded at 600 ºC in humidified 10% H_2/N_2 or He gas mixtures (pH_2O=0.032 atm) (inset-appearance of change in R4).

The above discussion, thus confirms R4 to be a resistive term that is related to diffusion polarisation. However, attempts to fit the experimental data using equations (6.2) and (6.4) (thick solid line in Fig. 6.10), result in poor approximations, with significant deviations noted in their gradient. Moreover, equation (6.3) also predicts a strong pH_2O dependence of diffusion polarisation resistance; as confirmed experimentally in oxide-ion conducting cermet anodes for SOFC [31]. In stark contrast to this expectation, R4 was shown to take negligible values throughout the measured pH_2O range in the previous section 6.2.3, Fig. 6.6, for both samples. Thus, it is clear that the one-dimensional stagnant

model commonly used to predict diffusion polariastion limitations in oxide-ion conducting SOFC anodes, equations (6.2, 6.3), is unsuccessful to explain the diffusion polarisation resistance of the Ni-BZO anode in the current work. On the other hand, if one assumes an absence of water vapour partial pressure variation between the bulk gas composition and that at the anode surface, such that equation (6.2) simplifies to

$$\eta_D = \frac{RT}{2F} \ln\left(\frac{C_{H_2,B}}{C_{H_2,A}}\right) \tag{6.4}$$

and equation (6.3) reduces to

$$R_D = \frac{\eta_D}{i} = \left(\frac{RT}{2F}\right).\frac{d}{P}\left(\frac{1}{X_{H_2}.D_{H_2-mix}}\right) \tag{6.5}$$

a good fit with the experimental data (thin line in Fig. 6.10) can be provided for a stagnant layer thickness of approximately 1 mm. Furthermore, such a scenario would also accommodate the observed absence of pH_2O dependence of R4 exhibited in section 6.2.3., Fig. 6.6. Fig. 6.7 showed that both ceramic cermet anode matrices of the current study, BZY and BZO offer some proton conductivity; a result that implies significant hydration of their cermet matrices [29]. The presence of such hydration offers a potential explanation for the absence of a notable deviation in water vapour partial pressure between the bulk gas composition and the electrode surface, due to effective buffering of the water vapour partial pressure experienced at the anode. In the Ni-BZO case such a phenomenon would lead to domination of the diffusion polarisation resistance by the pH_2 gradient between the bulk gas composition and that of the anode surface, eq (6.5), in agreement with the observed results. Nonetheless, the Ni-BZY anode does not concur with this hypothesis, instead showing negligible diffusion polarization resistance under all measured conditions. The matrix of the Ni-BZY cermet is proton conducting and, thus, would also expected to be hydrated leading to a negligible pH_2O dependence of polarisation resistance, as suggested for the Ni-BZO anode. However, the additional lack of pH_2 dependence of diffusion polarisation resistance must be addressed. The R3 polarisation term has previously been related to the consumption of H_2 by its dissociation at the anode surface [14]. Moreover, Fig. 6.7(a) and 6.10(a) show this polarisation resistance, R3, to be

significantly greater in the Ni-BZY anode than in Ni-BZO, due to different levels of hydration and competing adsorption of H_2O on the Ni surface. It is, therefore, likely that the much larger resistance to the dissociation of H_2 in the Ni-BZY case, limits the change in H_2 partial pressure experienced at the Ni-BZY anode surface, thereby, preventing a notable diffusion polarisation resistance, see eqs. 6.4 and 6.5.

6.3 Conclusions

The Ni-BZO and Ni-BZY cermet anodes were synthesized by acetate-H_2O_2 combustion method. The symmetrical anode/electrolyte/anode cell assemblies were prepared for Ni-BZO and Ni-BZY anodes by using co-pressing method and sintered at 1400 °C followed by reduction at 700 °C in 10% H_2/N_2 gas mixture. The impedance spectra have been recorded as a function of temperature, hydrogen partial pressure (pH_2) and water vapour partial pressure (pH_2O). The resultant microstructure of both cermet anodes was shown to be similar, facilitating electrochemical comparison. The high frequency polarization resistance, R2, of Ni-BZO anode was shown to be significantly higher than that of Ni-BZY anode. The results demonstrated strong links between the R2 polarisation resistance and proton conduction in the matrix phase of the cermet anodes. In reducing atmospheres the R2 value dominates the total polarisation resistance, leading to higher performance in the Ni-BZY anode, which contains the matrix material of highest proton conduction. The R2 polarisation resistances of Ni-BZO and Ni-BZY anodes were shown to be insensitive to pH_2, whereas strong negative pH_2 dependences of around unity were noted for the R3 polarisation resistances in agreement with previous literature that classified this response to be due to dissociative adsorption of H_2 on the anode surface. On the other hand, the magnitude of R3 for the Ni-BZO anode was shown to be lower than that obtainable for the Ni-BZY anode under similar conditions. This feature produced a lower total polarization resistance in the Ni-BZO material on moving to the least reducing conditions. An additional low frequency response, R4, was also noted for the Ni-BZO anode and was shown to be related to diffusion polarisation. Discussion relates these latter observations to expected differences in the levels of hydration of the two anode materials.

6.4 References

[1] Emiliana F, Daniele P, Enrico T. Electrode materials: a challenge for the exploitation of protonic solid oxide fuel cells. Sci Technol Adv Mater. 2010;11:044301.

[2] Fabbri E, Pergolesi D, Traversa E. Materials challenges toward proton-conducting oxide fuel cells: a critical review. Chem Soc Rev. 2010;39:4355-69.

[3] Orera A, Slater PR. New Chemical Systems for Solid Oxide Fuel Cells†. Chem Mater. 2009;22:675-90.

[4] Fabbri E, Bi L, Pergolesi D, Traversa E. Towards the next generation of solid oxide fuel cells operating below 600 °C with chemically stable proton-conducting electrolytes. Adv Mater. 2012;24:195-208.

[5] Nasani N, Dias PAN, Saraiva JA, Fagg DP. Synthesis and conductivity of $Ba(Ce,Zr,Y)O_{3-\delta}$ electrolytes for PCFCs by new nitrate-free combustion method. Int J Hydrogen Energy. 2013;38:8461-70.

[6] Sawant P, Varma S, Wani BN, Bharadwaj SR. Synthesis, stability and conductivity of $BaCe_{0.8-x}Zr_xY_{0.2}O_{3-\delta}$ as electrolyte for proton conducting SOFC. Int J Hydrogen Energy. 2012;37:3848-56.

[7] Fabbri E, Depifanio A, Dibartolomeo E, Licoccia S, Traversa E. Tailoring the chemical stability of $Ba(Ce_{0.8-x}Zr_x)Y_{0.2}O_{3-\delta}$ protonic conductors for Intermediate Temperature Solid Oxide Fuel Cells (IT-SOFCs). Solid State Ionics. 2008;179:558-64.

[8] Tao S, Irvine JTS. Conductivity studies of dense yttrium-doped $BaZrO_3$ sintered at 1325 °C. J Solid State Chem. 2007;180:3493-503.

[9] Antunes I, Mather GC, Frade JR, Gracio J, Fagg DP. Stability of $Ba(Zr,Pr,Y)O_{3-\delta}$ materials for potential application in electrochemical devices. J Solid State Chem. 2010;183:2826-34.

[10] Atkinson A, Barnett S, Gorte RJ, Irvine JTS, McEvoy AJ, Mogensen M, et al. Advanced anodes for high-temperature fuel cells. Nat Mater. 2004;3:17-27.

[11] Cowin PI, Petit CTG, Lan R, Irvine JTS, Tao S. Recent Progress in the Development of Anode Materials for Solid Oxide Fuel Cells. Adv Energy Mater. 2011;1:314-32.

[12] Mather GC, Figueiredo FM, Jurado JR, Frade JR. Synthesis and characterisation of cermet anodes for SOFCs with a proton-conducting ceramic phase. Solid State Ionics. 2003;162–163:115-20.

[13] Bi L, Fabbri E, Sun Z, Traversa E. $BaZr_{0.8}Y_{0.2}O_{3-\delta}$-NiO Composite Anodic Powders for Proton-Conducting SOFCs Prepared by a Combustion Method. J Electrochem Soc. 2011;158:B797.

[14] Narendar N, Mather GC, Dias PAN, Fagg DP. The importance of phase purity in Ni–$BaZr_{0.85}Y_{0.15}O_{3-\delta}$ cermet anodes – novel nitrate-free combustion route and electrochemical study. RSC Adv. 2013;3:859.

[15] Chevallier L, Zunic M, Esposito V, Di Bartolomeo E, Traversa E. A wet-chemical route for the preparation of Ni–$BaCe_{0.9}Y_{0.1}O_{3-\delta}$ cermet anodes for IT-SOFCs. Solid State Ionics. 2009;180:715-20.

[16] Zunic M, Chevallier L, Radojkovic A, Brankovic G, Brankovic Z, Di Bartolomeo E. Influence of the ratio between Ni and $BaCe_{0.9}Y_{0.1}O_{3-\delta}$ on microstructural and electrical properties of proton conducting Ni–$BaCe_{0.9}Y_{0.1}O_{3-\delta}$ anodes. J Alloys Compd. 2011;509:1157-62.

[17] Mather GC, Figueiredo FM, Fagg DP, Norby T, Jurado JR, Frade JR. Synthesis and characterisation of Ni–$SrCe_{0.9}Yb_{0.1}O_{3-\delta}$ cermet anodes for protonic ceramic fuel cells. Solid State Ionics. 2003;158:333-42.

[18] Rainwater BH, Liu M, Liu M. A more efficient anode microstructure for SOFCs based on proton conductors. Int J Hydrogen Energy. 2012;37:18342-8.

[19] Coors WG, Manerbino A. Characterization of composite cermet with 68wt% NiO and $BaCe_{0.2}Zr_{0.6}Y_{0.2}O_{3-\delta}$. Journal of Membrane Science. 2011;376:50-5.

[20] Narendar N, Ramasamy D, Brandão AD, Yaremchenko AA, Fagg DP. The impact of porosity, pH_2 and pH_2O on the polarisation resistance of Ni-$BaZr_{0.85}Y_{0.15}O_{3-\delta}$ cermet anodes for Protonic Ceramic Fuel Cells (PCFCs). Int J Hydrogen Energy.39:21231–41.

[21] Nasani N, Wang Z-J, Willinger MG, Yaremchenko AA, Fagg DP. In-situ redox cycling behaviour of Ni–$BaZr_{0.85}Y_{0.15}O_{3-\delta}$ cermet anodes for Protonic Ceramic Fuel Cells. Int J Hydrogen Energy. 2014;39:19780-8.

[22] Tao S, Irvine JTS. A Stable, Easily Sintered Proton- Conducting Oxide Electrolyte for Moderate-Temperature Fuel Cells and Electrolyzers. Adv Mater. 2006;18:1581-4.

[23] Antunes I, Brandão A, Figueiredo FM, Frade JR, Gracio J, Fagg DP. Mechanosynthesis of nanopowders of the proton-conducting electrolyte material Ba(Zr, Y)$O_{3-\delta}$. J Solid State Chem. 2009;182:2149-56.

[24] Tong J, Clark D, Hoban M, O'Hayre R. Cost-effective solid-state reactive sintering method for high conductivity proton conducting yttrium-doped barium zirconium ceramics. Solid State Ionics. 2010;181:496-503.

[25] Zhao F, Virkar A. Dependence of polarization in anode-supported solid oxide fuel cells on various cell parameters. J Power Sources. 2005;141:79-95.

[26] Bauerle JE. Study of solid electrolyte polarization by a complex admittance method. J Phys Chem Solids. 1969;30:2657-70.

[27] Ricote S, Bonanos N, Wang HJ, Haugsrud R. Conductivity, transport number measurements and hydration thermodynamics of $BaCe_{0.2}Zr_{0.7}Y_{(0.1-\xi)}Ni_{\xi}O_{(3-\delta)}$. Solid State Ionics. 2011;185:11-7.

[28] Balakireva VB, Kuz'min AV, Gorelov VP. Ionic conductivity in the $BaZ_{1-x}Y_xO_{3-\delta}$ system (x = 0.02–0.2) in H_2/H_2O and D_2/D_2O atmospheres. Russ J Electrochem. 2010;46:749-53.

[29] Kreuer KD. Proton-Conducting oxides. Ann Rev Mater Res. 2003;33:333-59.

[30] Ihara M, Kusano T, Yokoyama C. Competitive Adsorption Reaction Mechanism of Ni/Yttria-Stabilized Zirconia Cermet Anodes in H_2-H_2O Solid Oxide Fuel Cells. J Electrochem Soc. 2001;148:A209.

[31] Primdahl S, Mogensen M. Gas diffusion impedance in characterization of solid oxide fuel cell anodes. J Electrochem Soc. 1999;146:2827-33.

[32] Mohammed Hussain A, Høgh JVT, Jacobsen T, Bonanos N. Nickel-ceria infiltrated Nb-doped $SrTiO_3$ for low temperature SOFC anodes and analysis on gas diffusion impedance. Int J Hydrogen Energy. 2012;37:4309-18.

[33] Osinkin DA, Kuzin BL, Bogdanovich NM. Gas diffusion hindrances on Ni cermet anode in contact with $Zr_{0.84}Y_{0.16}O_{1.92}$ solid electrolyte. Russ J Electrochem. 2009;45:483-9.

Chapter 7

Fabrication and electrochemical performance of a highly stable, anode supported thin $BaCe_{0.4}Zr_{0.4}Y_{0.2}O_{3-\delta}$ electrolyte Protonic Ceramic Fuel Cell (PCFC)

Abstract

This chapter describes the fabrication and electrochemical characterisation of a potential protonic ceramic fuel cell based on a Ni-$BaZr_{0.85}Y_{0.15}O_{3-\delta}$ anode supported thin film proton conducting $BaCe_{0.4}Zr_{0.4}Y_{0.2}O_{3-\delta}$ electrolyte with a $Pr_2NiO_{4+\delta}$ cathode. Anode and electrolyte materials were prepared by an acetate-H_2O_2 combustion method. A thin (~5µm), dense and crack free $BaCe_{0.4}Zr_{0.4}Y_{0.2}O_{3-\delta}$ electrolyte film was successfully obtained on a porous anode support by spin coating and firing at 1450 °C. Maximum power densities of 234, 158, 102 and 63 mW/cm^2 at 700, 650, 600 and 550 °C, respectively were achieved for the Ni-$BaZr_{0.85}Y_{0.15}O_{3-\delta}$/$BaCe_{0.4}Zr_{0.4}Y_{0.2}O_{3-\delta}$/$Pr_2NiO_{4+\delta}$ single cell under fuel cell testing condtions. The electrode polarisation resistance was assessed at open circuit conditions by use of electrochemical impedance spectroscopy (EIS) and is shown to dominate the areas specific resistance at low temperatures. Postmortem analysis by scanning electron microsocpy (SEM), reveals that no delamination occurs at anode/electrolyte or electrolyte/cathode interfaces upon cell operation.

7.1 Introduction

Protonic ceramic fuel cells (PCFCs) are green energy devices that convert chemical energy to electrical energy with higher efficiency than combustion engines [1, 2]. The flexible nature of PCFCs, to potentially run on various non-carbonaceous and carbonaceous fuels with high efficiency, has generated extensive recent interest in these devices [2-4]. Additionally, the unique feature of PCFCs that formation of water occurs at the cathode side, so that fuel does not become diluted, provides an advantage over that of oxide-ion conducting SOFC and has attracted researchers towards the viability of its practical applications [2]. Among all available solid state proton conductors, alkaline earth doped cerate and zirconate based perovskite materials have shown the greatest promise for PCFC electrolytes, due to their high protonic conductivity and low activation energy at intermediate temperatures (400-700 °C) [5, 6]. However, alkaline earth cerates (acceptor doped barium cerate-$BaCe_{1-x}R_xO_{3-\delta}$, where R = rare earth) are unsuitable for PCFCs owing to their instability in H_2O and CO_2 containing atmospheres, in contrast with their zirconate analogues ($BaZr_{1-x}R_xO_{3-\delta}$) that are stable under these conditions [7]. Nonetheless, the refractory nature, low sinterability and high grain boundary resistance of the zirconates are the main hurdles limiting their wider acceptance for use in PCFC applications [5, 8, 9]. Several attempts have been made to improve the sinterability of the zirconates using transition and alkali metal oxides as sintering additives [10-14]. However, such sintering additives are shown to lower the bulk proton conductivity [15, 16].

Another possibility to use these proton conductors is to combine both barium cerate and zirconate materials. The solid solution $BaCe_{1-x-y}Zr_xY_yO_{3-\delta}$ (BCZY) has been proposed in the literature and properties of conductivity and stability have been studied as a function of Zr content [7, 9, 17, 18]. Among all compositions, the composition $BaCe_{0.4}Zr_{0.4}Y_{0.2}O_{3-\delta}$ (BCZY44) was shown to offer good chemical stability, while maintaining high levels of bulk and grain boundary conductivity at 400-700 °C [9, 19]. Nonetheless, the dense BCZY44 electrolyte membrane still can only be obtained above 1500 °C, where such high sintering temperatures may lead to volatilization of BaO [5, 20]. Guo et al. studied the densification of BCZY44 using ZnO as a sintering additive by applying three different sintering approaches, and showed that the electrolyte could be densified at 1450 °C. These authors subsequently fabricated a single cell with the zinc modified BCZY44 electrolyte of thickness 25μm and achieved a power density ~307 $mWcm^{-2}$ [21, 22]. Interestingly, these

results are contrary to their previous studies of a similar but slightly thicker BCZY44 electrolyte (35μm) single cell, which exhibited a power density of 190 $mWcm^{-2}$ under the same conditions when no sintering additive was applied [9]. Liu et al. has shown the viability and stability of BCZY44 electrolyte membrane deposited on a nickel cermet anode for the reforming of dimethyl ether and their studies revealed that nickel was prone to carbon deposition [23].

The production of thin electrolyte films is a method that is commonly used in oxide-ion conducting SOFC to minimize the ohmic loss at low operating temperatures [24]. On the other hand, only a limited number of studies have been performed to date on anode supported PCFCs, especially with the state of the art BCZY44 electrolyte [5, 16]. The electrochemical performance of a BCZY44 electrolyte based PCFC, formed by a co-pressing method using 20wt% starch as an anode pore former and with electrolyte thickness of 20 μm, was evaluated by Bi et al. and shown to produce maximum power densities of 181 and 281 $mWcm^{-2}$ at 700°C without and with an anode functional layer, respectively [25], suggesting that an anode functional layer can improve the cell performance. In contrast, Rainwater et al. [26] and Narendar et al. [27] have shown that anode porosity created by external pore formers can adversely affect the performance of PCFCs and the unique anode microstructure formed solely from the reduction of NiO to Ni is adequate for peak performance in typical PCFC working conditions. Recently our group has studied the effect of phase purity [28], porosity [27], redox stability [29] and the importance of the existence of the proton conducting phase [30] in Ni-$BaZr_{0.85}Y_{0.15}O_{3-\delta}$ PCFC anodes on the resultant electrochemical behavior. The concept of the present work is, thus, to assess the compatibility, stability and electrochemical performance of a peak performing Ni-$BaZr_{0.85}Y_{0.15}O_{3-\delta}$ anode when combined with a thin film proton-conducting electrolyte BCZY44 and $Pr_2NiO_{4+\delta}$ cathode.

Many researchers have used different strategic methods to prepare thin film electrolyte membranes, co-pressing [31, 32], tape casting [33], electrophoretic deposition (EPD) [34], pulsed laser deposition (PLD) [35, 36], dip coating, spray coating and spin coating by suspension [8, 10]. The current authors [8] and Luisetto et al. [10] have shown that the spin coating is a versatile technique for the deposition of thin electrolyte membranes on a porous cermet anodes for PCFC applications, forming a crack free and dense thin film. The current work shows that thin dense BCZY44 electrolyte films (~5 μm)

can be deposited successfully by spin coating technique on Ni-$BaZr_{0.85}Y_{0.15}O_{3-\delta}$ anodes and later covered with a $Pr_2NiO_{4+\delta}$ cathode to provide competitive electrochemical cell performance. The experimental details of the syntheses, fabrication and fuel cell testing can be found in Chapter 2 under section 2.1, 2.5 and 2.6.

7.2 Results and Discussion

7.2.1 Phase and microstructure analysis

Fig. 7.1 represents the XRD patterns of pure phases of electrolyte BCZY44, anode Ni-BZY (Ni and BZY) and cathode $Pr_2NiO_{4+\delta}$ powders. All the powders were synthesized by wet chemical combustion method with high homogeneity. The absence of the impurity phase BaY_2NiO_5 in the anode highlights that high purity Ni-BZY anode is obtained in the current work, in accordance with our previous reports [28].

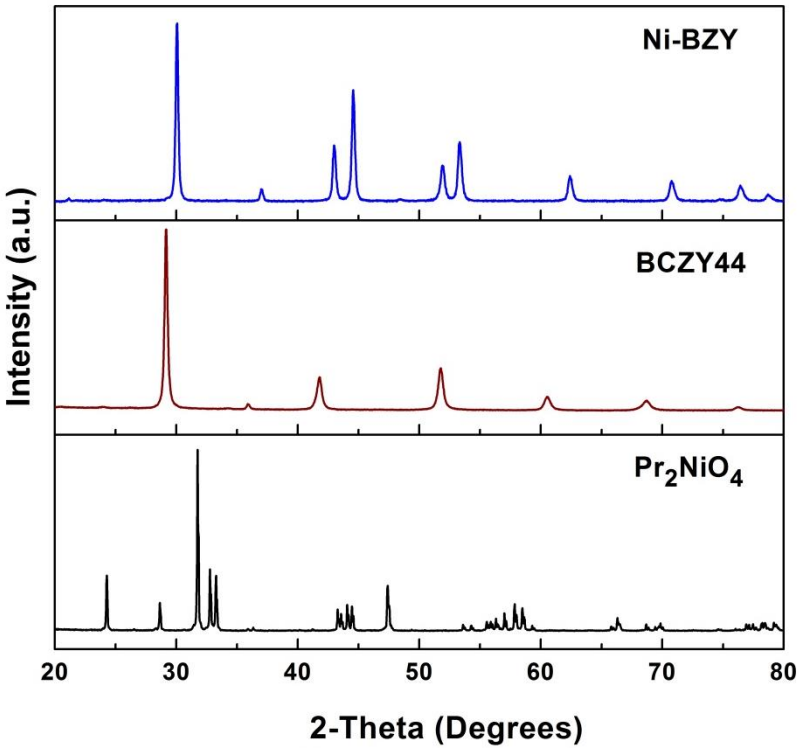

Figure 7.1. XRD patterns of anode, electrolyte and cathode powders.

The quality of the films was assessed by scanning electron microscopy. Fig. 7.2(a), (b) shows the SEM micrograph of surface microstructure of BCZY44 electrolyte film with high and low magnification scales. A homogenous dense and crack free electrolyte film

was attained without any pinholes on the surface. The thickness of electrolyte film was ~5 µm after two spin coated layers of the suspension prepared with only 2h milling time and was sintered at 1450 °C for 6h. The spin coated layers of the current work appear to be of high quality than those previously reported by Luisetto et al., who observed micro agglomerates on the surface of $BaZr_{0.80}Y_{0.16}Zn_{0.04}O_{3-\delta}$ thin films by spin coating when the suspension was prepared with longer milling times (10h) [10]. Fig. 7.2(c) shows the SEM micrograph of anode/electrolyte interface before the electrochemical testing. No delamination can be observed at the anode/electrolyte interface, with the electrolyte layer showing good adhesion.

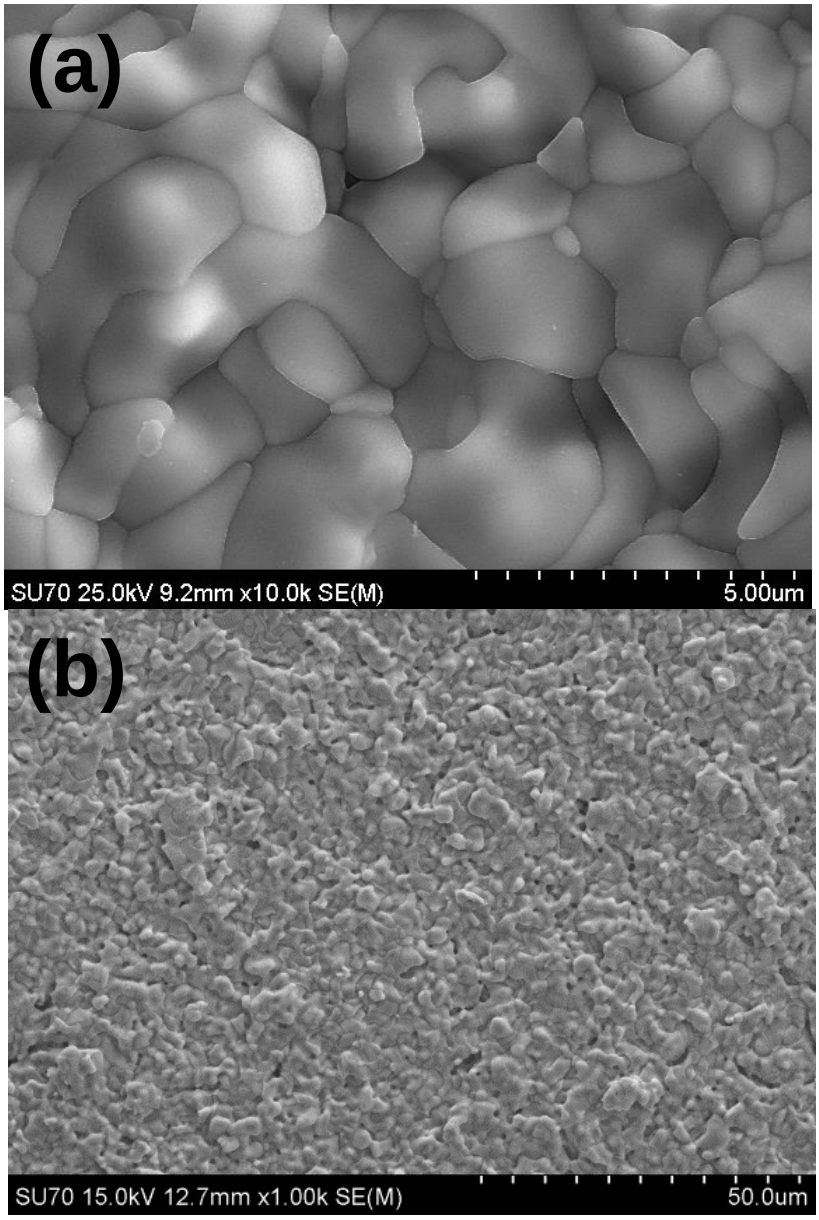

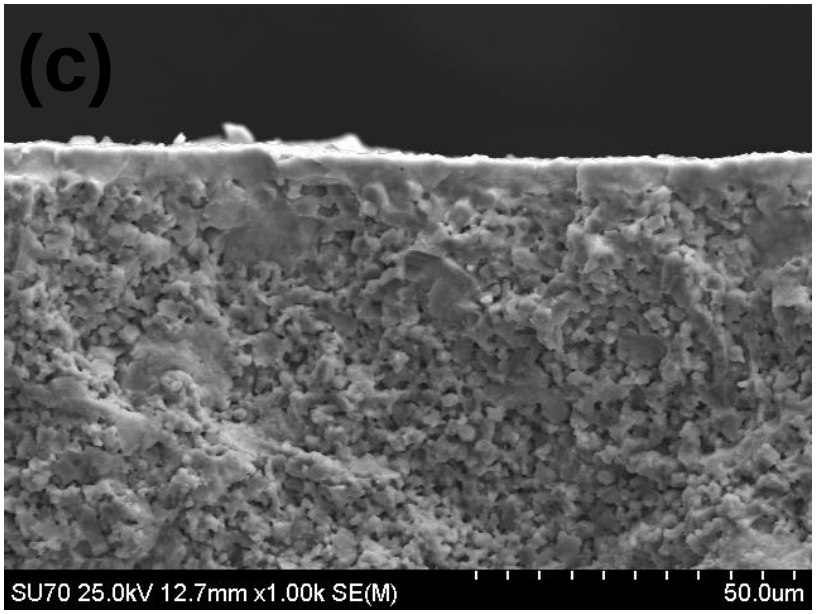

Figure 7.2. Scanning electron micrograph of (a) surface microstructure of electrolyte at high magnification, (b) low magnification and (c) anode/electrolyte interface before fuel cell test

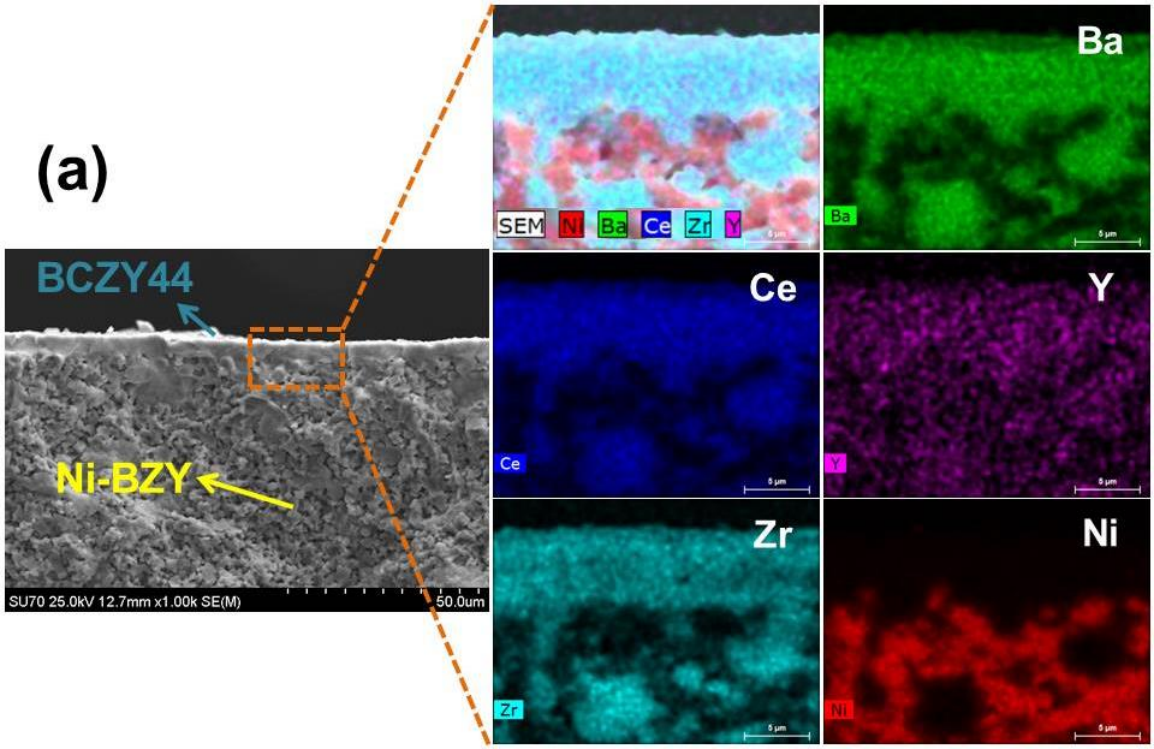

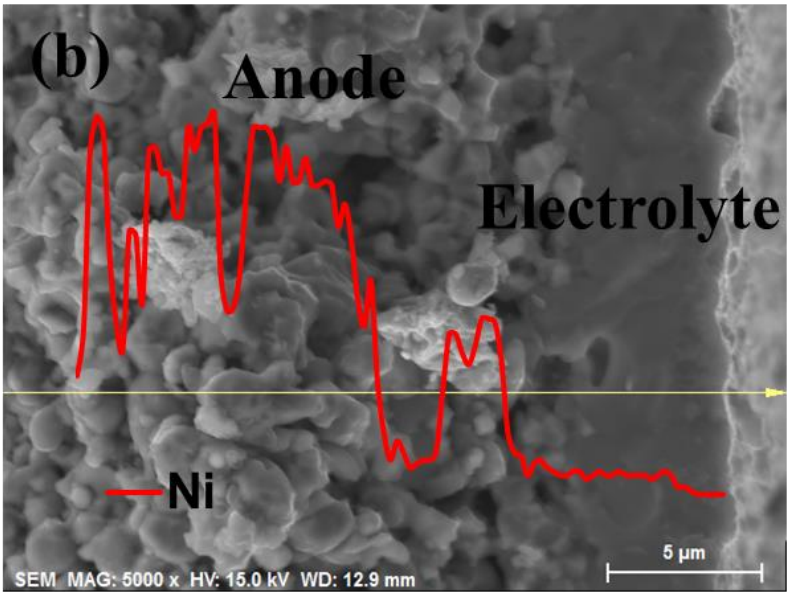

Figure 7.3. SEM-Energy dispersive X-ray spectroscopy (EDS) (a) elemental mapping and (b) line scan of anode/electrolyte interface

Fig. 7.3(a) presents the SEM-EDS elemental mapping of anode/electrolyte interface where homogeneity of all component elements can be clearly observed. Distinct percolation pathways of Ni and BZY networks in the anode can also be noted, Fig. 3(a), an important criterion to attain good fuel cell performance [37]. Fig. 7.3(b), demonstrates that no perceivable nickel diffusion from anode to electrolyte has occurred upon cell preparation. The macroscopic view of the single cell, consisting of anode, electrolyte and cathode (at the center) layers, is shown in Fig. 7.4 before the electrochemical fuel cell test.

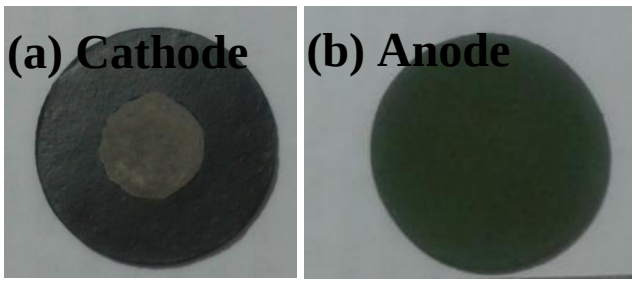

Figure 7.4. Digital photos of (a) cathode and (b) anode view of the single cell before the fuel cell test

Fig. 7.5 shows the SEM micrograph of single cell after fuel cell measurements. The image highlights that the good adherence of each layer, with no delamination and no cracks is retained after electrochemical measurements and that the cell components were stable. This result is in contrast to the work of Dailly et al. who also used a $Pr_2NiO_{4+\delta}$ cathode in the fabrication of a $BaCe_{0.9}Y_{0.1}O_{3-\delta}$ based PCFC single cell where degradation of the electrolyte/cathode interface was reported upon operation [32].

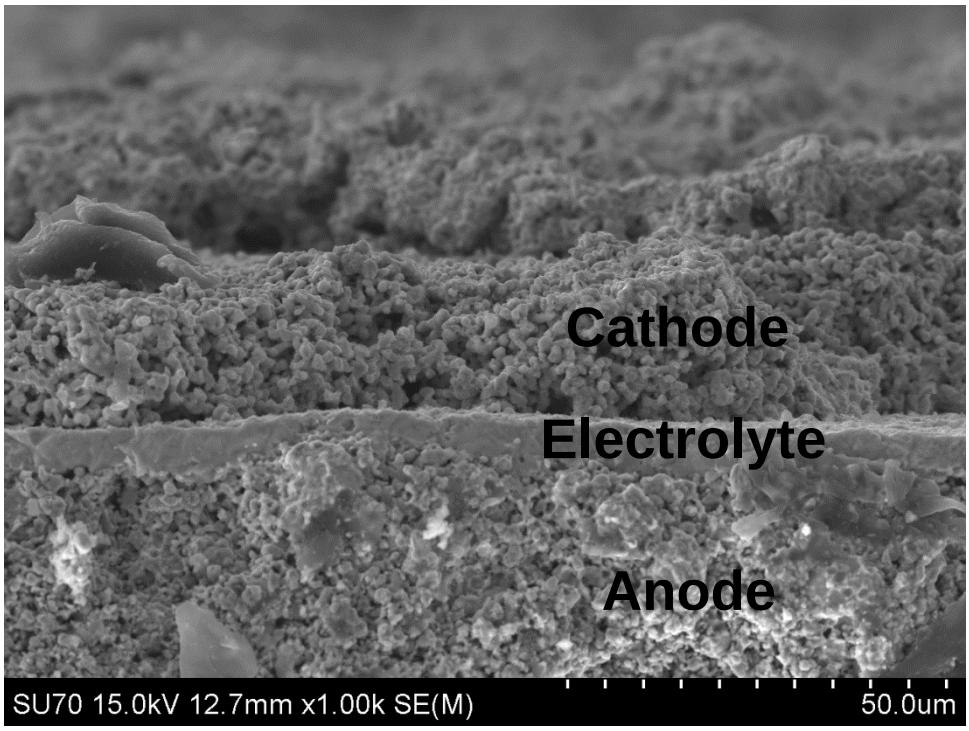

Figure 7.5. Scanning electron micrograph of Ni-BZY/BCZY44/$Pr_2NiO_{4+\delta}$ cell after electrochemical fuel cell test

7.2.2 Electrochemical performance of a single cell

The electrochemical performance of a single cell was assessed under flowing humid H_2 (3% H_2O) to the anode side and dry air to the cathode side in the temperature range of 700-550 °C. The current vs voltage (I-V) and current vs power density (I-P) characteristic cruves of a single cell based on BCZY44 electrolyte are shown in Fig. 7.6. The peak power densities 234, 158, 102 and 63 mW/cm^2 at 700, 650, 600 and 550 °C, respectively, were achieved for the Ni-BZY/BCZY44/$Pr_2NiO_{4+\delta}$ single cell. The maximum power density (PDmax) of 234 mW/cm^2 noted at 700 °C can be observed to be larger than

previous literature data obtained for BCZY44 and BZY electrolyte PCFCs summarised in Table 7.1. The area specific resistance (ASR) of the cell was calculated from the slope of the I-V curves at low current densities and shown in Table 7.2. Correspondingly, the ASR values obtained are less than those previously reported for BCZY44 electrolyte based PCFCs. The open circuit voltage (OCV) values of the single cell were 0.96, 0.99, 1.03 and 1.05 V at 700, 650, 600 and 550 °C, respectively, corresponding closely to the expected theoretical Nernst potential. The high OCV values highlight the absence of significant leakage, suggesting that the BCZY44 electrolyte was sufficintly densified and without cracks or open porosity.

Table 7.1. Electrochemical performance of anode supported PCFCs with different electrolytes at 700 °C

Anode	**Electrolyte**	**Cathode**	**PDmax ($mWcm^{-2}$)**	**Ref**
Ni-BZY	BCZY44 (5 μm)	$Pr_2NiO_{4+\delta}$	234	This work
Ni-BZY	BZY20_ZnO (20 μm)	Pt	90	[10]
Ni-BZY	BZY (4 μm)	LSCF-BCYb	110 (600 °C)	[35]
Ni-BZY	BZY-CaO (25 μm)	BZY-LSCF	141	[38]
Ni-BZYCu	BZY-CuO (10 μm)	LSCF-BZY	28.2 (600 °C)	[15]
Ni-BCZY44	BCZY44 (~35 μm)	BSCF	190	[9]
Ni-BCZY44	BCZY44 (20 μm)	BZCY-BSCFT	181	[25]
Ni-BCZY71	BZY (20 μm)	SSC-SDC	170	[31]
Ni-BCZY27	BCZY27 (20 μm)	LSCF	78	[39]

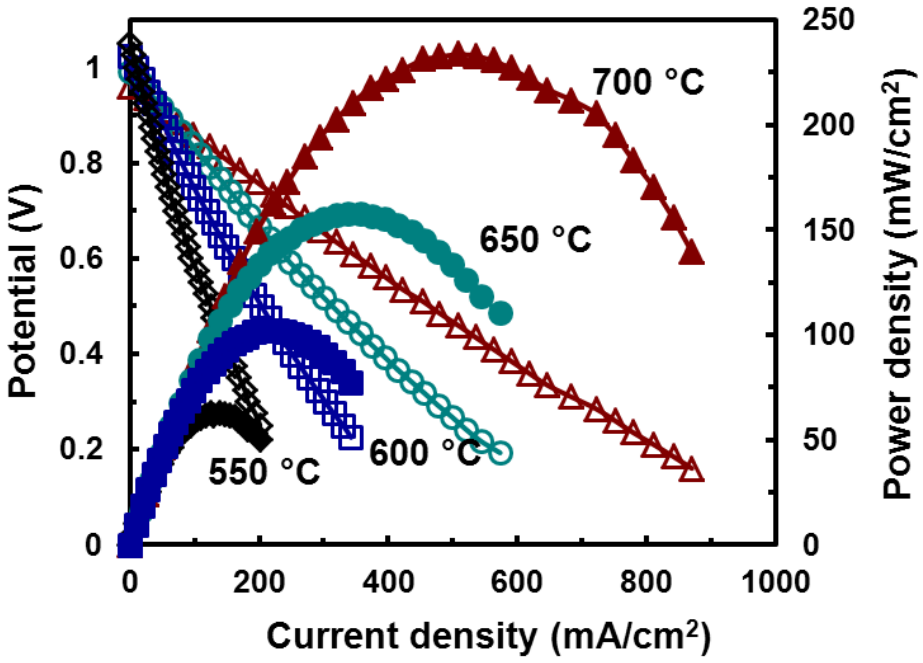

Figure 7.6. The I-V and power density curves of Ni-BZY/BCZY44/$Pr_2NiO_{4+\delta}$ single cell at different temperatures under humid H_2 (3%H_2O)and dry air

Electrochemical impedance spectra (EIS) were performed on the Ni-BZY/BCZY44/$Pr_2NiO_{4+\delta}$ single cell under open circuit conditions at each temperature. Typical nyquist plots at different temperatures are shown in Fig. 7.7. The ohmic resistance (Rohmic) of the single cell 0.555, 0.696, 0.769, 0.859 Ωcm^2 at 700, 650, 600 and 550 °C, respectively, was determined from the high frequency intercept with the real Z´-axis and is shown to increase with decreasing temperature, Fig. 7.8. Assuming that Rohmic can be principally attributed to the electrolyte resistance, the conductivity of electrolyte BCZY44 (~5 µm) thin film used in the current work was calculated from this data and shown to be 1.04×10^{-3}, 7.98×10^{-4}, 7.11×10^{-4} and 6.28×10^{-4} Scm^{-1} at 700, 650, 600 and 550 °C, respectively with an activation energy (E_a) of 0.30 eV, as shown in Fig. 7.9. The obtained low activation energy value is within the limit of a typical proton conducting oxide [5, 17]. On the other hand, the conductivity of electrolyte BCZY44 film sintered at 1450 °C in the present work is slightly lower than that of a bulk BCZY44 pellet sintered at 1500 °C [17], possibly due to differences in microstructure, for example, a smaller grain size in the BCZY film.

The total polarisation resistance (Rp=R2+R3) was calculated by fitting the impedance data at middle and low frequncy intercepts. The polarisation resistance (Rp)

increases on decreasing temperature as shown in Fig. 7.8. The area specific resistance (ASR) of the Ni-BZY/BCZY44/$Pr_2NiO_{4+\delta}$ single cell was calculated from the impedance spectrum as the sum of Rohmic and Rp and compared to that obtained from the I-V curves. A good match of ASR values between the EIS measurments and I-V curves was obtained, as shown in Table 7.2. Fig. 7.8 highlights that the ASR at the highest temperature is limited by the cell ohmic resistance, while at lower tempertures becomes dominated by the electrode polarization resistance. A similar trend was also observed by Sun et al. on Ni-BCZY71 anode supported BZY based single cell with SSC-SDC cathode, showing total ASR value of ~2.77 (Rohmic-1.47 and Rp-1.3) Ωcm^2 at 600 °C [31]. Bi et al. reported ASR values of 1.17 and 0.69 Ωcm^2 for a BCZY44 electrolyte (20 μm) based anode supported single cell using BZCY-BSCFT cathode with and without anode functional layer at 700 °C [25]. In the present work the Rohmic is lower than in the Bi et al. studies, due to the thinner electrolyte thickness in the present case, but the overall electrode polarisation resistance is slightly higher. The combination of these features leads to current ASR values that are comparable with those of the Bi et al. study for the same BCZY44 electrolyte based cell [25]. A larger Rohmic, 1.02 Ωcm^2 at 700 °C, was reported by Guo et al. in a similar anode supported BCZY44 (~35 μm) single cell with a BSCF cathode. These authors argued that the high Rohmic value came from anode or cathode/electrolyte contact resistance [9]. They also noted that ASR increased with decreasing temperature and BSCF was not a suitable cathode due to chemical interdiffusion between electrolyte/cathode layers [9]. Taillades et al. identified a relatively high cathode resistance of 1.59 Ωcm^2 at 600 °C on a symmetrical Pr_2NiO_4/BCY/Pr_2NiO_4 cell under moist air, while an anode supported BCY (~40 μm) based cell using the Pr_2NiO_4 cathode showed relatively poor electrochemical performance [40]. On further analysis they found an interlayer between the BCY electrolyte and the Pr_2NiO_4 cathode that was stated to block proton transfer from electrolyte to cathode, resulting in a high ASR value of 4.64 Ωcm^2 [40]. In the present work, Pr_2NiO_4 is also used as cathode. Nonethless, no observable chemical interaction between layers could be observed in the current case.

In summary, the thin, spin coated BCZY44 electrolyte membrane formed in the current work of only 5 μm thickness, provides cell ohmic resistances, Rohmic, that are lower than those previously obtained in the literature for cells containing a similar electrolyte. This low value of Rohmic allows the current cell performance to be limited by

electrode polarisation at lower tempertaures, even for total electrode polarisation resistances that are competative with those of previous literature studies [9, 15, 25, 31, 32]. As the Ni-BZY anode formed without the presence of a pore former has previously been documented to offer high electrochemical performance [27], it is likely that further improvements to the ASR of the current cell will be potentially acheived by alterations of cathode composition.

Table 7.2. The representative data from I-V characteristic curves and power densities at different temperatures

Temperature (°C)	OCV (V)	ASRcell (Ωcm^2)		PDmax ($mWcm^{-2}$)
		EIS	I-V slope	
700	0.96	0.94	0.947	234
650	0.99	1.52	1.52	158
600	1.03	2.58	2.51	102
550	1.05	4.72	4.67	63

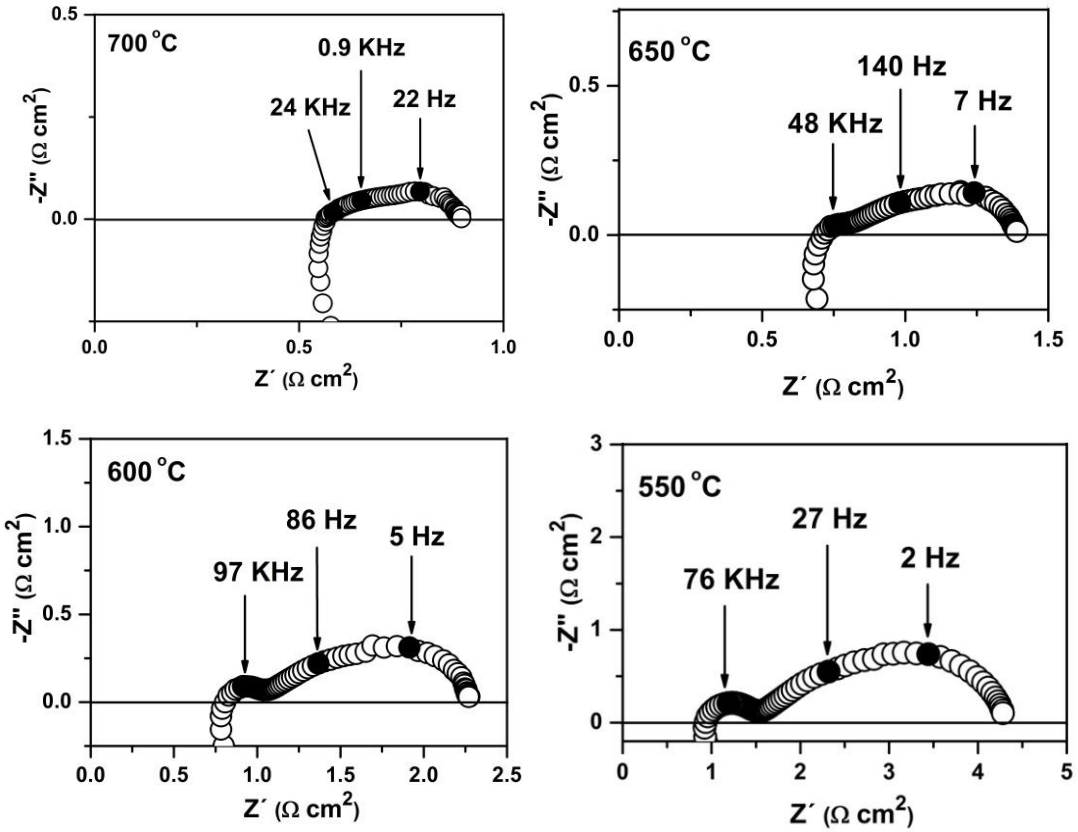

Figure 7.7. Electrochemical Impedance Spectra (EIS) of Ni-BZY/BCZY44/$Pr_2NiO_{4+\delta}$ single cell under open circuit conditions

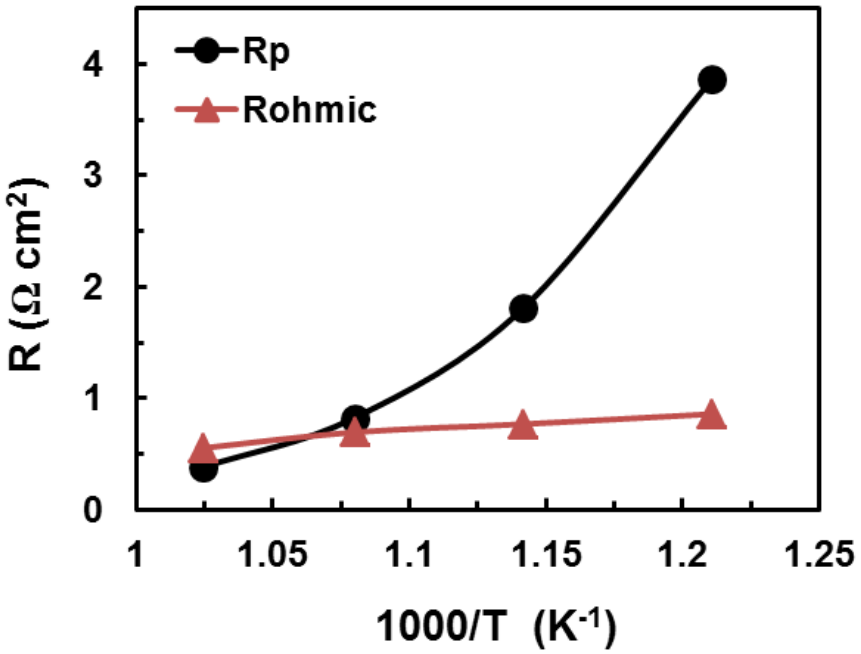

Figure 7.8. The polarization resistance (Rp) and ohmic resistance (Rohmic) of the Ni-BZY/BCZY44/$Pr_2NiO_{4+\delta}$ single cell at different temperatures under open circuit conditions (determined from impedance measurements)

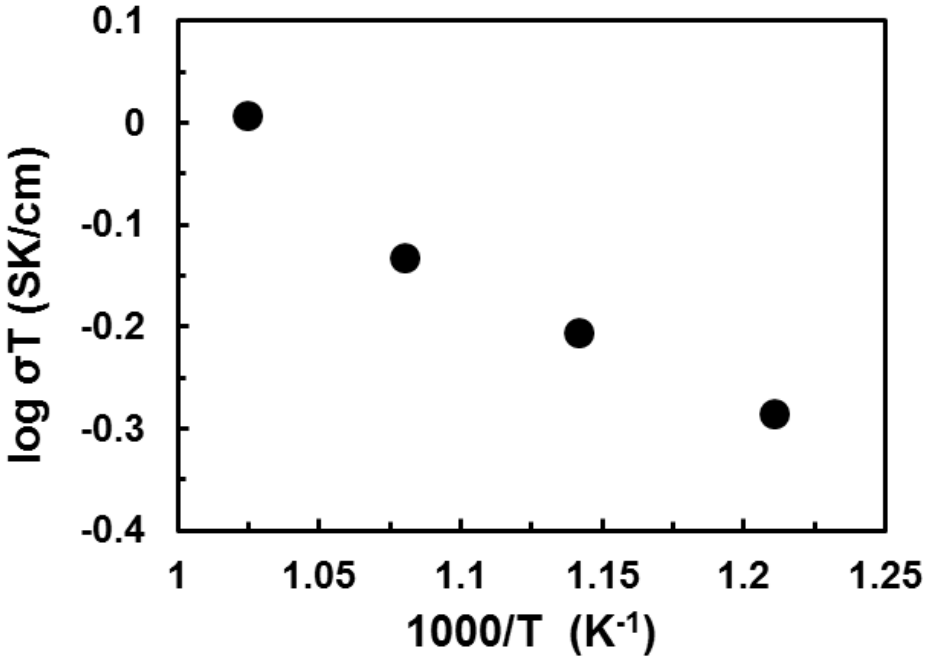

Figure 7.9. The total conductivity of thin BCZY44 electrolyte film measured as a function of temperature under fuel cell testing conditions

The time dependent stability of Ni-BZY/BCZY44/$Pr_2NiO_{4+\delta}$ single cell was monitored under a fixed potential of 0.75 V, Fig. 7.10. The cell was shown to be stable under these conditions for more than 18h, giving a stable current density of around 85 $mAcm^{-2}$ at 600 °C, Fig. 7.10. This result is in agreement with the post-mortem microstructural study, which demonstrated no delamination of cell layers or further cell microstructural degradation upon operation, Fig. 7.5.

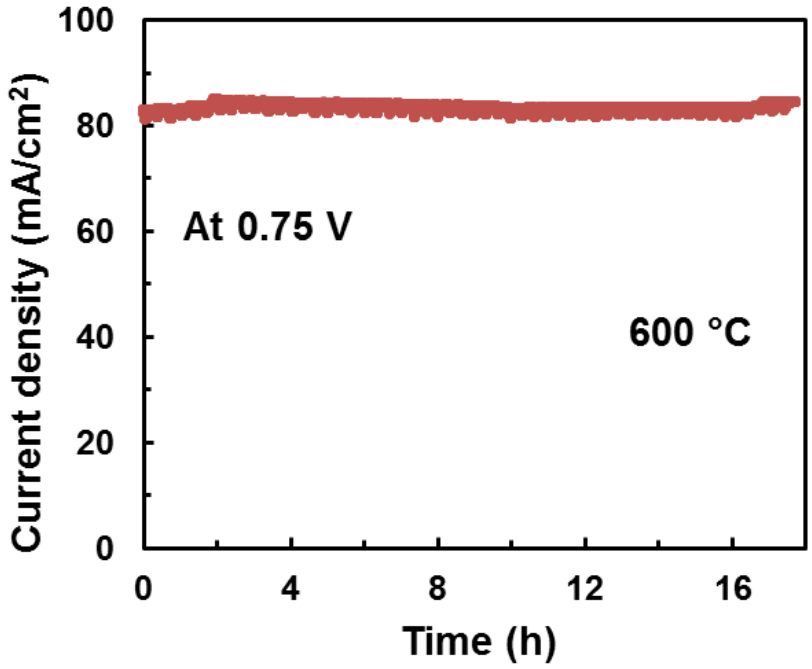

Figure 7.10. The time dependent current density of a single cell under constant potential of 0.75 V at 600 °C

7.3. Conclusions

A highly stable anode (Ni-BZY) supported thin BCZY44 electrolyte protonic ceramic fuel cell (PCFC) with $Pr_2NiO_{4+\delta}$ cathode was successfully fabricated by the spin coating technique. A dense electrolyte film of around ~5 μm in thickness was obtained by sintering at 1450 °C without using any sintering additives. No delamination or cracks could be observed at anode/electrolyte or electrolyte/cathode interface and good adherence of each layer was achieved. The electrochemical performance of the cell showed promising results, achieving higher maximum current densities than previous, analogous Ni-BZY anode supported cells reported in the literature. Maximum power densities of 234, 158, 102

and 63 mW/cm^2 at 700, 650, 600 and 550 °C respectively was achieved on Ni-BZY/BCZY44/$Pr_2NiO_{4+\delta}$ single cell under fuel cell testing condtions, with open circuit voltages (OCV) 0.96, 0.99, 1.03 and 1.05 V at 700, 650, 600 and 550 °C, respectively. The thin BCZY44 electrolyte thickness allows the performance of cell to be dominated by electrode polarisation losses at lower temperatures, even for values of electrode polarisation resistance that are competative with those of the literature. The single cell was stable for more than 18h under operation at a fixed potential of 0.75 V at 600 °C. The thin film Ni-BZY/BCZY44/$Pr_2NiO_{4+\delta}$ single cell, therefore, shows highly promising results, where tailoring of the electrode performance must now be improved.

7.4 References

[1] Stambouli AB, Traversa E. Solid oxide fuel cells (SOFCs): a review of an environmentally clean and efficient source of energy. Renewable Sustainable Energy Rev. 2002;6:433-55.

[2] Coors WG. Protonic ceramic fuel cells for high-efficiency operation with methane. J Power Sources. 2003;118:150-6.

[3] Shimada H, Li X, Hagiwara A, Ihara M. Proton-Conducting Solid Oxide Fuel Cells with Yttrium-Doped Barium Zirconate for Direct Methane Operation. J Electrochem Soc. 2013;160:F597-F607.

[4] Lin Y, Ran R, Guo Y, Zhou W, Cai R, Wang J, et al. Proton-conducting fuel cells operating on hydrogen, ammonia and hydrazine at intermediate temperatures. Int J Hydrogen Energy. 2010;35:2637-42.

[5] Fabbri E, Pergolesi D, Traversa E. Materials challenges toward proton-conducting oxide fuel cells: a critical review. Chem Soc Rev. 2010;39:4355-69.

[6] Kreuer KD. Proton-Conducting oxides. Ann Rev Mater Res. 2003;33:333-59.

[7] Fabbri E, Depifanio A, Dibartolomeo E, Licoccia S, Traversa E. Tailoring the chemical stability of $Ba(Ce_{0.8-x}Zr_x)Y_{0.2}O_{3-\delta}$ protonic conductors for Intermediate Temperature Solid Oxide Fuel Cells (IT-SOFCs). Solid State Ionics. 2008;179:558-64.

[8] Dias PAN, Nasani N, Horozov TS, Fagg DP. Non-aqueous stabilized suspensions of $BaZr_{0.85}Y_{0.15}O_{3-\delta}$ proton conducting electrolyte powders for thin film preparation. J Eur Ceram Soc. 2013;33:1833-40.

[9] Guo Y, Lin Y, Ran R, Shao Z. Zirconium doping effect on the performance of proton-conducting $BaZr_yCe_{0.8-y}Y_{0.2}O_{3-\delta}$ ($0.0 \leq y \leq 0.8$) for fuel cell applications. J Power Sources. 2009;193:400-7.

[10] Luisetto I, Licoccia S, D'Epifanio A, Sanson A, Mercadelli E, Di Bartolomeo E. Electrochemical performance of spin coated dense $BaZr_{0.80}Y_{0.16}Zn_{0.04}O_{3-\delta}$ membranes. J Power Sources. 2012;220:280-5.

[11] Tao S, Irvine JTS. A Stable, Easily Sintered Proton- Conducting Oxide Electrolyte for Moderate-Temperature Fuel Cells and Electrolyzers. Adv Mater. 2006;18:1581-4.

[12] Tao S, Irvine JTS. Conductivity studies of dense yttrium-doped $BaZrO_3$ sintered at 1325 °C. J Solid State Chem. 2007;180:3493-503.

[13] Soares HS, Zhang X, Antunes I, Frade JR, Mather GC, Fagg DP. Effect of phosphorus additions on the sintering and transport properties of proton conducting $BaZr_{0.85}Y_{0.15}O_{3-\delta}$. J Solid State Chem. 2012;191:27-32.

[14] Ricote S, Bonanos N. Enhanced sintering and conductivity study of cobalt or nickel doped solid solution of barium cerate and zirconate. Solid State Ionics. 2010;181:694-700.

[15] Choi SM, Lee J-H, Ji HI, Yoon KJ, Son J-W, Kim B-K, et al. Fabrication and characterization of $Ba(Zr_{0.84}Y_{0.15}Cu_{0.01})O_{3-\delta}$ electrolyte-based protonic ceramic fuel cells. Ceram Int. 2013;39:9605-11.

[16] Fabbri E, Bi L, Pergolesi D, Traversa E. Towards the next generation of solid oxide fuel cells operating below 600 °C with chemically stable proton-conducting electrolytes. Adv Mater. 2012;24:195-208.

[17] Nasani N, Dias PAN, Saraiva JA, Fagg DP. Synthesis and conductivity of $Ba(Ce,Zr,Y)O_{3-\delta}$ electrolytes for PCFCs by new nitrate-free combustion method. Int J Hydrogen Energy. 2013;38:8461-70.

[18] Koji K, Yoshirou K, Tetsuo S, Hiroyasu I. Protonic conduction in Zr-substituted $BaCeO_3$. Solid State Ionics. 2000;138:91-8.

[19] Ma X, Dai J, Zhang H, Reisner DE. Protonic conductivity nanostructured ceramic film with improved resistance to carbon dioxide at elevated temperatures. Surf Coat Technol. 2005;200:1252-8.

[20] Pornprasertsuk R, Piyaworapaiboon M, Jinawath S. Fabrication of Y-doped barium cerium zirconate thin films by electrostatic spray deposition technique for protonic ceramic fuel cell application. Ceram Int. 2014;40:9319-26.

[21] Guo Y, Ran R, Shao Z. Optimizing the modification method of zinc-enhanced sintering of $BaZr_{0.4}Ce_{0.4}Y_{0.2}O_{3-\delta}$-based electrolytes for application in an anode-supported protonic solid oxide fuel cell. Int J Hydrogen Energy. 2010;35:5611-20.

[22] Liu Y, Guo Y, Ran R, Shao Z. A novel approach for substantially improving the sinterability of $BaZr_{0.4}Ce_{0.4}Y_{0.2}O_{3-\delta}$ electrolyte for fuel cells by impregnating the green membrane with zinc nitrate as a sintering aid. Journal of Membrane Science. 2013;437:189-95.

[23] Liu Y, Guo Y, Wang W, Su C, Ran R, Wang H, et al. Study on proton-conducting solid oxide fuel cells with a conventional nickel cermet anode operating on dimethyl ether. J Power Sources. 2011;196:9246-53.

[24] Steele BCH, Heinzel A. Materials for fuel-cell technologies. Nature. 2001;414:345-52.

[25] Bi L, Fabbri E, Traversa E. Effect of anode functional layer on the performance of proton-conducting solid oxide fuel cells (SOFCs). Electrochem Commun. 2012;16:37-40.

[26] Rainwater BH, Liu M, Liu M. A more efficient anode microstructure for SOFCs based on proton conductors. Int J Hydrogen Energy. 2012;37:18342-8.

[27] Narendar N, Ramasamy D, Brandão AD, Yaremchenko AA, Fagg DP. The impact of porosity, pH_2 and pH_2O on the polarisation resistance of Ni-$BaZr_{0.85}Y_{0.15}O_{3-\delta}$ cermet anodes for Protonic Ceramic Fuel Cells (PCFCs). Int J Hydrogen Energy.39:21231–41.

[28] Narendar N, Mather GC, Dias PAN, Fagg DP. The importance of phase purity in Ni–$BaZr_{0.85}Y_{0.15}O_{3-\delta}$ cermet anodes – novel nitrate-free combustion route and electrochemical study. RSC Adv. 2013;3:859.

[29] Nasani N, Wang Z-J, Willinger MG, Yaremchenko AA, Fagg DP. In-situ redox cycling behaviour of Ni–$BaZr_{0.85}Y_{0.15}O_{3-\delta}$ cermet anodes for Protonic Ceramic Fuel Cells. Int J Hydrogen Energy. 2014;39:19780-8.

[30] Narendar N, Devaraj R, Antunes I, Perez J, Fagg DP. Electrochemical behaviour of Ni-BZO and Ni-BZY cermet anodes for Protonic ceramic fuel cells (PCFCs) - A comparative study. Electrochim Acta. DOI: 10.1016/j.electacta.2014.12.094.

[31] Sun W, Yan L, Shi Z, Zhu Z, Liu W. Fabrication and performance of a proton-conducting solid oxide fuel cell based on a thin $BaZr_{0.8}Y_{0.2}O_{3-\delta}$ electrolyte membrane. J Power Sources. 2010;195:4727-30.

[32] Dailly J, Marrony M, Taillades G, Taillades-Jacquin M, Grimaud A, Mauvy F, et al. Evaluation of proton conducting BCY10-based anode supported cells by co-pressing method: Up-scaling, performances and durability. J Power Sources. 2014;255:302-7.

[33] Azimova MA, McIntosh S. Properties and Performance of Anode-Supported Proton-Conducting $BaCe_{0.48}Zr_{0.4}Yb_{0.1}Co_{0.02}O_{3-\delta}$ Solid Oxide Fuel Cells. J Electrochem Soc. 2010;157:B1397.

[34] Zunic M, Chevallier L, Di Bartolomeo E, D'Epifanio A, Licoccia S, Traversa E. Anode Supported Protonic Solid Oxide Fuel Cells Fabricated Using Electrophoretic Deposition. Fuel Cells. 2011;11:165-71.

[35] Pergolesi D, Fabbri E, Traversa E. Chemically stable anode-supported solid oxide fuel cells based on Y-doped barium zirconate thin films having improved performance. Electrochem Commun. 2010;12:977-80.

[36] Shim JH, Park JS, An J, Gür TM, Kang S, Prinz FB. Intermediate-Temperature Ceramic Fuel Cells with Thin Film Yttrium-Doped Barium Zirconate Electrolytes. Chem Mater. 2009;21:3290-6.

[37] Bi L, Fabbri E, Sun Z, Traversa E. $BaZr_{0.8}Y_{0.2}O_{3-\delta}$-NiO Composite Anodic Powders for Proton-Conducting SOFCs Prepared by a Combustion Method. J Electrochem Soc. 2011;158:B797.

[38] Sun Z, Fabbri E, Bi L, Traversa E, Koc R. Electrochemical Properties and Intermediate-Temperature Fuel Cell Performance of Dense Yttrium-Doped Barium Zirconate with Calcium Addition. J Am Ceram Soc. 2012;95:627-35.

[39] Robinson S, Manerbino A, Grover Coors W, Sullivan NP. Fabrication and Performance of Tubular, Electrode-Supported $BaCe_{0.2}Zr_{0.7}Y_{0.1}O_{3-\delta}$ Fuel Cells. Fuel Cells. 2013;13:584-91.

[40] Taillades G, Dailly J, Taillades-Jacquin M, Mauvy F, Essouhmi A, Marrony M, et al. Intermediate Temperature Anode-Supported Fuel Cell Based on $BaCe_{0.9}Y_{0.1}O_3$ Electrolyte with Novel Pr_2NiO_4 Cathode. Fuel Cells. 2010;10:166-73.

Chapter 8

Conclusions and Future work

Owing to their high electrocatalytic activity towards fuel oxidation (in the present case hydrogen) nickel cermet anodes Ni-BZY were chosen as state-of-the-art materials for protonic ceramic fuel cell (PCFC) applications. In PCFCs, cermet anodes play a crucial role in the hydrogen oxidation reaction by elongating the three phase boundary length (TPB) at the anode/electrolyte interface since both nickel and proton conducting ceramic phases are considered as proton carriers, while only the Ni-phase is electronically conducting. Thus, the main emphasis of this thesis was to understand the behaviour of PCFC anodes and their characteristics. The anodes were characterized electrochemically by electrochemical impedance spectroscopy as a function of T, pH_2, pH_2O, porosity, composition, phase purity and when applied in a complete fuel cell.

The state-of-the-art phase pure Ni-BZY cermet anodes were prepared by a novel acetate-H_2O_2 combustion method as outlined in chapter 3. The advantages of this new combustion route and the importance of phase pure PCFC anodes were highlighted by comparison with anodes prepared by traditional nitrate-glycine combustion route on resultant polarisation behaviour. The important feature of this acetate combustion route is that avoids the decomposition of pre-prepared BZY powders, in contrast to the classical nitrate method where $Ba(NO_3)_2$ forms as an impurity phase in the precursor gel. The presence of this impurity subsequently leads to the formation of a BaY_2NiO_5 impurity phase in the anode. A range of Ni-BZY cermet anodes were studied with 20, 30, 40 and 50 vol% Ni content and percolation behaviour is achieved for Ni contents equal to or greater than 40 vol%. The electrochemical impedance spectrum for electrode polarisation appeared to consist of two main arcs R2, at high frequency, and R3, at low frequency at 600 °C. The R2 and R3 polarisation resistances are shown to be associated with proton transport in the oxide cermet phase and limiting charge transfer at the electrode surface, respectively.

The effect of anode porosity and atmosphere on the polarisation behaviour of PCFC Ni-BZY cermet anodes has been elaborated. The PCFC cermet anode with 34% porosity

(formed without porogen) shows lower polarisation resistance (Rp) values than anodes of higher porosity fabricated using porogens. This result is, therefore, contrary to the well-known oxide-ion conducting SOFC anodes in which much higher levels of porosity are required for optimal performance. The electrochemical results reveal that anodes show only a weak dependence of polarization resistance on pH_2O, but, in contrast, are highly pH_2 sensitive. The strong pH_2 dependence arises from the lower frequency R3 term that manifests a strong negative dependence on pH_2. The strong negative pH_2 dependence of unity of the R3 term has been related to the dissociative adsorption of H_2 on the anode surface. In contrast, the higher frequency polarization response, R2, is suggested be related to the migration of protons across the electrode/electrolyte interface at the TPB, with low atmosphere dependence but significant dependence on microstructure. These results draw parallels to that observed in oxide-ion conducting SOFC anodes.

During the PCFC operation, the cell may undergo several redox cycles if there is any fuel interruption or system shutdown. The *in-situ* redox cycling behavior of PCFC cermet anodes was also investigated under reducing and air atmospheres. The electrochemical impedance spectra show that both the high frequency, R2 and low frequency, R3 terms were increased by redox cycling. The ohmic resistance (Rohmic) was also increased due to delamination at anode/electrolyte interface, as confirmed by SEM analysis and micro-cracks were found after redox cycling. Environmental scanning electron microscopy (ESEM) analysis highlights that these micro-cracks and delamination formed due to the volume expansion of the Ni-cermet phase upon re-oxidation. The mechanism of anode cermet degradation upon redox cycling in PCFC anodes is shown to be very similar to that observed in the well-known oxide-ion conducting SOFC anodes. As such, a rapid depletion in performance is observed in peak performing PCFC anodes of low porosity upon redox cycling, despite their high initial connectivity and the potential for proton migration in both cermet phases.

The involvement of proton conducting ceramic oxide phase in cermet anode was studied by comparing the anode with a proton-conducting phase Ni-BZY to anode with non-proton conducting phase Ni-BZO. The impedance spectrum of Ni-BZO has shown three arcs at high frequency R2, middle frequency R3 and low frequency R4. The appeared

extra arc R4 was considered to be related to the diffusion polarization since R4 was shown to be reduced in 10%H_2/He atmospheres in comparison to that of 10%H_2/N_2 due to the significantly lower diffusion volume of He than N_2. The R2 and Rp, values of Ni-BZY were shown to be lower than that of Ni-BZO, under standard operating conditions, whereas for R3 this trend was reversed. These studies highlight that the R2 term is strongly related to level of proton conductivity in the ceramic oxide phase of the cermet anode.

Finally, the electrochemical performance and durability of anode Ni-BZY supported thin BCZY44 electrolyte with Pr_2NiO_4 cathode protonic ceramic fuel cell was evaluated for a peak performing Ni-$BaZr_{0.85}Y_{0.15}O_{3-\delta}$ anode, formed without porogen. A dense electrolyte film of around ~5 µm in thickness was obtained by sintering at 1450 °C without using any sintering additives by the spin coating method. A good compatibility and adherence between three components were observed. Maximum power densities of 234, 158, 102 and 63 mW/cm^2 at 700, 650, 600 and 550 °C, respectively were achieved for the Ni-BZY supported cell cell under fuel cell testing condtions, with open circuit voltages (OCV) 0.96, 0.99, 1.03 and 1.05 V at 700, 650, 600 and 550 °C, respectively. The cell was limited by electrode polarisation losses. Discussion relates this limitation to mainly the cathode behviour and, thus, may be overcome by further studies using a suitable proton and electron mixed conducting cathode. Nonetheless, this single cell showed promising results, with higher power densities offered than previous Ni-BZY supported cells in the literature. So far in our lab, such anode supported single cells have been fabricated up to a 2.5 cm cell size diameter by the spin coating method.

The nitrate-free combustion route, is a simple, low cost and rapid process to synthesize ceramic materials not only high-purity PCFC cermet anodes but also electrolyte materials as outlined in Appendix A.

The fundamental understanding on PCFC anodes that we explored in this thesis can be considered highly beneficial to PCFC community especially the fundamental information provided on anode electrochemical behaviour, effect of porosity and redox results. The inverse limitations of cell performance and redox cycling stability on porosity can be considered to be highly detrimental to practical exploitation of PCFCs in carbonaceous fuels. Thus, the study of methods to improve redox stability can be considered to be imperative before PCFCs may become commercially feasible.

The future work will be focussed on testing the performance of anode supported protonic ceramic electrochemical devices on wide range of carbonaceous and non-carbonaceous fuels such as, hydrocarbons, biogas, methanol, ammonia etc. and the durability of these devices in terms of long term stability.

Appendix-A

Synthesis and conductivity of $Ba(Ce,Zr,Y)O_{3-\delta}$ electrolytes for PCFCs by new nitrate-free combustion method ‡

Abstract

A new acetate-H_2O_2 combustion method was developed to synthesize $BaCe_{0.8-x}Zr_xY_{0.2}O_{3-\delta}$ (x = 0, 0.1, 0.4, 0.6 and 0.8) electrolyte membranes for proton ceramic fuel cells (PCFCs). The new method offers a cost effective, simple and environmentally friendly preparation route, which avoids the emission of NOx gases that are typical of traditional nitrate precursor routes. The route should also be applicable for the synthesis of other multi-element ceramic-oxide materials. Phase purity, compositional accuracy and powder morphology were investigated by X-ray diffraction analysis (XRD) and scanning electron microscopy (SEM) respectively. The novel combustion route produces powders with a fine crystallite size of 10-20 nm as synthesized, and 30-60 nm calcined. The presence of an intermediate peroxy (-OOH) bond has been identified by FT-IR and is suggested to aid the combustion reaction by harnessing the required oxidant in the form of labile peroxide complexes. The proton conductivities of the formed $BaCe_{0.8-x}Zr_xY_{0.2}O_{3-\delta}$ electrolytes were measured in the temperature range of 100-900 °C under wet N_2 atmosphere and shown to correspond with literature data.

‡ This Chapter has been published as Nasani N, Dias PAN, Saraiva JA, Fagg DP. Synthesis and conductivity of $Ba(Ce,Zr,Y)O_{3-\delta}$ electrolytes for PCFCs by new nitrate-free combustion method. Int J Hydrogen Energy. 2013;38:8461-70.

A.1. Introduction

Solid oxide fuel cells (SOFCs offer a low-pollution technology to generate electricity electrochemically with high efficiency [1]. It has been noted that reduction of the SOFC operating temperature to the range of 400-700°C would be desirable to reduce fabrication costs and overall improve durability [2]. This aim may be facilitated by the use of high temperature proton-conducting ceramics as electrolytes, due to their larger ionic conductivities at these temperatures than conventional oxide-ion conducting electrolytes [2, 3]. Moreover, proton-ceramic fuel cells (PCFCs) offer the advantage that they form water at the cathode and, hence, the fuel does not become diluted during cell operation, in contrast to oxide-ion conducting SOFCs [4-6]. To date, acceptor doped $BaCeO_3$ and $BaZrO_3$ perovskite materials have dominated the research field of high temperature proton conductors. Although doped $BaCeO_3$ materials exhibit the larger total conductivities, they have been shown to be chemically unstable in H_2O and CO_2-containing atmospheres, resulting in electrolyte degradation and difficult fuel cell deployment [1, 7]. In contrast, doped $BaZrO_3$ materials are regarded as potential candidates for electrolytes in PCFCs as they show an excellent chemical stability against H_2O and CO_2, as well as high bulk proton conductivity [5, 7, 8]. Nonetheless, the sinterability of BZY is notoriously poor, necessitating extremely high temperatures (~1600–1800 °C) to densify $BaZrO_3$ electrolyte membranes. Such high temperatures commonly lead to Ba evaporation, which can reduce conductivity. Moreover, these elevated temperatures can also seriously complicate cell fabrication by typical co-sintering techniques due to elemental inter-diffusion between components [8-10].

The chemical stability of barium cerates can be increased by the introduction of zirconium (e.g. $Ba(Ce,Zr)_{1-y}Y_yO_{3-\delta}$). However, this advantage comes at the cost of the level of total conductivity. Despite this limitation, it has been shown that upon adjustment the Ce:Zr ratio, one can achieve a compromise between the achievement of chemical and mechanical stability, while still retaining adequate conductivity for practical application [11-21]. Several synthesis procedures have been suggested in the literature for the preparation of $Ba(Ce,Zr)_{1-y}Y_yO_{3-\delta}$ materials including solid-state [17, 18, 21], glycine-nitrate combustion [3, 13-15, 17-19, 21], sol-gel [12, 14, 15] and pechini methods [19].

The poor suitability of the solid state route for the production of these materials was reported by Sawant et al. [19], who highlighted that pure perovskite phases could only be obtained after multiple regrinding and refiring steps to ensure homogeneity. Contrary to conventional solid-state synthesis, solution-based soft chemical synthesis routes offer more homogeneous, uniform mixing of the precursors at the atomic-level. Moreover, in the solution state, the oxidation state of the metal ions can be stabilized [19]. Nonetheless, all the previously reported soft chemical synthesis routes, glycine-nitrate combustion [3, 13-15, 17-19, 21], sol-gel [12, 14, 15] and pechini [19] have traditionally used metal nitrate precursors. These nitrate precursors release copious amounts of NO_x gases during the synthesis that are harmful to the environment, especially at the industrial scale. In addition, many of these solution-based routes often require expensive chemical precursors [11, 13-15, 19]. Thus, herein we report a new, simple and environmentally friendly acetate-H_2O_2 combustion process for the synthesis of multi-element ceramic oxide materials, such as BCZY electrolyte membranes, that avoids the use of polluting nitrate precursors. In addition, cost effective metal acetates and 30% H_2O_2 are only required as the starting precursors for this combustion synthesis.

The major difference between the traditional glycine-nitrate and the novel acetate-H_2O_2 combustion route, here described, is that the metallic precursors represent the fuel in the current process (metal acetates), whereas they represent the oxidant (metal nitrates) in traditional nitrate-based combustion processes. The main advantage of the new acetate-H_2O_2 combustion is that the pH of solution formed by acetate-H_2O_2 precursors is neutral and, therefore, does not require the addition of any further base to increase the pH of the solution. In contrast, the nitrate-glycine combustion process forms metal chelates with the corresponding metal cations with amino and carboxylic group present in glycine [12], forming an acidic resultant solution. Consequently, additional amounts of base (NH_4OH) are commonly added in the nitrate-glycine process to attempt to counter this factor and increase the pH of the final solution [11, 12, 15, 22-25]. Unfortunately, these additions further increase undesired NOx emissions. One should further be aware that the traditional nitrate based combustion route has also been reported to be inadequate for the formation of stoichiometrically correct barium zirconate materials [5]. The current work, therefore, aims to demonstrate a new acetate-H_2O_2 microwave assisted combustion synthesis that can offer

an advantageous, environmentally friendly and economical substitute for traditional nitrate-glycine preparation routes of $Ba(Ce,Zr)_{1-y}Y_yO_{3-\delta}$ proton-conducting electrolyte membranes, while confirming phase purity and retention of reported electrochemical behaviour.

A.2. Experimental Section

A.2.1 Materials Synthesis

$BaCe_{0.8-x}Zr_xY_{0.2}O_{3-\delta}$ (BCZY) electrolytes (x =0, 0.1, 0.4, 0.6 and 0.8) were synthesized by the new nitrate-free acetate-H_2O_2 combustion method as summarized in Fig. A.1. This new method was originally suggested by our group for nickel distribution in cermet-anode materials for proton ceramic fuel cells, as described elsewhere [25]. The current work now extends this knowledge to show that this technique is also valid for the formation of quaternary metal oxides. The samples are given the nomenclature BCZYab, where a and b represent the amount of cerium and zirconium respectively, e.g. $BaCe_{0.7}Zr_{0.1}Y_{0.2}O_{3-\delta}$≡ BCZY71.

$Ba(CH_3COO)_2$ (>99.9% pure, Sigma Aldrich), Zr(IV) $(CH_3COO)_x$ $(OH)_y$ (99.9% pure, Sigma Aldrich), $Ce(CH_3COO)_3$ $.1.5H_2O$ (99.9% pure, Alfa Aesar), $Y(CH_3COO)_3$ $.4H_2O$ (99.9% pure, Alfa Aesar) and 30% H_2O_2 (RiedeldeHaen, 30% by weight) were used as starting materials for the combustion method. Stoichiometric amounts of the metal acetates were dissolved in distilled water with constant stirring at 25 °C to obtain a clear, transparent solution. To the solution 30 % H_2O_2 was added slowly to achieve a fuel to oxidant ratio of unity as per the propellant chemistry [26]. An orange-brown color solution with bubbles was observed for cerium containing compositions. The solution was heated on a hot plate at 80 °C with constant stirring to form a viscous gel. During heating the orange-brown color converts to pale yellow. The viscous gel was then subjected to microwave heating, under rotation, in a domestic 2.45 GHz, 800W microwave oven set at the maximum power. After a few minutes, the dried gel burnt with a flame in a self-propagating combustion manner, releasing plentiful fumes, to form a black powder (for cerium containing compounds). The combustion powder was calcined at 1100 or 1350 °C for 6h in order to obtain the pure perovskite phase. Calcined powders were isostatically

pressed at 200 MPa and sintered at 1500 °C for 8h with a heating and cooling rates of 5 °C/min to produce dense bars for electrochemical measurements of approx. size 13 mm× 3mm × 4mm. Density measurements were performed by direct measurements of sample mass and geometry.

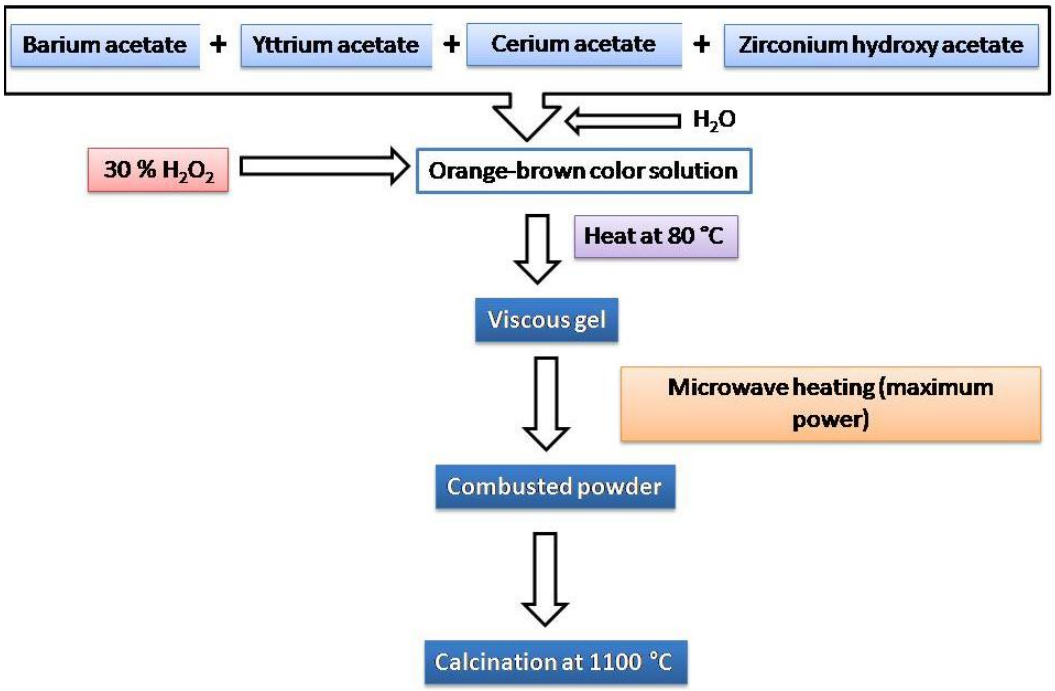

Figure A.1. A schematic representation of acetate-H_2O_2 combustion synthesis

A.2.2. Materials Characterization

Phase purity was confirmed by X-ray diffraction (XRD) using a Philips X´Pert diffractometer, Detector X'Celerator, Active length 2.5460º, step width 0.02° and counting time 30s / step. Lattice parameters were calculated by the Rietveld method using the Fullprof software [27]. The morphology of powders and surface of sintered pellets was investigated by using Scanning Electron Microscopy (SEM) (model Hitachi SU-70). The average crystallite size of the calcined powders was determined by using the Scherrer formula [28], where the experimental peak width was corrected using a LaB_6 standard reference.

$$D = \frac{0.9\lambda}{\beta\cos\theta} \qquad (A.1)$$

Where D is the crystallite size (nm), λ is the wavelength of X-ray radiation, θ is the angle of XRD peak, β is the full width half maximum (FWHM) of the diffraction peak (in radians). All particles were assumed to be spherical.

Infrared Spectroscopy (IR) was used to analyze the effect of H_2O_2 on cerium containing perovskites. Fourier transform infrared spectra of composition BCZY44 (before and after combustion) were obtained using a Bruker Tensor 27 FT-IR spectrometer, mixing the sample with KBr (Aldrich, 99%, FT-IR grade).

A.2.3 Electrical Measurements

Pt paste was painted on each end of dense bar shaped samples and sintered at 900 °C for 15 min. AC conductivity was measured under humidified N_2, using an impedance analyzer Electrochemie-Autolab PGSTAT302N (frequency range 0.1 Hz-1MHz) or Novocontrol Alpha-ATB analyzer (frequency range of 0.1 Hz- 40MHz), both with amplitude 50mV. Measurements were made at 50 °C intervals in the direction of decreasing temperature in the temperature range 900 – 100 °C. Data were corrected for stray capacitance, jig and lead resistance. Humidification was obtained by bubbling gases through water followed by a saturated KCl solution in contact with solid KCl, producing approximately 86% relative humidity at room temperature. Stability was confirmed by performing repeated impedance measurements at each temperature. Impedance spectra were fitted using the ZView software (Scribner Associates).

A.3. Results and Discussion

A.3.1 Phase analysis

XRD data of acetate-H_2O_2 combusted BCZY powders, calcined at 1100 °C, highlight the formation of the desired perovskite phase, Fig. A.2. Nevertheless, the presence of very small traces of $BaCO_3$ can be noted for some compositions at this

temperature. At the higher calcination temperature of 1350 ºC this trace $BaCO_3$ impurity is removed and a pure perovskite phase is obtained for all BCZY compositions, Fig. A.3. Note the achievement of phase purity in the current work is in contrast to that reported for the traditional nitrate-glycine combustion route, by Chien et al. [13]. These authors noted small impurity phases that persisted even after calcination at 1400 ºC. Although Chien et al. were unable to identify these impurity peaks, their position at 28º (2θ), may suggest that they correspond to the most intense (-1,1,1) reflection of monoclinic zirconia (baddeleyite: JCPDS file number 37-1484). The improved purity obtained in the current work was initially thought to be related to the new acetate combustion precursors used for the combustion reaction. However, as a control, a traditional glycene/nitrate synthesis, performed at a fuel/oxidant ratio of unity with an identical microwave assisted combustion technique, as described for the acetate process, also succeeded to achieve the formation of pure perovskite phases.

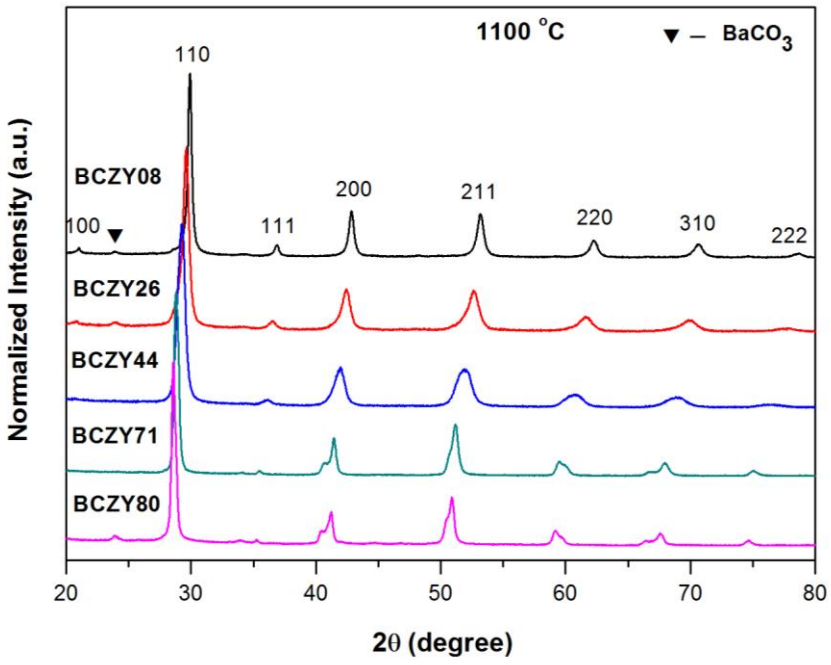

Figure A.2. XRD patterns of $BaCe_{0.8-x}Zr_xY_{0.2}O_{3-\delta}$ (BCZY) (X = 0, 0.1, 0.4, 0.6 and 0.8 powders calcined at 1100 °C

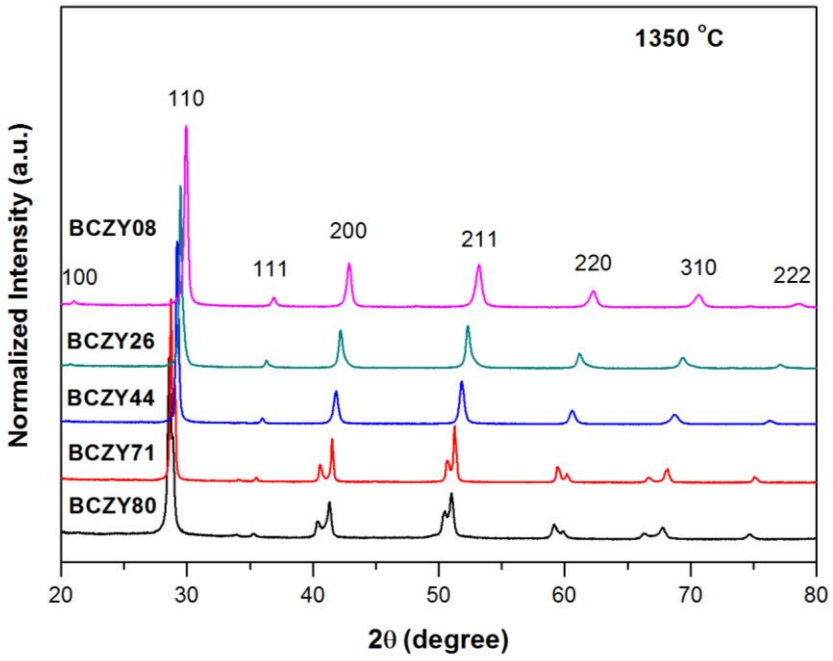

Figure A.3. XRD patterns of $BaCe_{0.8-x}Zr_xY_{0.2}O_{3-\delta}$ (BCZY) (X = 0, 0.1, 0.4, 0.6 and 0.8) powders calcined at 1350 °C

Fig. A.4 highlights this result for powders calcined at 1400 ºC for the two combustion techniques. Thus, the lower purity achieved by Chien et al. [13] is suggested to have probably arisen due to inefficient heat dispersion, characteristic of normal hotplate combustion reactions. In this respect, note the microwave technique used in the current work, has previously been shown to be beneficial for combustion reactions due to providing a homogenous reaction throughout the whole volume of the gel [22-25]. In contrast simple hot-plate reactions typically initiate the combustion reaction at the base of the gel in contact with the hotplate, with combustion subsequently propagating from this ignition point.

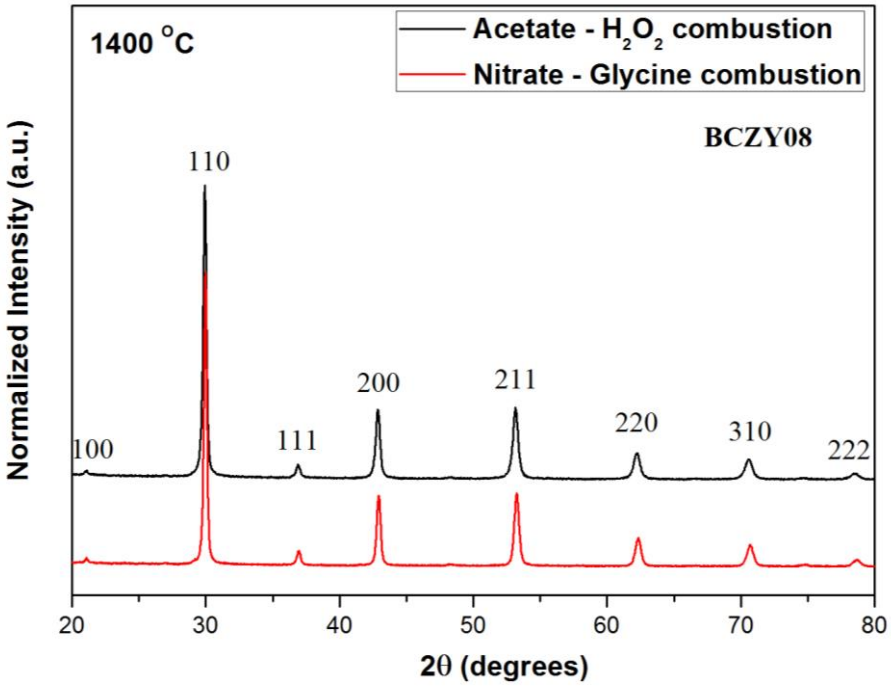

Figure A.4. XRD patterns of BCZY08 synthesized by both new acetate-H_2O_2 and nitrate-glycine combustion powder calcined at 1400 °C

The XRD data of the $BaCe_{0.8-x}Zr_xY_{0.2}O_{3-\delta}$ (BCZY) compositions show distinct peak shifts for the perovskite phase with changing composition. This trend is highlighted by the calculated unit cell volumes, which decrease with increasing Zr content, Table A.1. This is an expected trend, which is related to the larger ionic radius of Ce^{4+} (0.87 °A) in comparison with Zr^{4+} (0.72 °A). The compositions $BaCe_{0.8}Y_{0.2}O_{3-\delta}$ (BCY) and $BaCe_{0.7}Zr_{0.1}Y_{0.2}O_{3-\delta}$ (BCZY71) exhibit orthorhombic symmetry (Pnma), while all other compositions are cubic (Pm-3m) in agreement with the literature [3, 13-15, 17-19, 21]. Magrez et al. noted that the most suitable method of assessing compositional accuracy of this type of perovskite material was by lattice parameter assessment [5]. Thus, the very close match in lattice volumes of materials prepared by the novel acetate-combustion process and previous literature data of materials prepared by a sol gel method [19], Table A.1, highlights the accuracy and effectiveness of the current preparation method.

Table A.1: Lattice parameter and unit cell volume of $BaCe_{0.8-x}Zr_xY_{0.2}O_{3-\delta}$ materials synthesized by nitrate free acetate-H_2O_2 combustion method

x (Zr)	Lattice parameters (Å)			Space group	Unit cell volume	Lit. Unit cell volume[a]
	a	b	c		($Å^3$)	($Å^3$)
0	8.921	6.182	6.184	Pnma	341.03	-
0.1	8.859	6.160	6.162	Pnma	336.30	-
0.4	4.320	4.320	4.320	Pm-3m	80.61	79.67
0.6	4.268	4.268	4.268	Pm-3m	77.74	77.80
0.8	4.222	4.222	4.222	Pm-3m	75.29	74.84

[a] Comparison with literature unit cell volume data [15]

A.3.2 The multiple role of hydrogen peroxide (H_2O_2)

In the new acetate-H_2O_2 combustion synthesis of BCZY here presented, the principal role of hydrogen peroxide is that of an oxidant in the propellant chemistry. Nonetheless, the presence of H_2O_2 has also been reported to induce some intriguing effects when added to aqueous precursor solutions. H_2O_2 can alter the oxidation state of precursors, the mechanisms of reaction and the morphology of the resultant powders [29-36]. For example, several authors have noted such benefits in the preparation of nanocrystalline ceria [30, 35, 36]. The works, demonstrated H_2O_2 to offer a twofold action, i) to oxidize Ce^{3+} to the more easily hydrolysable Ce^{4+} oxidation state

$$Ce^{3+} + H_2O_2 + 2H^+ (aq.) \longrightarrow Ce^{4+} + 2H_2O + O_2 \qquad (A.2)$$

and ii) to form labile peroxide complexes that aid reaction in comparison to simple hydroxide precursors. Moreover, the presence of peroxo ligands is stated to disrupt the formation of compact M-O-M networks, to promote the formation of nanocrystallites during crystallization [30, 31]. Similar effects can be obtained in the synthesis of doped ceria, such as $Ce_{0.8}Sm_{0.2}O_{(1.9-x)}$ [34]. Moreover, H_2O_2 has also been shown to be effective

additive for the preparation of nanocrystalline ZrO_2 powders, where its presence has the additional effect to promote the formation of tetragonal crystallites [29, 32, 33].

For this reason, the role of H_2O_2 in the current acetate-H_2O_2 combustion synthesis was investigated by FT-IR spectroscopy for sample (BCZY44) before and after combustion, Fig. A.5. For the precursor sample, the FT-IR spectrum was recorded of a metal complex BCZY44 mixed solution that had been dried to form a gel at 80 °C. A broad absorption band can be located at 3400 cm^{-1} corresponding to the –OH stretching vibration of hydroxide intermediates. The absorption bands at nearly 1570 cm^{-1} can be attributed to the H_2O bending vibration [30], while the absorption peaks at 1000-550 cm^{-1} correspond to the presence of the metal oxides. The most significant feature is the presence of the hydroperoxyl ligand –OOH in the precursor gel that is confirmed by the stretching vibration observed at nearly 1400 cm^{-1} (represented, in Fig. A.5 by a dotted line). The low intensity of the -OOH band is probably associated to the aforementioned, liability of this bond. In this respect, note that Pappeccena et al. had used H_2O_2 in the co-precipitation synthesis of $Ce_{0.8}Sm_{0.2}0_{1.9-x,}$ however, these authors failed to identify the –OOH peak due to its short lifetime. After combustion, the –OOH peak is shown to be absent and only the –OH stretching vibration at 3400 cm^{-1} and the –C=O stretching vibration at nearly 1450 cm^{-1}can be identified, Fig. A.5. The presence of –C=O peak can be related to the formation of some $BaCO_3$ during combustion. Thus, the FT-IR spectroscopy confirms the participation of peroxide complexes in the acetate-H_2O_2 combustion mechanism.

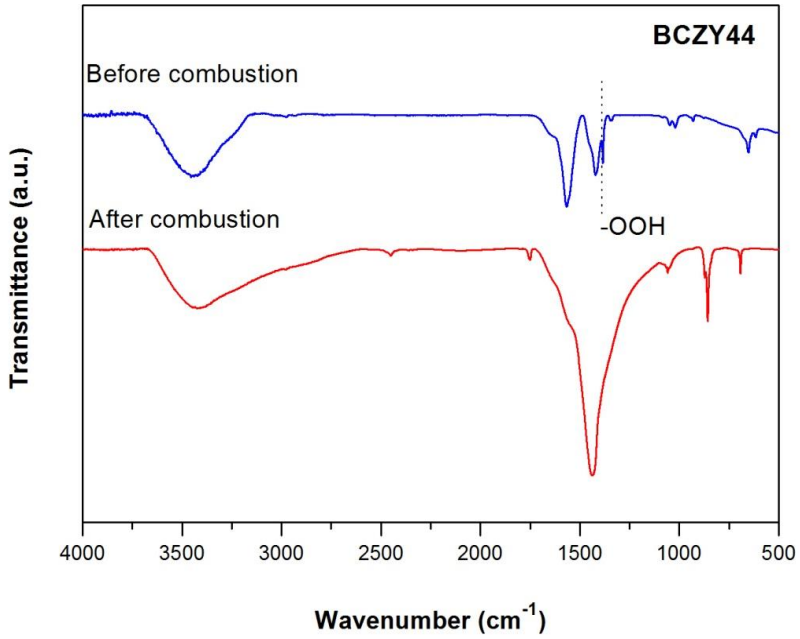

Figure A.5. FT-IR spectra of BCZY44 powder before and after combustion

The observance of an orange precipitate in the precursor solution is characteristic of the Ce(IV) hydroxyl peroxo species [35], while the yellow colour of the gel is characteristic of the presence of CeO_2 [35]. Thus, it appears that the presence of H_2O_2 in these precursor solutions may store oxygen both in the form of labile peroxide complexes and also by oxidation of cerium (III) to the (IV) oxidation state. Both these phenomenon are, therefore, typical effects that are expected on addition of H_2O_2 to such precursor solutions. Upon combustion, this stored oxygen would be liberated and is suggested to provide the required oxidant for the novel nitrate-free combustion reaction.

A.3.3 Microstructure and Morphology of the BCZY electrolytes

The microstructure and morphology of BCZY compounds were obtained by Scanning Electron microscopy (SEM). Fig. A.6 shows the morphology of as synthesized and calcined BZY powders at 1100 °C. After combustion the morphology of the powders presents a very small crystallite size in the nanometric range and these crystallites are agglomerated into micron-sized particles. The potential effect of H_2O_2 on crystallite size of BCZY powders were studied by XRD using the Scherrer formula. The average crystallite size of as synthesized and calcined powders (1250 ºC), were 10-20 nm and 30-60 nm

range, respectively. These values are similar to that of crystallite sizes reported for the traditional nitrate-glycine combustion process [13]. Thus, contrary to expectation, the formation of the intermediate peroxide species in the precursor combustion gel does not appear to have a beneficial effect to reduce powder crystallite size in the present case, unlike other soft chemical routes that involve H_2O_2 reported in the literature [29-36].

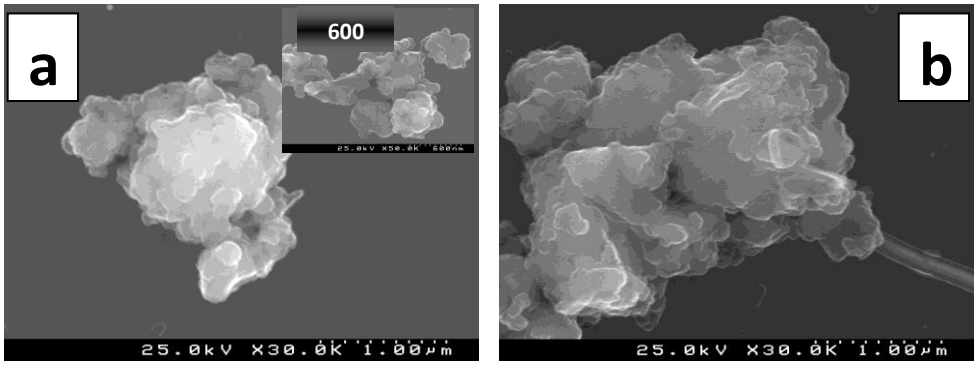

Figure A.6. Scanning electron micrographs of (a) as synthesized and (b) calcined at 1100 °C BCZY08 powder (inset: as synthesized BCZY08 nanopowder)

Fig. A.7 shows the unpolished surface micrographs of the BCZY pellets sintered at 1500 °C. The micrographs show the BCZY80, BCZY71 and BCZY44 pellets to be fully dense whereas BCZY26 and BCZY08 are significantly less dense after sintering at 1500 °C, Table A.2. The poor densificiation of materials of low cerium-content is a typical behaviour of this materials type. Dense zirconium-rich compounds can only be obtained only after sintering at high temperatures >1600 °C [4, 5, 7]. Table A.2 shows that, in general, average grain size decreases with increasing Zr-content, in agreement with that previously noted [14, 15, 17, 19].

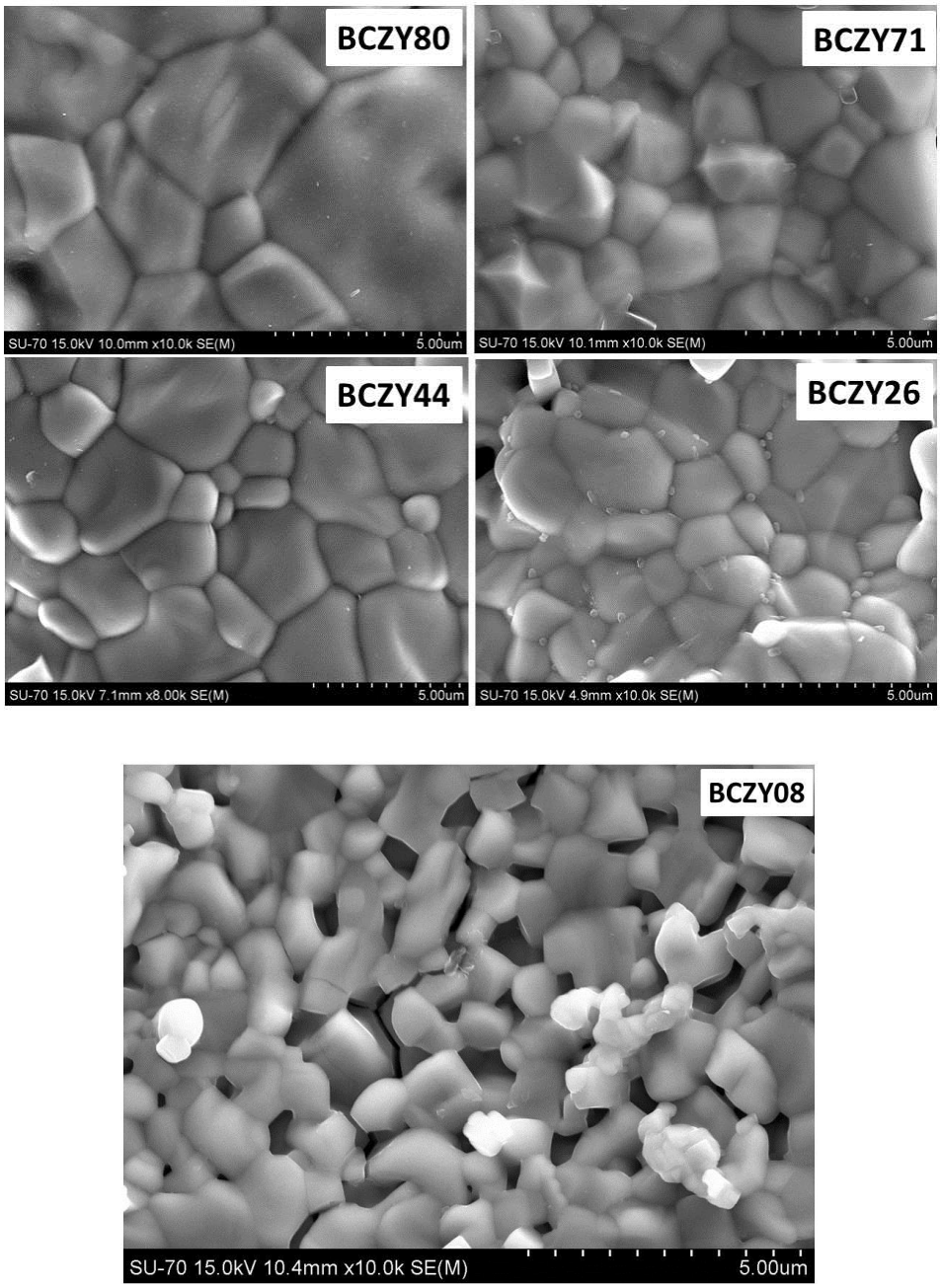

Figure A.7. Scanning electron micrographs of surface of BCZY pellets sintered at 1500 °C for 8h

A.3.4 Conductivity behavior

The conductivity behaviour of the series $BaCe_{0.8-x}Zr_xY_{0.2}O_{3-\delta}$ (x = 0.1, 0.4, 0.6) was assessed by A.C. impedance spectroscopy under wet N_2 atmosphere in the temperature range of 100-900 °C. The work focused on analysis of the intermediate compositions, $BaCe_{0.7}Zr_{0.1}Y_{0.2}O_{3-\delta}$ (BCZY71), $BaCe_{0.4}Zr_{0.4}Y_{0.2}O_{3-\delta}$ (BCZY44) and $BaCe_{0.2}Zr_{0.6}Y_{0.2}O_{3-\delta}$

(BCZY26) electrolytes to emphasize the applicability of the current synthesis route for the successful formation of quaternary perovskites. All studied compositions have densities ≥ 92% that of the theoretical, Table A.2.

Table A.2: Grain size and relative density of $BaCe_{0.8-x}Zr_xY_{0.2}O_{3-\delta}$ materials synthesized by nitrate free acetate-H_2O_2 combustion method, isostatically pressed at 200MPa and sintered at 1500 ºC for 8h.

x (Zr)	Relative Density	Grain size
	%	μm
0	98.5	4.73 ± 1.65
0.1	98	1.94 ± 0.63
0.4	96	2.61 ± 0.82
0.6	92	1.75 ± 0.51
0.8	82	0.97 ± 0.18

Example impedance spectra for these compositions are shown in Fig. A.8. Three distinct contributions can be observed and are ascribed to the bulk response, the grain boundary response and the electrode processes in the direction of decreasing frequency, as confirmed by their characteristic capacitance values, ~10^{-12}, 10^{-9}-10^{-10} and 10^{-5}-10^{-7} F/cm^2, respectively. The grain boundary response can be seen to dominate the impedance spectra, for all compositions, while the bulk response is only partially observable within the maximum frequency of the measurement at this temperature. The impedance spectra show characteristic shapes that correspond well to those previously reported for this type of material at similar temperatures and conditions [19]. An increasing dominance of the grain boundary phenomenon, over that of the bulk, is observed with increasing zirconium content.

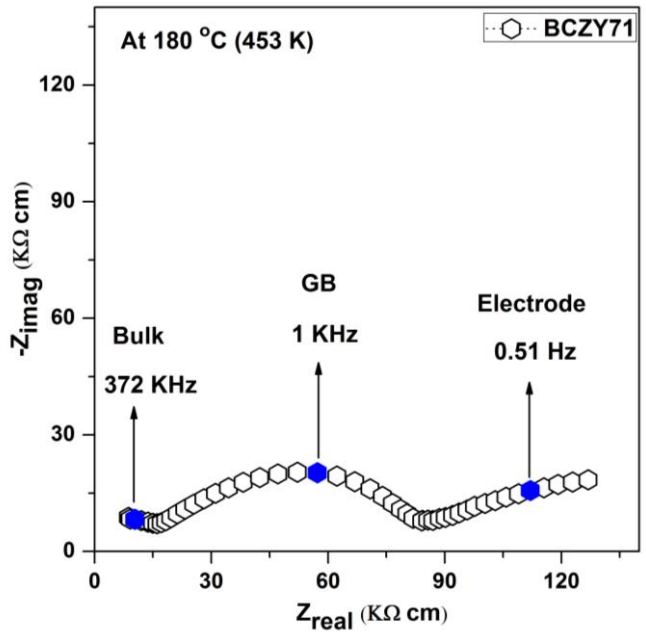
At 180 °C (453 K)
BCZY71
120
90
60
30
0
-Zimag (KΩ cm)
Bulk
372 KHz
GB
1 KHz
Electrode
0.51 Hz
0
30
60
90
120
Zreal (KΩ cm)

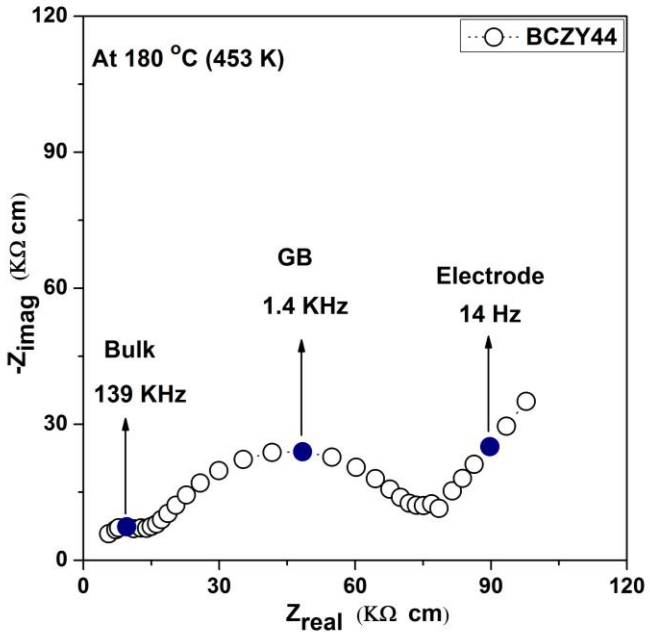
At 180 °C (453 K)
BCZY44
120
90
60
30
0
-Zimag (KΩ cm)
Bulk
139 KHz
GB
1.4 KHz
Electrode
14 Hz
0
30
60
90
120
Zreal (KΩ cm)

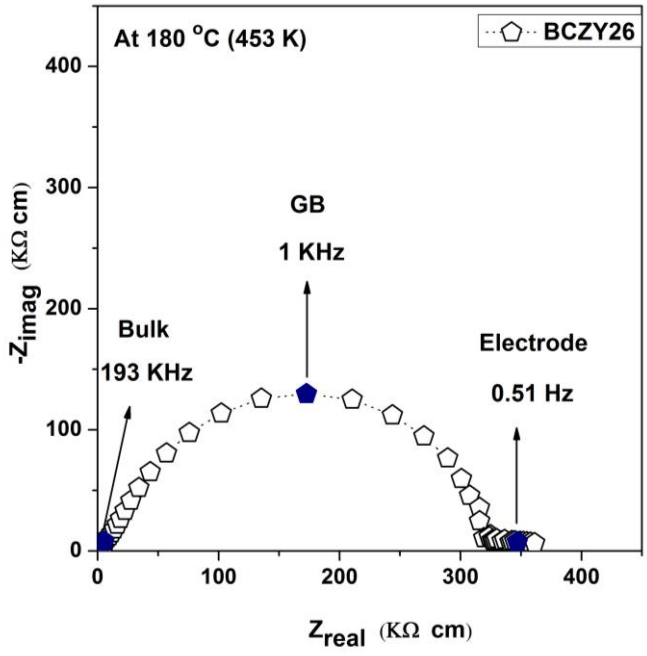

Figure A.8. Example impedance spectra measured for $BaCe_{0.8-x}Zr_xY_{0.2}O_{3-\delta}$ (x= 0.1, 0.4 and 0.6) materials under a wet N_2 atmosphere at 180ºC, pH_2O = 0.026 atm.

The impedance data were fitted to the equivalent circuit of (R1)(Q1)(R2)(Q2), where the fitting parameters extracted for each distributed arc are the resistance, R, the pseudo-capacitance, Q, and an additional parameter n which can be related to the true capacitance by the equation.

$$C = R^{(1-n)/n} Q^{1/n} \qquad \text{(A.3)}$$

The temperature dependencies of the total (bulk + grain boundary) conductivities are shown in Fig. A.9, and compared to literature values for identical compositions. One observes good correlation between literature values and the current results for compositions of the highest cerium contents, BCZY71 and BCZY44. On the other hand, the conductivity obtained for the composition BCZY26 is shown to be significantly lower than that of the literature value.

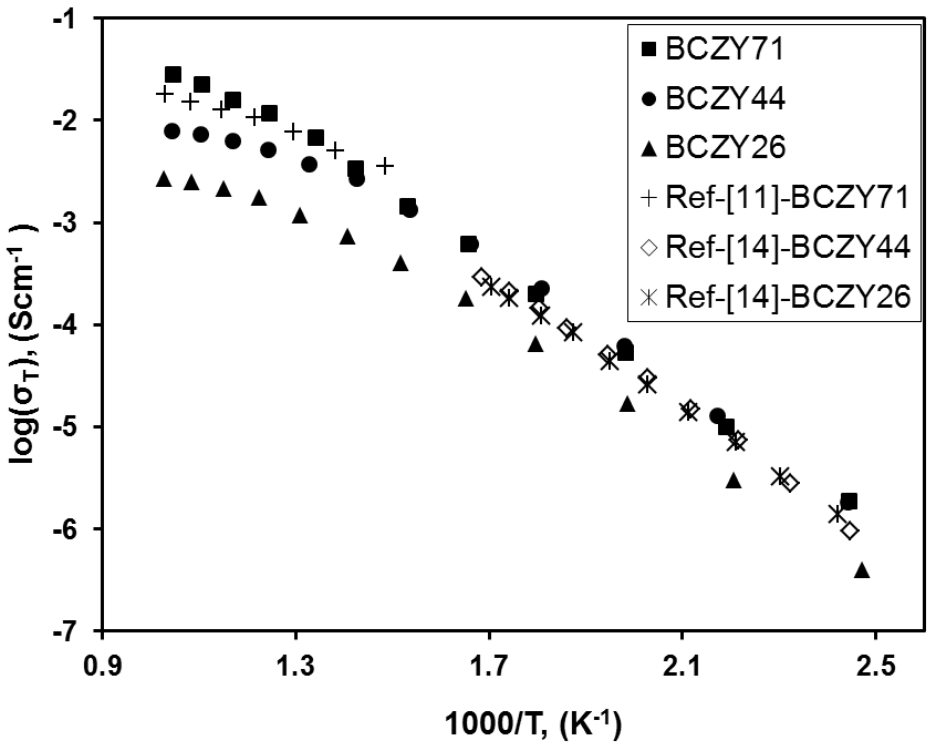

Figure A.9. The temperature dependence of the total conductivity for $BaCe_{0.8-x}Zr_xY_{0.2}O_{3-\delta}$ (x= 0.1, 0.4 and 0.6) materials under a wet N_2 atmosphere, pH_2O = 0.026 atm.

In order to investigate this behaviour further, bulk and grain-boundary responses have been de-convoluted. The bulk behaviour is shown in Fig. A.10(a). The bulk conductivity decreases with increasing Zr-content and this becomes more apparent with increasing temperature. This observation agrees well with previous literature data on $Ba(Ce,Zr,Y)O_{3-\delta}$ materials [8, 11, 17-19]. The corresponding activation energies for bulk transport are reported in Table A.3 and are shown to decrease with increasing Zr content. This trend also corresponds well with literature data for compositions that contain an identical acceptor dopant concentration, i.e. $Ba(Ce,Zr)_{0.9}Y_{0.2}O_{3-\delta}$ [19]. Nonetheless, the inverse trend has been documented in literature data for compositions of lower levels of acceptor dopant, $Ba(Ce,Zr)_{0.8}Y_{0.1}O_{3-\delta}$ [8, 11, 17, 18]. This change of behavior with acceptor dopant concentration, noted in the literature, is, therefore, intriguing and deserves further study.

Table A.3: The activation energies and grain sizes of $BaCe_{0.8-x}Zr_xY_{0.2}O_{3-\delta}$ (X = 0.1, 0.4, 0.6) proton conductors. Activation energies are calculated for data in the low temperature range (<400 ºC).

Composition	**Total E_a**	**Bulk E_a**	**Grain boundary E_a**
	eV	**eV**	**eV**
BCZY71	0.68	0.62	0.69
BCZY44	0.68	0.61	0.70
BCZY26	0.67	0.53	0.68

Analysis of the microstructure independent grain-boundary response σ_{gb}* was performed on plotting σ_{gb}* = σ_{gb}/D against temperature in the Arrhenius form (Fig. A.10(b)), where D represents the mean grain size measured by SEM analysis, Table A.2. This approach is commonly adopted in the literature [8, 37] to provide an estimation of the inherent grain-boundary properties independent of microstructure, on the assumption that the proportionality factor of the grain-boundary thickness (d) remains effectively constant. The results highlight that the microstructure independent grain boundary conductivities of compositions BCZY71 and BCZY44 (containing the larger fractions of cerium) are almost constant. In contrast, significantly lower grain boundary conductivity is obtained for the Zr-rich composition BCZY26. These results correspond to previous literature data on $Ba(Ce,Zr,Y)O_{3-\delta}$ materials that have shown only minor decreases in specific grain boundary conductivity with increasing Zr-content for cerium rich compositions [8, 11, 17], but substantial decreases in zirconium rich compositions [17, 18, 21]. The activation energy for grain boundary conduction is shown to be relatively insensitive to composition, Table A.3. From these observations, one can offer an explanation for the mismatch between the current total conductivity values of the composition BCZY26, Fig. A.9, and that of the literature value [19].

The total conductivities of materials containing large Zr-contents are highly susceptible to microstructural variations, due to their significantly lower specific grain boundary conductivities. The poor match of the total conductivity of composition BCZY26 with that of the literature is, therefore, most likely to be microstructure related and would suggest a smaller grain size in the current work. The less pronounced curvature of Fig. A.9 at higher temperature for the Ce-rich samples has previously been suggested by Ricote et al. to be a function of the non-negligible oxide-ion conductivity of these materials combined with their higher dehydration temperature [17, 18, 21].

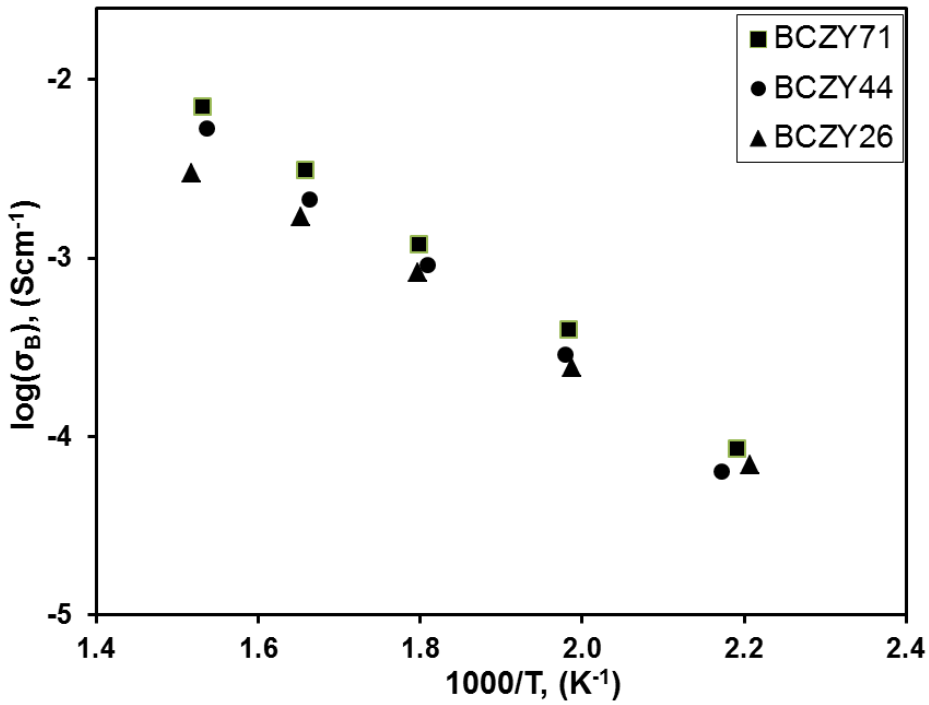

Figure A.10a. The temperature dependence of the bulk conductivity for $BaCe_{0.8-x}Zr_xY_{0.2}O_{3-\delta}$ (x= 0.1, 0.4 and 0.6) materials under a wet N_2 atmosphere, pH_2O = 0.026 atm.

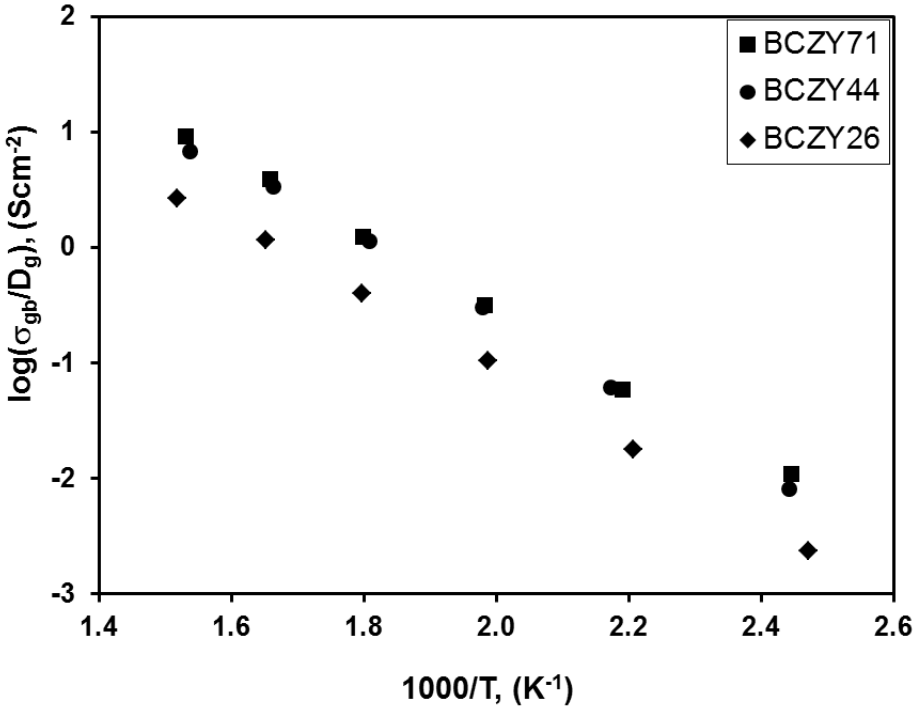

Figure A.10b. The temperature dependence of the grain boundary conductivity for $BaCe_{0.8-x}Zr_xY_{0.2}O_{3-\delta}$ (x= 0.1, 0.4 and 0.6) materials under a wet N_2 atmosphere, pH_2O = 0.026 atm.

A.4 Conclusions

$BaCe_{0.8-x}Zr_xY_{0.2}O_{3-\delta}$ (x = 0, 0.1, 0.4, 0.6 and 0.8) proton conductors were successfully prepared by a new acetate-H_2O_2 combustion method. The formation of peroxy (-OOH) bonds has been identified by FT-IR in the precursor solutions. Thus, the presence of H_2O_2 was shown to have a dual role, both as oxidizing agent for cerium, Ce^{3+} to Ce^{4+}, and in the formation of metal peroxide complexes. The combination of these phenomena is suggested to aid the new acetate-H_2O_2 combustion reaction by harnessing the oxidant required in the propellant chemistry. A close match between the lattice volumes of the current materials and those prepared by a sol gel process in the literature was noted, highlighting the efficiency of the new combustion process in the formation of stoichiometrically accurate quaternary oxides. Powders were shown to offer crystallite sizes in the nanometric range. The proton conductivity of $BaCe_{0.8-x}Zr_xY_{0.2}O_{3-\delta}$ (x = 0.1, 0.4 and 0.6) electrolytes was studied by AC impedance spectroscopy in wet N_2 atmosphere and was shown to

correspond to literature behaviour. Thus, a simple, efficient, cost effective and environmentally friendly acetate-H_2O_2 combustion method has been introduced for the synthesis of BCZY proton conductors. This new synthesis route can also be suggested for the preparation of many other ceramic oxide materials to replace classical nitrate-based processes.

A.5 References

[1] Stambouli AB, Traversa E. Solid oxide fuel cells (SOFCs): a review of an environmentally clean and efficient source of energy. Renewable Sustainable Energy Rev. 2002;6:433-55.

[2] Haile S. Fuel cell materials and components. Acta Mater. 2003;51:5981-6000.

[3] Tu C-S, Chien RR, Schmidt VH, Lee S-C, Huang C-C, Tsai C-L. Thermal stability of $Ba(Zr_{0.8-x}Ce_xY_{0.2})O_{2.9}$ ceramics in carbon dioxide. J Appl Phys. 2009;105:103504.

[4] Fabbri E, Pergolesi D, Traversa E. Electrode materials: a challenge for the exploitation of protonic solid oxide fuel cells. Sci Technol Adv Mater. 2010;11:044301.

[5] Magrez A, Schober T. Preparation, sintering, and water incorporation of proton conducting $Ba_{0.99}Zr_{0.8}Y_{0.2}O_{3-\delta}$: comparison between three different synthesis techniques. Solid State Ionics. 2004;175:585-8.

[6] Orera A, Slater PR. New Chemical Systems for Solid Oxide Fuel Cells†. Chem Mater. 2009;22:675-90.

[7] Fabbri E, Pergolesi D, Traversa E. Materials challenges toward proton-conducting oxide fuel cells: a critical review. Chem Soc Rev. 2010;39:4355-69.

[8] Yamazaki Y, Hernandez-Sanchez R, Haile SM. Cation non-stoichiometry in yttrium-doped barium zirconate: phase behavior, microstructure, and proton conductivity. J Mater Chem. 2010;20:8158-66.

[9] Iguchi F, Sata N, Yugami H. Proton transport properties at the grain boundary of barium zirconate based proton conductors for intermediate temperature operating SOFC. J Mater Chem. 2010;20:6265-.

[10] Peng R, Wu T, Liu W, Liu X, Meng G. Cathode processes and materials for solid oxide fuel cells with proton conductors as electrolytes. J Mater Chem. 2010;20:6218-25.

[11] Barison S, Battagliarin M, Cavallin T, Doubova L, Fabrizio M, Mortalò C, et al. High conductivity and chemical stability of $BaCe_{1-x-y}Zr_xY_yO_{3-\delta}$ proton conductors prepared by a sol–gel method. J mat chem. 2008;18:5120.

[12] Chick LA, Pederson LR, Maupin GD, Bates JL, Thomas LE, Exarhos GJ. Glycine-nitrate combustion synthesis of oxide ceramic powders. Mater Lett. 1990;10:6-12.

[13] Chien RR, Tu CS, Schmidt VH, Lee SC, Huang CC. Synthesis and characterization of proton-conducting $Ba(Zr_{0.8-x}Ce_xY_{0.2})O_{2.9}$ ceramics. Solid State Ionics. 2010;181:1251-7.

[14] Fabbri E, Depifanio A, Dibartolomeo E, Licoccia S, Traversa E. Tailoring the chemical stability of $Ba(Ce_{0.8-x}Zr_x)Y_{0.2}O_{3-\delta}$ protonic conductors for Intermediate Temperature Solid Oxide Fuel Cells (IT-SOFCs). Solid State Ionics. 2008;179:558-64.

[15] Guo Y, Lin Y, Ran R, Shao Z. Zirconium doping effect on the performance of proton-conducting $BaZr_yCe_{0.8-y}Y_{0.2}O_{3-\delta}$ ($0.0 \leq y \leq 0.8$) for fuel cell applications. J Power Sources. 2009;193:400-7.

[16] Ma X, Dai J, Zhang H, Reisner DE. Protonic conductivity nanostructured ceramic film with improved resistance to carbon dioxide at elevated temperatures. Surf Coat Technol. 2005;200:1252-8.

[17] Ricote S, Bonanos N, Manerbino A, Coors WG. Conductivity study of dense $BaCe_xZr_{(0.9-x)}Y_{0.1}O_{(3-\delta)}$ prepared by solid state reactive sintering at 1500 °C. Int J Hydrogen Energy. 2012;37:7954-61.

[18] Ricote S, Bonanos N, Marco de Lucas MC, Caboche G. Structural and conductivity study of the proton conductor $BaCe_{(0.9-x)}Zr_xY_{0.1}O_{(3-\delta)}$ at intermediate temperatures. J Power Sources. 2009;193:189-93.

[19] Sawant P, Varma S, Wani BN, Bharadwaj SR. Synthesis, stability and conductivity of $BaCe_{0.8-x}Zr_xY_{0.2}O_{3-\delta}$ as electrolyte for proton conducting SOFC. Int J Hydrogen Energy. 2012;37:3848-56.

[20] Zuo C, Zha S, Liu M, Hatano M, Uchiyama M. $Ba(Zr_{0.1}Ce_{0.7}Y_{0.2})O_{3-\delta}$ as an Electrolyte for Low-Temperature Solid-Oxide Fuel Cells. Adv Mater. 2006;18:3318-20.

[21] Ricote S, Bonanos N, Caboche G. Water vapour solubility and conductivity study of the proton conductor $BaCe_{(0.9-x)}Zr_xY_{0.1}O_{(3-\delta)}$. Solid State Ionics. 2009;180:990-7.

[22] Aruna ST, Mukasyan AS. Combustion synthesis and nanomaterials. Curr Opin Solid State Mater Sci. 2008;12:44-.

[23] Deganello F, Marcì G, Deganello G. Citrate–nitrate auto-combustion synthesis of perovskite-type nanopowders: A systematic approach. J Eur Ceram Soc. 2009;29:439-.

[24] Mohebbi H, Ebadzadeh T, Hesari FA. Synthesis of nano-crystalline (Ni/NiO)–YSZ by microwave-assisted combustion synthesis method: The influence of pH of precursor solution. J Power Sources. 2008;178:64-8.

[25] Narendar N, Mather GC, Dias PAN, Fagg DP. The importance of phase purity in Ni–$BaZr_{0.85}Y_{0.15}O_{3-\delta}$ cermet anodes – novel nitrate-free combustion route and electrochemical study. RSC Advances. 2013;3:859-69.

[26] Jain SR, Adiga KC, Pai Verneker VR. A new approach to thermochemical calculations of condensed fuel-oxidizer mixtures. Combust Flame. 1981;40:71-9.

[27] Rodríguez-Carvajal J. Recent advances in magnetic structure determination by neutron powder diffraction. Physica B. 1993;192:55-69.

[28] Patterson AL. The Scherrer Formula for X-Ray Particle Size Determination. Phys Rev. 1939;56:978-82.

[29] Cho S-Y, Kim I-T, Kim D-Y, Park SJ, Kim B-K, Lee J-H. Effects of H_2O_2 on the morphology of ZrO_2 powder prepared by ultrasonic spray pyrolysis. Mater Lett. 1997;32:271-3.

[30] Lee J-S, Choi S-C. Crystallization behavior of nano-ceria powders by hydrothermal synthesis using a mixture of H_2O_2 and NH_4OH. Mater Lett. 2004;58:390-3.

[31] Mandal BP, Grover V, Pai MR, Tyagi AK. Improvement of physico-chemical properties by addition of H2O2: An extensive case study on the RE-doped ceria system (RE = Gd, Sm). J Mater Res. 2011;24:2845-54.

[32] Navio JA, Colon G, Sanchez-Soto PJ, Macias M. Effects of H_2O_2 and SO_4^{2-} Species on the Crystalline Structure and Surface Properties of ZrO_2 Processed by Alkaline Precipitation. Chem Mater. 1997;4756:1256-.

[33] Panova TI, Popov VP, Glushkova VB, Domanskii AV. Preparation of nanodisperse solid solutions based on ZrO_2 and HfO_2 from hydroperoxides. Glass Phys Chem. 2007;33:652-7.

[34] Pappacena A, Porreca P, Boaro M, de Leitenburg C, Trovarelli A. Effect of process modification and presence of H_2O_2 in the synthesis of samaria-doped ceria powders for fuel cell applications. Int J Hydrogen Energy. 2012;37:1698-709.

[35] Scholes FH, Soste C, Hughes AE, Hardin SG, Curtis PR. The role of hydrogen peroxide in the deposition of cerium-based conversion coatings. Appl Surf Sci. 2006;253:1770-80.

[36] Woodhead JL. Process for preparing aqueous dispersion of ceria and resulting product. . U.S. Patent1980. p. 231893.

[37] Soares HS, Zhang X, Antunes I, Frade JR, Mather GC, Fagg DP. Effect of phosphorus additions on the sintering and transport properties of proton conducting $BaZr_{0.85}Y_{0.15}O_{3-\delta}$. J Solid State Chem. 2012;191:27-32.